

# Sheffield Hallam University

*Research and development of CdTe based thin film PV solar cells*

DISO, Dahiru Garba

Available from the Sheffield Hallam University Research Archive (SHURA) at:

<http://shura.shu.ac.uk/4941/>

## A Sheffield Hallam University thesis

This thesis is protected by copyright which belongs to the author.

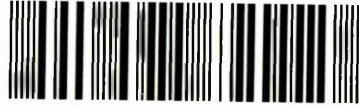
The content must not be changed in any way or sold commercially in any format or medium without the formal permission of the author.

When referring to this work, full bibliographic details including the author, title, awarding institution and date of the thesis must be given.

Please visit <http://shura.shu.ac.uk/4941/> and <http://shura.shu.ac.uk/information.html> for further details about copyright and re-use permissions.

Learning and Information Services  
Adsetts Centre, City Campus  
Sheffield S1 1WD

102 006 840 X



Sheffield Hallam University  
Learning and Information Services  
Adsetts Centre, City Campus  
Sheffield S1 1WD

**REFERENCE**

ProQuest Number: 10694443

All rights reserved

INFORMATION TO ALL USERS

The quality of this reproduction is dependent upon the quality of the copy submitted.

In the unlikely event that the author did not send a complete manuscript and there are missing pages, these will be noted. Also, if material had to be removed, a note will indicate the deletion.



ProQuest 10694443

Published by ProQuest LLC (2017). Copyright of the Dissertation is held by the Author.

All rights reserved.

This work is protected against unauthorized copying under Title 17, United States Code  
Microform Edition © ProQuest LLC.

ProQuest LLC.  
789 East Eisenhower Parkway  
P.O. Box 1346  
Ann Arbor, MI 48106 – 1346

# **Research and Development of CdTe based Thin Film PV Solar Cells**

**Dahiru Garba Diso**

**A thesis submitted in partial fulfilment of the requirements of  
Sheffield Hallam University  
for the degree of Doctor of Philosophy**

**October 2011**

---

## **Declaration**

I hereby declare that this thesis is my own work and it has not been submitted anywhere for any award.

## Abstract

The motivation behind this research is to bring cheap, low-cost and clean energy technologies to the society. Colossal use of fossil fuel has created noticeable pollution problems contributing to climate change and health hazards. Silicon based solar cells have dominated the market but its cost is high due to the manufacturing process. Therefore, the way forward is to develop thin film solar cells using low-cost attractive materials, grown by cheaper, scalable and manufacturable techniques.

The aim and objectives of this work is to develop low-cost, high efficiency solar cell using electrodeposition (ED) technique. The material layers include CdS and ZnTe as the window materials, while the absorber material is CdTe. Fabricating a suitable devices for solar energy conversion (i.e. glass/conducting glass/window material/absorber material/metal) structure. Traditional way of fabricating this structure is to grow window material (CdS) using chemical bath deposition (CBD) and absorber material (CdTe) using electrodeposition. However, CBD is a batch process and therefore creates large volumes of Cd-containing waste solutions each time adding high cost in manufacturing process. This research programme is therefore on development of an "All ED-solar cells" structure.

Material studies were carried out using photoelectrochemical (PEC) studies, UV-Vis spectrophotometry, X-ray diffraction (XRD), X-ray fluorescence (XRF), scanning electron microscopy (SEM), atomic force microscopy (AFM), Raman spectroscopy and X-ray photoelectron spectroscopy (XPS). Furthermore, the electrical characterisation of fully fabricated devices was performed using current-voltage (I-V) and capacitance-voltage (C-V) measurements.

This research programme has demonstrated that CdS and ZnTe window materials can be electrodeposited and used in thin film solar cell devices. The CdS electrolytic bath can be used for a period of 7 months without discarding it like in the CBD process which usually has life-time of 2-3 days. Further work should be carried out to increase the life-time of this bath, so that there can be used continuously minimising waste solution production in a manufacturing line.

An efficiencies showing up to 7% was achieved for complete devices. However, the consistency and reproducibility remains un-resolved due to production of efficiencies between (2 - 7)% efficient devices varying from batch to batch. One of the reasons has been identified as the growth of CdS nano-rods with spacing between them. This is the first observation of CdS nano-rods and could open up many applications in nano-devices area. In order to improve the consistency of the solar cell efficiency, CdS layers should be grown with nano-rods aligned perpendicular to the glass surface and with tight packing without gaps, or with uniform coverage of CdS over the conducting glass surface.

The possibility of growth of CdTe absorber layers with n- and p-type electrical conduction using change of stoichiometry was confirmed using the results presented in this thesis. This is a key finding, important to form multi-layer solar cell structures in the future.

## Acknowledgement

In the name of Allah, the most Beneficent, the most Merciful. Peace and blessing of Allah be upon to His noble prophet Muhammad (*Sallallahu Alaihi Wassallam*). Every *hamd*, every thanks, belong to Him by right.

I wish to express my profound gratitude to my Director of studies Professor I. M. Dharmadasa for immense guidance and excellent supervision in the course of the thesis and for his cooperation throughout my stay with him in the University. I also extend my intrinsic thanks to my second supervisor Dr. K. Vernon-Parry for her critical comments and advice. My thanks also go to Electronic Materials & Sensors Group members and all staff within MERI. My special thanks go to Mr. S. Creasy for carrying out SEM measurements.

I would not forget with the support from our two collaborators Institute for Materials Research, University of Leeds, UK in particular Mr. M. Murray and Prof. M. B. Dergacheva from Institute of Organic Catalysis & Electrochemistry, Kazakhstan for carrying out Raman, XPS and AFM measurements.

I also wish to express my special gratitude to Kano University of Science and Technology, Wudil-Nigeria for **FUNDING** my PhD programme. I wish to thank all my colleagues of Physics Department, KUST Wudil and the University at large. I am most grateful to all my *Dala'ilul Khairat* members, *Safinatul Khairi* Foundation members and Habeeb Family who assisted me a lot in carrying out this research in one way or the other.

I would like to express my appreciation to my beloved wife, Ummul-Khair and my children: Hajarat, Abubakar, Usman and Khadija. My sincere thanks go to my brother Siyudi Haruna and all my brothers and sisters who take care of my family while I was away during my study leave period in Sheffield. Above all, special thanks to Almighty Allah (*Subhanahu Wata'ala*) for sparing and guiding me throughout, and blessing continuously be upon to his noble prophet Muhammad (*Sallallahu Alaihi Wassallam*).

# Table of Contents

Declaration	i
Abstract	ii
Acknowledgement	iii
Contents	iv
List of publications	xi
List of abbreviations and symbols	xiii
<b>Chapter 1: Introduction</b>	<b>1</b>
1.1 Solar Radiation	1
1.1.1 The solar spectrum	1
1.2 Utilisation of Solar Energy	3
1.2.1 Types of Solar Energy Technology	4
1.3 Theory of solar cells	5
1.3.1 Semiconductor concepts	5
1.3.1.1 p-n junction	5
1.3.1.2 Metal-Semiconductor junction	7
1.4 Photovoltaic Effects	9
1.4.1 Photovoltaic Technologies	9
1.4.1.1 Silicon based photovoltaic devices	12
1.4.1.2 Other type of solar cells	16
1.5 Thin Films Solar Cells	19
1.5.1 CdTe	20
1.5.2 CIGS	24
1.5.3 Multi-junction solar cell	24
1.6 Window Materials	27
1.7 Transparent Conducting Oxides (TCOs)	28
1.8 Motivation, Aim and objectives	29
References	32

<b>Chapter 2:</b>	<b>Growth Techniques and Characterisation</b>	<b>38</b>
2.1	Growth Techniques	38
2.1.1	Physical Vapour Deposition (PVD)	38
2.1.1.1	Sputtering	38
2.1.1.2	Thermal evaporation	39
2.1.2	Chemical Vapour Deposition (CVD)	39
2.1.2.1	Metal-Organic CVD (MOCVD)	40
2.1.3	Molecular Beam Epitaxy (MBE)	41
2.1.4	Close Space Sublimation (CSS)	42
2.1.5	Liquid-Phase Deposition	44
2.1.5.1	Spray pyrolysis	44
2.1.5.2	Screen printing	45
2.1.5.3	Inkjet printing	46
2.1.5.4	Chemical Bath Deposition (CBD)	47
2.1.6	Electrodeposition (ED)	48
2.1.6.1	Over view of ED	48
2.1.6.2	ED in General	48
2.1.6.3	Theory of ED	52
2.1.6.4	Equation related to ED of CdS, ZnTe and CdTe	54
2.2	Material characterisation	55
2.2.1	X-ray diffraction (XRD)	55
2.2.2	Photoelectrochemical (PEC) cell	57
2.2.3	Optical absorption	59
2.2.4	Scanning Electron Microscopy (SEM)	60
2.2.5	Atomic Force Microscopy (AFM)	61
2.2.6	X-ray Fluorescence (XRF)	62
2.2.7	Raman Spectroscopy	63
2.2.8	X-ray Photoelectron Spectroscopy (XPS)	64
2.3	Device characterisation	65

2.3.1	Current Voltage (I-V) characteristics	65
2.3.2	Capacitance Voltage (C-V) characteristics	69
	References	71
<b>Chapter 3:</b>	<b>Experimental</b>	<b>76</b>
3.1	Introduction	76
3.2	Electrolyte preparation and deposition of CdS thin film	77
3.3	Electrolyte preparation and deposition of ZnTe thin film	78
3.4	Electrolyte preparation and deposition of CdTe thin film	78
3.5	Chemicals used to clean the substrates	79
3.6	Material characterisation	79
3.7	Solar cell completion	80
3.7.1	CdCl <sub>2</sub> /heat treatment	81
3.7.2	Surface etching	81
3.7.3	Formation of back metal contact	82
3.8	Current-Voltage (I-V) measurement	83
	References	84
<b>Chapter 4:</b>	<b>Electrodeposition of CdS (Window material-1)</b>	<b>85</b>
4.1	Motivation and objectives	85
4.2	Introduction	85
4.3	Linear sweep voltammogram	85
4.4	Visual Appearance	86
4.5	Characterisation of Electrodeposited CdS	88
4.5.1	X-ray diffraction	88
4.5.2	Photoelectrochemical (PEC) cell	89
4.5.3	Optical absorption	91
4.5.4	Scanning Electron Microscopy	93
4.5.5	Energy Dispersive X-ray	94
4.5.6	Atomic Force Microscopy	95

4.5.7	X-ray Fluorescence	97
4.5.8	Raman Spectroscopy	98
4.5.9	X-ray Photoelectron Spectroscopy	99
4.6	Summary	102
	References	104
<b>Chapter 5:</b>	<b>Electrodeposition of ZnTe (Window material-2)</b>	<b>106</b>
5.1	Motivation and objectives	106
5.2	Introduction	106
5.3	Linear sweep voltammogram	106
5.4	Visual Appearance	108
5.5	Characterisation of Electrodeposited ZnTe	108
5.5.1	X-ray diffraction	108
5.5.2	Photoelectrochemical (PEC) cell	110
5.5.3	Optical absorption	110
5.5.4	Scanning Electron Microscopy	111
5.5.5	Energy Dispersive X-ray	112
5.5.6	Atomic Force Microscopy	113
5.5.7	Raman Spectroscopy	114
5.5.8	X-ray Photoelectron Spectroscopy	115
5.6	Summary	118
	References	120
<b>Chapter 6:</b>	<b>Growth and Optimisation of CdTe deposition voltage</b>	<b>121</b>
6.1	Motivation and objectives	121
6.2	Introduction	121
6.3	Linear sweep voltammogram	121
6.4	Characterisation of CdTe	122
6.4.1	Photoelectrochemical (PEC) cell	122
6.4.2	X-ray diffraction	124

6.4.3	Optical absorption	128
6.4.4	Scanning Electron Microscopy	130
6.4.5	Energy Dispersive X-ray	132
6.4.6	Atomic Force Microscopy	133
6.4.7	Raman Spectroscopy	134
6.4.8	X-ray Photoelectron Spectroscopy	135
6.5	Device characterisation	137
6.5.1	Current Voltage (I-V) characteristics	137
6.6	Structure performance relationship	139
6.7	Summary	141
	References	143
<b>Chapter 7:</b>	<b>Effect of growth time on CdTe layer thickness</b>	<b>144</b>
7.1	Motivation and objectives	144
7.2	Introduction	144
7.3	Thickness Measurement	145
7.4	Characterisation of CdTe thickness	146
7.4.1	X-ray diffraction	146
7.4.2	Optical absorption	148
7.4.3	Scanning Electron Microscopy	151
7.4.4	Energy Dispersive X-ray	153
7.4.5	Raman Spectroscopy	154
7.5	Device characterisation	155
7.5.1	Current Voltage (I-V) characteristics	155
7.5.2	Capacitance Voltage (C-V) characteristics	161
7.6	Growth process performance relationship	162
7.7	Summary	163
	References	165

<b>Chapter 8:</b>	<b>Effect of CdCl<sub>2</sub>/heat treatment on CdS/CdTe solar cells</b>	<b>167</b>
8.1	Motivation and objectives	167
8.2	Introduction	167
8.3	Characterisation of CdTe	168
8.3.1	X-ray diffraction	168
8.3.2	Optical absorption	171
8.3.3	Scanning Electron Microscopy	175
8.3.4	Energy Dispersive X-ray	176
8.3.5	Raman Spectroscopy	176
8.4	Device characterisation	178
8.4.1	Current Voltage (I-V) characteristics	178
8.5	Process performance relationship	181
8.6	Summary	183
	References	185
<b>Chapter 9:</b>	<b>Effect of CdS thickness on CdS/CdTe solar cell performance</b>	<b>186</b>
9.1	Motivation and objectives	186
9.2	Introduction	186
9.3	Thickness measurement	187
9.4	Characterisation of CdTe	188
9.4.1	X-ray diffraction	188
9.4.2	Optical absorption	191
9.4.3	Scanning Electron Microscopy	193
9.4.4	Energy Dispersive X-ray	195
9.4.5	Raman Spectroscopy	196
9.5	Device characterisation	197
9.5.1	Current Voltage (I-V) characteristics	197
9.6	Process performance relationship	199
9.7	Summary	201

References	203
<b>Chapter 10: Effect of different Transparent Conducting Oxides (TCOs) on the CdTe layer</b>	<b>204</b>
10.1 Motivation and objectives	204
10.2 Introduction	204
10.3 Characterisation of CdTe on TCOs	205
10.3.1 X-ray diffraction	205
10.3.2 Optical absorption	208
10.3.3 Scanning Electron Microscopy	210
10.3.4 Energy Dispersive X-ray	212
10.3.5 Raman Spectroscopy	213
10.4 Device characterisation	215
10.4.1 Current Voltage (I-V) characteristics	215
10.5 Relationship between performance and TCOs	217
10.6 Summary	219
References	221
<b>Chapter 11: Future Work</b>	<b>222</b>

## List of Publications

### Journal papers:

1. D. G. Diso, G. Muftah, V. Patel and I. M. Dharmadasa, Growth of CdS layers to develop all-electrodeposited CdS/CdTe Thin Film Solar Cells, J. of Electrochem. Soc. 157(6), H647 (2010).
2. D. G. Diso, F. Fauzi, O. K. Echendu, A. R. Weerasinghe and I. M. Dharmadasa, Electrodeposition and characterisation of ZnTe layers for application in CdTe based multi-layer graded bandgap solar cells, Journal of Physics: Conference Series 286 (2011) 012040.

### Submitted:

1. D. G. Diso, A. R. Weerasinghe, O. K. Echendu, F. Fauzi and I. M. Dharmadasa, Effect of Zn concentrations on electrodeposited ZnTe thin films, Thin Solid Films, (TSF-D-11-01291), (June, 2011).

### Conference papers:

1. D. G. Diso, F. Fauzi, O. K. Echendu, A. R. Weerasinghe and I. M. Dharmadasa, Electrodeposition and characterisation of ZnTe layers for application in CdTe based multi-layer graded bandgap solar cells, In proc: CMMP 10 held at the University of Warwick, UK, (2011).
2. I. M. Dharmadasa, D. G. Diso, A. R. Weerasinghe, A. M. B. Chandima, D. S. M. de Silva, K. A. S. Pathiratne, M. B. Dergacheva, K.A. Mit and K. A. Urazov, Nano-Rod nature of CdS window materials used in thin film solar cells, 7<sup>th</sup> PVSAT at Heriot-Watt University, UK, (2011).
3. A. R. Weerasinghe, O. K. Echendu, D. G. Diso and I. M. Dharmadasa, Study of Electrodeposited ZnS thin films grown with ZnSO<sub>4</sub> and (NH<sub>4</sub>)<sub>2</sub>S<sub>2</sub>O<sub>3</sub> processor for use in solar cell, In proc: Solar Asia International Conference, Kandy, Sri Lanka, (2011).

4. O. K. Echendu, D. G. Diso, A. R. Weerasinghe, F. Fauzi and I. M. Dharmadasa, Electrodeposited II-VI Semiconductor Window materials for solar cells, In proc: 12<sup>th</sup> ECOF held at Sheffield Hallam University, UK, (2011).

**Submitted:**

1. D. G. Diso, O. K. Echendu, M. Murray, A. Jha, S. Creasy and I. M. Dharmadasa, Effect on different Transparent Conducting Oxides (TCOs) on electrodeposited CdTe, 11<sup>th</sup> Condense Matter & Material Physics Conference.
2. O. K. Echendu, A. R. Weerasinghe, D. G. Diso, F. Fauzi and I. M. Dharmadasa, Concentration dependence of the electrical conductivity of electrodeposited ZnS thin films, 11<sup>th</sup> Condense Matter & Material Physics Conference.

## List of abbreviations and symbols

### Abbreviations

CdS	Cadmium Sulphide
Cl	Chlorine
CIGS	Copper Indium Gallium Diselenide
CdTe	Cadmium Telluride
ZnTe	Zinc Telluride
ED	Electrodeposition
CBD	Chemical Bath Deposition
MBE	Molecular Beam Epitaxy
CSS	Close space sublimation
C-V	Capacitance Voltage
FF	Fill Factor
FTO	Fluorine doped Tin Oxide
i-ZnO	i-Zinc Oxide
ITO	Indium Tin Oxide
ZnO:Al	Aluminium doped Zinc Oxide
FWHM	Full Width at Half Maximum
I	Light Intensity
$I_0$	Intensity of the Incident Radiation
$J_{sc}$	Short Circuit Current Density
I-V	Current Voltage
M	Moles

n	Idiality Factor
A	Area
Abs	Absorbance
AM	Air Mass
XPS	X-ray Photoelectron Spectroscopy
EDX	Energy Dispersive X-ray
Au	Gold
CdO	Cadmium Oxide
T	Temperature (K)
T	Transmission
TCO	Transparent Conductive Oxide
$V_{oc}$	Open Circuit Voltage
XRD	X-ray diffraction
XRF	X-Ray Fluorescence
PEC	Photoelectrochemical Cell
R	Resistance
$R_s$	Series Resistance
$R_{sh}$	Shunt Resistance
S	Sulphur
Zn	Zinc
$TeO_2$	Tellurium Oxide
Te	Tellurium
SEM	Scanning Electron Microscopy

AFM	Atomic Force Microscopy
SnO <sub>2</sub>	Tin oxide
UV	Ultraviolet
IR	Infrared
PV	Photovoltaic
R&G	Recombination and Generation
CdCl <sub>2</sub>	Cadmium Chloride
V <sub>g</sub>	Growth Voltage
LO	Longitudinal optical phonon
TO	Transverse optical phonon

### Symbols

$\phi_b$	Potential barrier height
$\phi_m$	Work function of metal
$\phi_s$	Work function of semiconductor
G	Gibbs free energy
h	Planks constant
k	Boltzmann constant
N <sub>A</sub>	Acceptor concentration
N <sub>D</sub>	Donor concentration
n <sub>i</sub>	Intrinsic charge carrier density
R	Gas constant
t	Time (s)

$\nu$	Frequency
$V_{bi}$	Built in potential
$\alpha$	Absorption coefficient
$A^*$	Effective Richardson constant
$a_p$	Activity product
$a_r$	Activity reactant
$c$	Speed of light
$e$	Magnitude of electron charge
$\epsilon_0$	Permittivity of free space
$\epsilon_r$	Relative permittivity
$F$	Faradays constant
$E_i$	Internal Electric Field

# Chapter 1: Introduction

## 1.1 Solar Radiation

The sun is a star with a diameter of about  $1.39 \times 10^8$  km and accounts for about 98.6% by mass of all the solar system. The mean distance of the sun from the earth is approximately  $1.5 \times 10^8$  km, and its light travels this mean distance in 8 minutes and 19 seconds. The chemical elements primarily composing the sun's mass are: hydrogen (about 74%) and helium (25%); the rest is made up of trace quantities of heavier elements [1, 2]. All life on the earth is supported by the energy received from the sun through solar radiation via photosynthesis and the earth's climate and weather derived from it.

The solar energy reaching the periphery of the earth's atmosphere is considered to be constant for all practical purposes; this is called the **solar constant** and has the value of  $\sim 1.353 \text{ kWm}^{-2}$  [3]. The solar constant is estimated on the basis of the solar radiation received on a unit area exposed perpendicularly to the rays of the sun at an average distance between the sun and the earth.

### 1.1.1 The solar spectrum

The solar spectrum (and the electromagnetic radiation emitted by the sun) contains both ionizing radiation (x-rays and gamma rays) and non-ionizing radiation (UV, visible and Infrared).

Figure 1.1 shows the solar radiation spectrum. Both the intensity and spectral distribution of the radiation arriving at the earth's surface depend on the composition of the atmosphere as well as the path length of the radiation through the atmosphere. Nitrogen ( $\text{N}_2$ ), oxygen ( $\text{O}_2$ ) and water are the major constituents of the present atmosphere. Their percentage compositions are:  $\text{N}_2$   $\sim 78\%$ ,  $\text{O}_2$   $\sim 21\%$  and mineral constituents 1% which includes Ar (0.93%) and  $\text{CO}_2$  (0.03%) [4].

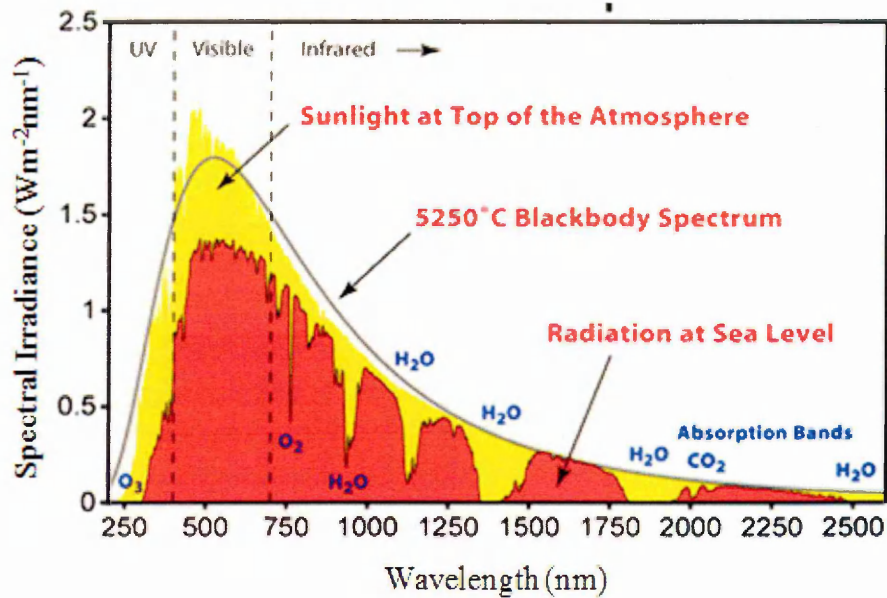


**Figure 1.1:** Solar radiation spectrum [5].

The solar spectrum can be divided into three main regions [3]:

1. 3UV region ( $\lambda < 400$  nm) contains ~5% of the irradiance
2. V3isible region ( $400$  nm  $< \lambda < 700$  nm) contains ~43% of the irradiance
3. Infrared region ( $\lambda > 700$  nm) contains ~52% of the irradiance.

When the sunlight passes through the atmosphere some of the radiation is reflected, some absorbed, and some diffusely scattered. The longer the path length of the sunlight through the earth's atmosphere, the more the sunlight is attenuated and the solar spectrum from the sun modified. The minimum path length will occur when the sun is directly overhead, and the path length increases the lower the sun is in the sky. The path length through the atmosphere is characterized by the term air-mass (AM). It is defined as the thickness of the air layer around the earth through which sunlight passes. Figure 1.2 shows the path length of sunlight through the atmosphere down to the earth's surface.

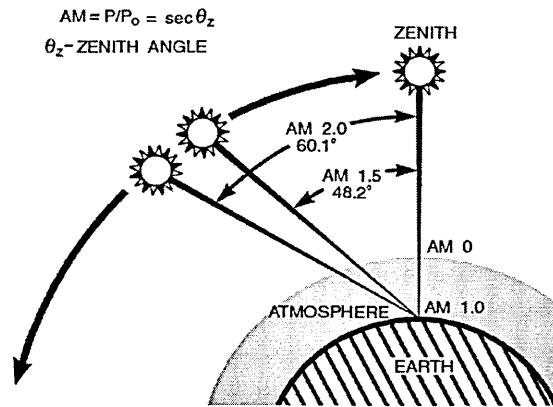


**Figure 1.2:** Path length of the sunlight through the atmosphere [6].

The air-mass may also be defined as;

$$AM = \frac{1}{\cos \theta_z} = \sec \theta_z \quad 1.1$$

where  $\theta_z$  is the angle made between the sun and the zenith.

The power level of the solar spectrum in outer space, where there is no absorption of the radiation is termed as air-mass-zero (AM0) spectrum and it is the most relevant for space applications. AM1.0 refers to the spectrum received on the earth's surface when the sun is directly over-head and the power incident per unit area is taken to be  $925 \text{ Wm}^{-2}$ . The AM1.5 spectrum is the most widely used terrestrial standard for evaluating solar cells. It is the solar spectral irradiance distribution incident at sea level from the sun at  $48.2^\circ$  from the normal to the position. The total incident power for AM1.5 is  $\sim 100 \text{ Wm}^{-2}$ .

## 1.2 Utilization of Solar Energy

Solar energy can be utilized in various ways either in stored energy in the forms of fossil fuels and nuclear power (called non-renewable energy), or directly from sources such as wind, tidal, photovoltaic/thermal, biomass and hydro-power (called renewable energy).

(a) **Non-Renewable Energy:** The use of non-renewable energy sources is responsible for the emission of many pollutants, e.g. coal and gas-fired power stations

release large quantities of oxides of carbon, sulphur and nitrogen into the atmosphere, polluting the global environment and causing health problems. Fossil fuels are the main source of this non-renewable energy. They are produced from fossilized remains of dead plants and animals by exposure to heat and pressure in the earth's crust over hundreds of millions of years. The major fossil fuels are coal, oil and gas.

(b) **Renewable Energy:** Renewable energies are clean, environmentally friendly and endless in supply. Among all the renewable energies, photovoltaic (PV) technology is the best because it converts the sun's rays directly into electricity without involvement of moving parts or emitting pollutants. It offers a clean, reliable source of electricity once installed.

### **1.2.1 Types of Solar Energy Technologies**

(a) **Passive solar system:** This is the process in which the sun's energy is converted directly into heat for use at the site where it is collected. Infrared radiation is absorbed by a surface which then heats up. This system does not require any moving parts and the technique is used to dry food and clothes. Sea water is also evaporated to produce salt.

(b) **Active solar system:** The process is similar to (a) above but the heat must be transferred from the collection area to the place of use. A pump and a system of pipes are required to transfer this heat. A device called a flat plate collector is used for this purpose. Water is circulated through tubes under a glass cover plate over a black background surface. The black surface absorbs the infrared radiation entering the glass box. The glass absorbs the longer wave radiation emitted from the black material, and therefore heats the circulating water in the tubes to  $\sim(38 - 93)^{\circ}\text{C}$ . An active solar system has moving parts; it also has operation and maintenance costs like any other heating or cooling system.

(c) **Photovoltaic:** A device that converts light energy directly into electrical energy is called a solar cell or photovoltaic cell. Light absorbing materials are required in all solar cells which absorb photons and generate electrons via the photovoltaic effect. PV modules and panels are fabricated from a collection of solar cells. When charged by the sun, the cell can be considered as a two terminal device which conducts like a diode in the dark and generates electric power. A module is a collection of cells connected in series and typically contains 28 to 36 cells which generate a d.c. output voltage of

desired values (say 12 V) in standard illumination conditions. For larger current and voltage output, an array can be generated by connecting the 12 V modules in parallel and series according to the power demanded by the application.

### 1.3 Theory of solar cells

#### 1.3.1 Semiconductors concepts

Materials which have a relatively small bandgap up to a few electron volts (0.40 - 4.00) eV in the distribution of allowed energy levels are called semiconductors. A pure semiconductor material become an insulator at temperature  $T = 0$  K and in this case the conduction band ( $E_c$ ) is completely empty and the valence band ( $E_v$ ) is completely filled with electrons. The probability  $F(E)$  of finding an electron in energy state  $E$  is given by Fermi-Dirac distribution relationship [7]:

$$F(E) = \frac{1}{1 + \exp\left(\frac{E - E_f}{kT}\right)} \quad 1.2$$

where  $k$  is the Boltzmann constant,  $T$  is the absolute temperature and  $E_f$  is the Fermi energy level.

##### 1.3.1.1 p-n junction

A p-n junction can be a homojunction, in which both sides of the junction are made of the same material, or a heterojunction, consisting of two different materials. Free electrons from the n-type region and free holes from the p-type region diffuse across the junction when they are brought in contact. At the junction, recombination takes place when an electron meets a hole and as a result it becomes depleted. The diffusion of electrons leaves positively charged ionised donors on the n-side and on the p-side negatively charged ionised acceptors are left behind after the diffusion of holes. An internal electric field  $E_i$  is developed between these two charged layers. Figure 1.3 (a) and (b) shows the schematic diagram of a simple p-n junction and its equivalent energy band diagram respectively.

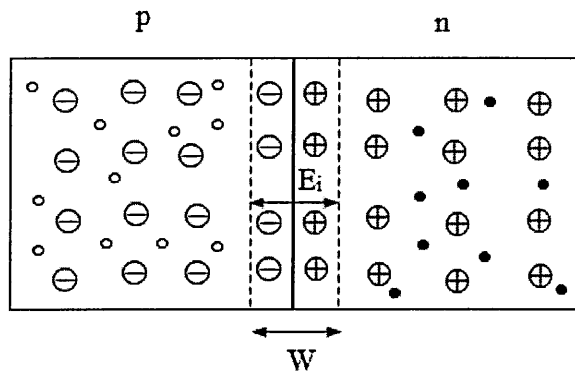


Figure 1.3 (a): Schematic diagram of a p-n junction [8].

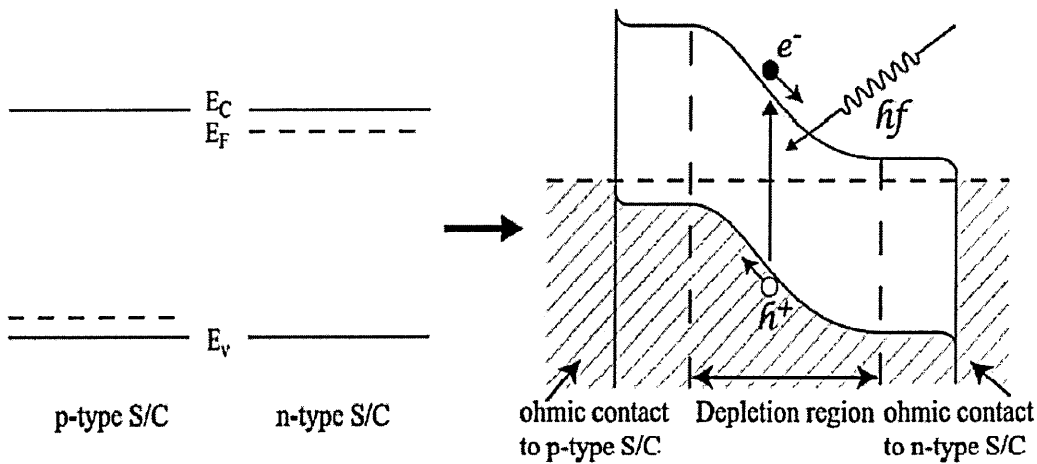


Figure 1.3 (b): Energy band diagram of a p-n junction [9].

When p-type and n-type semiconductors are in contact, three things happen:

- (a) Fermi level line up
- (b) Potential barrier ( $\phi_b$ ) develops
- (c) Internal electric field,  $E_i$  set up

The difference in the potential energy of electrons at the two sides of the junction, the built-in potential,  $V_{bi}$ , and the width of the depletion layer,  $w$  are given by [7];

$$V_{bi} = \frac{kT}{q} \ln \left[ \frac{N_A N_D}{n_i^2} \right] \quad 1.3$$

where  $k$  is the Boltzmann constant,  $T$  is the temperature,  $q$  is the magnitude of electronic charge,  $N_A$  is the acceptor concentration in the p-side,  $N_D$  is the donor concentration in the n-side and  $n_i$  is the intrinsic charge carrier density.

and 
$$w = \left[ \frac{2\varepsilon}{q} \left( \frac{N_A + N_D}{N_A N_D} \right) V_{bi} \right]^{\frac{1}{2}} \quad 1.4$$

where  $\varepsilon$  is the semiconductor permittivity and other symbols have their usual meanings.

When light falls on a semiconductor device, three main functions should occur in order to achieve higher conversion efficiencies. These are, namely:

- (a) Major parts of the solar spectrum should be absorbed,
- (b) Efficient creation of electron-hole pairs within the device, and
- (c) Charge carriers must be separated before recombination occurs and pass to the external circuit to create useful power.

### 1.3.1.2 Metal-semiconductor junctions (Schottky barriers)

When a metal with work function  $\varphi_m$  and a semiconductor having a work function  $\varphi_s$  are in intimate contact, a potential barrier develops after charge transfer occurs across the interface. This leads to the alignment of Fermi levels of the two materials. If the work function of the metal is greater than that of the semiconductor for n-type material (i.e.  $\varphi_m > \varphi_s$ ), the Fermi level of the semiconductor is higher than that of the metal before this contact is made. It is known that the current transport across the potential barrier at metal/semiconductor interface can occur by thermionic emission, recombination and generation, field emission and thermionic field emission [10]. Figure 1.4 shows the formation of a metal/n-type semiconductor junction and its band diagram. The built-in potential ( $V_{bi}$ ) and the electron barrier height  $\varphi_{bi}$  are given by [11];

$$V_{bi} = \varphi_m - \varphi_s \quad 1.5$$

and 
$$\varphi_{bi} = \varphi_m - \chi \quad 1.6$$

where  $\chi$  is the electron affinity of the semiconductor.

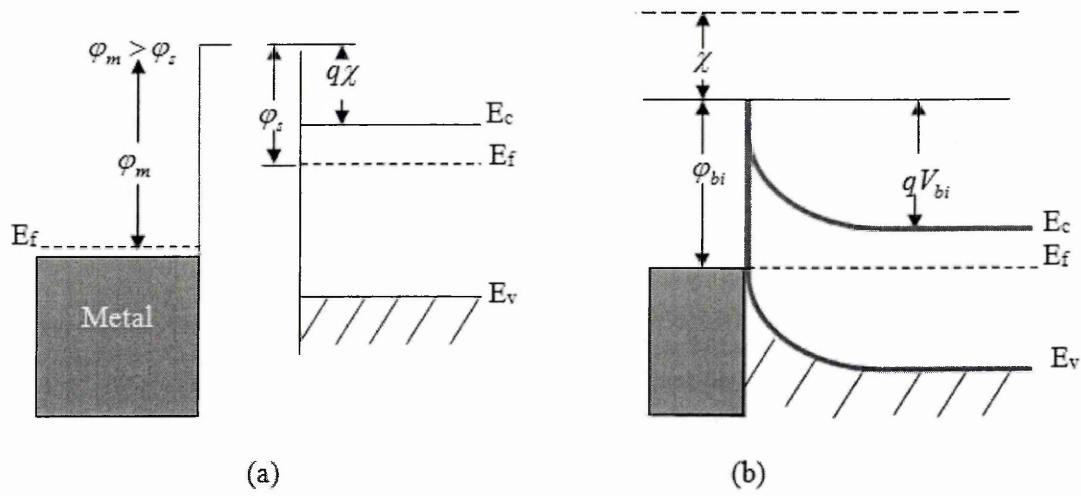


**Figure 1.4:** The formation of a Schottky barrier between a metal and an n-type semiconductor (a) before contact and (b) after an intimate contact, reproduced from [11].

Similarly, the reverse is the case for p-type semiconductor as shown in Figure 1.5. In this case ( $\phi_m < \phi_s$ ) and the barrier height for hole transport ( $\phi_{bp}$ ) is given by,

$$\phi_{bp} = E_g - (\phi_m - \chi) \quad 1.7$$

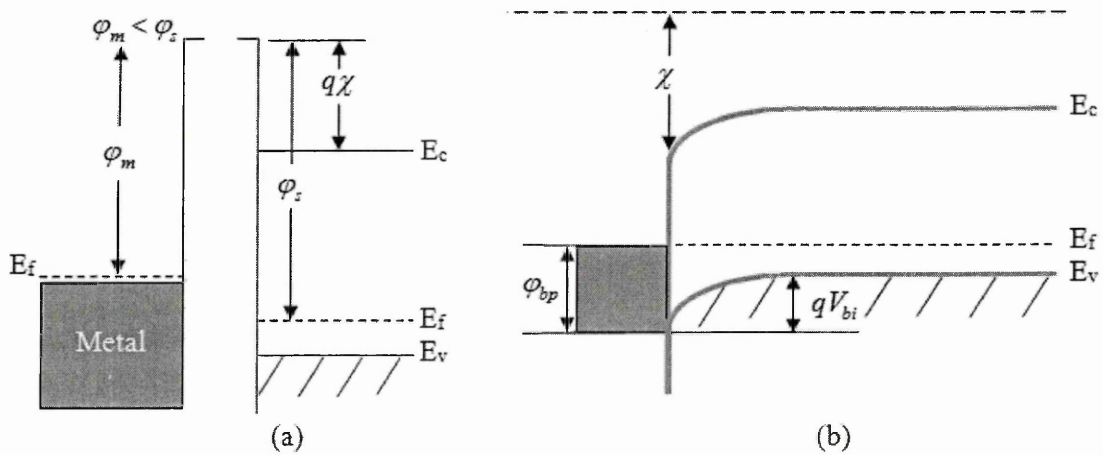


**Figure 1.5:** The formation of a Schottky barrier between a metal and a p-type semiconductor (a) before contact and (b) after an intimate contact, reproduced from [11].

## 1.4 Photovoltaic Effects

Edmund Becquerel in 1839 [12] discovered the photovoltaic effect when he observed that electricity was produced when platinum electrodes immersed in acidic solution were illuminated. A similar effect in a selenium diode was observed by Adams and Day in 1873 [13]. Se and CuO based PV devices were developed and an efficiency  $< 1\%$  [14-16] was achieved. In 1954 Chapin et al. [17] produced a crystalline silicon solar cell with an efficiency of 6% and this solar cell was considered for generating power. Due to the indirect bandgap nature of this material and its relatively low bandgap value,  $E_g = 1.10$  eV, researchers became interested in direct bandgap semiconductor materials with  $E_g$  value  $\sim 1.50$  eV which are close to the optimum such as GaAs [18] and CdTe [19, 20].

Another device of interest in 1970s [21, 22] is the CdS/Cu<sub>2</sub>S thin film solar cell because of its  $E_g$  value of 1.20 eV, but the stability and degradation of these devices were found to be problem. This is due to the rapid diffusion of Cu through the junction structure and the electrochemical decomposition of Cu<sub>2</sub>S at operating voltages of higher than 0.33 V. A CdS/CdTe thin film solar cell was first fabricated using an evaporation technique in 1969 by Adirovich et al. [23] with a conversion efficiency of 1%. An efficiency of (5-6)% was achieved at the Battle Institute in Frankfurt by Bonnet et al. in 1972 [24] using close space sublimation method in which a CdTe film was deposited on a CdS substrate. In late 1980s [25], Tyan and Perez produced a solar cell with an efficiency of 10% based on a CdS/CdTe thin film. Currently, CuInGaSe<sub>2</sub> (CIGS) and CdTe are the key materials used for thin film solar cells. CIGS-based solar cells are currently better with the record efficiency of 20.3% and 15% for small scale laboratory and module respectively [26], whereas CdTe-based solar cells have achieved a laboratory and module efficiency of 17.3% and 13.4% [27].

### 1.4.1 Photovoltaic Technologies

Materials that have electrical conductivities between metals and insulators are called semiconductors. Si and Ge are the common semiconductor materials and are called elemental semiconductors because they are composed of single species of atoms. Others are binary compounds [III-V (e.g. GaAs), II-VI (e.g. CdTe)], ternary compounds (e.g. In<sub>x</sub>Ga<sub>(1-x)</sub>As), and quaternary compounds (e.g. CuInGaSe<sub>2</sub>). To get a good device,

moderate doping should be used which is  $\sim(10^{14} - 10^{17}) \text{ cm}^{-3}$  [28]; higher doping produces a narrow depletion region which leads to tunnelling of electrons through the junction and lower doping gives a very wide depletion region in which the layer becomes resistive. Figure 1.6 shows the absorption coefficients of different photovoltaic solar energy materials [29].

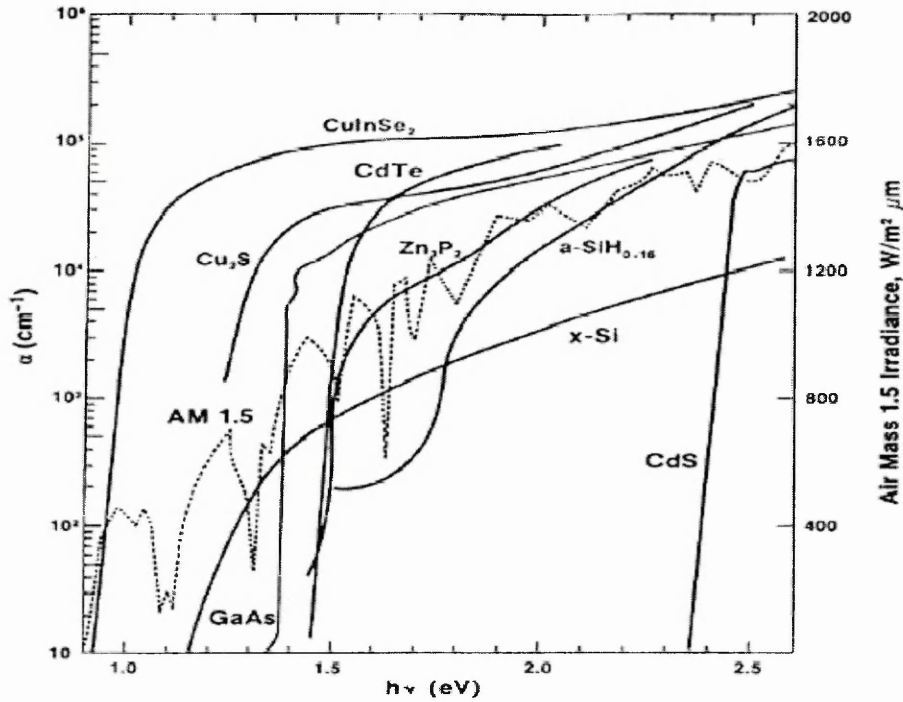


**Figure 1.6:** Absorption coefficients of different PV solar energy materials [29].

Semiconductors can have either direct or indirect bandgaps depending on the positions of the valence band (VB) maximum and the conduction band (CB) minimum. Direct bandgap semiconductors (e.g. GaAs) can absorb light more easily because an electron in the VB can be promoted directly to the CB without a change in momentum. Absorption of the photon's energy takes place without any lattice interaction, and there is a sharp absorption band transition with relatively large values of extinction coefficient. In indirect bandgap semiconductors (e.g. Silicon), the CB minimum and the VB maximum occurs at different  $k$  vectors, and hence for an electron to move from the VB to CB a phonon must be involved. A momentum change ( $k$ -vector) must undergo by the electron as well as energy changes. Figure 1.7 (a) shows the  $E$ - $k$  diagram of these two materials and (b) shows their absorption coefficient. Cost projections versus efficiency of different PV technologies from 2001 are shown in Figure 1.8. As the efficiency increases, and the cost/ $\text{m}^2$  decreases, the cells get closer to the 'market penetration' value of  $\$1/\text{W}$ .

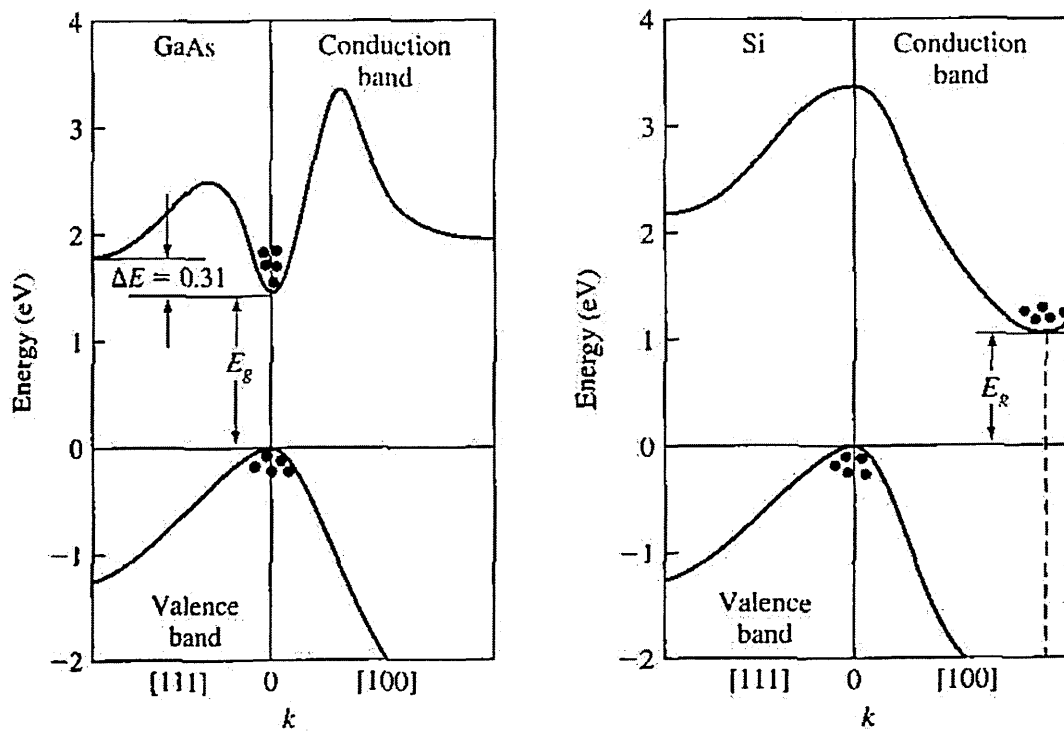


**Figure 1.7 (a):** E- $k$  diagram of direct (left) and indirect (right) bandgap semiconductors [11].

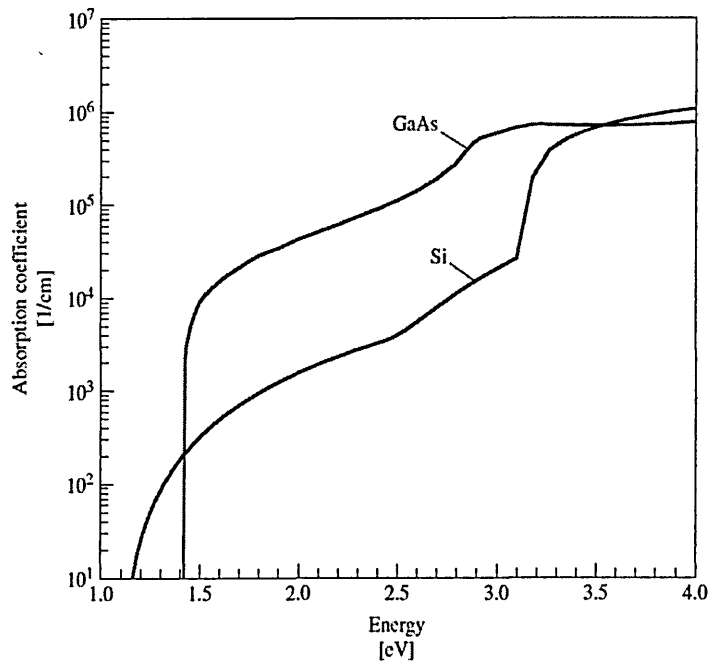


**Figure 1.7 (b):** Absorption coefficient vs. bandgap energy of Si (indirect) and GaAs (direct) semiconductors [29].

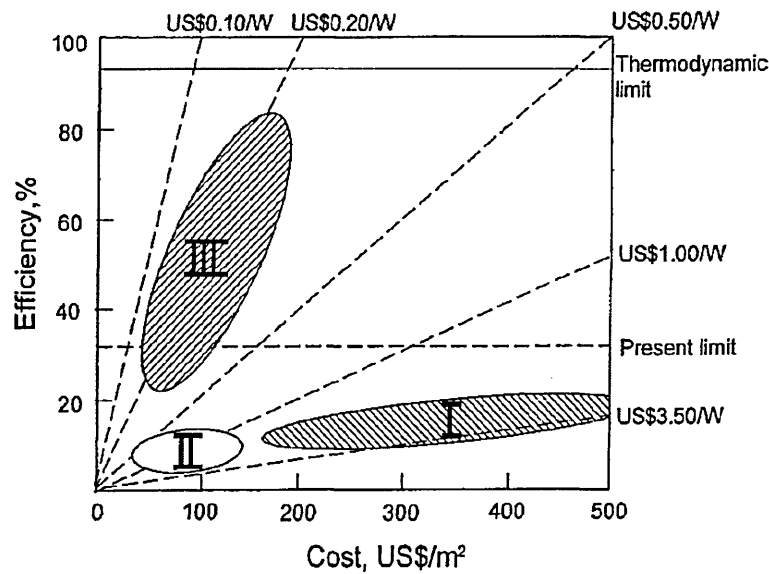


**Figure 1.8:** Efficiency vs. Cost projections for different photovoltaic technologies [30].

**N/B:** I – first generation solar cells (e.g. Si and GaAs), II – second generation solar cells (e.g. a-Si, CIGS and CdTe) and III – other types of solar cells (dye-sensitized solar cell, organic photovoltaic, multi-layers).

#### 1.4.1.1 Silicon based photovoltaic devices

Silicon technologies are leading the PV market because Si has been studied extensively for the past 70 years. About 85% of the solar panels sold each year are made out of silicon [31]. Silicon is one of the most abundant elements in the earth's crust and produced from natural sand in form of silicon (IV) oxide ( $\text{SiO}_2$ ). About 20% of the earth's crust is made of silicon but today's solar cells are obtained primarily from purified Si produced from the microelectronic industry as a form of poly-Si and scrap wafers. Four main steps are required before getting the silicon solar panels which are: purification process from sand, wafer production, silicon solar cells and solar panel assembly.

(a) **Crystalline Silicon (c-Si):** Two techniques are primarily used for fabricating this material. When a single crystal is pulled out slowly from a melt, the process is known as the Czochralski process. In this process, a large cylindrical single crystal is drawn from the melt and has a diameter of 10 - 15 cm and greater than or equal to 1 m in length [32]. Figure 1.19 shows a schematic diagram of the Czochralski crystal puller.

Similarly, if it formed gradually from a polycrystalline rod after passing a molten zone through it, the process is known as float zone as shown in Figure 1.20. The second method produces higher purity material but is considerably more expensive. Boron is used as a dopant to produce a p-type crystal and it is then sliced into wafers. A polishing process is carried out on the wafers. To get a p-n junction, phosphorous is used as n-type dopant on the wafer. Doping process of this material can either be one of this techniques: vapour phase (expose to  $N_2$ ), solid phase (CVD of  $PO_2$ ) or directly by ion implantation. An efficiency of 27.6% and 20.0% were achieved for lab scale silicon devices and modules respectively [34, 35].

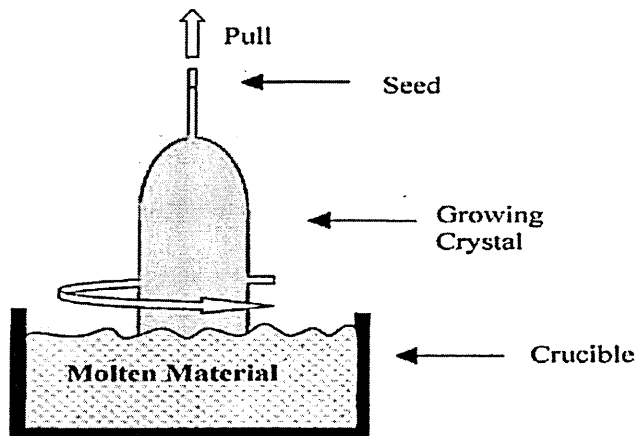


Figure 1.19: Schematic diagram of the Czochralski crystal puller [29].

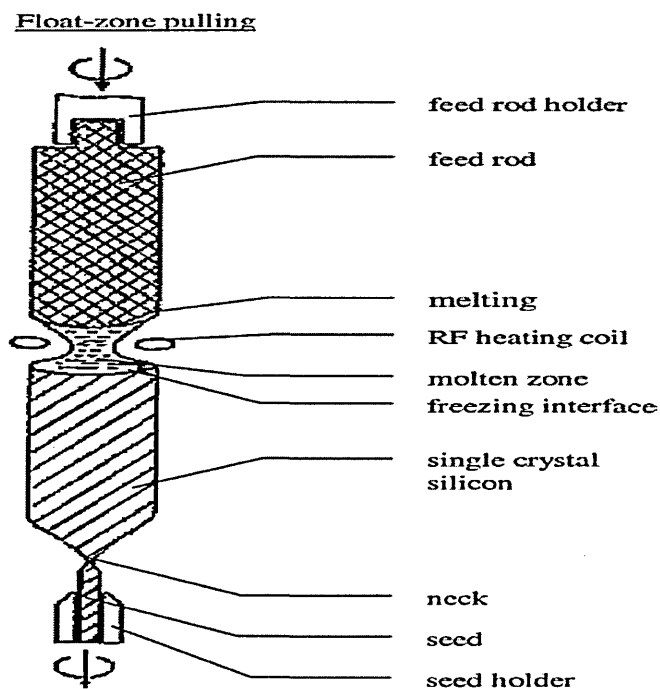
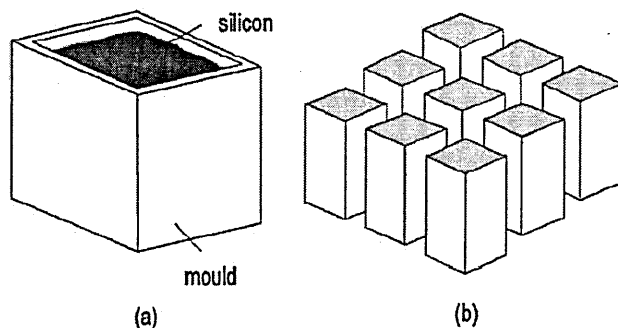


Figure 1.20: Principle of the float zone technique [33].

(b) **Multicrystalline Silicon:** This material is produced by a casting process in which molten Si is poured into a mould. Figure 1.21 (a) shows the solidification process of a large block of multicrystalline Si and (b) smaller ingots [32]. The Si ingot obtained is sliced into wafers. Since these wafers are produced from casting process, they are not as efficient as c-Si due to the imperfections in crystal structure, grain boundaries and contamination from crucible. The current lab efficiency of multicrystalline silicon is about 25.0% [34].



**Figure 1.21:** (a) Directional solidification of a large block of multicrystalline Si from a melt and (b) smaller ingots prior to slicing into multicrystalline wafers [32].

Generally, both c-Si and multicrystalline silicon have indirect bandgap and therefore light absorption is very weak (see section 1.4.1 for more details).

(c) **Amorphous Silicon (a-Si):** This material is composed of randomly oriented Si atoms in a homogenous layer rather than a crystal structure. The absorption of light is higher than in c-Si, leading to a use of thin layers. For this reason a-Si is also among the thin film solar cells and has a direct bandgap. The film is produced by decomposition of silane ( $\text{SiH}_4$ ) and can be deposited on a wide range of substrates. Figure 1.22 shows a schematic of a typical RF glow discharge deposition chamber [29]. A pump controls the flow of silicon-containing gas (i.e. a mixture of  $\text{SiH}_4$  and  $\text{H}_2$ ) into the vacuum chamber. An RF power is applied between the two electrode plates which are installed in the vacuum. Plasma will be generated at a certain range of gas pressures at a given RF voltage across the plates. This leads to the decomposition of the gas in the chamber. Generation of radicals and ions occurs and thin films of hydrogenated silicon deposits on the substrate(s) mounted on either electrodes or both. The growth pressure range is

between 0.05 and 2.00 Torr. At lower pressure the growth is not uniform and microcrystalline film are produced at higher pressure. RF power is in the range 10 - 100 mW/cm<sup>2</sup> and plasma maintaining is difficult below 10 mW/cm<sup>2</sup>. Silicon polyhydride is created when the pressure is greater than 100 mW/cm<sup>2</sup> and the film growing is contaminated.

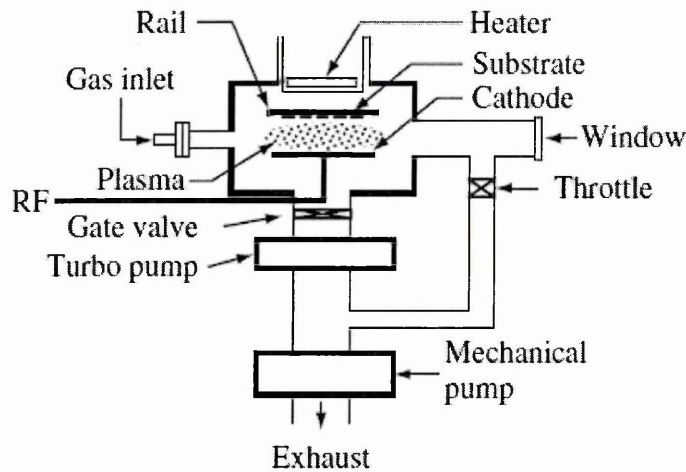


**Figure 1.22:** Schematic of a typical RF glow discharge deposition chamber [29].

The conductivity of a-Si can be increased either by mixing some phosphine (PH<sub>3</sub>) gas giving n-type material or some diborane (B<sub>2</sub>H<sub>6</sub>) gas with the silane to give p-type. a-Si made from plasma deposition process is much superior in optoelectronic properties than its counterpart using evaporated silicon. This process incorporates a significant percentage of H<sub>2</sub> atoms ~ (20-30)% bonded into a-Si structure which help in improving the electronic properties and is known as hydrogenated a-Si [a-Si:H]. One of the disadvantages facing all a-Si based solar cells is a decline in efficiency during their first few hundred hours of illumination, known as Staebler-Wronski effect [36]. In order to reduce recombination losses, a p-i-n structure is used which consists of thin p- and n-doped layers at the front and rear part. An intrinsic layer (i-type) is used at the centre which serves as the photon absorbing layer as shown in Figure 1.23 [37]. An electrical contact to the n-type surface can be done using Ag contact fingers by screen printing method. At the back p-type surface, Al paste is used to make the contact. Luque and Hegedus [29] reported that 30% losses of single-junction cell and 15% losses of triple-junction modules were observed after 1000 hours of the first efficiency as shown in Figure 1.24. An efficiency of 12.5% was achieved for single-junction lab scale devices [34].

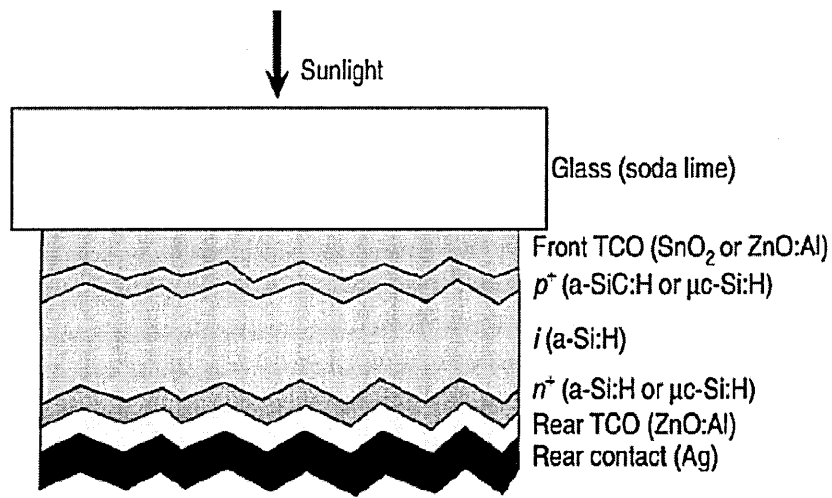


**Figure 1.23:** Schematic of a state-of-the-art p-i-n a-Si:H solar cells on a glass substrate [37].

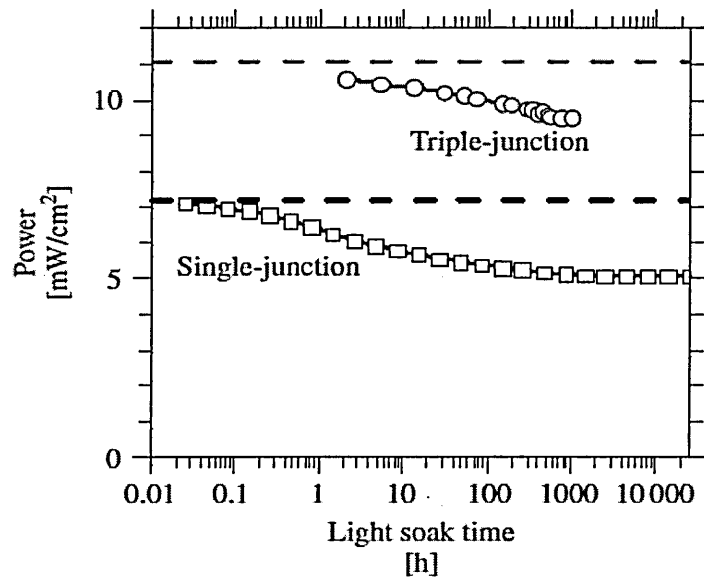


**Figure 1.24:** Efficiency declination of a-Si:H-based solar cells [29].

#### 1.4.1.2 Other type of solar cells

(a) III-V semiconductors: Gallium Arsenide (GaAs) is a widely researched III-V semiconductor and is very suitable for solar energy conversion. Other possible materials include Indium Phosphide (InP) and Gallium Antimonide (GaSb), and ternary alloys such as Al<sub>x</sub>Ga<sub>(1-x)</sub>As, In<sub>x</sub>Ga<sub>(1-x)</sub>As and In<sub>x</sub>Ga<sub>(1-x)</sub>P. Single crystal cells from III-V's are expensive and are usually grown by MOCVD and MBE techniques. The size of the cell

can be kept small and are suited to concentrator systems. Due to its resistance to degradation under radiation InP is used for solar cells for space applications.

GaAs is a direct bandgap semiconductor with  $E_g$  value of 1.42 eV at room temperature [38] and its temperature coefficient is better than Si. It is known that as the temperature of solar cells increases, the efficiency tends to decrease because of increasing carrier recombination and the bandgap decreasing. This gives a better chance for GaAs since it performs well where the cell operates at higher temperature. It can be doped n-type during growth by introducing controlled amounts of Si to replace some Ga atoms in the lattice. For p-type doping, carbon is used to replace arsenic or beryllium can also use to replace Ga. K. Nakayama et al. [39] grew GaAs solar cell on (100) n-GaAs substrate using MOCVD with Zn as the p-type dopant and Si as the n-type dopant. Figure 1.25 shows a structure of the GaAs solar cell. The efficiency of a single junction and three junction devices are 32.6% and 43.5% respectively [34].

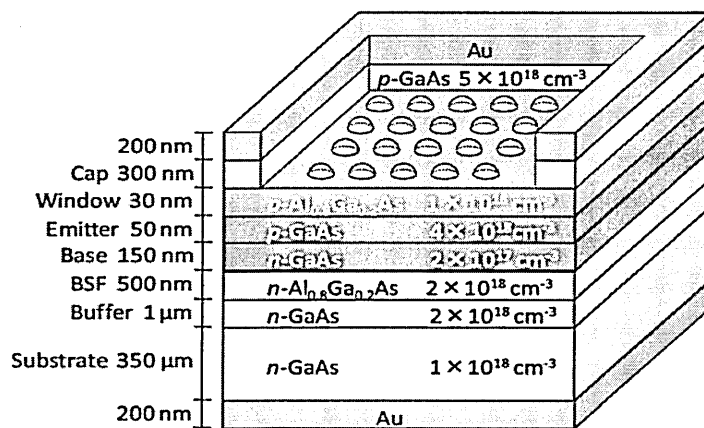


**Figure 1.25:** A structure of the GaAs solar cell [39].

(b) Organic photovoltaic and Dye-sensitised solar cells (OPV & DSSC): Polymers and dyes as the absorber materials to be used in PV devices have been under intense research. The cost of production of these materials compared with semiconducting thin films is very low.

Conjugated polymers are typically used to develop OPV in which it acts as electron donors and high or low molecular organic materials as electron acceptors. Electrons are excited from highest occupied molecular orbital (HOMO) to the lowest unoccupied molecular orbital (LUMO) when subjected to illumination. The difference between the

work function of the cathode and the anode determines the built-in electric field. Figure 1.26 shows a schematic of PV effect in organic solar cell via donor/acceptor approach. The basic structure of this solar cell is shown in Figure 1.27. The organic material layer is sandwiched between two different electrodes. One is semi-transparent (ITO) in which the organic material is deposited directly on top while the coater electrode usually aluminium is on top of the organic layer.

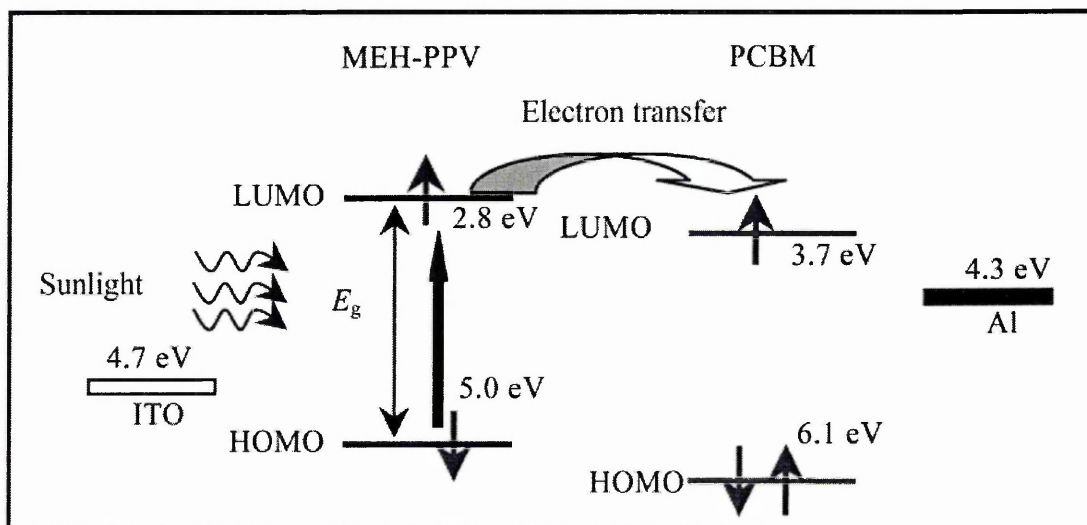


**Figure 1.26:** Schematic of photovoltaic effect in organic solar cell [40].

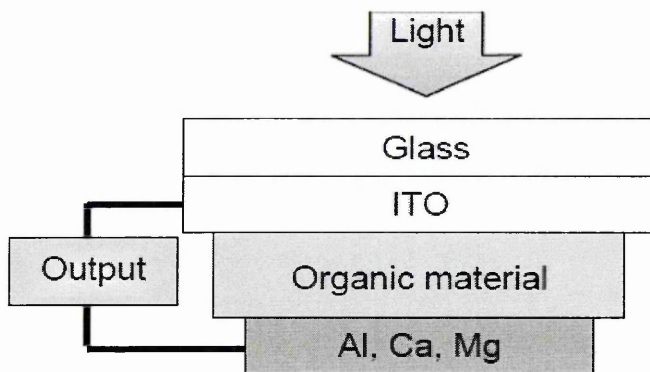


**Figure 1.27:** Basic structure of organic solar cell [41].

The DSSC was invented by B. O'Regan and M. Grätzel in 1991 [42]. The DSSC is known as Grätzel cell and in 2010 he won the Millennium Technology Prize for this invention. DSSC consists of photosynthetic dye and other substances. The cell structure comprises TCO coated with porous nanocrystalline  $\text{TiO}_2$  (nc- $\text{TiO}_2$ ), dye molecules attached to the surface of the nc- $\text{TiO}_2$ , an electrolyte containing a reduction oxidation

couple such as  $I^-/I_3^-$  and a catalyst coated counter-electrode. On the illumination, the cell produces voltage over and current through an external load connected to the electrodes as shown in Figure 1.28. The DSSC has achieved a laboratory efficiency of 11.1% and OPV gives 10.1% [34].

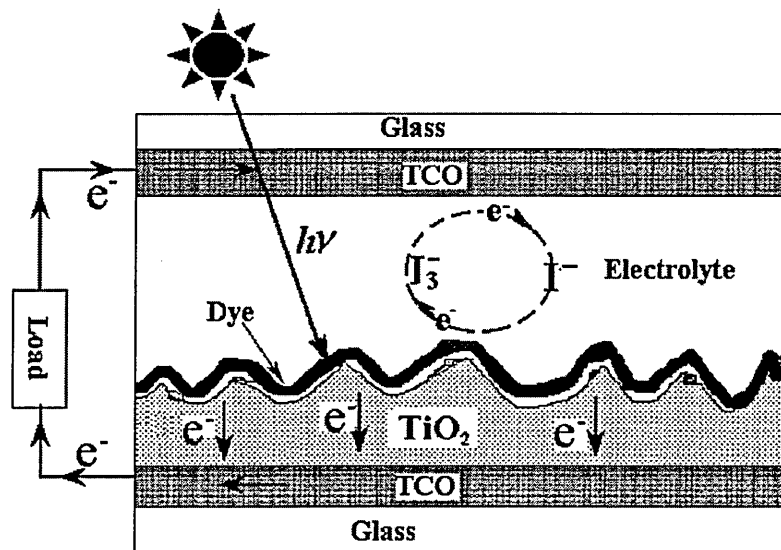


**Figure 1.28:** The basic structure of a DSSC [43].

### 1.5 Thin Films solar cells

Thin Film solar cells may also be referred to as second generation solar cells. It groups into four which includes: a-Si, CdS/Cu<sub>2</sub>S, CdTe and CIGS. CdTe and CIGS thin films solar cells are currently under intense research world-wide. Of these, CIGS-based solar cells are currently best with a record efficiency of 20.3% and 15% for small scale laboratory and module respectively [26], whereas CdTe-based solar cells have achieved a laboratory and module efficiency of 17.3% and 13.4% [27]. Some of the advantages of these technologies include lower material requirements, variety of processing methods and lightweight modules. A thickness of ~2-4  $\mu\text{m}$  of thin film solar cells is enough for light absorption, whereas c-Si needs to be ~180-300  $\mu\text{m}$  thick to absorb all incident radiation efficiently. Due to the thinner layer produced, this leads to the faster processing steps and yield reducing the capital cost.

### 1.5.1 CdTe

CdTe thin film solar cell basically consists of two semiconducting layers. A CdS layer serves as the n-type window material with energy bandgap,  $E_g = 2.42$  eV and a CdTe layer (absorber) deposited on top with  $E_g = 1.45$  eV. Table 1.1 shows some properties of CdS window material and CdTe absorber material.

**Table 1.1:** Properties of CdS and CdTe.

Properties	CdS	Ref	CdTe	Ref.
crystal structure	Hexagonal & Cubic	44	Zinc blend (cubic)	44
Appearance	Yellow-orange	44	Grey-dark	44
density ( $\text{gcm}^{-3}$ )	4.82	44	6.2	44
melting point ( $^{\circ}\text{C}$ )	980	47	1092	44
boiling point ( $^{\circ}\text{C}$ )	1474	44	1130	44
lattice constant (Å)	4.295	47	6.481	45, 46
thermal expansion coefficient at room temperature ( $\text{K}^{-1}$ )	$4.7 \times 10^{-6}$	45	$4.9 \times 10^{-6}$	45, 46
thermal conductivity [ $\text{W}(\text{cmK})^{-1}$ ]	0.25	48	0.075	45, 46
molar mass ( $\text{gmol}^{-1}$ )	144.48	44	240.01	44
Bandgap (eV)	2.42	28	1.45	49

Cadmium sulphide (CdS) is among the binary compounds of group II-VI family and its thin films are widely used in various materials such as light emitting diodes (LEDs), solar cells, electronic and optoelectronic devices [50-52]. Various methods have been employed to deposit CdS thin films, the details of which are discussed in the next chapter. CdS, being an n-type window material, can be combined with  $\text{CuInGaSe}_2$  (CIGS) or CdTe to form a good heterojunction. Figure 1.29 shows the atomic structure of CdS.

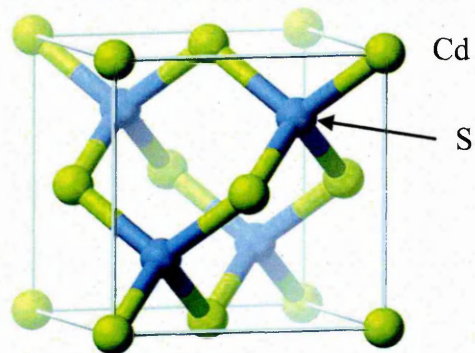


**Figure 1.29:** Atomic structure of CdS [44].

Cadmium telluride (CdTe) thin film based PV devices is one of the most suitable materials for use in PV structures such as sensors, nano-devices, solar cells and other electronic devices [53-55]. It is one of the primary candidates in the field of PV energy conversion due to its specific advantages. These include the near ideal bandgap energy of 1.45 eV for the achievement of the theoretical maximum photovoltaic conversion efficiency of 31% and a high optical absorption coefficient of over 99% of the incident sunlight with only about 2  $\mu\text{m}$  of active thickness [56, 57]. Theoretical calculation shows that semiconductors with bandgap energy of 1.00 - 2.00 eV are suitable for solar energy conversion with an optimum bandgap value of 1.40 eV [58, 59]. CdTe films can be deposited using different techniques as discussed in details in the next chapter. The atomic structure of CdTe is shown in Figure 1.30.

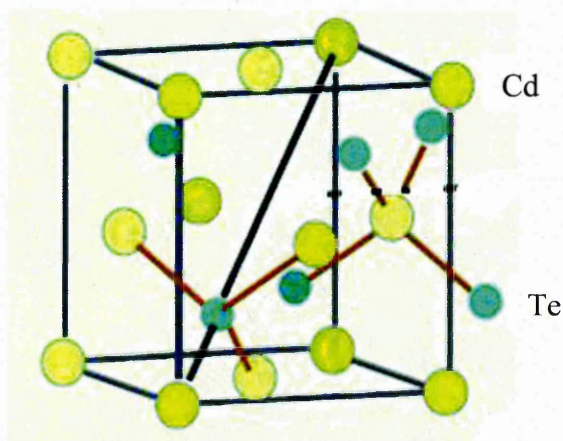


**Figure 1.30:** Atomic structure of CdTe [44].

The schematic diagram of the CdS/CdTe solar cell structure is shown in Figure 1.31. The device structure is then a simple n-p heterojunction with an ohmic contact at the p-CdTe/metal interface. This structure is based on the Basol model who fabricated such a device using electrodeposited CdTe with a conversion efficiency of ~10% in 1984 [49]. This is illustrated in Figure 1.32 (a).

Dharmadasa et al. in 2002 [28] proposed a new model and explained that CdS/CdTe is not a simple p-n heterojunction but an n-n heterojunction with a large Schottky barrier at the CdTe/metal interface, and also reported that there is no type conversion during annealing process. There are five possible Fermi level position at  $E_1 - E_5$  (i.e. 0.4 - 1.18) eV identified below the conduction band which acts as defects on the surface and behave as electron traps (see Figure 1.32 (b)).

The defect levels  $E_1 - E_4$  must be identified and removed or passivated in order to produce a stable & efficient solar cell. The Fermi level needs to be pinned at  $E_5$  so that the largest possible Schottky barrier can be obtained, which is very important for an efficient solar cell. Weak band bending is obtained at the lowest barrier of 0.4 eV which makes the solar cell very poor.

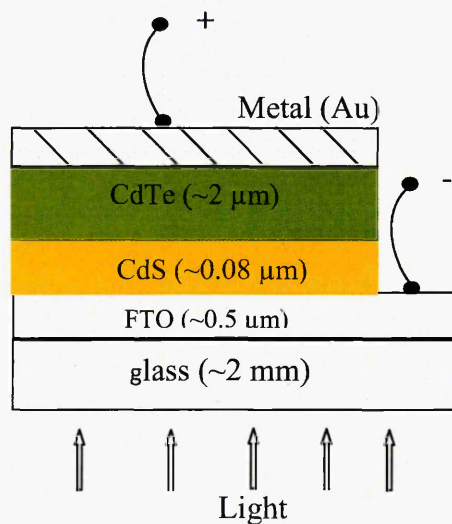


**Figure 1.31:** The basic structure of the glass/TCO/CdS/CdTe/metal thin-film solar cell (diagram not to scale).

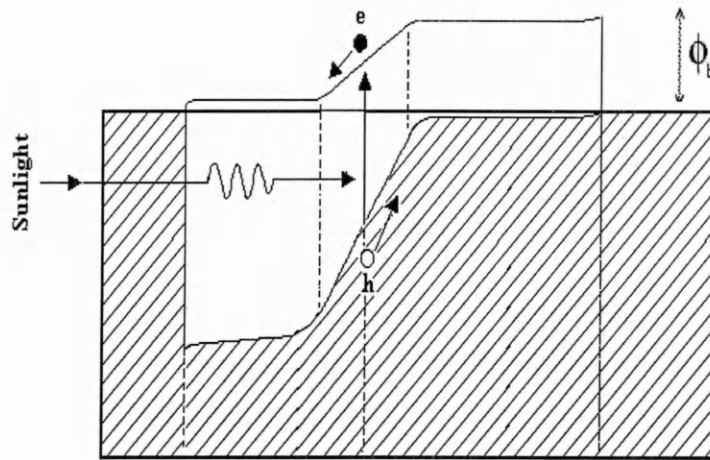


**Figure 1.32 (a):** Band diagram according to Basol model for CdS/CdTe solar cell [28].

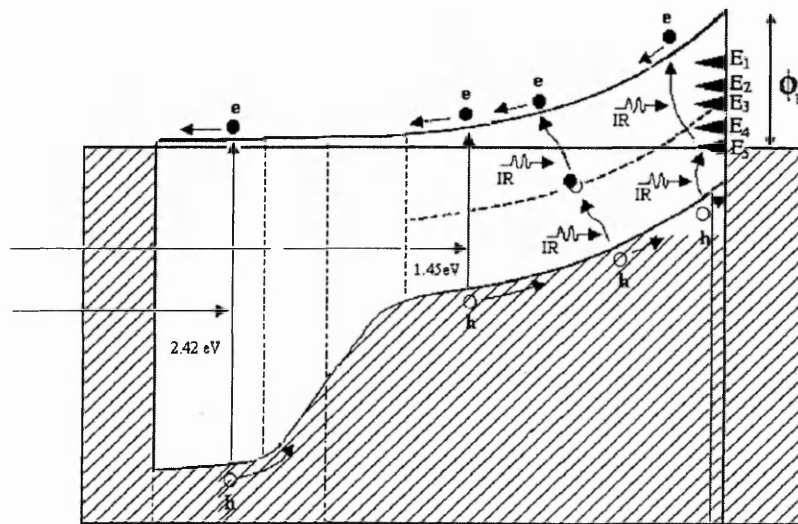


**Figure 1.32 (b):** Energy band diagram of an n-CdS/n-CdTe heterojunction, together with a large Schottky barrier at the back metal contact, based on the new model [28].

Due to the toxic nature of cadmium as an element, solar cells based on CdTe have had some marketing issues which later its perception changes. About ~20,000 tonnes per annum of Cd element are produced as a by-product of Zn and Cu mining. A large proportion of this Cd is used in Ni/Cd batteries, with the rest ending up in landfill, but its compound in the form of CdTe solar cells is very stable which locks up the Cd and produce clean energy.

## 1.5.2 CIGS

The production of CIGS solar cell needs two processes. Firstly, the elements Cu, In, Ga and Se are co-evaporated onto a heated substrate and secondly selenization in which thin layer is exposed to a Se containing gas such as  $\text{H}_2\text{Se}$  or Se vapour. CIGS has a high absorption coefficient,  $\alpha = 10^5 \text{cm}^{-1}$  [60], lattice constant,  $a = 5.78 \text{ \AA}$ , density =  $5.75 \text{ gcm}^{-3}$  [61], thermal conductivity at 273 K =  $0.086 \text{ W(cmK)}^{-1}$  and bandgap energy = 1.02 eV [62]. A soda-lime glass substrate is used and Mo layer is sputtered on it as a back contact. CIGS is deposited using co-evaporated technique followed by CdS using chemical bath deposition technique. A high resistance ZnO layer and a doped high-conductivity ZnO layer are deposited, usually by sputtering or chemical vapour deposition. The basic structure of CIGS solar cell is shown in Figure 1.33. One of the main reasons of using this materials in thin film solar cells is the bandgap tailoring from 1.00 eV – 2.40 eV possible by changing the In/Ga and Se/S ratios [64].

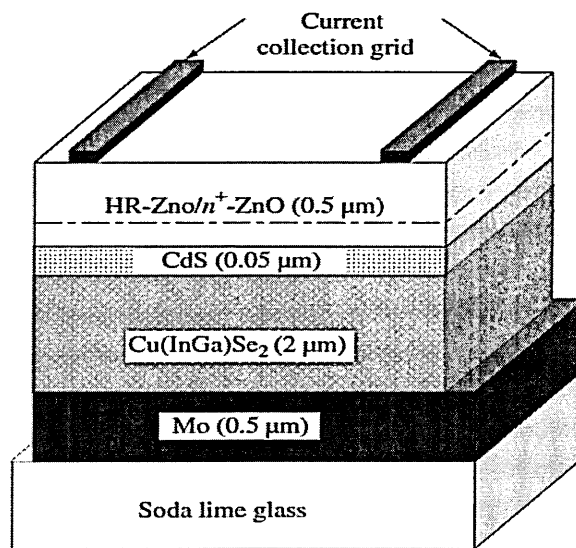


Figure 1.33: The basic structure of the CIGS solar cell [63].

## 1.5.3 Multi-junction solar cells

The absorption of light can be increased efficiently by using multi-layered cells. It is reported that a theoretical conversion efficiency of 86.6% [65] can be achieved using a multi-layer structure. Efficiencies of 32.6% and 43.5% have been achieved using two and three junction solar cells respectively [34]. Materials with different bandgaps are

used, with each layer absorbing a different range of energies photon. High energy photons are absorbed at the front of solar cell structure which is made of wide bandgap energy and at the rear of this structure absorption of lower energy photons take place. Two ways of getting this structure are by connecting them in series or parallel as shown in Figure 1.34 (a) and (b) respectively [66].

Series connection is done by making contact of the conduction band of one device and the valence band of the other using a tunnel-junction. One of the disadvantages of using this connection is a substantial recombination at the interfaces in which electron and hole are created and recombine again. The parallel connection gives an excellent result in which a large bandgap material  $E_{g1}$  is used at the front of the structure and gradually decreases to a lower bandgap material  $E_{g8}$  at the rear. High energy photons absorption ultra violet (UV) takes place at the front of the structure with bandgap  $E_{g1}$  and the lower energy photons are transmitted to the other layers in which it stop the hot-carrier creation, reduce recombination and generation process. The smallest bandgap material  $E_{g8}$  at the rear of the structure absorbs the infra-red (IR) photons while the intermediate layers absorb the photons between UV and IR.

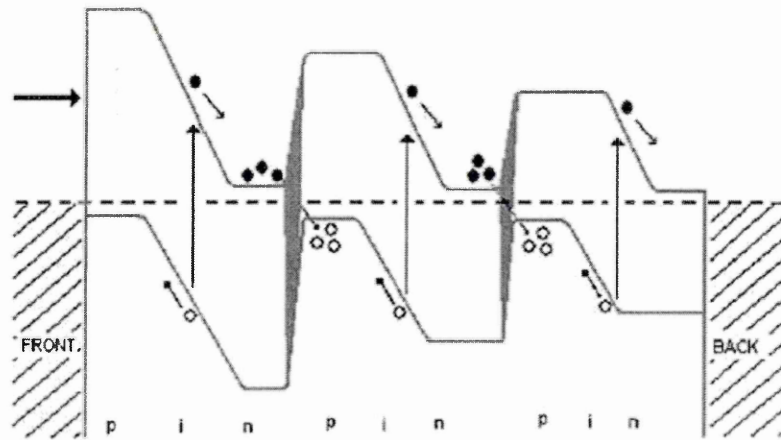


**Figure 1.34 (a):** Multi-layer solar cells connected in series [66].

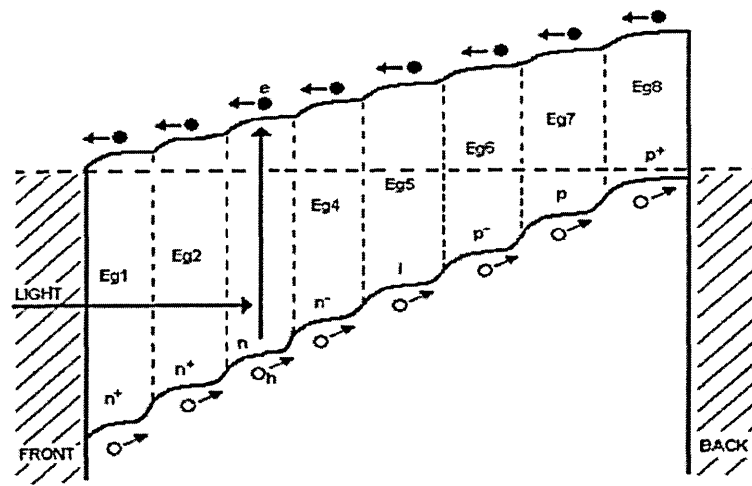


Figure 1.34 (b): Multi-layer graded bandgap solar cells connected in parallel [66].

Table 1.2 shows a summary between different types of solar cells.

Table 1.2: Summary of different types of solar cells.

Solar cell /properties	Silicon	a-Si	GaAs	CdTe	CIGS	DSSC	OPV	Ref.
source	SiO <sub>2</sub>	SiH <sub>4</sub> / H <sub>2</sub>	Ga & As	Cd & Te	Cu, In, Ga & Se	dyes	polymers	29, 34, 44
growth technique	Czochralski & float zone	CVD	MOCVD & MBE	CSS, ED etc	Co-evaporated	dipping	thermal, CVD etc.	29, 33, 39, 41
thickness (μm)	~(180 - 300)	~1.0	~1.8	~2.0	~2.0	-	-	29, 44, 56, 63
energy bandgap (eV)	1.10	1.70	1.42	1.45	1.02	-	-	11, 44, 38, 49, 62
bandgap type	indirect	direct	direct	direct	direct	-	-	29, 11, 44
laboratory efficiency (%)	27.6	12.5	32.6 (single) 43.5 (triple)	17.3	20.3	11.1	10.1	34, 27, 26
module efficiency (%)	20.0	-	-	13.4	15.0	-	-	44, 27, 26

## 1.6 Window Materials

The window materials used in solar cells includes CdS, CdSe, ZnS, ZnSe, ZnTe and ZnO. In this section, the emphasis is given to only ZnTe since it is one of the window material used in this thesis, while CdS has been discussed previously in section 1.5.1. The remaining materials will be discussed in brief.

Zinc telluride (ZnTe) is a p-type window material with a wide and direct bandgap of 2.21 – 2.26 eV at room temperature with electron affinity of 3.53 eV [67, 68]. Thin film solar cells need at least two kinds of semiconducting layers; a wide bandgap window material and a narrow bandgap absorber material. The most common window material used to develop thin film solar cells based on CdTe and CuInGaSe<sub>2</sub> absorber materials is n-CdS. Due to the toxic nature of Cd- containing waste produced during growth of CdS using chemical bath deposition (CBD), an alternative, more environmentally benign window material is required. ZnTe is an environmentally benign compound that can be potentially used as window layer to replace the CBD-CdS currently used. Figure 1.35 shows the atomic structure of ZnTe.

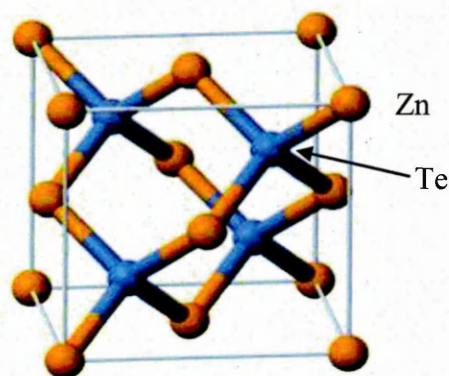


**Figure 1.35:** Atomic structure of ZnTe [44].

The development of ZnO, ZnS, ZnSe and CdSe has been reported in the literature [69 - 72]. Table 1.3 gives the properties of these materials.

**Table 1.3:** Properties of ZnO, ZnS, ZnSe, CdSe and ZnTe window materials

Material/ Properties	ZnTe	ZnS	ZnO	CdSe	ZnSe	Ref.
molecular mass (gmol <sup>-1</sup> )	193.01	99.47	81.41	191.37	144.35	44
crystal structure	zinc blend cubic	zinc blend wurtzite	-	wurtzite	cubic	44

appearance	red crystal	colourless	white solid	black, translucent admantive crystal	light yellow solid	44
density (gcm <sup>-3</sup> )	6.34	4.09	5.61	5.82	5.27	70, 44
refractive index	3.0	2.2 - 2.4	2.0	2.5	2.4	44, 73
melting point (°C)	1238.5	1185	1975	1268	1525	44
bandgap (eV)	2.21 - 2.26	3.68	3.20	1.74	2.67	68-72

## 1.7 Transparent Conducting Oxides (TCOs)

Transparent Conducting Oxides (TCOs) are suitable for a great variety of applications due to their high transparency and near-metallic electrical conductivity. TCOs are key components in most optoelectronic devices. In solar cells, TCOs are used as the current collector; they are applied as an n-type transparent electrical contact with a free carrier concentration between  $10^{18} \text{ cm}^{-3}$  and  $10^{20} \text{ cm}^{-3}$  [74, 75]. p-type TCO has also been reported [76] but is not highly conductive. The bandgap energy,  $E_g$  of these oxide layers is in the range of 3.50 to 4.30 eV and their optical transmission is in the range of 80 - 85% in the visible-near IR range depending on the deposition process [75, 77, 78].

TCOs show a transparency in the visible light range from  $0.4 < \lambda < 0.7 \mu\text{m}$  [79]. In the IR region, its metallic properties lead to reflection and in the UV region they become an absorbing layer due to excitation of electrons across the energy gap. Various methods have been employed to deposit TCOs which includes chemical vapour deposition, CVD [80], radio frequency sputtering [81], sol-gel dip-coating [82], spray pyrolysis [83], thermal evaporation [84], MOCVD [85] and electrostatic assisted vapour deposition technique [86]. Details of the working principle of some of these techniques will be discussed in the next chapter.

It was reported from the literature [87] that the appropriate quantitative measure of the performance of TCOs is known as the figure of merit. Coutts et al. [88] reported that the figure of merit is independent of film thickness and larger value indicates a better performance. It is defined as the ratio of electrical conductivity ( $\sigma$ ) to the visible absorption coefficient ( $\alpha$ ) and is given by [87]:

$$\frac{\sigma}{\alpha} = -\{R_s \ln(T + R)\}^{-1} \quad 1.8$$

where,  $R_s$  is the sheet resistance in ohms per square,  $T$  is the total visible transmission and  $R$  is the total visible reflectance.

Tin oxide is used for making good electrical contact and is often doped with either indium or fluorine to have high conductivity, forming indium-doped tin oxide [ $\text{In}_2\text{O}_3:\text{Sn}$  (ITO)] or fluorine doped tin oxides [ $\text{SnO}_2:\text{F}$  (FTO)]. Different types of TCOs have been reported in the literature [74, 87 - 90], but the TCOs used in this thesis are FTO (TEC-7 & TEC-15), aluminium doped zinc oxide (ZnO:Al), i-ZnO and indium tin oxide (ITO). Due to their cost and availability, the work is concentrated on FTO TEC-7. Table 1.4 shows the properties of various TCOs used in this thesis.

**Table 1.4:** Properties of various TCOs.

TCOs	$d$ ( $\mu\text{m}$ )	$n$ ( $\text{cm}^{-3}$ )	$\mu$ ( $\text{cm}^2\text{V}^{-1}\text{s}^{-1}$ )	Figure of merit ( $\Omega^{-1}$ )	$\rho$ ( $\Omega\text{cm}$ )	$R_{sh}$ ( $\Omega/\square$ )	Ref.
ZnO:Al	0.5	$4 \times 10^{19}$	20	5	$1.5 \times 10^{-4}$	3.8	94, 87, 91
i-ZnO	0.7	$4 \times 10^{20}$	15	0.2	$8.0 \times 10^{-4}$	20	91, 87
ITO	0.7	$6 \times 10^{20}$	35	4	$2.0 \times 10^{-4}$	6	91, 87
TEC-7	0.4	$8 \times 10^{20}$	23	3	$1.4 \times 10^{-3}$	7	92, 91, 87, 94
TEC-15	0.5	$10 \times 10^{20}$	7.1	-	-	15	92, 91, 87, 94

**N/B:**  $d$  is the thickness,  $n$  is the carrier concentration,  $\mu$  is the carrier mobility,  $\rho$  is the resistivity and  $R_{sh}$  is the sheet resistance.

## 1.8 Motivation, Aim and objectives

### Motivation

Rapid growth of the world population, from 7 billion today towards 10 billion by the middle of the 21<sup>st</sup> century, is going to drastically increase the energy demand. Conventional fossil fuels are getting expensive due to extraction difficulties and hence the world is going to face a widening gap between the supply and demand. Colossal use

of fossil fuel has created noticeable pollution problems contributing to climate change and health hazards. There are two solutions to this problem; the use of conventional energy with improved efficiency and rapid introduction of clean energy technologies to the society. Photovoltaic (PV) solar energy is at the top of the renewable energy list and capable of providing "Energy for All". But the initial cost of the manufacturing remains high at present, and therefore the market penetration is slow. Therefore, the worldwide PV community is engaged in an active research programme to reduce this cost, in order to accelerate the take-up of solar energy applications in society. The motivation of this work is to contribute to this collective effort.

### **Aim and objectives**

The main aim of this research project is to contribute towards developing a low-cost and high efficiency photovoltaic solar cell. Silicon based solar cells have progressed forward over the past five decades and brought down the cost to about (2-3)  $\text{\$W}^{-1}$  level. However, the further reduction is extremely slow due to the high cost of silicon material. Therefore, the way forward is to develop thin films solar cells using low-cost attractive materials, grown by cheaper, scalable and manufacturable techniques. The objectives include:

- To produce solar panels costing less than 1  $\text{\$W}^{-1}$  to achieve grid parity.
- To grow three alternative solar energy materials (ZnTe, CdS and CdTe) using electrodeposition as a growth technique.
- To fabricate suitable devices for solar energy conversion (i.e. glass/conducting glass/window material/absorber material/metal structures).

### **Summary of key findings**

This research programme has demonstrated that CdS and ZnTe window materials can be electrodeposited and used in thin film solar cell devices. CdS electrolytic bath can be used for a period of 7 months without discarding it unlike in CBD technique. Further work should be carried out to increase the life-time of this bath, so that these can be used continuously minimising waste solution production in a manufacturing line.

The glass/conducting glass/window/absorber/metal structures were fabricated with efficiencies showing up to 7%. However, the consistency and reproducibility remains un-resolved due to production of devices with efficiencies between (2 - 7)% varying from batch to batch.

One of the reasons for above observation has been identified as the growth of CdS nano-rods with spacing between them. This is the first observation of CdS nano-rods and could open up many applications in nano-devices area. In order to improve the consistency of the solar cell efficiency, CdS layers should be grown with nano-rods aligned perpendicular to the glass surface and with tight packing without gaps, or with uniform coverage of CdS over the conducting glass surface.

The possibility of growth of CdTe absorber layers with n- and p-type electrical conduction using change of stoichiometry was confirmed using the results presented in this thesis. This is a key finding, important to form multi-layer solar cell structures in the future.

## References

1. S. Kalogirous, Solar Energy Engineering: Process and Systems 1<sup>st</sup> edition, Academic Press Ltd., USA, (2009).
2. K. Lidders, The Astrophysical Journal 591, 1220 (2003).
3. J. Twidell and T. Weir, Renewable Energy Resources 2<sup>nd</sup> edition, E&FN Spon Ltd., (2006).
4. B. Sorenson, Renewable Energy 3<sup>rd</sup> edition, Elsevier Science Publishers, New York, (2004).
5. [http://org.ntml.no/pics/chap2/solar\\_spectrum.png](http://org.ntml.no/pics/chap2/solar_spectrum.png), Retrieved on 25<sup>th</sup> March, 2009.
6. [www.newport.com](http://www.newport.com), Retrieved September, 2011.
7. S. M. Sze and Ng. K. Kwok, Physics of Semiconductor Devices 3<sup>rd</sup> Edition, Wiley-Interscience, (2007).
8. G. J. Tollan, PhD Thesis, Sheffield Hallam University, (2008).
9. I. M. Dharmadasa Advances in Thin-Film Solar Cells, Pan Stanford Publishing Company, (2011).
10. E. H. Rhoderick and R. H. Williams, Metal-Semiconductor Contacts 2<sup>nd</sup> edition, Oxford University Press, New York, (1988).
11. D. A. Neumann, Semiconductor Physics and Devices 3<sup>rd</sup> edition, McGraw-Hill Companies, Inc., (2003).
12. E. Becquerel, Compt. Rend. 9, 145 (1839).
13. W. G. Adams and R. E. Day, Royal Soc. Proc. 24, 163 (1876).
14. W. smith, Journal Soc. Telegraph Engineers 2, 31 (1873).
15. C. E. Pritts, Am. Journal Science 26, 465 (1883).
16. L. O. Grondahl, Physics Review 27, 813 (1926).
17. F. M. Chapin, C. S. Fuller and G. L. Pearson, J. Appl. Phys. 25, 676 (1954).

18. M. Wolf, In Proc: 25<sup>th</sup> Power Sources Symp., 490 (1978).
19. R. Hill, Active and Passive Thin Films, Academic Press London, (1978).
20. A. L. Fahrenbruch and R. H. Bube, Fundamentals of Solar Cells, Academic Press London, (1983).
21. A. G. Stanley, Appl. Solid State Sciences 5, 251 (1976).
22. W. Plaz, J. Besson, T. Nguyen and J. Vedel, In Proc: 10<sup>th</sup> IEEE PVSC, 69 (1973).
23. E. I. Adirovich, Y. M. Yuabov and G. R. Yagudaev, Sov. Phys. Semicond. 3, 61 (1969).
24. D. Bonnet and H. Robenhorst, In Proc: 9<sup>th</sup> IEEE PVSC, 129 (1972).
25. Y-S Tyan and E. A. Perez-Albuerne, In Proc: 16<sup>th</sup> IEEE PVSC, 794 (1982).
26. P. Jackson, D. Hariskos, E. Lotter, S. Paetel, R. Wuerz, W. Wischmann, and M. Powalla, In proc: 25<sup>th</sup> EUPVSEC WCPEC-5, Valencia, Spain, (2010).
27. <http://www.firstsolar.com/> retrieved July, 26<sup>th</sup> 2011.
28. I. M. Dharmadasa, A. P. Samantilleke, J. Young and N. B. Chaure, Semicond. Sci. Technol. 17, 1238 (2002).
29. A. Luque and S. Hegedus, Handbook of Photovoltaic Science and Engineering, John Wiley and Sons, Ltd. (2003).
30. M. A. Green, Prog. Photovolt: Res. Appl. 9, 123 (2001).
31. L. Chen, X. Yu, P. Chen, P. wang, X. Gu, J. Lu and D. Yang, Sol. Energy Mater. Sol. Cells 95, 3148 (2011).
32. M. A. Green, Energy Policy 28, 989 (2000).
33. A. Goerzberger, C. Hebling and H-W Shock, Mater. Sci. & Eng. R 40, 1 (2003).
34. <http://wikipedia/solar cells/>, Retrieved September, 2011.
35. <http://solarbuzz.com/>, Retrieved September, 2011.

36. D. Staebler and C. Wronski, *Appl. Phys. Lett.* 31, 292 (1977).
37. A. G. Arbele, *Thin Solid Films* 517, 4706 (2009).
38. J. Nelson, *The Physics of Solar Cells*, Imperial College press, London, (2003).
39. K. Nakayama, K. Tanabee and H. A. Atwater, *Appl. Phys. Lett.* 93, 121904 (2008).
40. L. LiGui, L. U. GuangHao, Y. XiaoNui and Z. Enle, *Chinese Science Bulletin* 52(2), 145 (2007).
41. H. Spanggaard and F. C. Krebs, *Sol. Energy Mater. Sol. Cells* 83, 125 (2004).
42. B. O'Regan and M. Grätzel, *Nature* 353, 737 (1991).
43. S. Dai, J. weng, Y. Sui, C. Shi, Y. Huang, S. Chen, X. Pan, X. Fang, L. Hu, F. Kong and K. Wang, *Sol. Energy Mater. Sol. Cells* 84, 125 (2004).
44. [www.wikipedia.com](http://www.wikipedia.com), Retrieved December, 2011.
45. F. V. Wald, *Revue De Physique Appliquée* 12, 277 (1977).
46. A. J. Strauss, *Revue De Physique Appliquée* 12, 167 (1977).
47. T. L. Chu and S. S. Chu, *Solid State Electronics* 38(3), 533 (1995).
48. [www.springermaterial.com](http://www.springermaterial.com), Retrieved December, 2011.
49. B. M. Basol, *J. Appl. Phys.* 55(2), 601(1984).
50. A. Izgorodi, O. W-Jensen, B. W-Jensen and D. R. MacFarlane, *Physical Chemistry Chemical Physics* 11, 8532 (2009).
51. M. Bicer, A. O. Ayalin and I. Sisman, *Electrochimica Acta* 55, 3749 (2010).
52. S. Peabहार, N. Suryanarayanan and D. Kathirvel, *Chalcogenite Letter* 6(11), 577 (2009).
53. H. Mattousi, J. M. Mauro, E. R. Goldman, G. P. Anderson, V.C. Sundar, F. V. Mikulec and M. G. Bawendi, *J. Am. Chem. Soc.* 122, 12142 (2000).
54. J. Hu, T. W. Odom and C. M. Lieber, *Acc. Chem. Res.* 32, 435 (1999).

55. M. Grätzel, *Nature* 414, 338 (2001).
56. M. Hädrich, C. Kraft, C. Löffler, H. Metzner, U. Reislöhner and W. Witthuhn, *Thin Solid Films* 517, 2285 (2009).
57. E. Colombo, A. Basio, S. Calusi, L. Giuntini, A. Lo Guidic, C. Manfredotti, M. Massi, P. Olivero, A. Romeo, N. Romeo and E. Vittone, *Nucl. Instrum. Math. B* 267, 2181 (2009).
58. A. Goerzberger, C. Hebling and H-W Shock, *Mater. Sci. & Eng. R* 40, 1 (2003).
59. W. Jaegermann, A. Klein and T. Mayer, *Advance Mater.* 21, 4196 (2009).
60. A. Gupta and S. Isomura, *Sol. Energy Mater. Sol. Cells* 53, 385 (1998).
61. D. Suri, K. Nagpal and G. Chadha, *J. Appl. Crystallography* 22, 578 (1989).
62. H. Neumann, *Solar Cells* 16, 317 (1986).
63. D. Mattox, *Handbook of Physical Vapour Deposition (PVD) Processing*, Naves Publ., Park Ridge, NJ (1998).
64. M. Kaelin, D. Rudmann, F. Kurdesau, H. Zogg, T. Meyer and A. N. Tiwari, *Thin Solid Films* 480-481, 486 (2005).
65. T. Takamoto, T. Agui, E. Ikeda and H. Kurita, *Sol. Energy Mater. Sol. Cells* 66, 511 (2001).
66. I. M. Dharmadasa, *Sol. Energy Mater. Sol. Cells* 85, 29 (2005).
67. T. Mahalingam, V. S. John, G. Ravi and P.J. Sebastian, *Crystal Research Technol.* 37(4), 329 (2002).
68. M. Neumann-Spallart and C. Königstein, *Thin Solid Films* 265, 33 (1995).
69. J. S. Wellings, N. B. Chaure, S. N. Heavens and I. M. Dharmadasa, *Thin Solid Films* 516, 3893 (2008).
70. J. P. Borah and K. C. Sarma, *Acta Physica Polonica A* 114(4), 713 (2008).
71. Q. Peng, Y. Dong and Y. Li, *Angew. Chem. Int.* 42, 3027 (2003).
72. R. B. Kale, S. D. Sartale, B. K. Chougale and C. D. Lokhande, *Semicond. Sci. Technol.* 19, 980 (2004).
73. [www.ispotics.com](http://www.ispotics.com), Retrieved December, 2011.

74. A. Bosio, N. Romeo, S. Mazzamuto and V. Canevari, *Prog. in Cryst. Growth and Charact. of Mater.* 52, 247 (2006).
75. B. Szyszka, P. Loebmann, A. Georg, C. May and C. Elsaesser, *Thin Solid Films* 518, 3109 (2010).
76. D. C. Look, *Semicond. Sci. Technol.* 20, 555 (2005).
77. D. Bonnet, In proc: 14<sup>th</sup> EUPSEC, Barcelona, Spain, 2688 (1997).
78. J. Britt and C. Ferekides, *Appl. Phys. Lett.* 62, 2851 (1993).
79. C. G. Granqvist, *Sol. Energy Mater. Sol. Cells* 91, 1529 (2007).
80. B. Kuhn, D. Le Bellac, B. Rech, J. Hüpkes and G. Schöpe, In proc: 21<sup>st</sup> EUPVSEC & Exhibition, Germany, Dresden, 1733 (2006).
81. W. Bayer, J. Hüpkes and H. Stiebig, *Thin Solid Films* 516, 147 (2007).
82. Z. Gu, P. Liang, X. Liu, W. Zhang and Y. Le, *J. of Sol-Gel Sci. Technol.* 18, 159 (2000).
83. B. Thangaraju, *Thin Solid Films* 402, 71(2002).
84. W. Y. Chung, C. H. Shim, S. D. Choi and D. D. Lee, *Sens. Act. B* 20, 139 (1994).
85. J. R. Brown, P. W. Haycock, L. M. Smith, A. C. Jones and E. W. Williams, *Sens. Act. B* 63, 109 (2000).
86. R. Chandrasekhar and K. L. Choy, *J. of Crystal Growth* 231, 215 (2001).
87. R. G. Gordon, *MRS Bulletin*, 52 (Aug, 2000).
88. T. J. Coutts, X. Wu, W. P. Mulligan and J. M. Webb, *J. of Electronics Materials* 25(6), 935 (1996).
89. K. L. Chopra, S. Major and D. K. Pandya, *Thin Solid Films* 102, 1 (1983).
90. N. Romeo, A. Bosio, V. Canevari, M. Terheggen and L. V. Roca, *Thin Solid Films* 431 - 432, 364 (2003).

91. K. L. Chopra, P. D. Paulson and V. Dutta, Prog. in Photovol. Research & Appl. 12, 541(2004).
92. [www.pilkington.com/na](http://www.pilkington.com/na), Retrieved December, 2011.
93. M. Oshima, Y. Takemoto and K. Yoshio, Physica Status Solidi C 6(5), 1124 (2009).

## Chapter 2: Growth Techniques and Characterisation

### 2.1 Growth Techniques

The techniques used to grow CdTe thin films include [1]:

- (a) Vapour-phase deposition; this includes physical vapour deposition (PVD) and chemical vapour deposition (CVD).
- (b) Liquid-phase or solution deposition, which includes chemical solution deposition (CSD) and electrochemical deposition (ECD).

#### 2.1.1 Physical vapour deposition (PVD)

The PVD includes sputtering and thermal evaporation. The deposition of the material on the substrate is by physical means. A material to be deposited is heated above its melting point in an evacuated chamber, and evaporation occurs.

**2.1.1.1 Sputtering:** This is the process whereby atoms/molecules are ejected from a solid target material due to bombardment of the target by energetic particles. Smentkowski [2] defined sputtering as erosion of solid surfaces during ion bombardment. Figure 2.1 shows the schematic set-up for sputtering process.

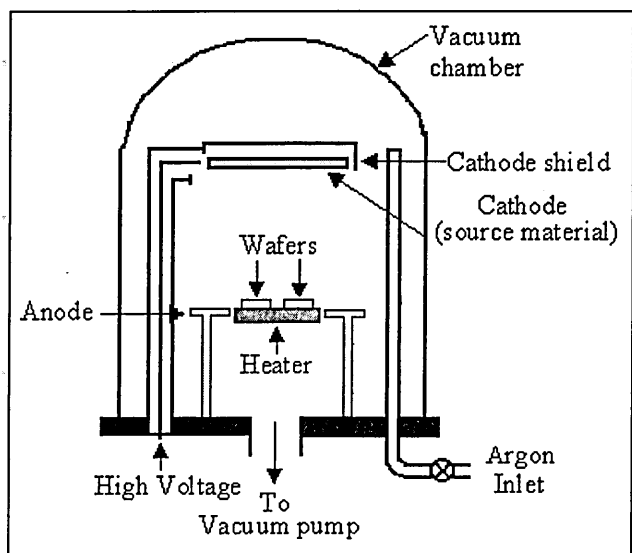


**Figure 2.1:** Schematic set-up for sputtering technique [3].

An inert gas (usually argon) is introduced at low pressure into the vacuum chamber where the substrate and the source material are placed. The gas becomes ionized after gas plasma is bombarded using an RF power source. The accelerated ions move towards the surface of the target and cause the break off of the atoms from the source in vapour form which then condense on a substrate to form a film. Mandal et al. [4] have grown CdTe thin films by this technique. The deposition of CdS and ZnTe thin films were also successful as reported in the literature [5, 6].

**2.1.1.2 Thermal evaporation:** This is a process in which a solid material placed in a boat is heated to the point where it starts to evaporate and later condenses onto a cooler substrate to form a film. The evaporation rate depends on the crystal face from which evaporation takes place. The vacuum pressure is less than  $10^{-3}$  Pa for good coating [7]. Figure 2.2 shows a set-up for thermal evaporation technique. CdTe thin films have been deposited by Ali et al. [8] by this method, using Cd granules and Te powder placed inside a boat at  $\sim 10^{-6}$  mbar vacuum pressure. Lee et al. [9] and Patel et al. [10] grew CdS and ZnTe thin films using this technique.

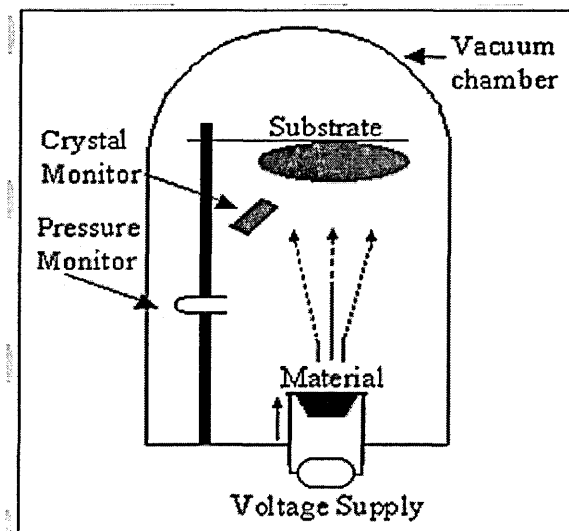


**Figure 2.2:** Thermal evaporation technique set-up [3].

### 2.1.2 Chemical vapour deposition (CVD)

The CVD is also known as vapour-phase epitaxy (VPE). It involves depositing a solid material from a gaseous phase. The deposition must be carried out in pressure ranging anywhere from several atmosphere down to high vacuum [1]. At approximately ambient

temperature, the precursor gases are delivered into the reaction chamber and pass over or come in contact with a heated substrate. Choy [11] reported that, the formation of the stable solid is due to the dissociation and/or chemical reactions of gaseous reactants in activated (heat, light, plasma) environment. CVD equipment consists of three main components as follows:

- chemical vapour precursor supply system
- CVD reactor and
- effluent gas handling system.

Figure 2.3 shows a schematic diagram of a CVD process. A comprehensive review of this technique has been reported in the literature [11]. CVD technique includes Plasma CVD and Metal-organic CVD (MOCVD) among others.

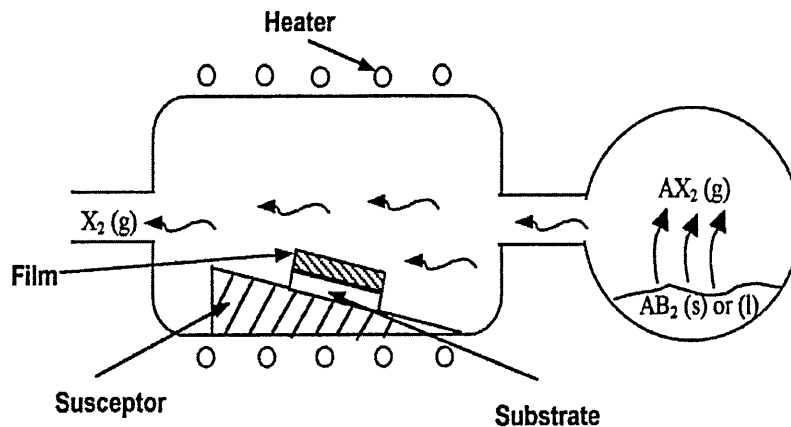


**Figure 2.3:** Schematic diagram of CVD process [11].

**2.1.2.1 Metal-organic CVD (MOCVD):** An epitaxial layer is deposited using this technique. Organic molecules (precursors) are decomposed thereby release atoms while passing over the hot substrate in which the deposition occurs. The precursors are metal-organic and are generally undergo decomposition or pyrolysis reactions. It was reported in the literature [11] that MOCVD reaction process is kinetically limited at deposition temperatures below  $500^\circ\text{C}$ . When the temperature is in the ranges  $(550 - 750)^\circ\text{C}$ , diffusion-rate reaction is limited and at temperature of  $800^\circ\text{C}$ , the reaction is limited by homogenous reaction. Berrigan et al. [12] have grown both CdS and CdTe thin films by this technique. CdS is nucleated from dimethylcadmium and ditertiarybuttylsulphide at

290°C. CdTe deposition is from DMCD and diisopropyltelluride at 300 - 310°C. ZnTe thin films growth by this technique has also been reported [13].

### 2.1.3 Molecular Beam Epitaxy (MBE)

This is a high vacuum epitaxial growth technique via the interaction of several molecular or atomic beams on the heated substrate surface. Epitaxial films of a wide variety of materials, ranging from oxides, semiconductors and metals can be deposited. Figure 2.4 shows a schematic front view of a basic MBE growth chamber. The source ovens are used to evaporate the constituent molecules or atoms and direct them to the substrate which is mounted on a heater block. The beams are switched on and off through mechanical shutters driven from outside the vacuum chamber. The system background pressure remains very low due to the chilled walls surrounding the source ovens and the substrate; this make the beams to have a single pass through the chamber before condensing on the walls. The reflection high energy electron diffraction (RHEED) gun operates without damage from corrosive reaction without residual vapour. This produces a high purity growing film.

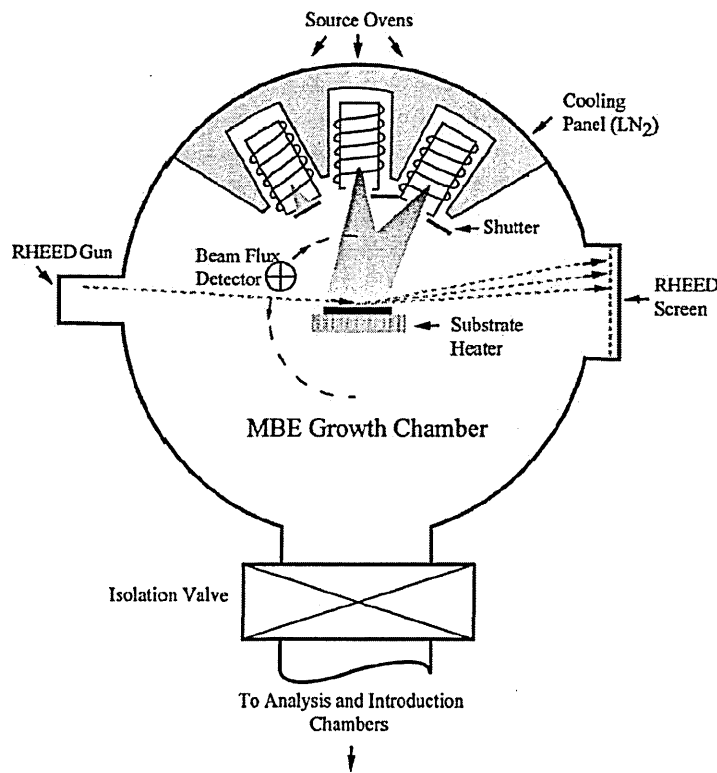


Figure 2.4: Schematic front view of a basic MBE growth chamber [14].

The deposition takes place at pressure  $\sim 10^{-8}$  Pa in a high vacuum system. The deposition rate is very slow (typically  $< 1000$  nm per hour); this gives epitaxial layers on the deposited substrate. Quasi-Knudsen effusion cells are used to heat the elements and as a result the elements sublime, to condense later on the target substrate. Two of the limitations on MBE growth are slow process and very expensive equipment used. Large area deposition is not possible. Boieriu et al. [15] have grown CdS by this technique using a Cd flux and a valves S cracker cell with a source temperature of  $130 - 135^{\circ}\text{C}$  and a cracking zone of  $500^{\circ}\text{C}$ . A conventional effusion cell was used as In source for n-type doping. Growth temperatures between  $150^{\circ}\text{C}$  and  $350^{\circ}\text{C}$  were used and the pressure ranges were  $6 \times 10^{-8}$  to  $1.5 \times 10^{-7}$  Torr. The deposition growth rate was  $\sim 0.3$  nms $^{-1}$ .

It also reported that ZnTe thin film has been deposited using this method by combining elemental Zn and Te (all 6N in purity) as the source materials. The base pressure of the growth chamber was  $6.0 \times 10^{-10}$  Torr [16]. Similarly, the deposition of CdTe using this technique has been reported using CdTe crystal as the source at a growth rate of  $0.3$   $\mu\text{m h}^{-1}$  [15].

#### **2.1.4 Close Space Sublimation (CSS)**

The CSS growth technique is described as follows [17];

- (a) Diffusion-limited transport: The deposited materials migrate to the substrate through the ambient gas and collide several times with gas molecules before condensing on the substrate.
- (b) Langmuir's theory: The deposited materials are moved directly to the substrate without any gas phase collision.

The schematic diagram of the CSS system is shown in Figure 2.5 (a) and (b) shows the position of the source and substrate sandwiched in the growth chamber. The source and substrate are separated by spacers enclosed in a reaction chamber and held between two graphite susceptors inside a quartz reactor. The source of heating is from visible or infra-red lamps outside the reactor facing the blocks of graphite. A set of thermocouples monitored the temperature of the graphite blocks for both the source and the substrate. A diffusion controlled transport mechanism takes place during the temperature

difference and the material from the source transfers to the substrate. The deposition rate depends upon the source, spacing, substrate temperature and ambient gas nature. The material to be deposited is placed on a boat and heated by a halogen lamp ~1000 W. This lamp is connected to the main power through temperature controller with K-type thermocouple. The substrate is heated by a second halogen lamp ~500 W at a distance of 1-4 mm from the source material. Deposited material is now condensed on the heated substrate due to reduced temperatures.

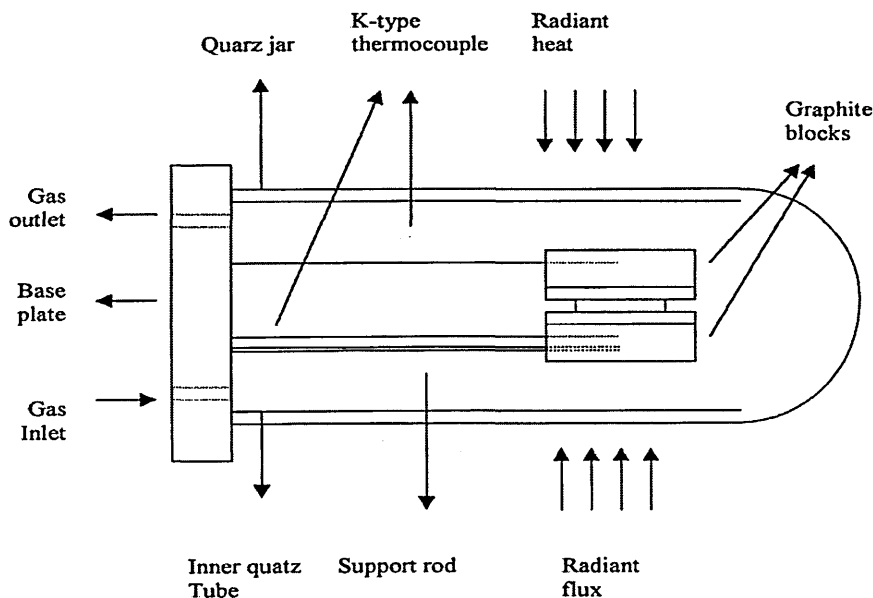


Figure 2.5 (a): Schematic of the CSS system [18].

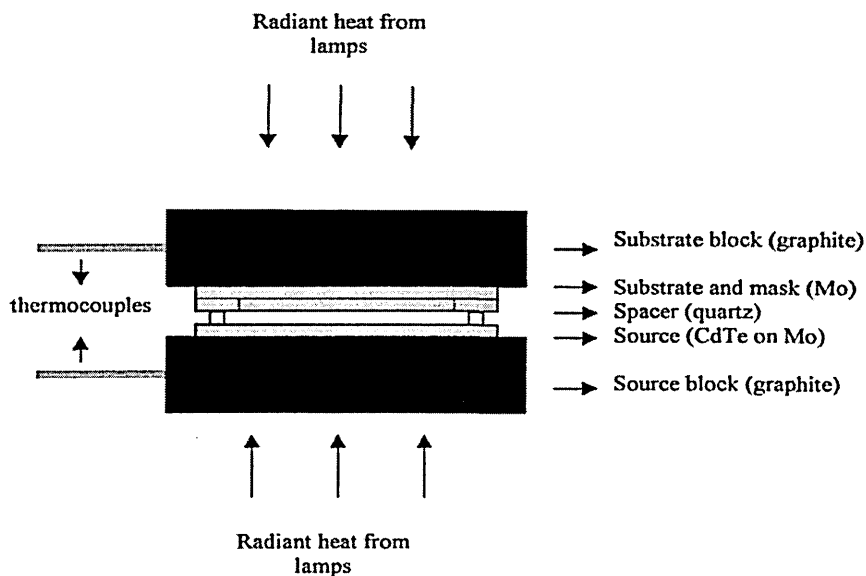


Figure 2.5 (b): Schematic showing the source and the substrate sandwiched in the growth chamber [18].

Han et al. [19] have grown CdS thin films by this technique using CdS crystal. The source temperature was 680°C and substrate was kept at 520°C. CdS thin films were deposited in 20 minutes with a thickness ~150 nm. ZnTe thin films have been deposited using this technique by evaporating pure ZnTe ingots in a molybdenum boat inside a 12-inch vacuum chamber [20]. The chamber pressure was maintained at  $\sim 10^{-5}$  Pa. The substrate temperature ranged from 300°C to 553°C and the deposition rate was maintained about 30 nm per min. The thickness of ZnTe film deposited ranged from 300 – 900 nm. First solar in July 2011 [21] announce the world record CdTe thin films solar cells using CSS technique and devices with an efficiency of 17.3% have been achieved.

### **2.1.5 Liquid-phase deposition**

This technique involve liquid medium as the means of deposition and is always present in ionic form. It involves inherently chemical and/or electrochemical reactions for the formation of the deposit material. The deposition is normally at low temperature and no vacuum is required.

#### **2.1.5.1 Spray pyrolysis**

In this method, a solution containing material precursor ions, in form of droplets is sprayed onto a heated substrate in air from the source to form a coating. The sprayed solution is diluted either in water or alcohol or both. The temperature of the substrate is at 350°C - 500°C. Figure 2.6 shows a typical spraying system [22]. The main components of the system are: substrate heater, temperature controller, air compressor and spray nozzle. The quality of the films produced by this technique depends upon some parameters which include the spray rate, substrate temperature, droplet size, cooling rate, carrier gas and ambient atmosphere.

This is a non-vacuum technique and the deposition can be scaled up for industrial applications. CdS thin film can be deposited by this technique using equal concentrations of  $\text{Cd}^{2+}$  and  $\text{S}^{2-}$  ions [23]. The glass/FTO substrate is heated to 420°C and CdS films deposited directly on the substrate. Merchant and Cocivera [24] deposited ZnTe thin films using two steps spray pyrolysis. Spray pyrolysis was first used to form ZnO. ZnTe thin films were obtained by the reaction between Te vapour and ZnO. The conductivity of the film can be p- or n-type depending on the Zn and Te

content in the film. Similarly, CdTe thin films of thickness 1 – 4  $\mu\text{m}$  have been deposited by this technique. The molarity of CdTe was 0.0375M and the deposition time was 15 – 60 minutes. The spray rates were 3 – 5 ml per min and the substrates temperature during this deposition ranged from 425 – 500°C [25].

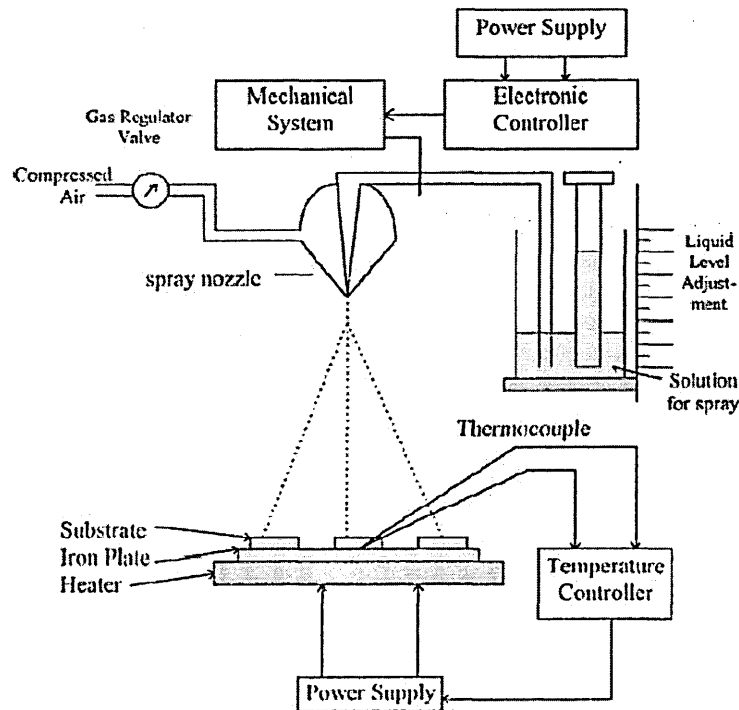


**Figure 2.6:** Schematic set-up for spray pyrolysis technique [22].

### 2.1.5.2 Screen printing

This is a technique that uses a woven mesh to support an ink-blocking stencil and transfers the ink or other materials pressed through the mesh as a sharp image onto a substrate. The active material is carried to the surface of the substrate using a paste as shown in Figure 2.7. The paste can be organic solvent, conducting material or glass frit [26]. Pressure is applied to the squeegees after the paste has been dispensed; this makes the screen to be in contact with the substrate. The squeegees are moved to and fro of the screen and releasing the paste in front of it by dragging and pressing it. The substrate and the screen should not be in contact, the distance separating them is called the snap-off.

Arita et al. [27] have grown CdS thin film by this technique using CdS paste deposited on a glass substrate. The growth of CdTe thin film have also been reported [28] using a slurry consisting of CdTe powder, 10% wt. of CdCl<sub>2</sub> and an appropriate amount of ethylene glycol. CdCl<sub>2</sub> was used as an adhesive and ethylene glycol as a binder. Paste prepared was screen printed on ultra clean glass substrate.

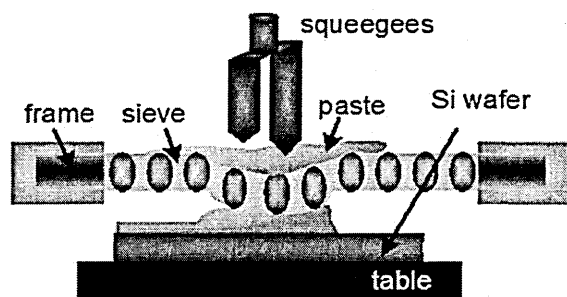


**Figure 2.7:** Schematic set-up of screen printing technique [26].

### 2.1.5.3 Inkjet printing

This is the technique in which tiny droplets (with a diameters in the range 50 - 100  $\mu\text{m}$ ) [29] composed of either solution or dispersion of functional materials are ejected onto addressable sites on a substrate. A fixed quantity of ink in chamber is ejected from a nozzle through a sudden, quasi-adiabatic reduction of the chamber volume via piezoelectric action as shown in Figure 2.8. The liquid is contracted in response to the application of an external voltage from a chamber. A shockwave is set up in the liquid upon the sudden reduction in its volume. As a result, a liquid drop is ejected from the nozzle. Under the action of gravity and air resistance, the ejected drop impinges on the substrate, spreads on the surface and dries through solvent evaporation.

It was reported in the literature [29] that CdTe Nanocrystal polymer was grown by this technique using solution of CdTe NCs containing 1 wt % PVA, in which the amount of ethylene glycol varied from 0 - 20 vol %.

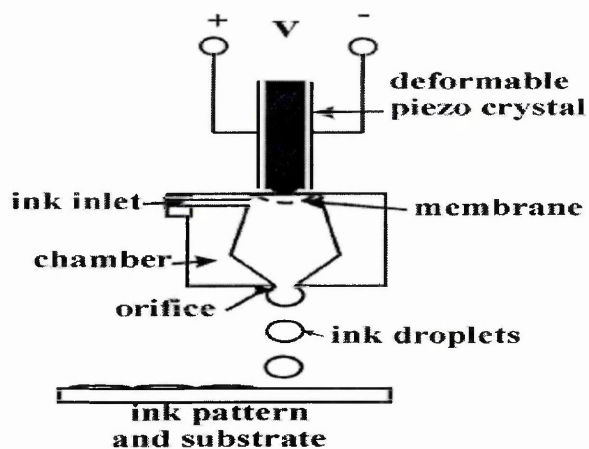


**Figure 2.8:** Inkjet printing set-up [30].

#### 2.1.5.4 Chemical Bath Deposition (CBD)

This technique involves manipulated precipitation in which a chemical reducing agent in solution reduces metallic ions to the metal. One of the disadvantages of using CBD is sulphur and CdS precipitation in the electrolytic bath and generating of Cd-containing waste in the CdS deposition. Semiconductor materials such as CdS and ZnS are the most common materials grown using this technique. Figure 2.9 shows a typical set-up of CBD. Han et al. [19] have grown CdS by this technique using a liquid chemical solution containing  $1.5 \times 10^{-3} \text{ molL}^{-1}$  cadmium acetate and  $5 \times 10^{-2} \text{ molL}^{-1}$  thiourea. The bath temperature is  $\sim 75^\circ\text{C}$  and pH  $\sim 11.0$ . Thin film CdS deposited on the substrate in 60 minutes had thickness of approximately 150 nm.

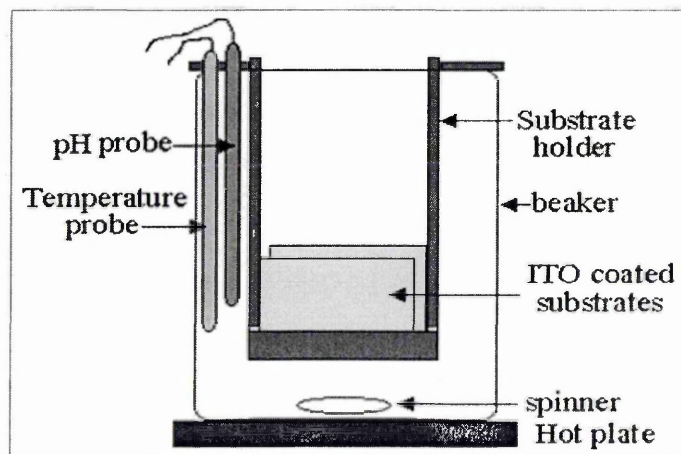


**Figure 2.9:** Typical CBD se-up [3].

## 2.1.6 Electrodeposition (ED)

### 2.1.6.1 Overview of electrodeposition

The first semiconductor electrodeposited is elemental silicon by Ulik [31] using electrolysis containing a solution of  $K_2SiF_6$  in KF. Silicon electrodeposition began in the 1930's after an intensive systematic research [32]. The electrochemical synthesis of III-V compounds started with GaP in 1968 by Cuomo and Gambino [33], a thickness up to 100  $\mu m$  of GaP on silicon substrate was prepared. Electrodeposition of GaAs has been reported by DeMattei et al. [34] in 1978. An electrolyte in the form of molten salt solution was used which contained  $NaAsO_2$  and  $Ga_2O_3$  in a  $B_2O_3$ -NaF solvent at 720 - 760°C.

Hodes et al. [35] reported the first aqueous electrodeposition of II-VI compound semiconductor, CdSe on titanium substrate. The anodization of cadmium and bismuth in polysulphide solution produced the CdS and  $Bi_2S_3$  in 1976 by Miller and Heller [36]. In 1978, Panicker et al. [37] reported electrodeposition of CdTe from aqueous solution using  $CdSO_4$  and  $TeO_2$ . The deposition was carried out using three electrode cell. A conversion efficiency of 0.4% has been achieved on electrodeposited CdTe deposited on titanium substrate [38]. Electrodeposition of CdS started using an aqueous solution containing  $Cd^{2+}$  and  $SO_3^{2-}$  ions in 1981 [39].

### 2.1.6.2 Electrodeposition in General

The deposition of a substance on an electrode by the action of an external source (electricity) is known as electrodeposition (ED). It is carried out in an electrochemical cell consisting of a reaction vessel of two or three electrodes. In the two electrode cell, the reaction is controlled by the current applied between the working electrode and counter electrode. A reference electrode is used to control or measure the potential of the working electrode in the three electrode cell, and the deposition is carried out by controlling the current whilst monitoring the potential, or by controlling potential whilst measuring the current. Figures 2.10 (a) and (b) show typical set-ups of three and two electrode systems respectively.

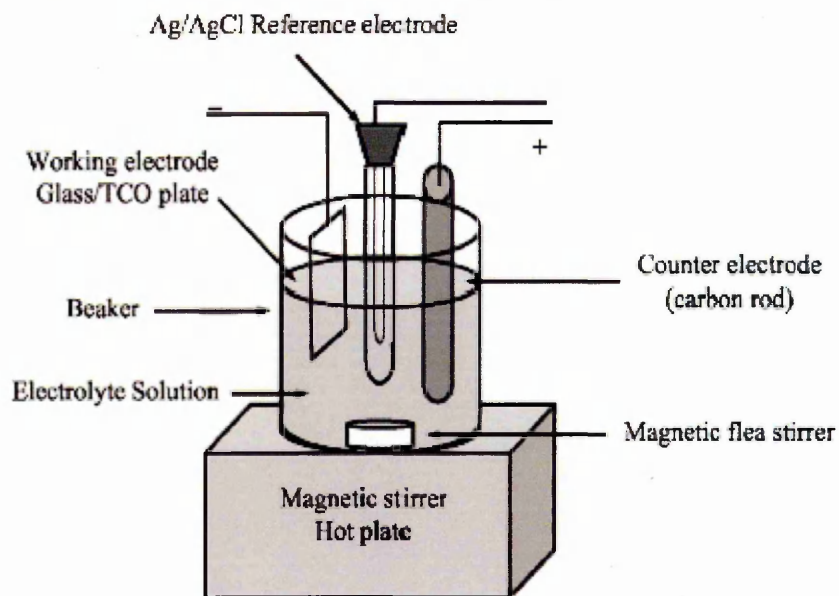


**Figure 2.10 (a):** Typical set-up of three electrode system [40].



**Figure 2.10 (b):** A photograph of a typical two electrode set-up.

An ED system consists of an electrolyte, two electrodes and a power supply (for two electrode system). The electrolyte must be electrically conductive and it can be aqueous, non-aqueous or molten and must contain suitable metal salts. The electrodes must consist of at least the cathode (working electrode) and anode (counter electrode). The counter electrode is a high purity graphite plate; the working electrode is

glass/conducting glass substrate where semiconductor material is deposited on. For three electrode system, a reference electrode is added.

As reported in the literature [40], the use of reference electrode in electrodeposition such as standard calomel or Ag/AgCl may be a problem because if such ions (especially  $\text{Ag}^+$ ) leaks into the bath, it poisons the bath and therefore reduces the efficiencies of the solar cells. This result has been confirmed by Dennison [41]. For this reason, in this work, two electrode systems were used because of its simplicity and reduction of manufacturing cost.

ED is a non-vacuum technique and it offers excellent control over the properties of the thin films through the influence of parameters such as deposition potential, bath temperature, pH, deposition time and electrolytes concentration [42]. In comparison with CBD, which is the other common liquid phase deposition technique, ED is more readily controlled and the precursor solutions are stable. ED has the additional advantages of very high utilization of constituent chemicals, which reduces the amount of Cd-containing waste generated. Films can be deposited onto the desired area of the substrate and the electrolyte can be used for a long period of time. One of the main disadvantages of ED is that the substrate must be conductive and its sheet resistance must be low.

CdTe films have been electrodeposited by BP, and CdTe solar panels were manufactured. The plant had eight identical reaction chambers, each tank capable of handling 40, 0.55 m<sup>2</sup> (14" × 61") substrates or 24, 0.94 m<sup>2</sup> (24" × 61") substrates [43]. In 2001, BP produced CdTe modules with area of 0.81 m<sup>2</sup> and has conversion efficiency 10.7% [44].

In general terms, the reaction in the aqueous medium involved in electrodeposition is governed by Faraday's two laws. These laws were discovered in 1843 by Michael Faraday [42].

Faraday's 1<sup>st</sup> Law of Electrolysis: States that the mass of a substance altered at an electrode during electrolysis is directly proportional to the quantity of electricity transferred at electrode. "Quantity of electricity" refers to electrical charge, typically measured in Coulombs.

Faraday's 2<sup>nd</sup> Law of Electrolysis: States that the masses of the different substances liberated in the electrolysis are proportional to their chemical equivalent weights.

Faraday's laws can be summarized as [42]:

$$m = \left(\frac{Q}{F}\right)\left(\frac{M}{z}\right) \quad 2.1$$

Equation 2.2 gives the Faraday's equation which is used to calculate the theoretical thickness of the deposited films:

$$T = \frac{1}{nFA} \left(\frac{itM}{\rho}\right) \quad 2.2$$

where  $m$  is the mass of the substance altered at an electrode,  $Q$  is the total electric charge passed through the substance,  $F = 96,485 \text{ Cmol}^{-1}$  is the Faraday constant,  $M$  is the molar mass of the substance,  $\rho$  is the density of the deposited film,  $i$  is the average current density,  $A$  is the area,  $T$  is the thickness,  $t$  is the time and  $z$  is the valence number of ions of the substance (electrons transferred per ion).

The cell potential  $E$  is related to the Gibbs free energy from the thermodynamic view. It is the chemical potential when a system reaches equilibrium at constant temperature and pressure and this change in the free energy is given by [42]:

$$\Delta G = -nFE \quad 2.3$$

where,  $E$  is the electrochemical cell potential and  $n$  is the electron number.

The sign of  $\Delta G$  gives the direction of the reaction; at positive potential, the free energy is negative which makes the reaction spontaneous. The free energy is positive at negative potential and therefore the reduction reaction must be forced. The Nernst equation is used to measure the potential of an electrochemical cell ( $E$ ) and it provides information of how far from the equilibrium is the redox reaction. Equation 2.25 gives the Nernst equation [42]:

$$E = E_o - \frac{RT}{nF} \ln \left[ \frac{ap}{ar} \right] \quad 2.4$$

where,  $E_o$  is the standard reference potential measured against SHE, concentration 1.0M, pressure 1 and temperature 25°C,  $R$  is the Gas constant,  $T$  is the temperature in K,

$n$  is the number of electrons,  $F$  is the Faraday's constant,  $ap$  is the activity of products and  $ar$  is the activity of reactants.

Electrodeposition from aqueous solution does not exceed  $100^{\circ}\text{C}$  because at this temperature the electrolyte starts to boil. The non-aqueous media such as ethylene glycol allow an increase in temperature  $\sim 170^{\circ}\text{C}$  [45]. The deposition of  $\text{CdS}_x\text{Se}_{(1-x)}$  from non-aqueous solution containing  $\text{CdCl}_2$  and S in an ethylene glycol has been reported [45]. The temperature of the electrolytes solution reaches  $\sim 170^{\circ}\text{C}$ . Similarly, Gore et al. [46] reported CdTe films deposition on Nickel substrate using non-aqueous solution containing AR-grade  $\text{CdCl}_2$ , KI and  $\text{TeCl}_4$  in ethylene glycol. The stability of the bath is within the temperature ranges  $25 - 180^{\circ}\text{C}$ . Ethylene glycol starts boiling at temperature greater than  $180^{\circ}\text{C}$ . The deposition of CdTe takes place at temperature  $\sim 160^{\circ}\text{C}$ .

### 2.1.6.3 Theory of Electrodeposition

#### (a) Cyclic Voltammogram

This technique used to identify the regions where the deposition of thin film material takes place. The electrical properties of species in a solution as well as at the electrode/electrolyte interface can be studied using cyclic voltammogram. Figure 2.11 show a typical cyclic voltammogram of CdTe bath containing 1.0M ( $3\text{CdSO}_4 \cdot 8\text{H}_2\text{O}$ ), 4 ml  $\text{TeO}_2$  solution and 1000 ppm  $\text{CdCl}_2 \cdot \text{H}_2\text{O}$ . Detailed explanation of this technique will be discussed in chapters 3, 4 and 5 for electrodeposition of CdS, ZnTe and CdTe respectively.

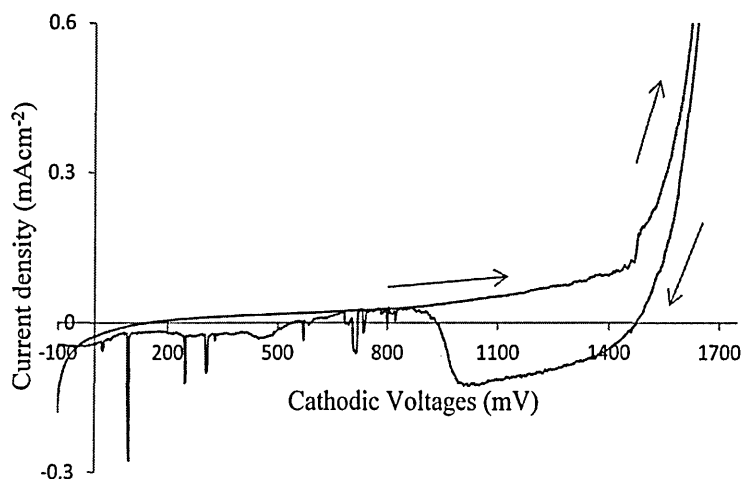


**Figure 2.11:** Typical cyclic voltammogram for electrolytic baths used for deposition of CdTe.

Hydrogen evolution occurs at cathodic voltages above 1.20 V due to splitting of water molecules by hydrogen evolution which has disadvantage in one way or the other. The quality of the film being deposited deteriorates and sometimes falls away completely during vigorous H<sub>2</sub> evolution. It is useful if not vigorous, as hydrogen passivation is automatically provided.

(b) Pourbaix Diagram

A Pourbaix diagram shows the dependence of the deposition potential on the pH value of an electrolyte. It is an isothermal phase diagram, which represents metal-ion-oxide equilibria plotted with deposition potential and pH as coordinates. Parameters that can be assessed using this diagram include effect of pH, oxidation potentials, corrosion etc. A Pourbaix diagram was used only as a guide to know exactly the stable pH of the CdTe bath condition. Figure 2.12 shows a Pourbaix diagram related to aqueous electrodeposition of CdTe thin film developed by Volushchuk et al. [47]. From the Figure, stability limits of solid CdTe are represented by lines 1 and 4 (lower limit) and 5, 11 and 12 (upper limit). This shows that CdTe is thermodynamically stable in this region. In acidic, neutral and basic solution at potential above the lower stability limits, hydrogen is released at the cathode. CdTe reduces to Cd and H<sub>2</sub>Te at pH values of 2.0 and cathodic potential greater than -1.5 V. Similarly, it corrodes to Cd<sup>2+</sup> and Te at smaller cathodic potential less than 0.1 V.

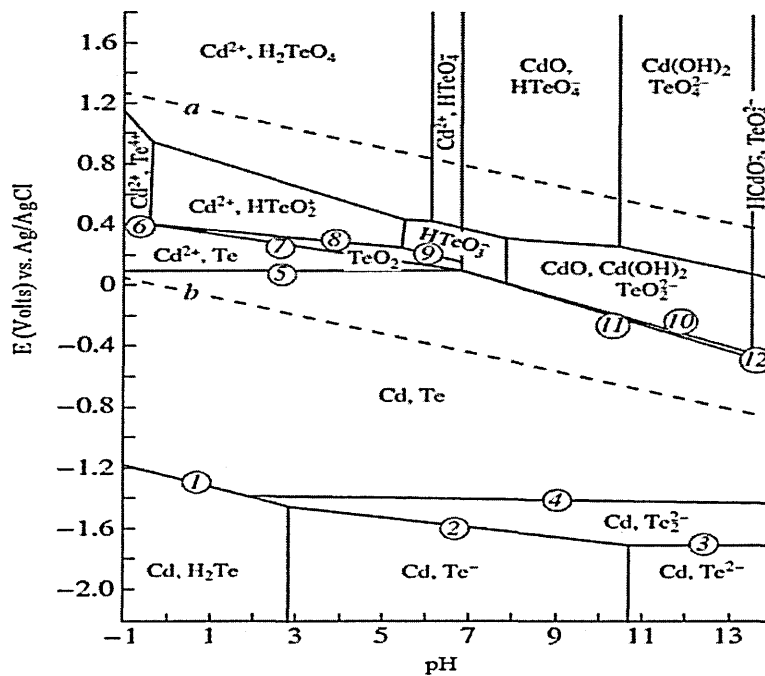


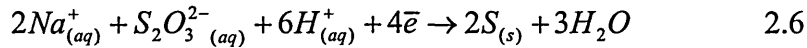
Figure 2.12: Pourbaix diagram of the CdTe-H<sub>2</sub>O system [47].

### 2.1.6.4 Equations related to deposition of CdS, ZnTe and CdTe

(a) CdS thin films:

CdS thin films were cathodically deposited from a solution containing  $Cd^{2+}$  and  $S^{2-}$  ions according to the following equations [48]:

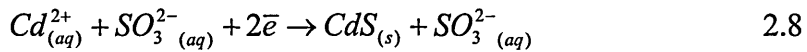
The cathodic reactions leading to the formation of CdS formation are;



The thiosulphate ion is:



The overall electrode reaction is given by equations 2.5 and 2.7 as;



(b) ZnTe thin film:

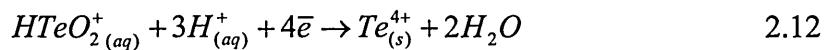
Mahalingam et al. [49] gives the following equation related to the ZnTe thin film using electrodeposition method as:



(c) CdTe thin film:

The following are the equation related to CdTe thin film deposition [50]:

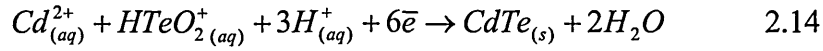
Reduction of Tellurium



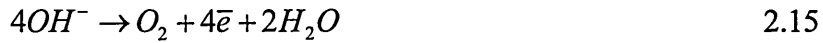
Deposition of Tellurium with the  $Cd^{2+}$  ions



Generally, the overall cathode reaction is



Similarly, anode reaction is



Therefore, the formation of CdTe compound can be obtained from the cathode reaction.

## 2.2 Materials Characterisation

### 2.2.1 X-ray diffraction (XRD)

XRD is used to identify the structure and phases of a material and is a non-destructive technique. Other uses include determination of texture and residual stress in films. Wilhelm Roentgen in 1895 [51] while he was experimenting with a Crookes tube discovered X-rays. The scattering centres for x-rays rely on the fact that crystals are composed of regularly spaced atoms. X-ray waves interact with the atoms in a crystal as shown in Figure 2.13, in such a way as to produce interference. Diffraction will occur if the wavelength of the x-ray and the atomic spacing of the crystal are comparable.

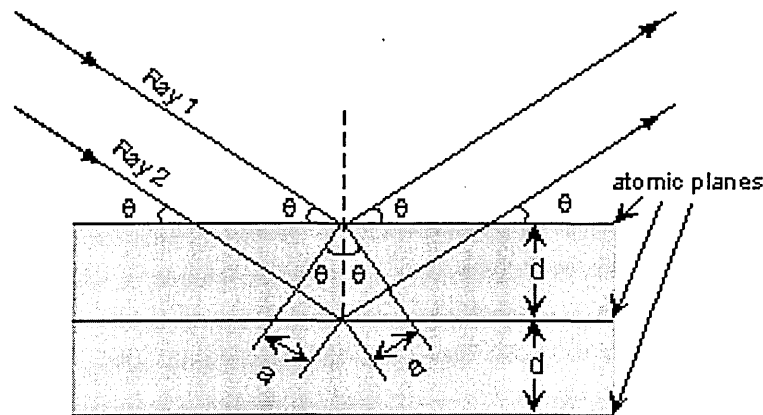


Figure 2.13: X-ray diffraction beam through a parallel section of crystal lattice [52].

Let  $\theta$  be the angle which the x-rays enters a crystal with one of these atomic planes and  $2a$  be the path difference between two rays. For constructive interference to occur [52];

$$2a = n\lambda \quad 2.16$$

From the Figure above,

$$a = d \sin \theta, \quad \therefore 2d \sin \theta = n\lambda \quad 2.17$$

where,  $n$  is an integer,  $\lambda$  is the wavelength of x-rays incident on a crystal and  $d$  is the distance between lattice planes.

Equation 2.17 is known as Bragg's Law for x-ray diffraction.

A strong diffracted beam occurs if the rays scattered by all the atoms in the planes interfere constructively and are in phase. Furthermore, constructive interference would fail if the scattering atoms were not arranged in a regular periodic manner and the scattered rays would have random phase.

In a Bragg Brentano diffractometer, the x-ray intensity is measured by a scintillation counter which is mounted to a measuring device called a goniometer at an angle. The sample and the counter are both rotated (but the rotation of the counter is on the diffractometer circle). A practical XRD instrument comprises three main elements; an x-ray source, a prepared sample and a detector as shown in Figure 2.14

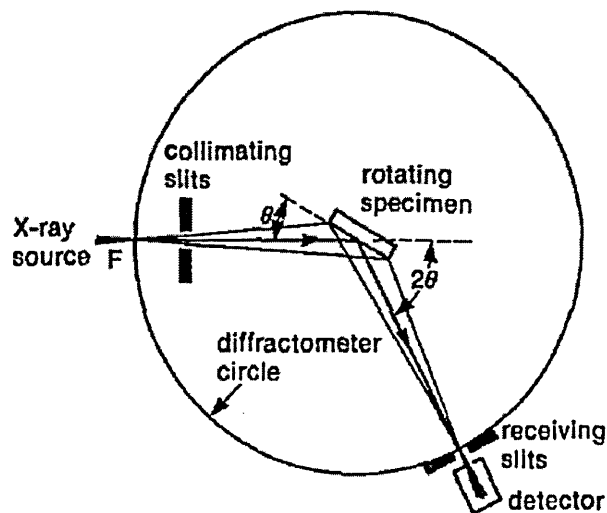


**Figure 2.14:** Configuration of glancing angle diffractometer [53].

All XRD spectra are presented in a log-linear form in which the horizontal  $2\theta$  axis has a linear scale and the vertical (count) axis uses a log scale. The diffraction peaks are analysed using equation 2.17 to determine the  $d_{hkl}$  spacing of the plane causing that peak. The characteristics of the unit cells of each phase present in the material can be determined from the intensity and position of the peaks. The material can be identified by comparing peak positions with standard data files called Joint Committee on Powder Diffraction Standard (JCPDS). From the full width at half maximum (FWHM), the strain, grain size and lattice parameters can be calculated as follows:

The Scherer equation is used to calculate the grain size,  $D$  [51];

$$D = \frac{k\lambda}{\beta \cos \theta} \quad 2.18$$

where  $\beta$  is the full width at half maximum of the peak corrected for instrumental broadening,  $\lambda$  is the wavelength of the x-rays,  $\theta$  is the Bragg angle and  $k$  is the Scherer constant taken to be 0.94.

The Hull equation is used to calculate the strain ( $\varepsilon$ ) and is given by [51];

$$\beta \cos \theta = \varepsilon \sin \theta + \frac{\lambda}{D} \quad 2.19$$

The lattice parameters for a hexagonal crystal can be calculated using the equation below [51];

$$\frac{1}{d^2} = \frac{h^2 + k^2}{a^2} + \frac{l^2}{c^2} \quad 2.20$$

### 2.2.2 Photoelectrochemical (PEC) cell

The conductivity type of a semiconductor can be determined using a PEC cell measurement. Working and counter electrodes are connected to a potentiometer and placed in a suitable electrolyte to form a solid/liquid junction. Once connected, the voltages between the two electrodes are measured under both dark and white

illumination conditions. The difference between these two voltage values gives the open circuit voltage of the liquid/solid junction or the PEC signal. The sign of the PEC signal determines the conductivity type of the semiconducting layer, and the magnitude of the signal indicates the doping concentration. A zero PEC signal is produced for both metallic and insulating layers and the largest PEC signal is produced by semiconductor with optimum doping. Figures 2.15 (a) and (b) show the band diagrams of n-type and p-type semiconductor/liquid junctions respectively.

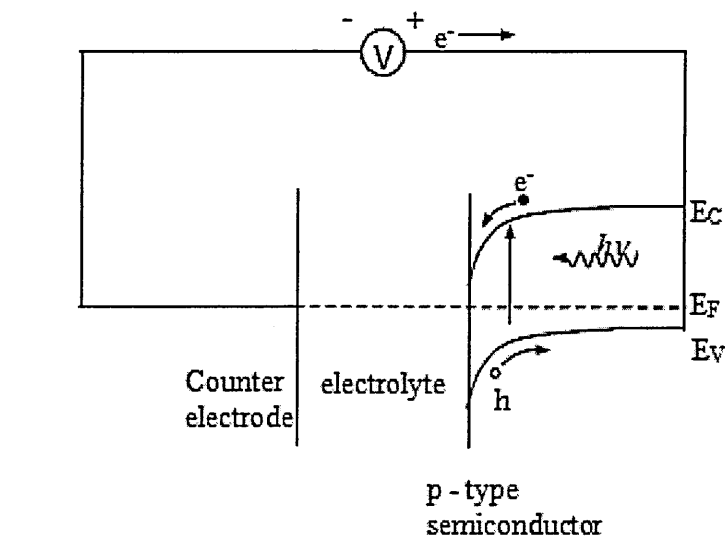
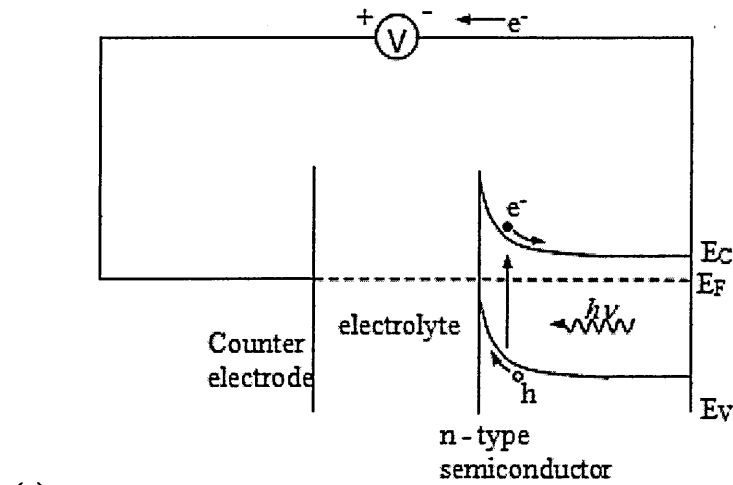


**Figure 2.15:** Band diagrams of solid/liquid junction for (a) n-type and (b) p-type semiconductors [54].

For n-type semiconductor, the holes move towards the surface of the semiconductor and the electrons move into the bulk of the material. In the case of a p-type semiconductor electron flow is opposite to that of a n-type semiconductor system.

### 2.2.3 Optical absorption

Optical absorption measurements were carried out to evaluate the bandgap of the semiconducting materials. The value of the bandgap indicates how the semiconducting layers perform as absorbers of light. The absorption coefficient,  $\alpha = f(\lambda)$  is a function of the wavelength of the light. The bandgap energy,  $E_g$  values were derived from mathematical treatment of data obtained from optical absorbance versus wavelength with the Stern relationship [55] of near absorption edge data using;

$$\alpha = \frac{k(h\nu - E_g)^n}{h\nu} \quad 2.21$$

where,  $\nu$  is the frequency,  $h$  is Planck's constant, and  $n$  carries the value of either 1 or 4, (the value of  $n$  is 1 and 4 for direct and indirect transitions respectively).

Equation (2.21) shows that  $\alpha$  increases sharply as the energy of photons exceeds  $E_g$ , so that a well-defined absorption edge is expected in semiconductor materials with a direct bandgap. To obtain transmission spectra, the same instrument is used with the transmission data mode selected from the menu of the instrument. The bandgap energy of the semiconductor determines the percentage transmission of light of known wavelength, through the material.

Figure 2.16 shows the main features of the spectrophotometer. It consists of four main components: (i) the light source which produces the required region of the spectrum, (ii) the monochromator which receives the input from the light source and outputs is tuneable highly monochromatic light, (iii) the sample chamber where the sample to be analysed was placed, and (iv) the detector [56].

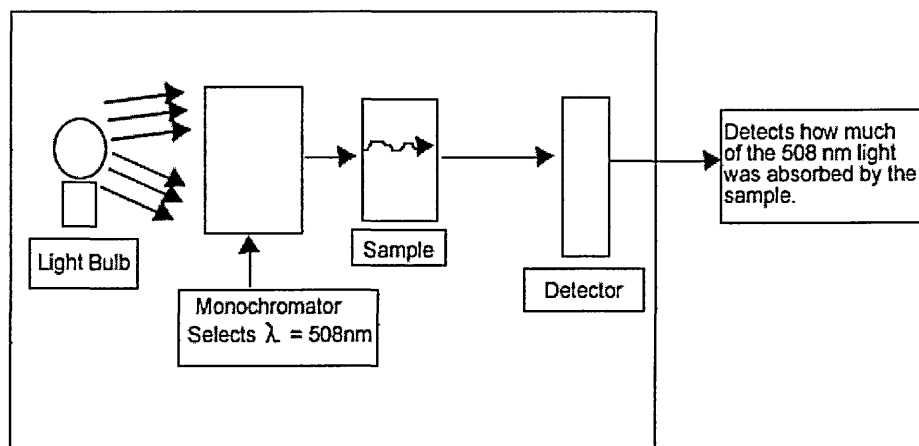


**Figure 2.16:** The main features of a spectrophotometer [56].

#### 2.2.4 Scanning Electron Microscopy (SEM)

SEM studies were carried out to investigate the surface morphology, grain size and orientation of materials making up the sample. Figure 2.17 shows the schematic diagram of the SEM. An electron gun is used to generate a monochromatic electron beam which passes through the first condenser lens with condenser aperture attached. The aperture is used to eliminate some high angle electrons. A focussed beam is now generated by fine focussing using second condenser lens. A grid pattern is now produced by the deflection coils and scanned onto the desired area of the sample by the final lens. A vacuum is required in order to avoid scattering and absorption. Several interactions take place when the electron beam is focused on the sample surface and what is emitted from the surface is detected by a suitable detector.

Chemical information about the sample may be obtained from the characteristics x-rays emitted from the specimen. An energy dispersive x-ray (EDX) spectrometer consists of a solid state x-ray detector mounted within the SEM chamber. It usually made from lithium-drifted silicon, Si(Li); and signal processing electronics. An x-ray energy histogram is displayed as a result of the signal conversion by the Si(Li) detector after the emitted x-rays are detected. A series of peaks representative of each element displayed with their relative amount and the atomic composition of the element can be estimated [57].

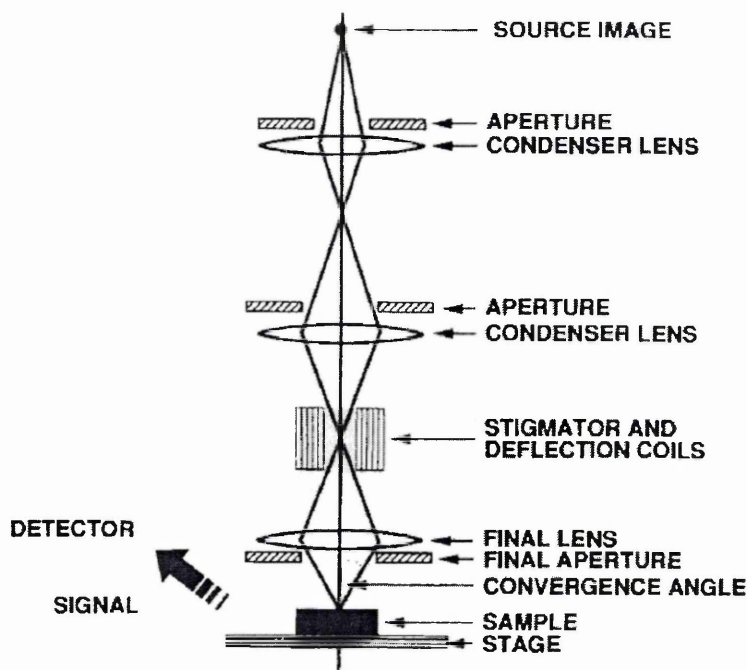


Figure 2.17: Schematic diagram of SEM [53].

### 2.2.5 Atomic Force Microscopy (AFM)

This technique developed in 1986 [58] and it resolve images down to a single atom and has a huge advantage over electron and conventional optical microscopes. It gives 2D & 3D-images and can give a true topographic view of the sample with its vertical view. Figure 2.18 shows a schematic diagram of a typical AFM instrument. A micro fabricated cantilever is used as the probe which forces sensors placed on the sharp tip that is positioned on or below the sample surface. Generally, the piezoelectric actuator which is under computer control moves the sample very precisely while the tip is stationary. AFM can be operated in three modes which includes contact mode (true), non-contact mode and intermittent (called tapping) mode.

- (a) Contact mode: Soft silicon nitride cantilever is typically used to probe the surface. Tip is kept at a fixed height at or above the surface and the cantilever deflection is used to generate an image.
- (b) Non-contact mode: Tip is oscillated at its resonant frequency at some small distance above the surface. The signal applied to the piezoelectric actuators needed to keep the resonant frequency constant is then used to generate a topographic image.

(c) Intermittent mode: The cantilever is initially oscillated at its resonance frequency at amplitudes much greater than those utilized in non-contact mode. Tip comes in contact with the surface as it brought close to the surface and its amplitude is reduced. This is the preferred method of imaging when atomic resolution is not needed [59].

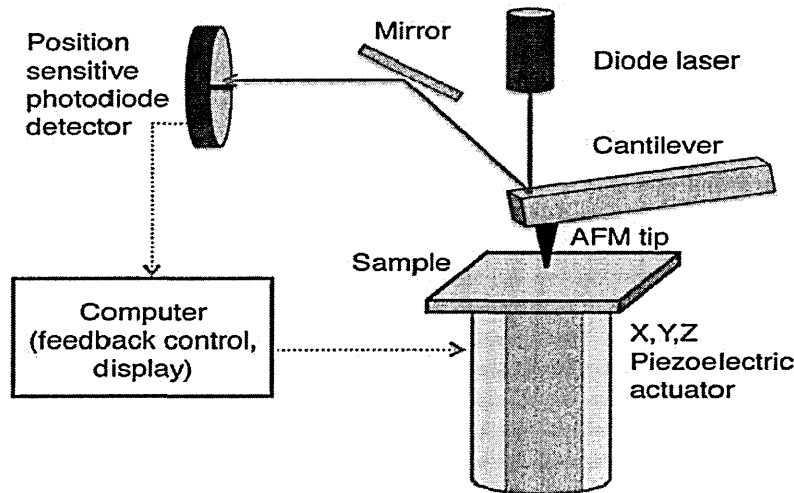


**Figure 2.18:** Schematic diagram of a typical AFM instrument [59].

### 2.2.6 X-ray Fluorescence (XRF)

This technique involves excitation by high energy x-ray or gamma ray bombardment of materials, thereby creating the emission of characteristic secondary (or fluorescent) x-rays from it. It is a destructive technique and gives the atomic percentage of the individual elements in the material. Figure 2.19 shows a schematic diagram of XRF spectrometer. When the x-rays strike the sample, diffraction occurs which later send through focusing slit to analysing crystal. Photons are diffracted with various wavelengths from the analysing crystal and collected by the detector which transfers them to the computer.

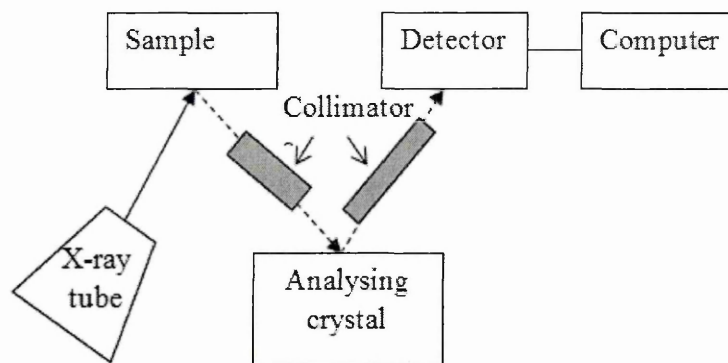


**Figure 2.19:** Schematic diagram of XRF spectrometer [60].

### 2.2.7 Raman Spectroscopy

Raman spectroscopy is a technique used to identify and provide information on chemical structures and physical forms from the characteristic spectral pattern (finger prints) of the material. In 1928, Raman and Krishnan [61] first experimentally observed the phenomenon of inelastic scattering of light after it was postulated by Smekal [62] in 1923. Later on, this phenomenon was named as Raman spectroscopy.

Raman spectroscopy relies on inelastic scattering of monochromatic light, usually from a laser in the visible, near IR or near UV range. Light interacts with phonons or other excitation in the system and as a result the incident photon's energy shifts up or down. Figure 2.20 shows the schematic diagram of a Raman spectrometer instrument. A Laser is focussed through a pinhole and then collected as an expanded parallel beam. The beam is used to collect the laser focused through a pinhole. A notch filter is used for the radiation which serves as interference filters. The charged coupled device (CCD) detector detects the light after passing into monochromator.

The wavenumber scale for most vibrations extends from  $50 \text{ cm}^{-1}$  to about  $1800 \text{ cm}^{-1}$  with some molecular vibrations extending to  $3500 \text{ cm}^{-1}$ . Line widths are on the order of  $1\text{-}5 \text{ cm}^{-1}$ .

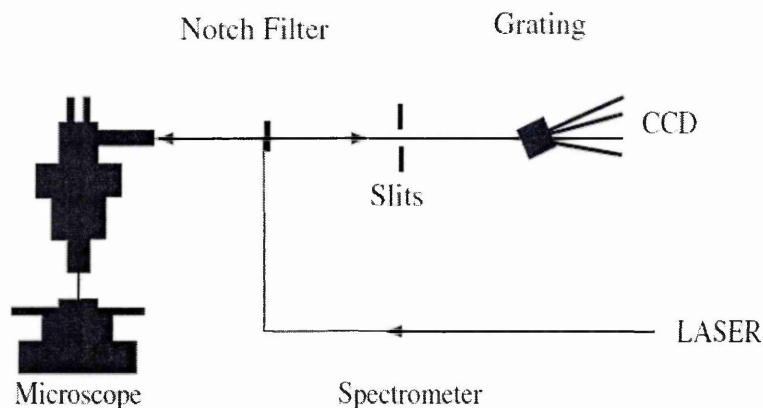


**Figure 2.20:** Schematic diagram of a Raman spectrometer instrument [63].

## 2.2.8 X-ray Photoelectron Spectroscopy (XPS)

The XPS technique uses single energy x-ray photons as a source of irradiation to the sample and detects the photoelectrons emitted from the surface. The photoelectric effect is the basic principle of XPS, was first discovered by Hertz, and later K. Siegbahn extended it to surface analysis [64, 65]. The technique is also useful for quantitative analysis of surface composition. The binding energies of all elements can be detected except hydrogen and helium. The kinetic energy of the x-ray photons used ranges from 300 to 1500 eV. Due to the short range of the x-ray photons, inelastic scattering is absent during electron travelling.

Figure 2.21 shows the schematic diagram of photoemission process used for XPS. An electron is emitted from the surface of the sample when a photon is absorbed. The kinetic energy of the emitted electron is given by [66];

$$KE = h\nu - BE - \varphi_s \quad 2.22$$

where,  $h\nu$  is the characteristics energy of the x-ray photon,  $BE$  is the binding energy of the core level electron and  $\varphi_s$  is the work function of the spectrometer.

Spectral lines or photoelectron peaks as a function of binding energy appear due to the electrons emitted from the sample without loss of inelastic energy. A spectral background also appears as a result of energy lost by the electrons. This binding energy of the ejected electrons is given by [66];

$$BE = h\nu - KE - \varphi_s \quad 2.23$$

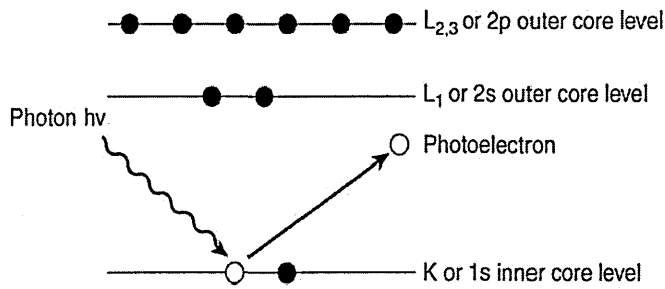


**Figure 2.21:** Schematic diagram of photoemission process used in XPS [59].

Two different modes are used to collect the XPS data:

- (a) Wide scans or survey spectra are used to get more information about the true nature of the surface composition. A wide energy range, typically  $\sim 1000$  eV, is employed.
- (b) Narrow scans with smaller energy windows are used at higher energy resolution to determine the chemical state of a specific element.

## 2.3 Device characterisation

### 2.3.1 Current Voltage (I-V) characteristics

I-V measurements are the most important technique used to obtain information on the PV and electrical properties of the fully fabricated devices. A device is said to be ohmic (non-active) or rectifying (active) from the shape of the I-V characteristics. Figure 2.22 shows a typical I-V curve under both the dark and illumination conditions.

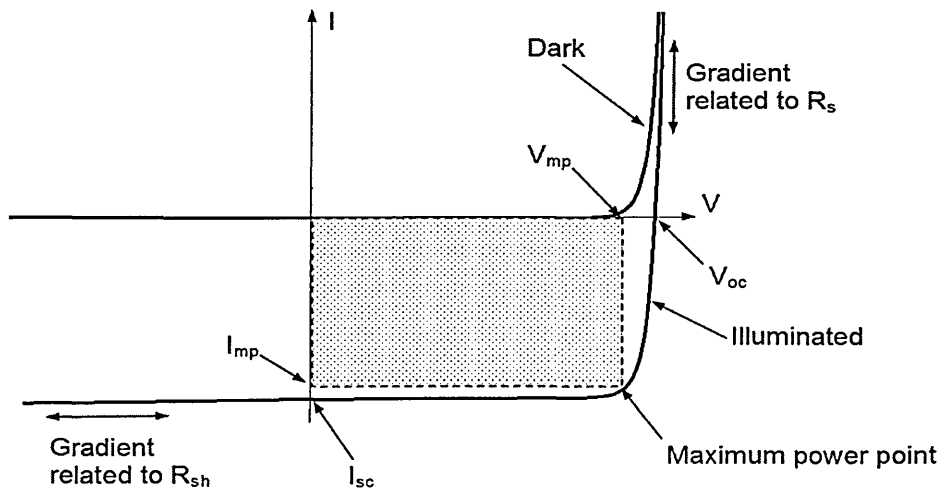


**Figure 2.22:** A typical I-V curve measured under dark and illuminated condition [54].

Four parameters can be deduced from the I-V characteristic which includes:

- (i) Open-circuit voltage ( $V_{oc}$ ): It is the voltage obtained when the terminals are open and no current is flowing in the external circuit.  $V_{oc}$  is obtained when current density is zero. Therefore [55];

$$V_{oc} = n \left[ \phi_b + \frac{kT}{e} \cdot \ln \left( \frac{J_{sc}}{AT^2} \right) \right] \quad 2.24$$

where,  $n$  is the diode ideality factor,  $k$  is the Boltzmann constant,  $T$  is the temperature,  $e$  is the electron charge,  $J_{sc}$  is the short-circuit current density,  $\phi_b$  is the barrier height and  $A$  is the diode area.

The  $V_{oc}$  can be increased by increasing the barrier height, minimising defects and reducing the temperature of the cell.

- (ii) Short-circuit current density ( $J_{sc}$ ): This parameter can be obtained when the external terminals are short circuited. The potential drop across the sample will be zero when the terminals are shorted.

$J_{sc}$  can be increased by reducing the grain boundaries, increasing charge carrier mobility ( $\mu$ ), maximising absorption of solar radiation, increasing the internal electric field ( $E_i$ ), reducing recombination and generation mechanism effectively, separating electron-hole pairs and using graded bandgap devices.

- (iii) Fill factor (FF): The ratio of the experimental power square and theoretical square is called the FF and is given by [55]:

$$FF = \frac{V_m J_m}{V_{oc} J_{sc}} \quad 2.25$$

where,  $V_m$  is the maximum voltage and  $J_m$  is the maximum current.

The FF can also be increased by increasing the internal electric field and minimising defects present in the device structure.

Series resistance ( $R_s$ ) and shunt resistance ( $R_{sh}$ ) are the two main factors to consider for increasing these three parameters. The  $R_s$  must be minimised and  $R_{sh}$  must be maximised in order to improve the FF.

(iv) Efficiency ( $\eta$ ): The conversion efficiency is given by [55]:

$$\eta = \frac{P_{out}}{P_{in}} = \frac{V_{oc} J_{sc} FF}{P_{in}} \quad 2.26$$

where,  $P_{in} = 100 \text{ Wm}^{-2}$  under AM1.5 condition.

Figure 2.23 shows the equivalent circuit of a solar cell which is considered as a diode with shallow junction depth to collect solar radiation and has  $R_{sh}$  in parallel in conjunction with  $R_s$  in series. These two resistances play crucial roles as follows:

- (a) In the ideal situation,  $R_{sh}$  should tend to infinity or to be finite (i.e. very large), when this happens it would block the leakage current. In a practical device, this is not the case and therefore defect levels/recombination centers reduce the value of  $R_{sh}$  within the cell. This makes the current to have an alternative less resistive path to flow (i.e. leakage current). The gradient of the I-V curve in the reverse direction gives the value of  $R_{sh}$ .
- (b)  $R_s$  should be zero in an ideal situation but it is the total resistance of the bulk of semiconductor and other interfaces. The  $R_s$  can be evaluated from the forward direction of the I-V curve gradient.

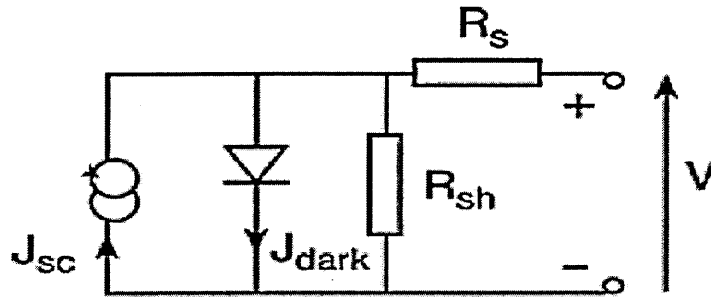


Figure 2.23: Equivalent circuit of a solar cell [67].

Size and Kwok state the current-voltage (I-V) relationship of a diode under dark condition as [55]:

$$I = SA^*T^2 \exp\left(\frac{-e\phi_b}{kT}\right) \left[ \exp\left(\frac{eV}{nkT}\right) - 1 \right] \quad 2.27$$

where,  $S$  is the area of contact,  $A^*$  is the effective Richardson constant  $= 12 \times 10^4 \text{ AKm}^{-2}$  and the other symbols have their usual meanings.

Equation (2.27) can be written as:

$$I = I_o \left[ \exp\left(\frac{eV}{nkT}\right) - 1 \right] \quad 2.28$$

where,  $I_o$  is the saturation current of the diode.

The I-V relationship under illumination is given by:

$$I = I_o \left[ \exp\left(\frac{e(V - IR_s)}{nkT}\right) - 1 \right] + \left[ \frac{V - IR_s}{R_{sh}} \right] - I_{sc} \quad 2.29$$

For an applied voltage greater than  $\sim 0.075$  V,  $\exp\left(\frac{eV}{nkT}\right) \gg 1$ ,  $R_{sh} \rightarrow \infty$  and  $R_s = 0$ , then equation 2.29 reduced to:

$$I = I_o \exp\left(\frac{eV}{nkT}\right) - I_{sc} \quad 2.30$$

Equation 2.30 can be rearranged to get more information as follows:

$$\text{Log}_{10} I = \left( \frac{e}{2.303nkT} \right) V + \log_{10}(I_o) \quad 2.31$$

The diode quality factor ( $n$ ) and the barrier height ( $\phi_b$ ) can be deduced from the straight line obtained when a graph of  $\log_{10}(I)$  vs ( $V$ ) is plotted.

The value of  $n$  for pure thermionic emission of electrons over the barrier is 1.00 and  $n = 2.00$  for pure recombination and generation [55]. The gradient of the curve can be used to calculate the diode quality factor as:

$$\text{Gradient} = \left( \frac{e}{2.303nkT} \right) \quad 2.32$$

Similarly, the value of  $\phi_b$  can be calculated from the intercept  $I_o$  and is given by:

$$I_o = SAT^2 \exp\left(\frac{-e\phi_b}{kT}\right) \quad 2.33$$

### 2.3.2 Capacitance Voltage (C-V) measurements

The technique used to estimate doping concentration ( $N_d$ ) of the semiconductor and the diffusion voltage of the Schottky diode is the C-V measurement. The depletion width ( $w$ ) and the barrier height ( $\phi_b$ ) can also be calculated. A high frequency AC signal of ~1 MHz is used as modulation frequency for the measurement. The junction is probed by the AC signal which contained charges on both side and the depletion region associated with the device. A graph of  $1/C^2$  versus  $V$  gives a straight line from which the diffusion voltage ( $V_d$ ) can be determined from the intercept on the V-axis. A straight line graph is obtained if the material is uniformly doped and its gradient gives the doping concentration using [68]:

$$\frac{1}{C^2} = \left( \frac{2}{\epsilon_s A^2 e N_d} \right) (V + V_{bi}) \quad 2.34$$

if  $N_A \gg N_D$

where,  $V_{bi}$  is the built in potential,  $\epsilon_s$  is the permittivity of the semiconductor and other symbols have their usual meanings.

Equation 2.35 is used to determine the  $\phi_b$  which depends on the  $V_{bi}$  [68] and Figure 2.24 shows the Schottky diode for an n-type semiconductor:

$$\phi_b = V_{bi} + \xi \quad 2.35$$

where,  $\xi$  is the energy difference between Fermi level and the CB for an n-type semiconductor and VB for a p-type semiconductor. The value of  $\xi$  is ~0.1 eV for moderately doped semiconductors.

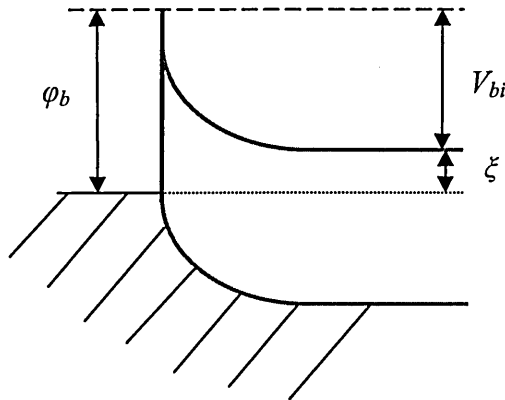


**Figure 2.24:** Schottky diode for an n-type semiconductor, reproduced from [55].

Similarly, the depletion width can be calculated from equation 2.36 and is given by [55]:

$$W = \sqrt{\frac{2\epsilon_0\epsilon_s}{eN_d}(V + V_{bi})} \quad 2.36$$

## References

1. K. L. Chopra and S. R. Das, *Thin Film Solar Cells*, Plenum Press, NY (1983).
2. V. S. Smehtkowski, *Prog. in Surface Science* 64, 1 (2000).
3. <http://wwwold.ece.utep.edu/research/webedl/cdte/Fabrication/index.htm>, Retrieved, December, 2011.
4. S. K. Mandal, S. Chaudhuri and A. K. Pal, *Thin Solid Films* 357, 102 (1999).
5. P. Taneja, P. Vasa and P. Ayyub, *Material Letter* 54, 343 (2002).
6. F. El Akkad and M. Thomas, *Phys. Stat. Sol. C* 2(3), 1177 (2005).
7. H. O. Pierson, *Handbook of Chemical Vapour Deposition (CVD): Principles, Technology and Applications*, 2<sup>nd</sup> edition, Noyes Publication, Park Ridge, NJ U.S.A., (1999).
8. A. Ali, N. A. Shah and A. Maqsood, *Solid State Electronics* 52, 205 (2008).
9. Y. H. Lee, W. J. Lee, Y. S. Kwon, G. Y. Yeon and J. K. Yoon, *Thin Solid Films* 341, 172 (1999).
10. K. D. Patel, G. K. Solanki, C. J. Panchal, K. S. Hingarajiya and J. R. Ghandi, *J. Nano-Electron. Phys.* 3(1), 41 (2011).
11. K. L. Choy, *Progress in Material Science* 48, 57 (2003).
12. R. A. Berrigam, N. Maung, S. J. C. Iroine, D. J. Cole-Hamilton and D. Ellis, *J. of Crystal Growth* 195, 718 (1998).
13. M. Lindurer, G. F. Schötz, P. Link, H. P. Wagner, W. Kuhn and W. Gebhardt, *J. Phys: Condense Matter* 4, 6401 (1992).
14. J. R. Arthur, *Surface Science* 500, 189 (2002).
15. P. Boieriu, R. Sporcken, Y. Xin, N.D. Browaning and S. Sivawanthan, *J. of Electronic Mater.* 29(6), 718 (2000).
16. J. Zhao, Y. Zeng, C. Liu and Y. Li, *Appl. Surface Science* 256, 6881 (2010).

17. S. N. Alamri, *Phys. Stat. Sol. a* 200(2), 352, (2003).
18. A. Seth, G. B. Lush, J. C. McChue, V. P. Singh and D. Flood, *Sol. Energy Mater. Sol. Cells* 59, 35 (1999).
19. J. Han, C. Liao, T. Jiang, C. Spanheimer, G. Haindl, G. Fu, V. Krishnakumar, K. Zhao, A. Klein and W. Jaegermann, *J. of Alloys & Compounds* (2010), doi:10.1016/j.jallcom.2010.12.085.
20. G. K. Rao, K.V. Bangera and G. K. Shivakumar, *Vacuum* 83, 1485 (2009).
21. [www.firstsolar.com](http://www.firstsolar.com), Retrieved July, 2011.
22. P. S. Patil, *Materials Chemistry and Physics* 59, 185 (1999).
23. J. Toušková, D. Kindl and J. Konanda, *Thin Solid Films* 214, 92 (1992).
24. J. De Merchant and M. Coceiver, *J. Electrochem. Soc.*, 143(12), 4054 (1996).
25. A. K. Berry, *Mater. & Engineering B* 8, 57 (1996).
26. A. Luque and S. Hegedus, *Handbook of Photovoltaic Science and Engineering*, John Wiley & Sons, Ltd., U.S.A., (2003).
27. T. Arita, A. Hanafusa, N. Ueno, Y. Nishiyama, S. Kitamura and M. Murozono, *Solar Energy Material* 23, 371 (1991).
28. V. Kumar, J. K. Gaur, M. K. Sharma and T. P. Sharma, *Chalcogenide Letters* 5(8), 171 (2006).
29. E. Tekin, J. Smith, S. Hoepfner, A. M. J. Vanden Berg, A. S. Susha, A. L. Rogach, J. Feldmann and U. S. Schubert, *Advance Functional Materials* 17, 23 (2003).
30. R. Parashkov, E. Becker, T. Riedl, H-H Johnnes and W. Kowalsky, *In Proc: IEEE* 93(7), 1321 (2008).
31. F. Ullik, *Ber. Akad. Wien* 52, 115 (1865).
32. M. Ddero, *Compt. Rend. Acad. Sci. Paris* 109, 556 (1934).
33. J. J. Combo and R. J. Gambino, *J. Electrochem. Soc.* 115(7), 755 (1968).

34. R. C. DeMattei, D. Elwell and R. S. Feigelson, *J. Crystal Growth* 43, 643 (1978).
35. G. Hodes, J. Manassen and C. Cahen, *Nature* 261, 403 (1976).
36. B. Miller and A. heller, *Nature* 262, 680 (1976).
37. M. P. R. Panicker, M. Knaster and F. A. Kröger, *J. Electrochem. Soc.* 125, 566 (1978).
38. W. J. Danaher and L. E. Lyon, *Nature* 271, 139 (1978).
39. J. F. MaCann and K. M. Skylas, *J. Electroanal. Chem.* 119, 409 (1981).
40. I. M. Dharmadasa and J. Haigh, *J. Electrochem. Soc.* 153(1), G47 (2006).
41. S. Dennison, *J. Mater. Chem.* 4(1), 41 (1994).
42. R. K. Pandey, S. N. Sahu and S. Chandra, *Handbook of Semiconductor Electrodeposition*, Marcel Dekker, Inc. New York, (1996).
43. D. Cunningham et al. *Conf. rec. 16th EPSSEC*, 281 (2000).
44. M. A. Green, K. Emery, Y. Hisikawa and W. Warta, *Prog. Photovolt: Res. Appl.* 15, 425 (2007).
45. K. Premaratne, S. N. Akuranthilaka, I. M. Dharmadasa and A. P. Samantilleka, *Renewable Energy* 29, 549 (2003).
46. R. B. Gore, R. K. Pandey and S. K. Kulkarni, *Solar Energy Material* 18, 159 (1989).
47. A. G. Voloshchuk, N. I. Tsipishchuk, *Inorganic Materials* 38(11), 1114 (2002).
48. J. F. McCann and M. Sk. Kazacos, *J. Electroanal. Chem.* 119, 409 (1981).
49. T. Mahalingam, V. S. John, S. Rajindran, G. Ravi and P.J. Sebastian, *Surface and Coating Technol.* 155, 245 (2002).
50. W. J. Danaher and L. E. Lyons, *Aust. J. Chem.* 37, 689 (1984).

51. B. D. Cullity and S. R. Stock, Elements of X-ray Diffraction 3<sup>rd</sup> edition, Prentice Hall, Inc. Upper Saddle River, New Jersey, U. S. A., (2001).
52. <http://Serc.carleton.edu/research./geochemsheets/technique/XRD.html>. Retrieved, October 2011.
53. C. R. Brundle, C. A. Evans Jr, and S. Wilson, Encyclopaedia of Mater. Charact.: Surfaces, Interfaces and Thin Films, Butterworth-Heinemann Inc. USA, (1992).
54. G. J. Tolan, PhD. Thesis, Sheffield Hallam University, UK (2008).
55. S. M. Sze and Ng. K. Kwok, Physics of Semiconductor Devices 3<sup>rd</sup> Edition, Wiley-Interscience, (2007).
56. <http://www.wellesley.spectrophotometer>. Retrieved, October 2011.
57. R. F. Egerton, Physical Principles of Electron Microscopy: An Introduction to TEM, SEM and AFM, Springer Science+Business Media, Inc. (2005).
58. A. T. Hubbard, The Handbook of Surface Imaging and Visualization, CRC Press Ltd., (1995).
59. P. M. Martin, Handbook of Deposition Techniques 3<sup>rd</sup> edition, Elsevier Sci. & Technol., USA, (2010).
60. I. Salaoru, P. A. Buffat, D. Laub, A. Amariel, N. Apetroaei and M. Rusu, J. of Optoelectronics & Adv. Mater. 8(3), 939 (2006).
61. C. V. Raman and K. S. Krishnan, Nature 21, 501 (1928).
62. A. Smekal, Naturwissenschaften 43, 873 (1923).
63. E. Smith and G. Dent, Modern Raman Spectroscopy: A Practical Approach, John Wiley & Sons, Ltd., England, (2005).
64. D. Briggs and M. P. Seah, Practical Surface Analysis, John Wiley, Chichester (1990).

65. K. Siegbahn, Alpha- Beta- and Gamma-Ray Spectroscopy, North-Holland, Amsterdam, (1965).
66. J. F. Moulder, J. Chastain, R. C. King, in: Handbook of X-Ray Photoelectron Spectroscopy: A Reference Book of Standard Spectra for identification and Interpretation of XPS Data, Physical Electronics, Eden prairie, MN, (1995).
67. M. Pagliaro, G. Palmisano and R. Ciriminna, Flexible Solar Cells, Wiley-VCH Verlag GmbH & Co. KGaA, Weinheim, (2008).
68. E. H. Rhoderick and R. H. Williams, Metal-Semiconductor Contacts 2<sup>nd</sup> edition, Oxford University Press, NY, (1988).

## Chapter 3: Experimental

### 3.1 Introduction

This chapter describes the experimental techniques used to electrodeposit two window materials (CdS and ZnTe) onto glass/FTO substrate and an absorber material CdTe onto glass/FTO/CdS substrate. Due to the peeling off of ZnTe in acidic CdS and CdTe baths, the complete structure of the devices is based only on glass/FTO/CdS/CdTe/Au contact.

Prior to deposition of CdS and ZnTe, the substrates were washed thoroughly with soapy water, methanol, acetone, dilute HNO<sub>3</sub> and finally rinsed in glacial acetic acid. The glass/FTO substrates were rinsed in de-ionized water between the different solvents, while only glacial acetic acid is used to clean the glass/FTO/CdS layer and rinsed in de-ionized water prior to CdTe deposition. All chemicals used for electrodeposition were analytical reagent grade of purity 5N (99.999%) from Fisher Scientific Ltd., and Sigma-Aldrich, UK. Details of substrate cleaning process are discussed in the next section.

The working and counter electrodes were held vertically using Teflon tape. Potentiostatic deposition in a conventional single compartment cell was carried out using a two-electrode set-up. The glass/FTO or glass/FTO/CdS conductive substrate formed the working electrode and a graphite carbon electrode as a counter electrode. A typical experimental set-up is shown in Figure 2.10 (b) in section 2.1.6.2 of chapter 2. The electrolyte was stirred constantly using a magnetic stirrer throughout deposition at moderate rate. The electrodeposition mechanism was studied using a cyclic voltammogram. Cyclic voltammetry was performed using a Gill AC computerised potentiostat system (S/N 1313 ACM Instruments), the details of which are discussed in chapters 4, 5 and 6.

The deposited layers were rinsed with de-ionized water, dried under nitrogen air at room temperature and subjected for further analysis. Conductivity type, optical, structural, surface morphology, molecular structure, chemical composition and atomic percentage of the deposited films were studied using Photoelectrochemical (PEC) studies, UV-Vis spectrophotometer, X-ray diffraction (XRD), scanning electron microscopy (SEM)/ atomic force microscopy (AFM), Raman spectroscopy, X-ray photoelectron spectroscopy (XPS) and X-ray fluorescence (XRF) measurements respectively.

Furthermore, the electrical characterisation of fully fabricated devices was performed using current-voltage (I-V) and capacitance-voltage (C-V) measurements.

### 3.2. Electrolyte preparation and deposition of CdS thin film

$\text{CdCl}_2 \cdot \text{H}_2\text{O}$  and  $\text{Na}_2\text{S}_2\text{O}_3$  were used as the source of Cd and S ions respectively. The electrolytic bath was a 1000 ml water-jacketed glass beaker and a 500 ml plastic beaker which contained the 300 ml of electrolyte (aqueous solution). The following are the quantity of each chemical:

- 18.126 g of  $\text{CdCl}_2 \cdot \text{H}_2\text{O}$  (0.3M)
- 2.234 g of  $\text{Na}_2\text{S}_2\text{O}_3$  (0.03M)

The temperature of the electrolytes initially was kept at  $70^\circ\text{C}$  &  $\text{pH} = 5.00 \pm 0.03$  and later reduced to  $45^\circ\text{C}$  &  $\text{pH} = 1.40 \pm 0.02$ . Deposition of CdS thin film was performed at this condition.

CdS deposition starts at  $70^\circ\text{C}$  and  $\text{pH} = 5.00 \pm 0.03$ , after 20 – 30 minutes the electrolyte in the bath suddenly started to turn from colourless to yellow. During this growth the stability of the electrolyte is poor. This means that the CBD-process also takes place under the conditions occurring within the bath. The pH was adjusted from 5.00 – 2.50 by adding a few drops of HCl and the temperature were reduced to  $55^\circ\text{C}$ . A set of 14 samples of CdS layers were grown at different cathodic potentials (set 1). To maintain the stability of the bath, the pH and temperature were reduced to 1.4 and  $46^\circ\text{C}$  respectively. Another set of 21 samples were grown at different cathodic potentials (set 2). The areas of the samples were typically in the range of  $3\text{-}5 \text{ cm}^2$ , and the growth time was limited to  $\sim 2$  hrs. The CdS layer thickness using this growth period was  $\sim 70 \pm 3 \text{ nm}$  deduced using Faradays equation discussed in section 2.1.6.2 of chapter 2. The experimental conditions used for the two sets are summarized in Table 3.1.

**Table 3.1:** Experimental conditions for the two set.

Parameters/Conditions	Set 1	Set 2
pH	2.5	1.4
$\text{CdCl}_2 \cdot \text{H}_2\text{O}$	0.3 M	0.3 M
$\text{Na}_2\text{S}_2\text{O}_3$	0.03 M	0.03 M
Temperature ( $^\circ\text{C}$ )	55	46
Deposition Voltages (mV)	700 – 950	1300 – 1600

### 3.3 Electrolyte preparation and deposition of ZnTe thin film

ZnTe thin films were cathodically electrodeposited onto glass/FTO substrate at  $\sim 87^{\circ}\text{C}$  using an aqueous solution of  $\text{pH} = 3.50 \pm 0.02$  containing 0.15M  $\text{ZnSO}_4 \cdot 7\text{H}_2\text{O}$ , 0.5M  $\text{Na}_2\text{SO}_4$  and 3 ml  $\text{TeO}_2$  (i.e. first set at higher  $\text{Zn}^{2+}$  concentration). The quantities of the chemical used are given below;

- 34.50 g of  $\text{ZnSO}_4 \cdot 7\text{H}_2\text{O}$  (0.15M)
- 2.27 g of  $\text{Na}_2\text{SO}_4$  (0.5M)
- 0.5 g of  $\text{TeO}_2$  in 100 ml de-ionized water

A second set of films was grown with lower  $\text{Zn}^{2+}$  concentrations as follows:

- 5.75 g of  $\text{ZnSO}_4 \cdot 7\text{H}_2\text{O}$  (0.02M)
- 2.27 g of  $\text{Na}_2\text{SO}_4$  (0.5M)
- 0.5 g of  $\text{TeO}_2$  in 100 ml de-ionized water

$\text{ZnSO}_4 \cdot 7\text{H}_2\text{O}$  and  $\text{Na}_2\text{SO}_4$  were dissolved in 800 ml of de-ionized water to make the electrolyte. Similarly, 3 ml of  $\text{TeO}_2$  was added into the electrolyte. ZnTe thin film deposition was performed at this condition.

Two set of ZnTe layers were deposited at lower and higher concentration of  $\text{Zn}^{2+}$  (i.e. 0.02M and 0.15M) respectively, while other condition remains the same. The thickness of ZnTe layers after 60 minutes of growth was  $\sim 70 \pm 3$  nm (measured using the Dektak technique). The theoretical estimate using Faraday's relation given using equation 2.2 on section 2.1.6.2 in chapter 2, predicted a value of  $\sim 65 \pm 3$  nm.

### 3.4 Electrolyte preparation and deposition of CdTe thin film

CdTe thin films were cathodically electrodeposited onto glass/FTO/CdS substrates at  $\sim 85^{\circ}\text{C}$  using an aqueous solution ( $\text{pH} = 2.00 \pm 0.02$ ) containing 1.0M  $\text{CdSO}_4$  which has 99.8% purity. Initially, the electrolyte containing only the Cd source was electro-purified for  $\sim 100$  hrs to remove any source of impurity. 4 ml of  $\text{TeO}_2$  solution and 1000 ppm of  $\text{CdCl}_2 \cdot \text{H}_2\text{O}$  were then added into the bath. The following are the quantities of the chemicals used:

- 208.46 g of  $\text{CdSO}_4$  (1.0M)
- 0.5 g of  $\text{TeO}_2$  in 100 ml de-ionized water

- 0.208 g of CdCl<sub>2</sub>.H<sub>2</sub>O

800 ml of de-ionized water was used to dissolve CdCl<sub>2</sub>.H<sub>2</sub>O and CdSO<sub>4</sub> which make the electrolyte. Furthermore, 4 ml of TeO<sub>2</sub> was added into the electrolyte. Deposition of CdTe thin film was performed at this condition. CdTe films of  $\sim 1.2 \pm 0.01$   $\mu\text{m}$  thick were deposited in about 5 hrs using Faradays equation discussed in section 2.1.6.2 of chapter 2 while the solution is moderately stirred continuously.

### 3.5 Chemicals used to clean the substrates

- (a) Methanol: It is a highly polar organic solvent which is capable of dissolving most organic compounds such as finger print, dirt and so on but is not volatile.
- (b) Acetone: This is also a polar organic solvent and can dissolve many solvent but is volatile.
- (c) Dilute Nitric acid: It can dissolve any inorganic substance which may not be soluble in organic solvents (e.g. methanol and acetone).
- (d) Acetic acid: It is a polar solvent and weak acid, used at the end of the cleaning process to improve adhesion.

### 3.6 Material characterisation

The techniques used to characterise the deposited films include photoelectrochemical (PEC) studies, optical absorption, X-ray diffraction (XRD), X-ray fluorescence (XRF), scanning electron microscopy (SEM), atomic force microscopy (AFM), Raman spectroscopy and X-ray photoelectron spectroscopy (XPS). Details of these techniques have been discussed in section 2.2 of chapter 2. In this section, only the equipment model is stated.

- (a) X-ray diffraction (XRD): All XRD analysis data were obtained using a Philips PW 3710 x-ray diffractometer using CuK <sub>$\alpha$</sub>  radiation ( $\lambda = 1.5416$  Å) in the range of  $2\theta = (10 - 70)^\circ$  for structural analysis of the deposited film. The x-ray generator tension and current were 40 kV and 40 mA respectively.

- (b) Photoelectrochemical (PEC) studies: 0.1M of  $\text{Na}_2\text{S}_2\text{O}_3$  is used as the electrolyte solution in the PEC measurements reported in this thesis. PEC equipment used includes DC power source and DC voltmeter.
- (c) Scanning electron microscopy (SEM): A Philips XL 30 ESEM-Field Emission Gun with accelerating voltage of 20 kV was used to study the surface morphology of the thin film layers using secondary electron to form the image.
- (d) Raman spectroscopy: Raman spectra of the samples were recorded using a Raman spectrometer (RENISHAW InVia Raman Microscope) with  $\text{Ar}^+$  laser having wavelength 514 nm and 15 mW as the power source.
- (e) Optical absorption: A Cary 50 Scan UV-Visible spectrometer (Varian) was used for the bandgap measurements.
- (f) X-ray fluorescence (XRF): The XRF measurements were carried out using a Philips Magix PRO PW 2440 sequential x-ray fluorescent spectrometer.
- (g) Atomic force microscopy (AFM): AFM measurement was carried out using AFM JOEL-5200 for 2D and 3D images.
- (h) X-ray photoelectron spectroscopy (XPS): XPS studies have been performed using an Escalab 250 spectrometer with a monochromatized Al anode x-ray source ( $h\nu = 1486.6$  eV). The binding energies obtained from the XPS analysis were standardized for specimen charging using C 1s as the reference at 284.5 eV.

### 3.7 Solar cell completion

The complete solar cell structure (glass/TCO/CdS/CdTe/Au contact) is shown in Figure 1.31 in section 1.5.1 of chapter 1. The role of each layer has already been discussed in that section. Similarly, the roles of TCOs have been discussed in details in section 1.7 of the same chapter. The back contact (metal contact) is the remaining part to be explained in details in this section. The following processes were carried out before making the back contact.

### 3.7.1 CdCl<sub>2</sub>/heat treatment

CdCl<sub>2</sub>/heat treatment is necessary on deposited layers before their use in active PV solar cells. This treatment provides interfacial intermixing and device activation. The grains of as deposited samples are disconnected and have a high defect density which limits the efficiency of the solar cells. Heat treatment removes and eliminates these defects and increases the grains to become very large. Samples are heated rapidly and cooled down slowly allowing optimum grain growth during recrystallisation, and therefore improve the overall efficiency of the solar cells. Many researchers in the field [1-4] have reported that, during this treatment chlorine helps the n-type doping, reduce the series resistance and improve the FF. Another benefit mentioned is the cementing effect of chlorine to form larger grains.

Some of the methods used for this treatment includes: vapour [5], evaporated [6] and solution [7] CdCl<sub>2</sub> treatments. Kampmann et al. [8] reported that solution CdCl<sub>2</sub> treatment is the most common and simple process which involves soaking the deposited films in methanol containing dissolved CdCl<sub>2</sub> powder, drying and then heat treatment. Heat treatment was carried out using CARBOLITE furnace model: ELF 11/6B. The temperature used for CdS, ZnTe and CdTe films were 400°C for 20 minutes, 300°C for 10 minutes and 450°C for 15 minutes respectively.

### 3.7.2 Surface etching

The samples were washed with de-ionized water after heat treatment and then etched in oxidizing and reducing etchants. Table 3.2 shows the etchant composition and etching times.

**Table 3.2:** Etchant composition.

Etchants	Etchant composition	Etching time
Oxidizing etch	0.03 g K <sub>2</sub> Cr <sub>2</sub> O <sub>7</sub> + 2 drops of concentrated H <sub>2</sub> SO <sub>4</sub> dissolve in 20 ml de-ionized water	5 seconds
Reducing etch	2 pellets each of NaOH + Na <sub>2</sub> S <sub>2</sub> O <sub>3</sub> dissolve in 20 ml de-ionized water + heat at ~50°C	2 minutes

It was reported in the literature [9] that acidic etching preferentially removes the cadmium and makes the surface to be Te-rich, while Cd-rich surface is obtained after basic etching. To produce high quality Schottky barriers at metal/n-CdTe interfaces the CdTe surface must be rich in cadmium.

### 3.7.3 Formation of back metal contact

Samples were transferred quickly after etching to an EDWARD Auto 306 coater NXN 532000 metalliser which has both rotary and diffusion pumps. A shadow mask with holes of 2.0 mm in diameter was used to load the sample and mounted in the vacuum chamber. Gold (Au) loaded tungsten filament was used to evaporate gold contacts at a pressure of  $\sim 10^{-6}$  mbar. A thickness of  $\sim 20$  nm was measured by quartz thickness monitor. These completed the glass/TCO/CdS/CdTe/Au structures. Figure 3.1 shows the photograph of an EDWARD metalliser used in this device fabrication.



**Figure 3.1:** A photograph of an EDWARD metalliser.

### 3.8 Current-Voltage (I-V) measurement

I-V measurement is used to obtain information on the photovoltaic and electrical properties of the fully fabricated devices. A Keithly 280 programmable voltage source and a Keithly 619 Electrometer/Multimeter were used for I-V measurements. It is contained in a box and has a solar simulator in which solar cell I-V characteristics were obtained. A 250 W tungsten-halogen source was illuminated and adjusted to give  $100 \text{ mWcm}^{-2}$ . A standard Si-solar cell was used as a reference for calibration. Micropositioned probes were used to make contact to the sample at the front (TCO) and back (metal). A general purpose interface board (GPIB) link attached to the system which was under computer control collected and stored the relevant I-V characteristics automatically. From the dark I-V measurement the following parameters can be deduced: barrier height ( $\phi_b$ ), diode ideality factor ( $n$ ) and rectification factor ( $RF$ ). Figure 3.2 shows the photograph of the I-V system set-up.

Front contact  
to TCO

Back metal  
contact

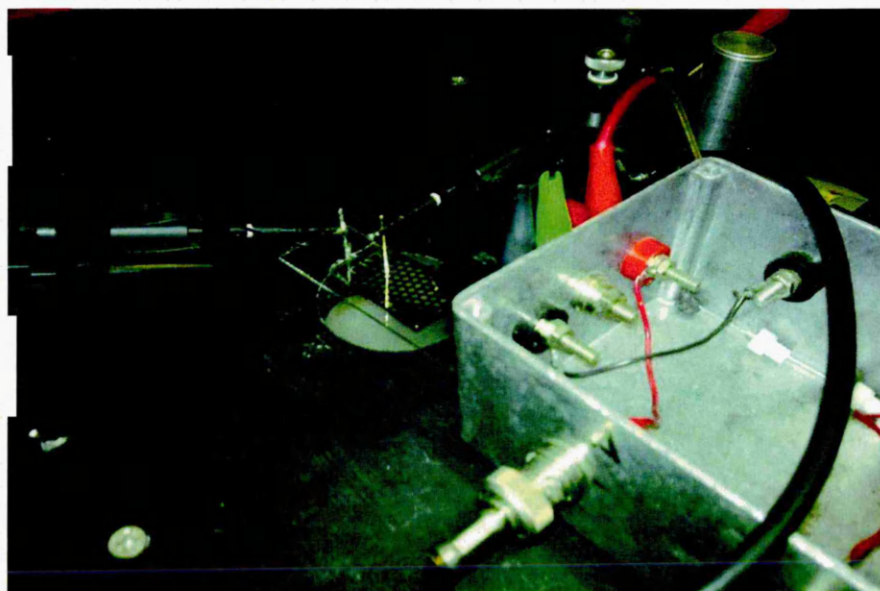


**Figure 3.2:** A photograph of the I-V system.

## References

1. I. M. Dharmadasa, A. P. Samantilleke, N. B. Chaure and J. Young, *Semiconductor Science Technology* 17, 1238 (2002).
2. P. D. Paulson and V. Dutta, *Thin Solid Films* 370, 299 (2000).
3. M. Rami, E. Benamar, M. Fahoume, F. Chraibi and A. Ennaoui, *Material Journal Condense Matter* 3(1), 66 (2000).
4. I. M. Dharmadasa, S. M. McGregor, I. Wadsworth and C. M. Care, *Optical Materials* 6, 75 (1996).
5. A. Rios-Flores, J. L. Peña, V. Castro- Peña, O. Ares, R. Castro-Rodríguez and A. Bosio, *Solar Energy* 84, 1020 (2010).
6. S. Mazzamuto, L. Vaillant, A. Bosio, N. Romeo, N. Armani and G. Salviati, *Thin Solid Films* 516, 7079 (2008).
7. T. Potlog, L. Ghimpu, P. Gashin, A. Pudov, T. Nagle and J. Sites, *Sol. Energy Mater. Sol. Cells* 80, 327 (2003).
8. A. Kampmann and D. Lincot, *J. Electroanal. Chem.*, 418, 73 (1996).
9. I. M. Dharmadasa, J. M. Thornton and R. H. Williams, *Appl. Phys. Lett.* 54(2), 137 (1989).

## Chapter 4: Electrodeposition of CdS (Window material-1)

### 4.1 Motivation and objectives

The aim of this chapter is to reduce the amount/quantity of toxic Cd-containing waste produced during growth of CdS using chemical bath deposition (CBD). In the CBD process, the chemical reaction takes place within a few minutes and CdS particles deposit on all surfaces and in the solution. Therefore the Cd-containing electrolytes should be discarded and need a replacement. Growth of CdS thin films using electrodeposition gives an alternative and the electrolytic bath can be used for a long periods without discarding it unlike in CBD technique.

### 4.2 Introduction

Cadmium sulphide (CdS) is among the binary compounds of group II-VI family and has a direct bandgap of 2.42 eV at room temperature. CdS, being an n-type window material, can be combined with CuInGaSe<sub>2</sub> (CIGS) or CdTe to form a good heterojunction. CIGS-based solar cells are currently leading with the record efficiency of 20.3% [1], whereas CdTe-based solar cells have achieved 17.3% [2] for small scale laboratory devices to date.

Electrodeposition is a non-vacuum technique and it offers excellent control over the properties of the thin films through the influence of parameters such as deposition potential, bath temperature, time, pH and concentration of ions [3]. Details of the deposition of CdS thin film have been discussed in section 3.2 of chapter 3.

### 4.3 Linear sweep voltammogram

A typical cyclic voltammogram related to the electrodeposition of CdS thin films is shown in Figure 4.1. The formation of the CdS compound takes place beyond 1200 mV cathodic voltage as can be seen from the Figure. In the reverse direction, a small peak was observed which attributed to the removal of cadmium around 1150 mV.

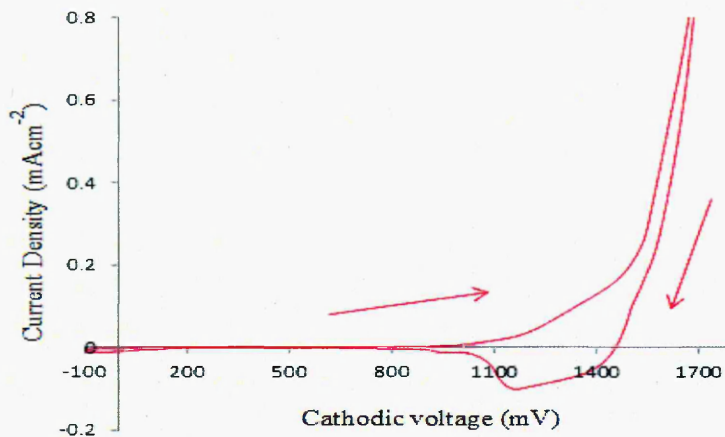


**Figure 4.1:** A typical voltammogram for an electrolytic bath used for deposition of ED-CdS.

#### 4.4 Visual Appearance

The visual appearance of 14 ED-CdS layers (set 1) deposited as a function of growth voltage is shown in Figure 4.2. From the figure it is observed that at higher cathodic potential i.e. 950 mV the sample was very dark in colour with poor adherence to the substrate which indicate a Cd- rich film and at lower cathodic potential i.e. 700 mV the sample was slightly yellow in colour which indicate S-richness. The samples grown at 950 mV and 700 mV cannot give the actual requirement of CdS analysis because of the Cd and S richness. In the intermediate voltages, the layers appear orange-yellow, similar to that of bulk CdS material.

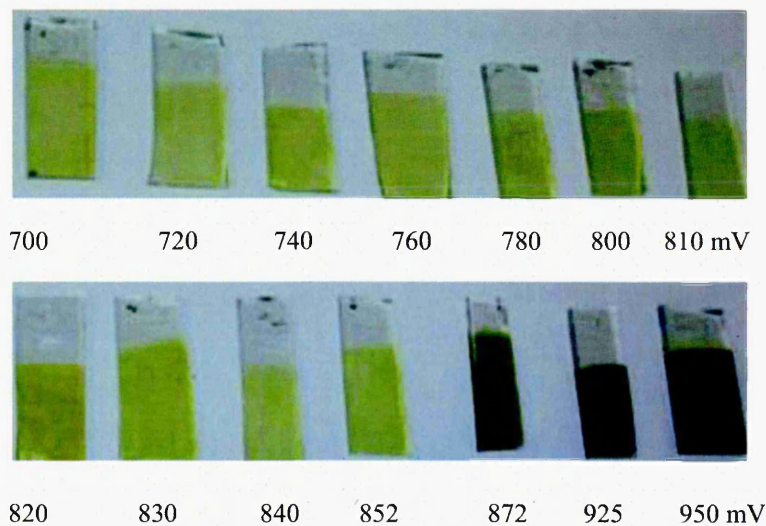


**Figure 4.2:** The appearance of as deposited ED-CdS layers (set 1) grown on glass/FTO substrate at different growth voltages.

Figure 4.3 shows another set of 21 ED-CdS layers (set 2) grown at different cathodic voltages. As the pH decreased, the cathodic voltage shifted upwards. It is observed from the Figure; the highest and lowest cathodic voltages were 1600 mV and 1300 mV as against 950 mV and 700 mV for set 1 respectively. The deposited layers require heat treatment at 400°C for 20 minutes in air before their use in active photovoltaic solar cells. After heat treatment, the darker samples in both sets become orange-yellow and attain a higher degree of transparency indicating two possible occurrences. One possibility is the chemical reaction between elemental Cd and S present in the layer forming more CdS. Another explanation is that the elemental Cd in the film indicated by the initial dark colour, and oxidises to form CdO during heat treatment. The bandgap values reported for CdO showing semiconducting properties from the scientific literature are 2.28 eV [4], 2.20 eV [5] and 2.45 eV [6]. The average bandgap of CdO is very similar to that of CdS, and therefore, these electrodeposited and heat treated layers must contain a mixture of CdS and CdO compounds.

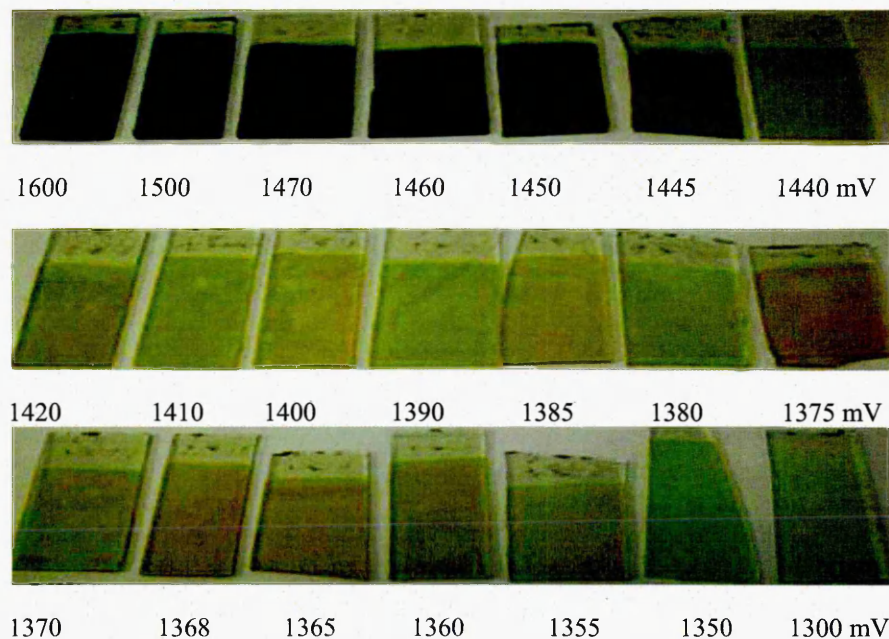


**Figure 4.3:** The appearance of as deposited ED-CdS layers (set 2) grown on glass/FTO substrate at different growth voltages.

## 4.5 Characterisation of Electrodeposited CdS

### 4.5.1 X-ray diffraction

To identify different phases present and study the bulk structure of the layers, sample which showed orange-yellow colour grown at 1500 mV was selected for XRD measurement. The XRD used  $\text{CuK}_\alpha$  radiation ( $\lambda = 1.5418 \text{ \AA}$ ) in the range of  $2\theta = (20 - 50)^\circ$ . Figure 4.4 shows the XRD diffractogram obtained for glass/FTO substrate, as deposited and heat treated CdS. From the Figure, the results show that the films have highly oriented crystallites with the hexagonal structure (Wurtzite type) with preferential orientation along the c-axis  $\{(101) \text{ direction}\}$  with diffraction peaks producing  $d = 3.160 \text{ \AA}$  perpendicular to the substrate plane with low intensity of (102) and (103) peaks. Other peaks identified from the diffractogram are (100) and (110), as reported by most of the researchers in the field [7-10]. These peaks were assigned according to the Joint Committee on Powder Diffraction Standards, JCPDS (00-001-0780) data on hexagonal CdS.

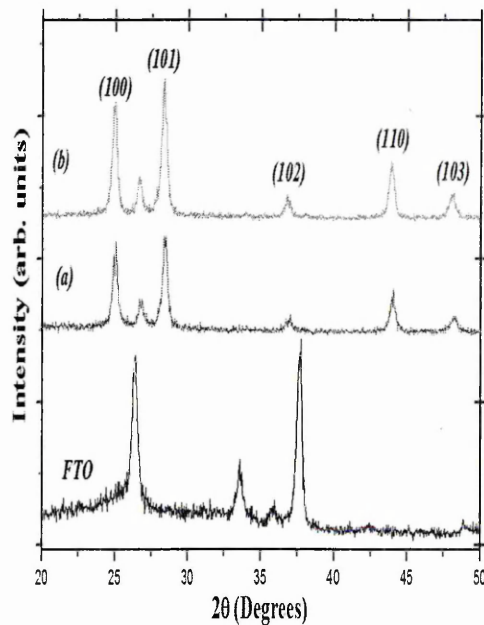


**Figure 4.4:** X-ray diffraction patterns of ED-CdS thin films grown at 1500 mV (a) as deposited and (b) heat treated.

After heat treatment in air at  $400^\circ\text{C}$  for 20 minutes, the intensity of all the peaks increases and sharpens which indicates the formation of large grains and the

improvement of bulk crystalline properties. The heat treatment enhances the recrystallisation of CdS films reducing any stress within the films. The values of  $d$ ,  $D$  and FWHM are presented in Table 4.1 using equation 2.17 and 2.18 from section 2.2.1 in chapter 2.

**Table 4.1:** Structural parameters of ED-CdS thin films grown at 1500 mV.

	2 $\theta$ (Degrees)		Lattice spacing $d$ (Å)		Crystallite size $D$ (nm)	FWHM	hkl
	RP	OB	RP	OB			
AD	24.993	24.962	3.560	3.592	80.0	0.015	100
HT	24.993	24.962	3.560	3.572	95.0	0.012	100
AD	28.401	28.367	3.140	3.160	51.5	0.030	101
HT	28.401	28.367	3.140	3.150	85.0	0.015	101
AD	43.694	43.801	2.070	2.085	26.9	0.060	110
HT	43.694	43.801	2.070	2.078	36.3	0.045	110

**N/B:** RP – reported values, OB – observed from the XRD, AD – as deposited and HT – heat treated.

From the Table, it is observed that crystallite size for heat treated sample increases and the FWHM decreases; this is due to the coalescence of small crystals and the formation of large grains. A further decrease in the lattice spacing is observed for the heat treated sample. The observed lower value of  $d$  for heat treated sample is an evidence of stress release after the heat treatment. Similarly, the same trend is observed for FWHM.

#### 4.5.2 Photoelectrochemical (PEC) cell

The Photoelectrochemical cell values for as deposited and heat treated ED-CdS samples (set 1) grown at 14 different growth voltages from one bath are shown in Table 4.2.

**Table 4.2:** PEC cell results for as deposited and heat treated ED-CdS (set 1).

S/N	Growth Voltages, $V_g$ (mV)	PEC Signal for as deposited ED-CdS (mV)	PEC Signal for heat treated ED-CdS (mV)
1	700	-60	-126
2	720	-68	-131

3	740	-63	-102
4	760	-86	-128
5	780	-72	-81
6	800	-60	-153
7	810	-71	-110
8	820	-104	-120
9	830	-83	-131
10	840	-104	-115
11	852	-67	-143
12	875	-30	-25
13	925	-25	-92
14	950	-5	-77

From the above Table, the polarities of the PEC signal were all negative which indicates n-type electrical conduction. The electrical conductivity type of the deposited layers were all n-type and the largest PEC signal arises because of the formation of PV active depletion region at the CdS/electrolyte interface as a result of moderate doping in the range  $\sim 10^{14}$ - $10^{17}$   $\text{cm}^{-3}$ . The signal close to zero indicates a very thin or non-existent depletion region either due to heavy doping greater than  $10^{18}$   $\text{cm}^{-3}$  or due to an insulating material. After heat treatment, the material layers show an enhanced PEC signal, indicating improved optical properties. Figure 4.6 (a) and (b) shows the PEC signals for set1 of the CdS film, both as deposited and after heat treatment CdS layers at  $400^\circ\text{C}$  for 20 minutes in air.

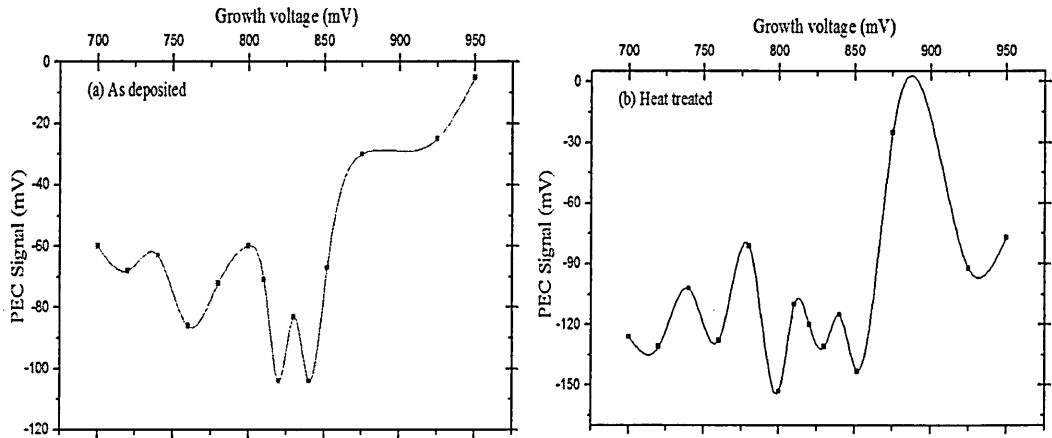


**Figure 4.6:** PEC signal as a function of growth voltage for (a) as deposited and (b) heat treated ED-CdS layers (set 1) grown on glass/FTO substrates.

### 4.5.3 Optical absorption

The graphs of optical absorption for as deposited and heat treated ED-CdS of some selected samples (set 1 and 2) are shown in Figures 4.7 and 4.8. The values of  $E_g$  were determined by plotting the square of absorption ( $A^2$ ) against photon energy ( $h\nu$ ). From Figure 4.7, the best growth voltages for as deposited and heat treated sample (set 1) are 852 mV and 925 mV respectively. Similarly, for the second set Figures 4.8 the growth voltages were shifted up due to the low pH and the best growth voltage is 1500 mV after the heat treatment.

From the graphs shown in Figure 4.7, it is observed that the sample grown at the cathodic voltage 925 mV as deposited produced close to 0.0 eV bandgap. This is expected because this is Cd-rich surface and possesses the bandgap of the metal which is zero. After heat treatment at 400°C in air for 20 minutes, the bandgap decreased to 2.42 eV which agrees with the theoretical value of CdS thin films [7-10]. However, the sample grown at 852 mV has a bandgap 2.42 eV as grown that decreases to 2.25 eV after heat treatment. The same trends were observed for the second set of the samples.

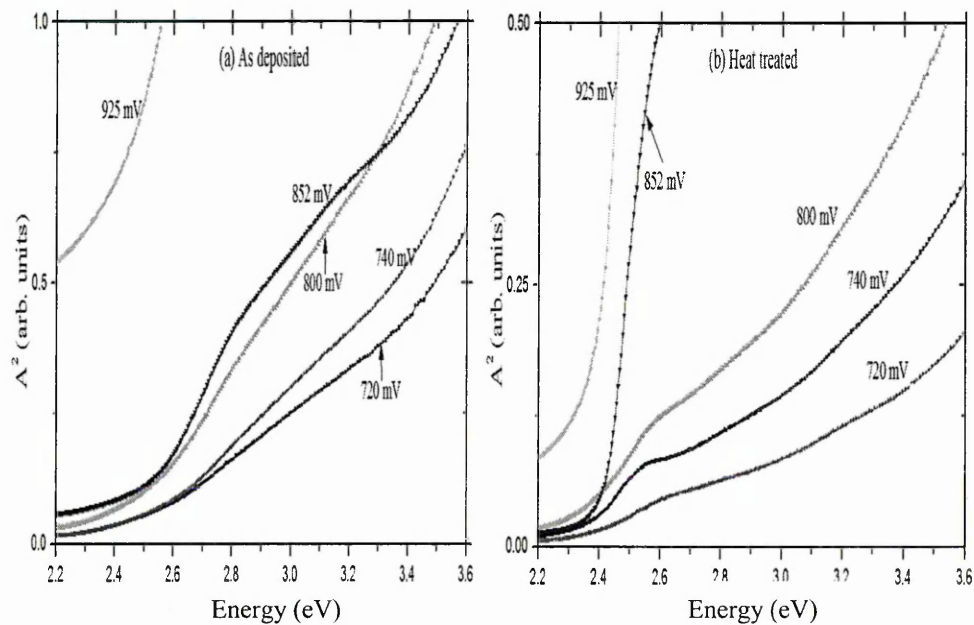


**Figure 4.7:** Optical absorption curves [set 1] for (a) as deposited and (b) heat treated ED-CdS grown at different voltages on glass/FTO substrates.

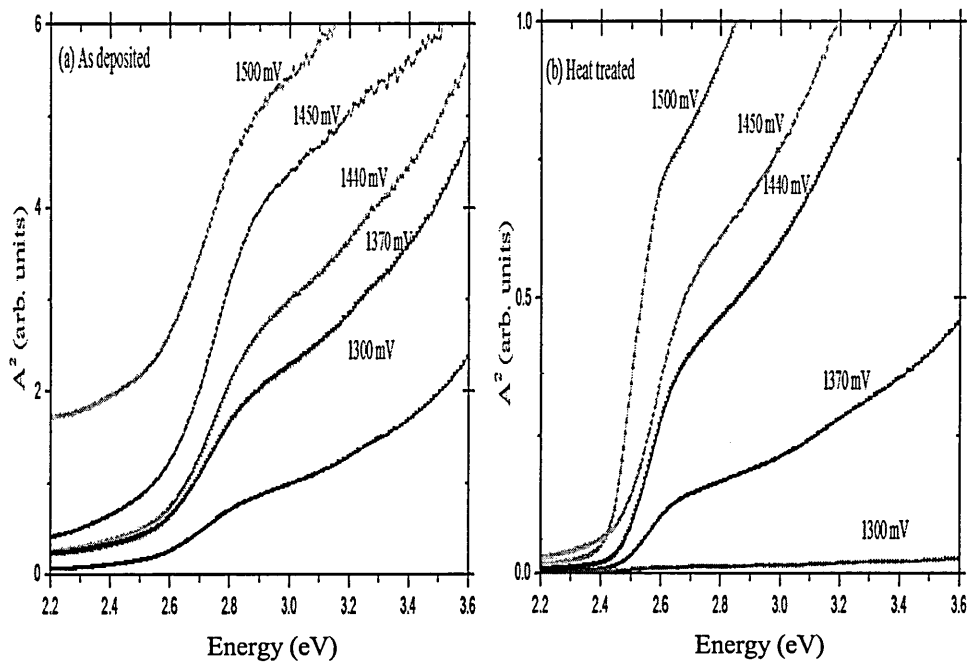


**Figure 4.8:** Optical absorption curves [set 2] for (a) as deposited and (b) heat treated ED-CdS grown at different voltages on glass/FTO substrates.

Therefore, heat treatment is a vital step, similar to the growth process. Samples are heated rapidly and cooled down slowly allowing optimum grain growth during recrystallisation, and therefore improve the overall efficiency of the solar cells. Table 4.3 below shows the growth voltages and bandgaps for as deposited and heat treated samples (set 1 and 2). Figures 4.9 and 4.10 are the graphs for the bandgaps against the growth voltages for the two sets of ED-CdS samples grown.

**Table 4.3:** Growth voltages and bandgaps for as deposited and heat treated ED-CdS.

Set 1			Set 2		
Growth Voltage (mV)	$E_g$ (eV) for AD-CdS	$E_g$ (eV) for HT-CdS	Growth Voltage (mV)	$E_g$ (eV) for AD-CdS	$E_g$ (eV) for HT-CdS
720	2.47	2.23	1300	2.40	1.80
740	2.44	2.30	1370	2.52	2.49
800	2.45	2.32	1440	2.52	2.48
852	2.42	2.23	1450	2.53	2.45
925	0	2.42	1500	2.34	2.42

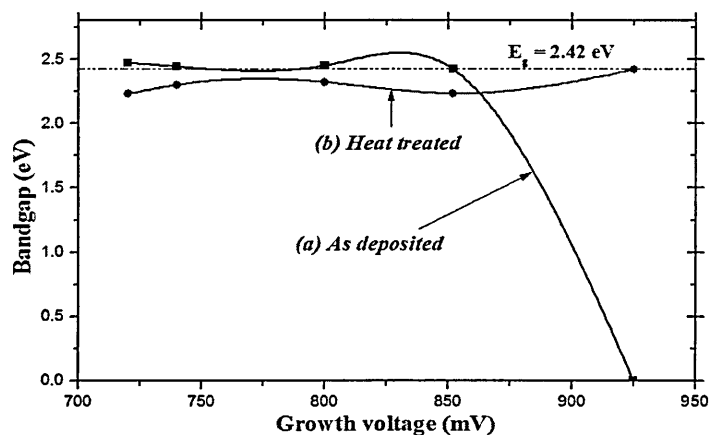


**Figure 4.9:** Bandgap as a function of growth voltages for (a) as deposited and (b) heat treated CdS layers (set 1) grown on glass/FTO substrate.

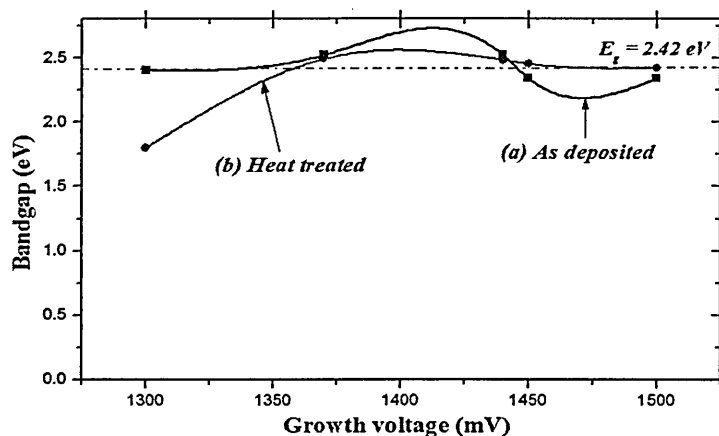


**Figure 4.10:** Bandgap as a function of growth voltages for (a) as deposited and (b) heat treated CdS layers (set 2) grown on glass/FTO substrate.

From the Table above, it is observed that the bandgaps of most as-deposited samples decreased after heat treatment for both sets. Similarly, the bandgaps for darker samples of both sets (925 mV and 1500 mV) were shifted up to give the required value of 2.42 eV. This confirmed that heat treatment is a crucial issue in the process of thin films devices.

#### 4.5.4 Scanning Electron Microscopy

SEM studies were carried out to investigate the surface morphology, grain size and uniformity of ED-CdS layers. Secondary electron micrographs of as deposited and heat treated samples grown at 1500 mV are shown in Figure 4.11. The material clusters are

in the nanoscale range with an average size of ~60 nm. These grains seem to be isolated from each other with gaps in between, and there is no apparent change in morphology or material cluster size observed after heat treatment. From the Figure, the SEM images show gaps or pin holes between the grains which indicates the growth of CdS as islands. Therefore, it is possible during CdTe growth; some CdTe layers grow on the FTO while others are on the CdS film. This creates some gaps or pin holes and when contacts are made with Au for complete devices it will provide shorting paths making devices low in efficiency.

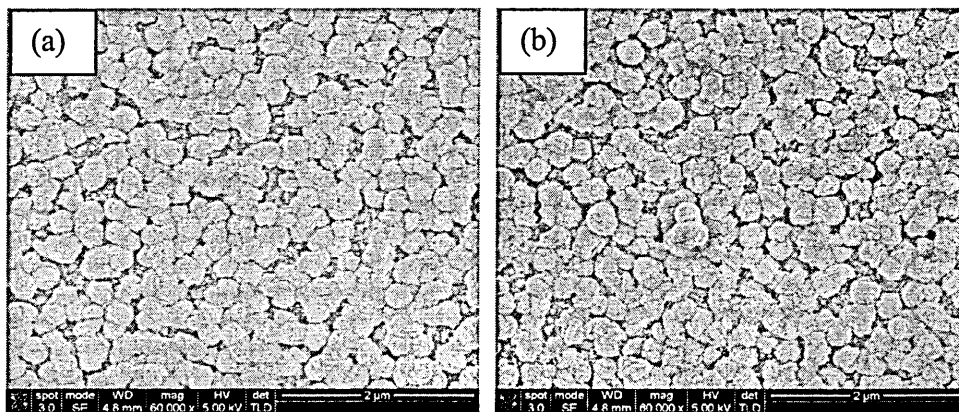


**Figure 4.11:** SEM images of ED-CdS grown at 1500 mV on glass/FTO substrate (a) as deposited and (b) heat treated.

#### 4.5.5 Energy Dispersive X-ray

The qualitative analysis of the ED-CdS layers was carried out by using energy dispersive x-ray (EDX) spectroscopy on both as deposited and heat treated films. Figure 4.12 shows the EDX spectrum of ED-CdS layers grown at 1500 mV. From the Figure both Cd and S are present and the remaining elements identified are due to the background of the glass/FTO substrate. The atomic composition ratio estimated from the spectra of Cd:S is 56:44.

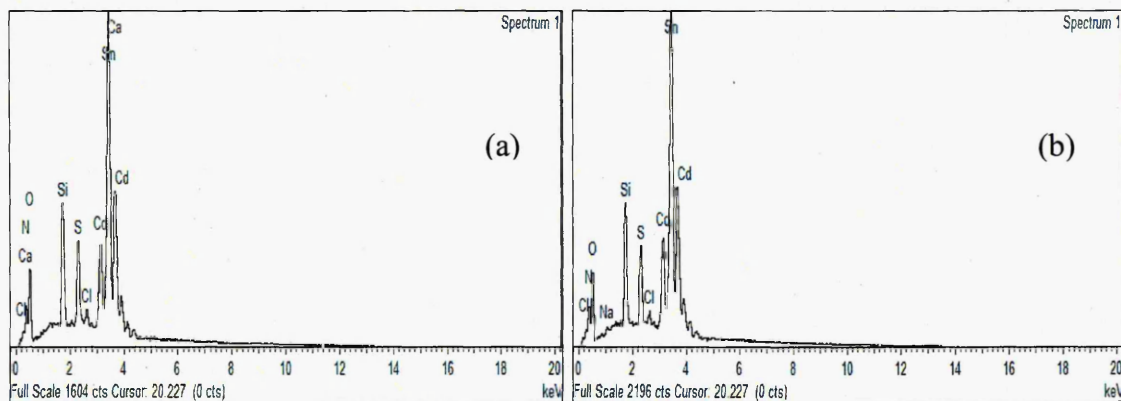


**Figure 4.12:** EDX spectrum of ED-CdS grown at 1500 mV on glass/FTO substrate (a) as deposited and (b) heat treated.

#### 4.5.6 Atomic Force Microscopy

Figure 4.13 show 2-D AFM pictures of heat treated ED-CdS grown at 1500 mV on glass/FTO substrates. The AFM images show large clusters of CdS with cauliflower-like features which indicate the uniform distribution of grain size and columnar growth.

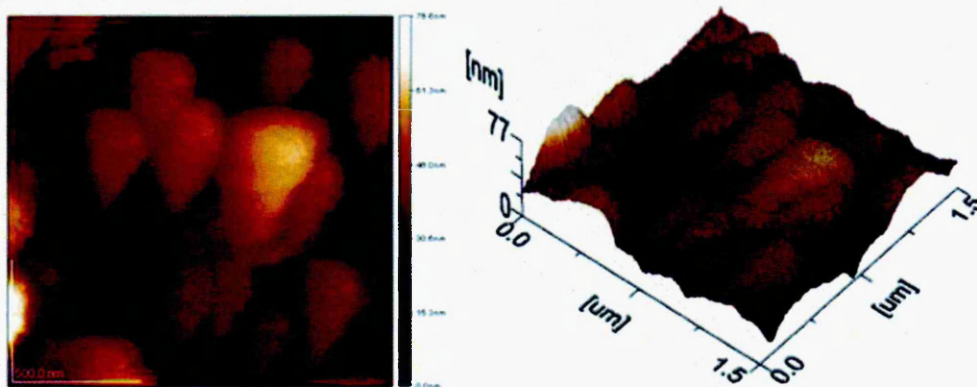


**Figure 4.13:** 2D-AFM image of ED-CdS grown at 1500 mV on glass/FTO substrate (courtesy: Inst. of Org. Catalysis & Electrochem., Kazakhstan).

The 3D-AFM picture of ED-CdS is shown in Figure 3.14. From the Figure, CdS fabricated have highly ordered and densely packed nano-rod arrays oriented perpendicular to the glass/FTO substrates and grow upwards after nucleation on the FTO surface. There are many empty spaces between nano-rods; these observations are

consistent with the SEM results shown in Figure 4.11. The 3D-AFM reveals the existence of tightly packed nano-rods with length equal to  $\sim 70$  nm (thickness of the CdS layer) and diameter of  $\sim 40$  nm. The presence of nano-rods provides advantages because of band bending due to enhanced surfaces and hence creating an additional internal electric field perpendicular to their axis. It also minimises recombination of electrons and holes in which the electrons flow along the axis of the nano-rod and holes could flow in the opposite direction along the vicinity of the surface layer of the nano-rod.

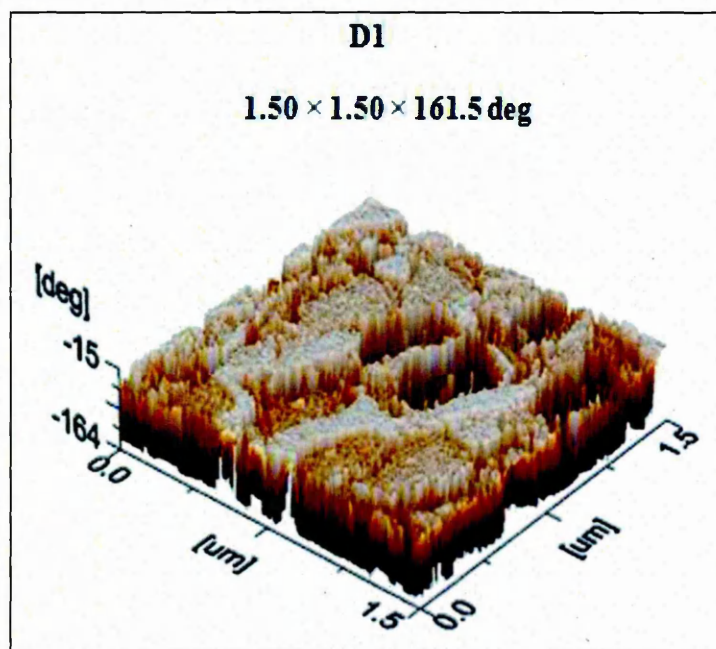


**Figure 4.14:** 3D-AFM image of ED-CdS grown at 1500 mV on glass/FTO substrate (courtesy: Inst. of Org. Catalysis & Electrochem., Kazakhstan).

The SEM cross-section of ED-CdS is shown in Figure 4.15, with its thickness of  $\sim 60$  nm. According to [11], CdS layer of  $\sim 90$  nm can absorb about 63% of the incident radiation with photon energy greater than the bandgap energy.

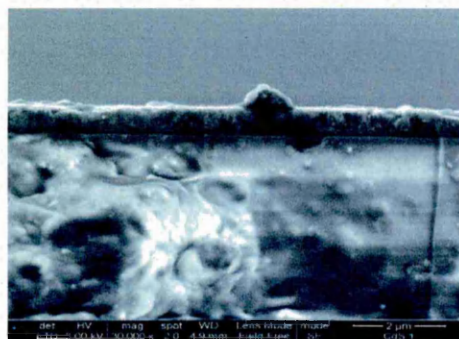


**Figure 4.15:** SEM cross-section of ED-CdS grown at 1500 mV on glass/FTO substrate.

#### 4.5.7 X-ray Fluorescence (XRF)

The stoichiometry of the ED-CdS layers was investigated using XRF in order to correlate the material and atomic percentages of individual elements. Figure 4.16 shows the XRF analysis for both as deposited and heat treated CdS layers. From the Figure, at low cathodic voltages, S deposits preferentially and Cd deposition increases as the cathodic voltage is increased. At voltages close to 1590 mV, the material becomes stoichiometric, reaching 50 atom% for both materials. Table 4.4 shows the atomic percentage of S and Cd for individual growth voltages for as deposited and heat treated ED-CdS (set 2) samples.

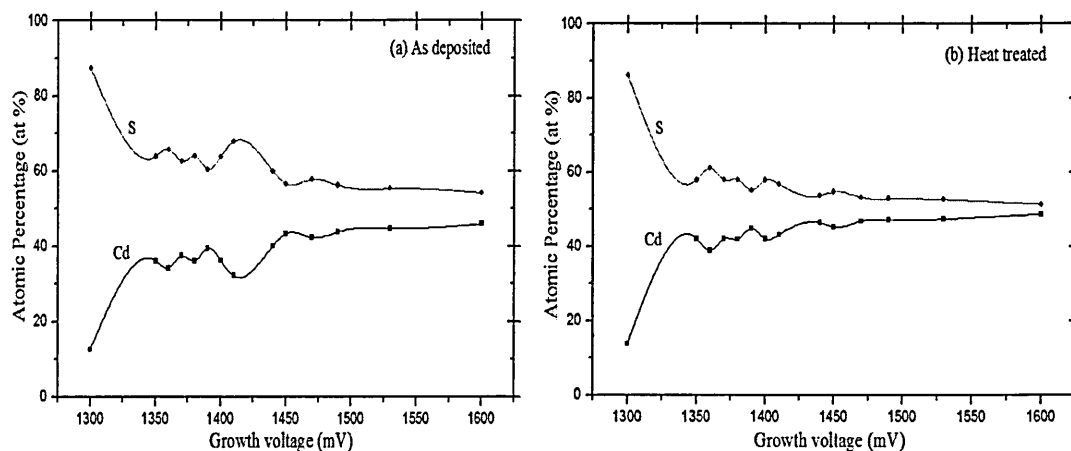


**Figure 4.16:** XRF analysis showing the atomic percentages of Cd and S for (a) as deposited and (b) heat treated ED-CdS layers grown on glass/FTO substrates.

**Table 4.4:** Atomic percentages of Cd and S for as deposited and heat treated ED-CdS layers as a function of growth voltage.

Growth voltage (mV)	AS deposited		Heat treated	
	Atom% Cd	Atom% S	Atom% Cd	Atom% S
1300	12.65	87.35	13.81	86.19
1350	36.13	63.87	42.12	57.88
1360	34.20	65.80	38.93	61.07
1370	37.46	62.54	42.06	57.94
1380	36.10	63.90	42.02	57.98
1390	39.52	60.48	44.86	55.14
1400	36.26	63.74	42.12	57.88

1410	32.18	67.82	43.17	56.83
1440	40.06	59.94	46.38	53.62
1450	43.37	56.63	45.26	54.74
1470	42.29	57.71	46.78	53.22
1490	43.81	56.19	47.15	52.85
1530	44.72	55.28	47.38	52.62
1600	45.90	54.10	48.67	51.33

#### 4.5.8 Raman spectroscopy

The Raman spectra of ED-CdS were recorded using (RENISHAW InVia Raman Microscope). This technique gives information about the molecular structure of the material. The Raman spectra of bulk CdS and nano-particle CdS are shown in Figure 4.17 for comparison [12]. Figure 4.18 shows the Raman spectra of ED-CdS layers grown at 1500 mV on glass/FTO substrate. Two peaks were observed at  $303\text{ cm}^{-1}$  and  $608\text{ cm}^{-1}$  which correspond to the first and second order longitudinal optical phonons (1LO) and (2LO) respectively. It was reported by most of the researchers that the 1LO is between  $300\text{-}305\text{ cm}^{-1}$  and the 2LO is in the range  $600\text{-}606\text{ cm}^{-1}$  [13-15]. Froment et al. [16] reported that for single crystal CdS bulk, the 1LO peak position and FWHM are typically  $305\text{ cm}^{-1}$  and  $9\text{-}10\text{ cm}^{-1}$  respectively. The FWHM of the 1LO calculated from this spectrum is  $19\text{ cm}^{-1}$ , this increase may be due to the grain size effect (i.e. effect of finite size on vibrational properties in small crystallites [17]).

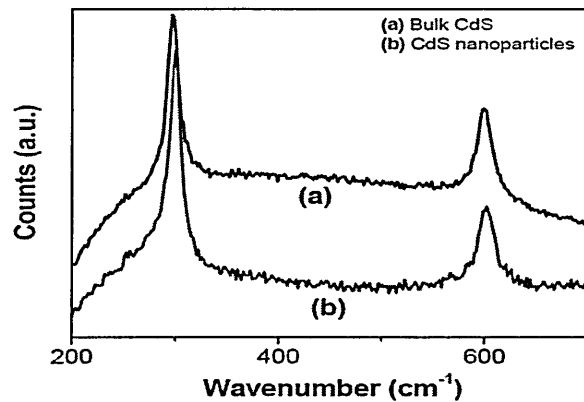


**Figure 4.17:** Raman spectra of CdS Bulk and nanoparticles [12].

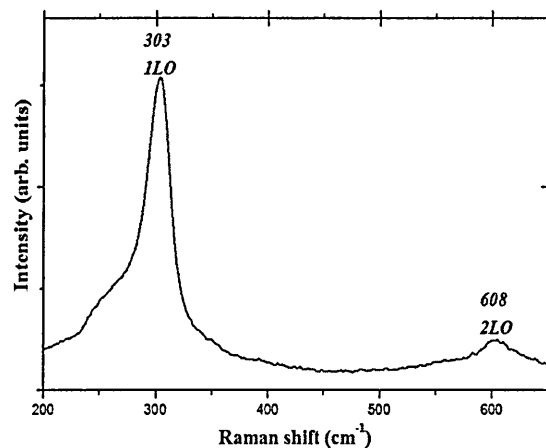


**Figure 4.18:** Raman spectra of ED-CdS grown at 1500 mV on glass/FTO substrate (courtesy: Inst. of Mater. Research, Univ. of Leeds).

#### 4.5.9 X-ray photoelectron spectroscopy (XPS)

This technique gives both quantitative and qualitative analysis of surface chemical states. The XPS spectrum of vacuum cleaved CdS is shown in Figure 4.19 together with spectrum obtained for an ED-CdS layer grown at 1500 mV in Figure 4.20 for comparison. The two XPS spectra reveals that electrodeposited CdTe has a similar spectrum to that of a clean cleaved CdTe except for the additional presence of C and O peaks which may be due to surface contamination.

From Figure 4.20, two distinct Cd 3d peaks (i.e.  $3d_{5/2}$  and  $3d_{3/2}$ ) are observed and presented more clearly in Figure 4.21. The binding energies associated with Cd ( $3d_{5/2}$  and  $3d_{3/2}$ ) appeared at  $\sim 405.6$  and  $\sim 412.3$  eV respectively. Similarly, Figure 4.22 shows the S 2p peak and has a binding energy of  $\sim 162.5$  eV. The atomic ratio for Cd:S given

from the XPS spectra is 52.9:47.1. This experimental result confirmed the XRF measurements discussed in section 4.5.7. All these peaks and binding energies are very close to those found by other researchers and summarised in Table 4.5 [18-21].

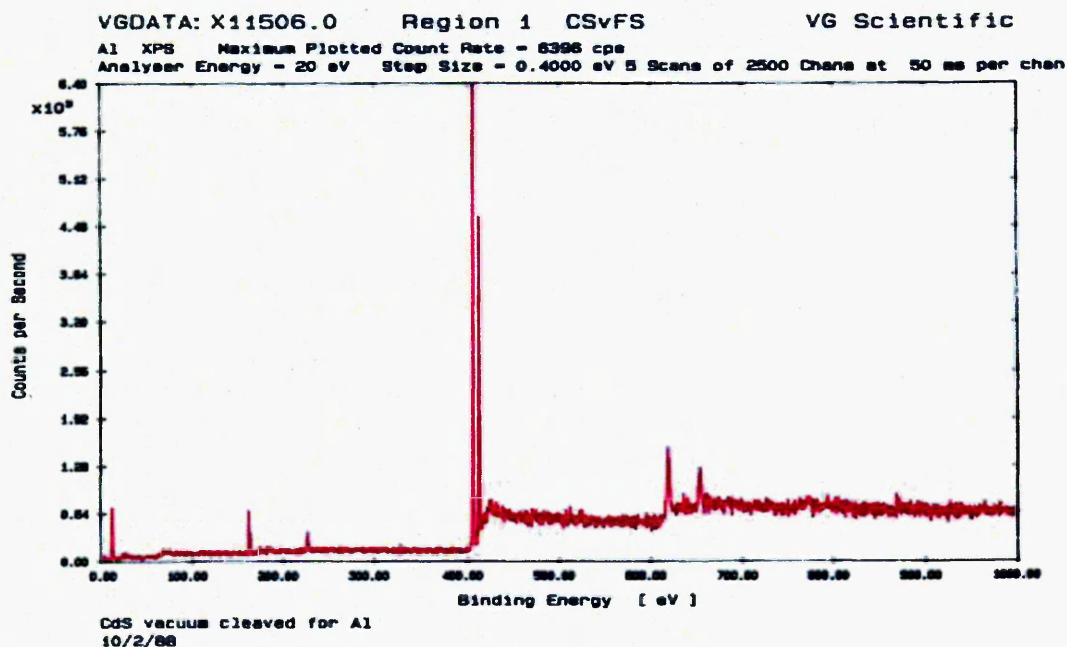


Figure 4.19: XPS spectrum of CdS cleaved in vacuum (courtesy: Prof. I. M. Dharmadasa).

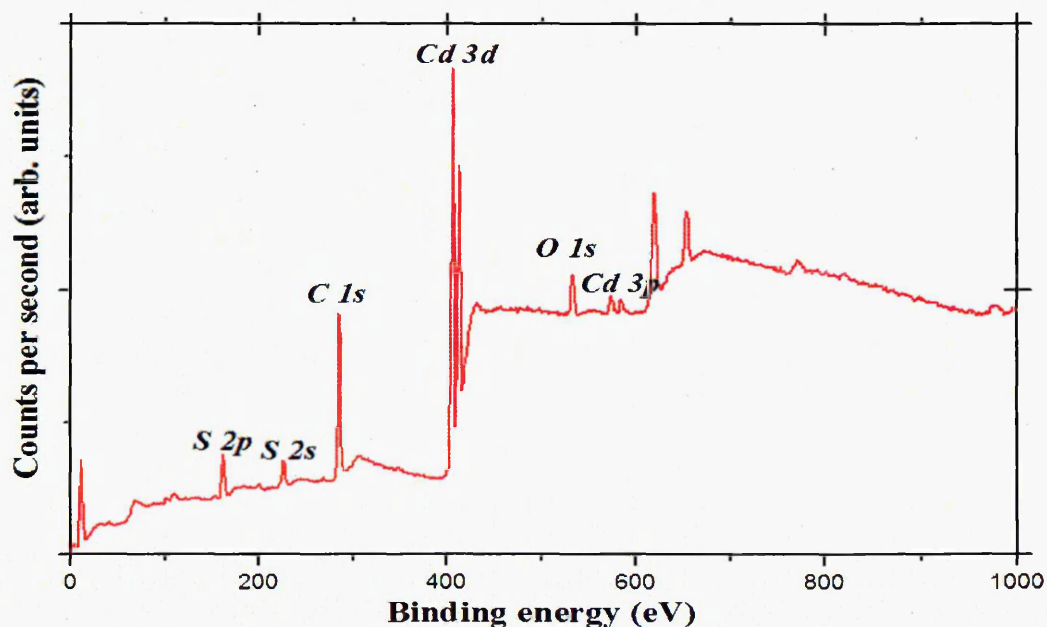
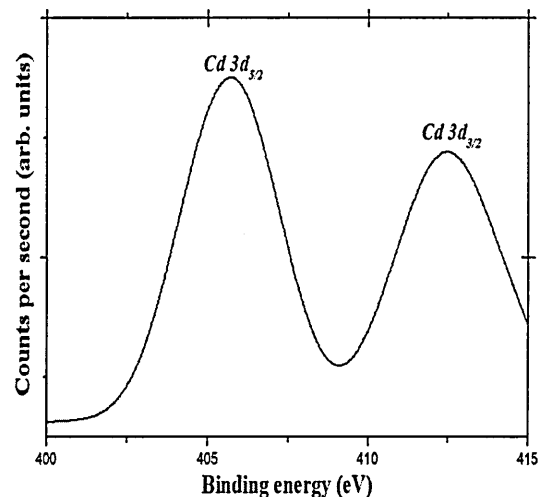
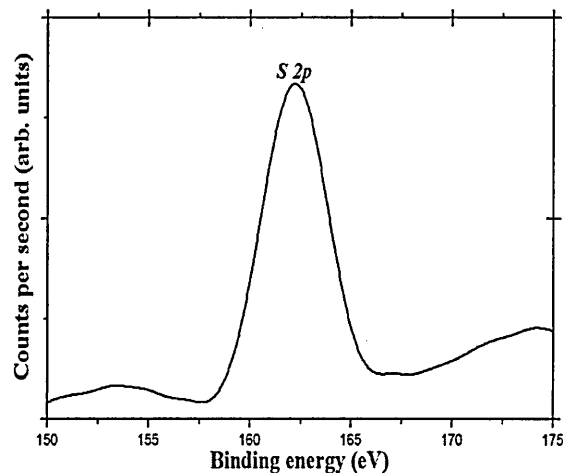


Figure 4.20: Typical XPS survey spectrum of the ED-CdS pattern grown at 1500 mV (courtesy: Inst. of Mater. Research, Univ. of Leeds).



**Figure 4.21:** XPS spectrum of ED-CdS grown at 1500 mV close-up survey for Cd 3d core (courtesy: Inst. of Mater. Research, Univ. of Leeds).



**Figure 4.22:** XPS spectrum of ED-CdS grown at 1500 mV close-up survey for S 2p core (courtesy: Inst. of Mater. Research, Univ. of Leeds).

**Table 4.5:** Summary of CdS XPS results

Method	Binding energy (eV)			Ref.
	Cd 3d <sub>5/2</sub>	Cd 3d <sub>3/2</sub>	S 2p	
CBD	405.5	412	161.70	21
ammonia-free chemical process	405.1 - 405.3	411.8 - 412	161.6 - 161.8	19
ED	405.2	412	162	18
RF magnetron sputtering	405	412	161	20
ED	405.6	412.3	162.5	this work

## 4.6 Summary

CdS have been deposited on glass/FTO substrates using a low-cost aqueous electrodeposition method. The XRD results indicates that both as deposited and heat treated ED-CdS layers are polycrystalline and have a hexagonal crystal structure with preferential orientation along the (101) direction. From the literature [22], it is known that hexagonal structure performs better in terms of light absorption. Therefore this could be an added advantage to increase the device performance.

The electrical conductivity type of the deposited layers were all n-type and the largest PEC signal arises because of the formation of PV active depletion region as a result of moderate doping in the range  $\sim 10^{15}$ - $10^{18}$   $\text{cm}^{-3}$ . Optical absorption measurements gives a bandgap of  $\sim 2.42$  eV for heat treated sample which shows dark-orange colour. XRF analysis shows that at low cathodic voltages, S deposits preferentially and Cd deposition increases as the cathodic voltage is increased.

SEM studies indicate the film form in columnar grain clusters are in nanoscale range with an average diameter of  $\sim 60$  nm. The images show gaps or pin holes between the grains. This shows that, the growth of CdS as islands and CdTe columnar growth on top of this layer. Therefore, it is possible during CdTe growth; some CdTe layers grow on the FTO while others are on the CdS film. This creates some gaps or pin holes and when contacts are made with Au for complete devices it will provide shorting paths making devices low in efficiency. Therefore, methods should be developed to grow uniform cover of CdS on FTO surfaces.

3D-AFM measurements shows that the ED-CdS layers have highly ordered and densely packed nano-rod arrays oriented perpendicular to the glass/FTO substrates. The nano-rod nature of the CdS layers could reduce the recombination and generation and hence minimise scattering at grain boundaries. The 2D-AFM image show large clusters of CdS with cauliflower-like features.

Raman spectroscopy has proven to be a fast and convenient technique to use as a quality control method. Two peaks observed at  $303 \text{ cm}^{-1}$  and  $608 \text{ cm}^{-1}$  corresponding to the first and second order longitudinal optical phonons (1LO) and (2LO) act as a finger prints to identify CdS layers.

---

The XPS spectra measurement identified two distinct Cd 3d peaks (i.e.  $3d_{5/2}$  and  $3d_{3/2}$ ) with their binding energies at  $\sim 405$  and  $\sim 412$  eV respectively. The S 2p peak has a binding energy of  $\sim 162$  eV. XPS results indicate that the composition of CdS layers is 52.9:47.1. This is in agreement with the XRF data. The electrolytic bath used in this work can be used for a period of 7 months, therefore the objective have been achieved.

## References

1. P. Jackson, D. Hariskos, E. Lotter, S. Paetel, R. Wuerz, W. Wischmann, and M. Powalla, In proc: 25<sup>th</sup> EUPVSEC WCPEC-5, Valencia, Spain, (2010).
2. <http://www.firstsolar.com/> retrieved July, 26<sup>th</sup> 2011.
3. I. M. Dharmadasa and J. Haigh, *J. of Electrochem. Soc.* 153(1), G47 (2006).
4. R. A. Isma'il and O. A. Abdulrazaq, *Sol. Energy Mater. Sol. Cells* 91, 903 (2007).
5. K. T. R. Reddy, G. M. Shanthini, D. Johnston and R. W. Miles, *Thin Solid Films* 427, 397 (2003).
6. J. U. Trenty, D. Mao, X. Kaydanov, T. R. Ohna, D. L. Williamson, R. Collins and T. E. Furtak, NREL-Final Technical Report, 20/03/1995-15/06/1998.
7. I. M. Dharmadasa, S. M. McGregor, I. wadsworth and C. M. Care, *Optical Materials* 6, 75 (1996).
8. M. Rami, E. Benamar, M. Fahoume, F. Chraibi and A. Ennaoui, *Mater. J. Condense Matter* 3(1), 66 (2000).
9. L. A. Patil and P. A. Wani, *Cryst. Res. Technol.* 36(4-5), 372 (2001).
10. I. Salaoru, P. A. Buffat, D. Laub, A. Amariel, N. Apetroaei and M. Rusu, *J. of Optoelectronics & Advance Materials* 8(3), 939 (2006).
11. T. L. Chu and S. S. Chu, *Solid State Electronics* 38(3), 533 (1995).
12. V. Singh and P. Chauhan, *Chalcogenide Letters* 6(8), 421 (2009).
13. S. Chu, Y. Jang, J. Kim and D. Kim, *J. of Crystal Growth* 326, 152 (2011).
14. K. Shirai, Y. Moriguchi, M. Ichimura, A. Usami and M. saji, *Japanese J. Appl. Phys.* 35(1), 2057 (1996).
15. A. P. Samantilleke, M. F. Cerqueira, S. Heavens, P. warren, I. M. Dharmadasa, G. E. A. Muftah, C. J. R. Silva and B. Mari, *Thin Solid Films* (2011), doi:10.1016/j.tsf.2010.12.218.

16. M. Froment, M. C. Bernard, R. Cortes, B. Mokili and D. Lincot, *J. Electrochem. Soc.* 142(8), 2642 (1995).
17. D. S. Chu and C-M. Dai, *Phys. Rev. B* 45, 11805 (1992).
18. I. M. Dharmadasa, J. M. Thornton and R. H. Williams, *Appl. Phys. Letters* 54(2), 137 (1989).
19. D. A. Mazón-Montijo, M. Sotelo-Lerma, L. Rodríguez-Fernández and L. Huerta, *Appl. Surf. Sci.* 256, 4280 (2010).
20. R. S. Vemuri, S. K. Gullapalli, D. Zubia, J. C. McChure and C. V. Ramana, *Chemical Physics Letters* 495, 232 (2010).
21. M. Karimi, M. Rabiee, F. Moztafzadeh, M. Tahriri and M. Bodaghi, *Current Appl. Phys.* 9, 1263 (2009).
22. S. M. McGregor, PhD Thesis, Sheffield Hallam University, (1999).

## Chapter 5: Electrodeposition of ZnTe (Window material-2)

### 5.1 Motivation and objectives

The purpose of this chapter is to develop ZnTe thin films using electrodeposition and use it in graded bandgap multi-layer solar cells. Our target structure is glass/FTO/ZnTe/CdTe/CdS/Al contact. It is reported in the literature that multi-layer solar cells produce higher efficiency due to the higher electric field ( $E_i$ ) created within the device.

### 5.2 Introduction

Zinc telluride (ZnTe) is a p-type window material with a wide and direct bandgap of 2.21 – 2.26 eV at room temperature with electron affinity of 3.53 eV [1, 2]. Thin film solar cells need at least two kinds of semiconducting layers; a wide bandgap window material and a narrow bandgap absorber material. The most common window material used to develop thin film solar cells based on CdTe and CuInGaSe<sub>2</sub> absorber materials is n-CdS. Due to the toxic nature of Cd- containing waste produced during growth of CdS using chemical bath deposition (CBD), an alternative, more environmentally benign window material is required. ZnTe is an environmentally benign compound that can be potentially used as window layer to replace the CBD-CdS currently used.

The recent work reported by Dharmadasa et al. [3, 4] on multi-layer graded bandgap solar cells based on AlGaAs/GaAs structures with p-type window materials have demonstrated highest  $V_{oc}$  (1100 - 1175 mV) and excellent FF (0.80 - 0.87) values. The development of ZnTe layers using electroplating enables the fabrication of next generation graded bandgap solar cells using low-cost materials. Experimental details of ZnTe deposition have been discussed in section 3.3 of chapter 3.

### 5.3 Linear sweep voltammogram

Figure 5.1 shows a typical cyclic voltammograms related to the electrodeposition of ZnTe thin films from two electrolytes. Te starts to deposit from ~200 mV cathodic voltage and deposition of Te-rich ZnTe compound is expected at ~800 mV to 1400 mV cathodic voltages. ZnTe thin films deposition takes place beyond 1480 mV cathodic voltage as can be deduced from these Figures. Two peaks were observed in the reverse

direction which are attributed to the removal of metallic zinc and tellurium at (1368 & 710) mV and (858 & 349) mV cathodic voltages for 0.02M and 0.15M  $Zn^{+2}$  concentrations respectively. The pH is among the key parameters necessary to be considered for the deposition of ZnTe layers. According to references [2, 5], at lower pH ( $3.50 \pm 0.01$ ), free tellurium deposited and at comparatively higher pH ( $5.50 \pm 0.01$ ), the solution becomes cloudy due to the precipitation of  $TeO_2$  or  $Cd(OH)_2$ . Furthermore, the deposition current density has a strong influence on the structure of the ZnTe thin films grown. It has been reported that higher deposition current densities ( $>400 \mu Acm^{-2}$ ) led to films with rough surfaces, whereas films deposited at lower current densities ( $\approx 100 \mu Acm^{-2}$ ) had smooth surfaces [6].

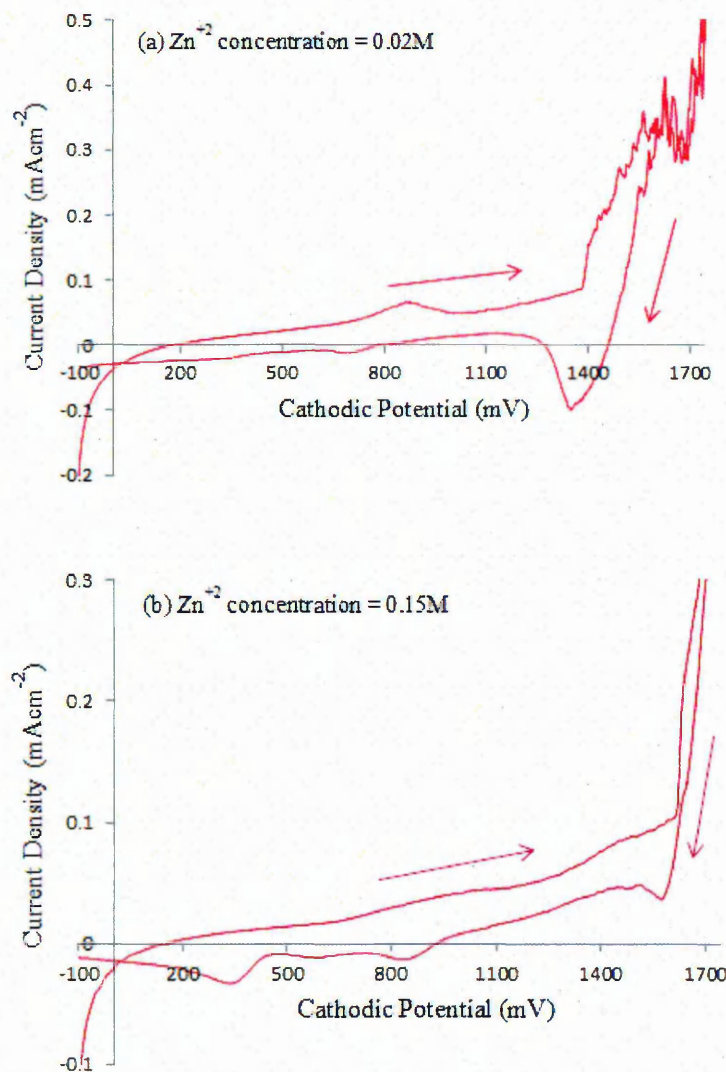


**Figure 5.1:** A typical voltammogram for an electrolytic bath used for deposition of ED-ZnTe using lower and higher  $Zn^{+2}$  concentration (a) and (b) respectively.

## 5.4 Visual Appearance

Figure 5.2 shows the visual appearance of ZnTe layers deposited as a function of growth voltage. As shown in the Figure, at higher and lower cathodic voltages, the samples become dark which are attributed to the Zn and Te richness. In the intermediate voltages, the layers appear reddish brown, similar to that of bulk ZnTe material [1, 2].

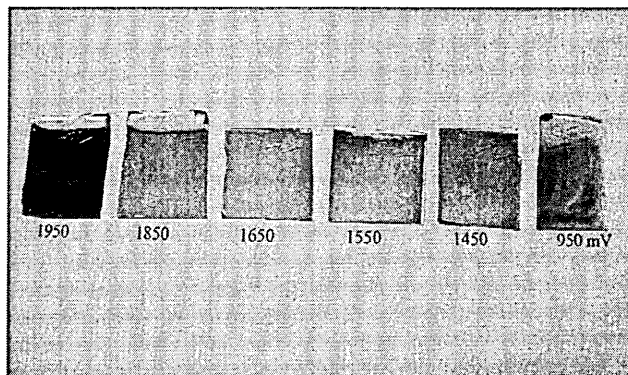


**Figure 5.2:** The appearance of as-deposited ED-ZnTe layers grown on glass/FTO substrate.

## 5.5 Characterisation of Electrodeposited ZnTe (ED-ZnTe)

### 5.5.1 X-ray diffraction

The XRD investigations of ED-ZnTe grown at 1513 and 1560 mV from 0.02M and 0.15M  $\text{Zn}^{+2}$  concentrations are shown in Figure 5.3. The diffractograms show that at lower Zn concentration a strong peak is observed at  $2\theta = 24.05^\circ$  which corresponds to preferred orientation along (100) plane of hexagonal phase. This peak agrees with the JCPDS (01-075-2082) data on hexagonal ZnTe. Other peaks identified from the graphs are ZnO peak and (103). At the higher concentration of  $\text{Zn}^{+2}$  the preferred orientation of ZnTe disappears with (102), (200) and (202) appearing in addition to (100). Mahalingam et al. [5] reported that ZnTe films crystallise at lower concentration and the results confirmed this observation. The values of  $d$ ,  $D$  and FWHM of the strongest peak evaluated for results shown on panel 1 are presented in Table 5.1 using equation (2.17) and (2.18) from section 2.2.1 in chapter 2. Furthermore, due to the nature of the weak XRD peaks on panel 2 it is difficult to calculate these parameters.

**Table 5.1:** Structural parameters of ED-ZnTe thin films.

S/N	2θ (Degrees)		Lattice spacing d (Å)		Crystallite size D (nm)	FWHM	hkl
	RP	OB	RP	OB			
1	24.029	24.050	3.7005	3.7761	4.4	0.334	100
2	24.029	24.050	3.7005	3.7305	8.8	0.169	100

N/B: 1 - as deposited, 2 - heat treated, RP - reported value from the JCPDS card, OB - observed value from the XRD Figure on panel 1.

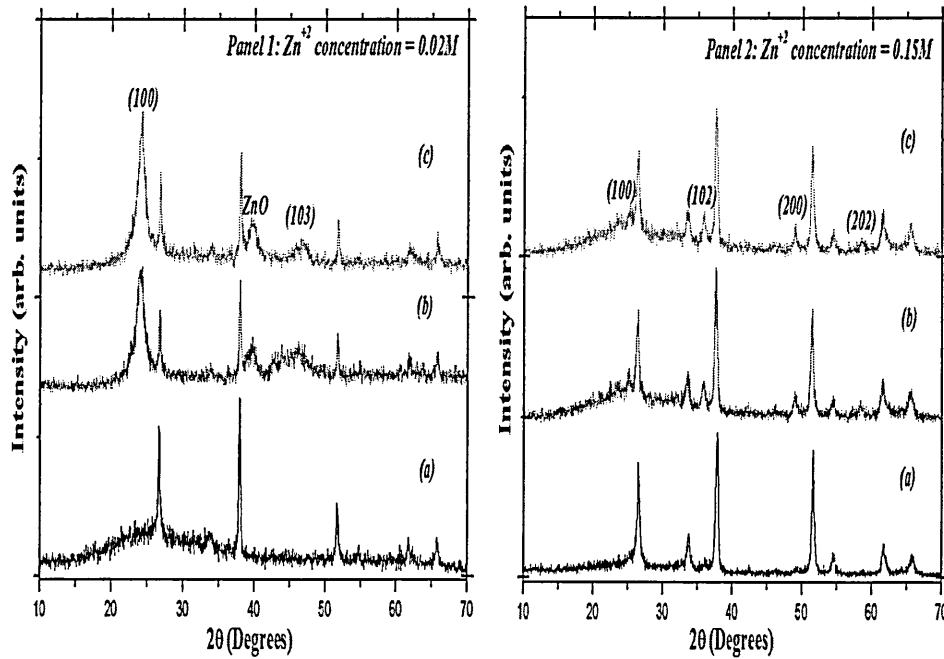


**Figure 5.3:** X-ray diffraction patterns of ED-ZnTe thin films grown at lower [panel 1  $V_g = 1513$  mV] and higher [panel 2  $V_g = 1590$  mV] concentrations of  $Zn^{+2}$ ; (a) glass/FTO, (b) as deposited and (c) heat treated ED-ZnTe.

From the Table, it is observed that crystallite size for heat treated sample increases and the FWHM decreases; this is due to coalescence of small crystals and formation of large grains. A further decrease in the lattice spacing is observed for the heat treated sample which is in agreement with the work of Lalitha et al. [6]. The observed lower value of d for heat treated sample is an evidence of removal of tensile strain by the heat treatment. The same trend is observed for FWHM; the crystallite size increases due to the increase in the grain sizes and the relaxation of excessive strains in the lattice.

### 5.5.2 Photoelectrochemical (PEC) cell

PEC signal measurements were carried out on all the samples from the two concentrations and the results are shown in Figure 5.4. PEC studies provide vital information on electrical conductivity type and hence help in design and fabrication of electronic devices using these films. These results indicate that all ED-ZnTe layers grown at the indicated voltages were p-type in electrical conduction. It should be noted that  $\text{Na}_2\text{SO}_4$  has been used as a supporting electrolyte to grow ZnTe. The presence of sodium in the electrolyte could act as a p-type dopant in ZnTe producing always p-type ZnTe layers.

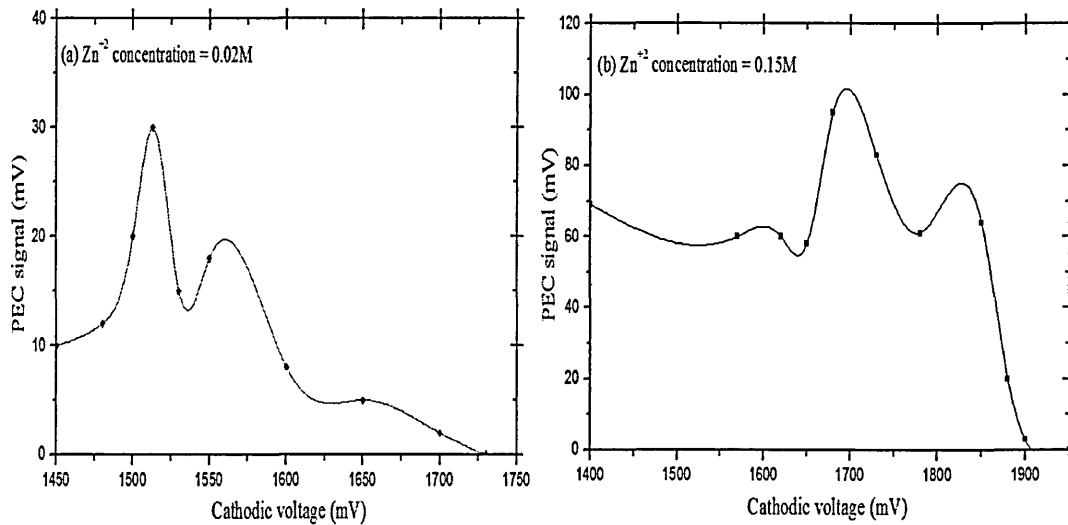


**Figure 5.4:** PEC signal as a function of growth voltage for as deposited ED-ZnTe layers for  $\text{Zn}^{+2}$  concentrations (a) 0.02M and (b) 0.15M.

### 5.5.3 Optical absorption

Optical absorption measurements were carried out in order to evaluate the bandgap. The absorption spectra of ED-ZnTe using 0.02M and 0.15M  $\text{Zn}^{+2}$  concentrations are shown in Figure 5.5. Using equation (2.21) on section 2.2.3 in chapter 2, the bandgap energy,  $E_g$ , was estimated by plotting the square of absorbance ( $A^2$ ) against photon energy ( $h\nu$ ). The intercept on the energy axis gives the values of the direct bandgap of the as deposited ZnTe;  $E_g$  as  $\sim (2.32 - 2.50)$  eV and  $(2.65 - 2.78)$  eV for 0.02M and 0.15M for  $\text{Zn}^{+2}$  concentration respectively.

Figure 5.5 (a) clearly shows the progressive sharpening of the absorption edge, which is due to the lower concentration of  $\text{Zn}^{+2}$  sources. This result goes together with the XRD spectra presented on panel 1 of Figure 5.3. The minimum value of 2.32 eV from the

lower concentration is very close to the reported bandgap of crystalline ZnTe layer (2.21 – 2.26) eV [1, 2]. The larger value observed in the films with a higher concentration of Zn in the bath indicates that the layers formed consist of nano-crystals, producing larger bandgap values due to quantum effects. This increase could also be due to incorporation of ZnO ( $E_g = 3.08 - 3.26$ ) eV [7, 8] and hence reducing the crystallinity of the deposits.

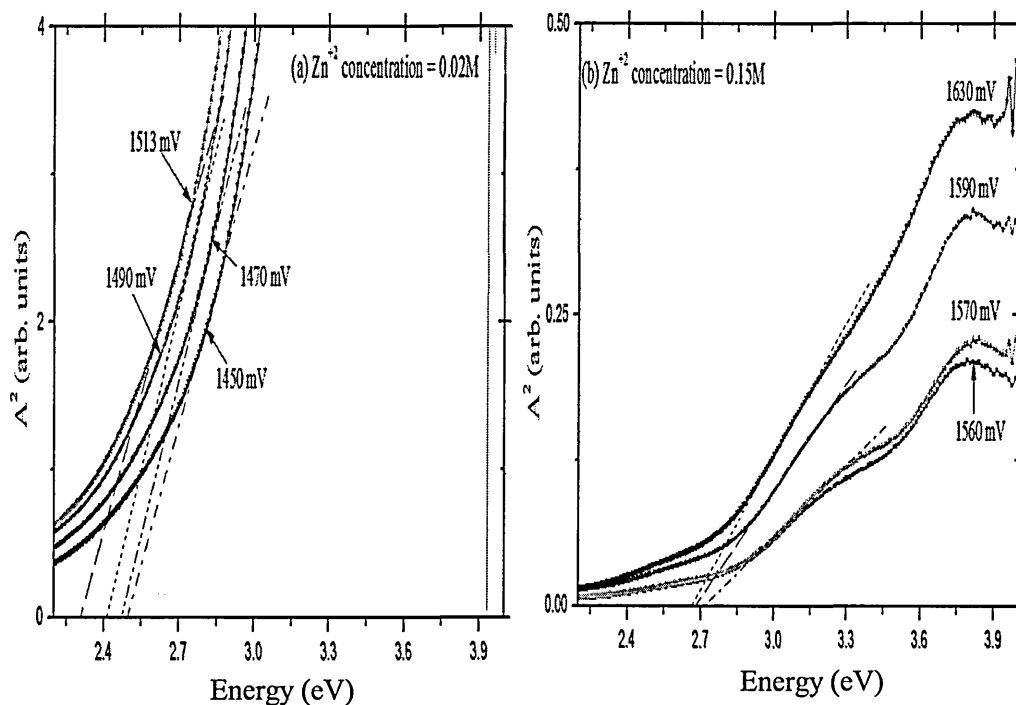
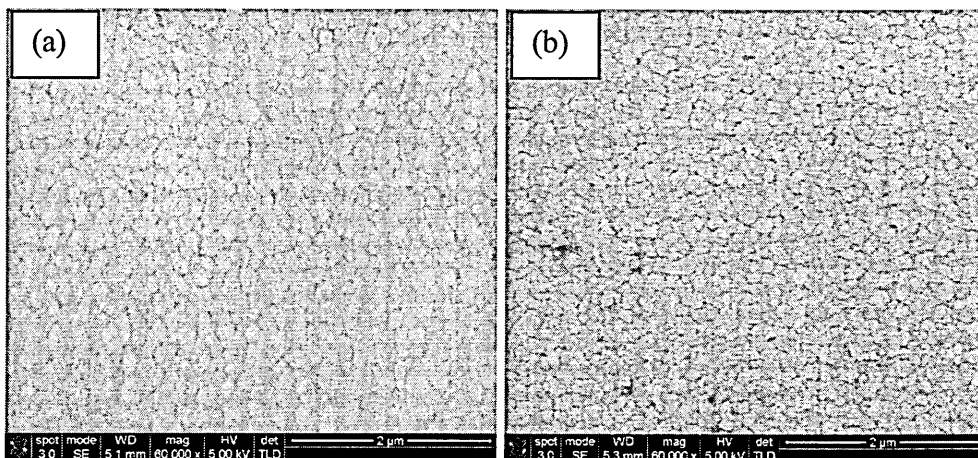


**Figure 5.5:** Optical absorption edges for as deposited ED-ZnTe for  $Zn^{+2}$  concentrations (a) 0.02M and (b) 0.15M.

#### 5.5.4 Scanning Electron Microscopy

SEM studies were carried out to investigate the surface morphology and uniformity of ED-ZnTe layers. The SEM pictures of as deposited ZnTe layers are shown in Figure 5.6 (a) and (b) from two different  $Zn^{+2}$  concentrations. The appearance indicates the uniform distribution of grains size of  $\sim 15$  nm and  $\sim 10$  nm from lower and higher concentrations of  $Zn^{+2}$  respectively.

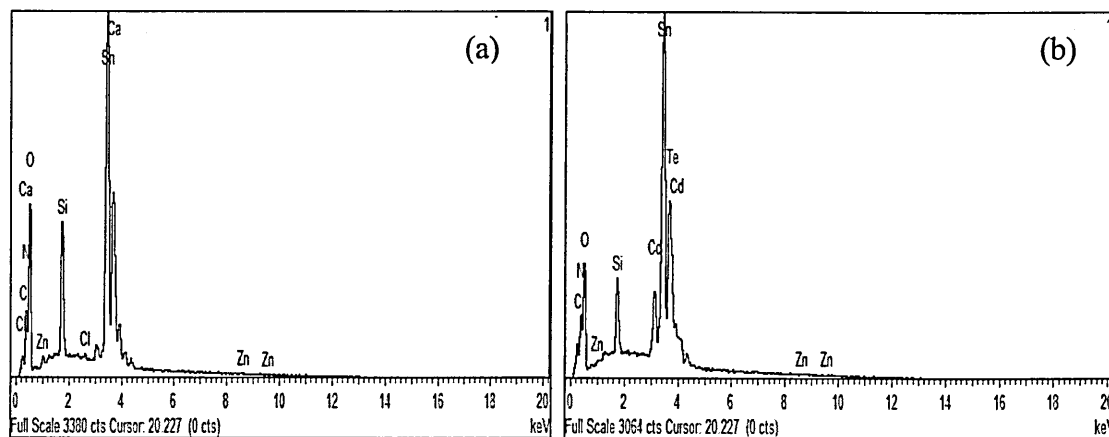
Reproducibility of the films is one of the main challenges facing most of the growth techniques. In this work, the main difficulties are the right control of parameters such as pH, tellurium addition, temperature of the electrolytic bath, deposition potential etc.



**Figure 5.6:** SEM images of ED-ZnTe grown on glass/FTO substrates for  $Zn^{+2}$  concentrations (a) 0.02M  $V_g = 1513$  mV and (b) 0.15M  $V_g = 1590$  mV.

### 5.5.5 Energy Dispersive X-ray

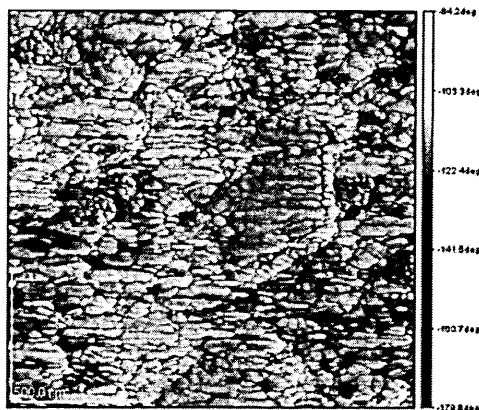
The qualitative analysis of the ED-ZnTe layers was carried out using energy dispersive x-ray (EDX) spectroscopy on both lower and higher  $Zn^{+2}$  concentrations. Figure 5.7 shows the EDX spectra of ED-ZnTe layers. From the Figures, both Zn and Te elements are present and the remaining elements identified are due to the background of the glass/FTO substrate. The atomic composition of Zn:Te estimated is 25:75.



**Figure 5.7:** EDX spectra of ED-ZnTe grown on glass/FTO substrates for  $Zn^{+2}$  concentrations (a) 0.02M  $V_g = 1513$  mV and (b) 0.15M  $V_g = 1590$  mV.

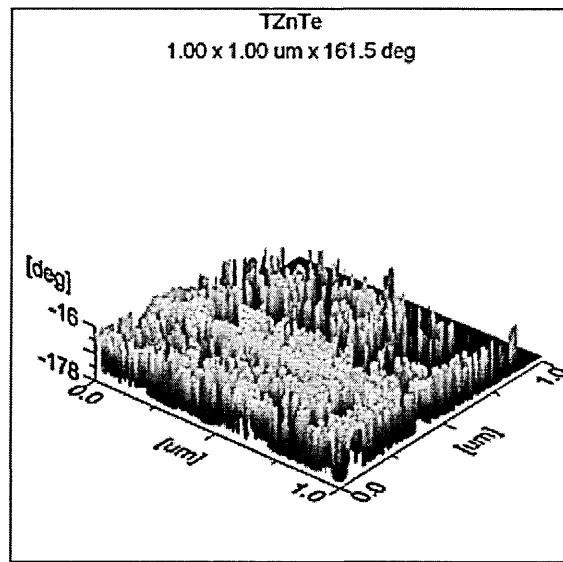
### 5.5.6 Atomic Force Microscopy

Figure 5.8 shows the 2D-AFM pictures of heat treated ED-ZnTe grown on glass/FTO substrate at 1513 mV from lower concentration. The AFM image shows small clusters of ZnTe which indicates the uniform distribution of grain size, and very consistent with the SEM results shown in Figure 5.6.



**Figure 5.8:** 2D-AFM image of ED-ZnTe grown on glass/FTO substrate at 1513 mV (courtesy: Inst. of Org. Catalysis & Electrochem., Kazakhstan).

The 3D-AFM picture of ED-ZnTe grown at 1513 mV from lower concentration is shown in Figure 5.9. From the Figure there is a sign of nano-rod similar to the ED-CdS discussed in chapter 4. Since ZnTe is a II-VI compound similar to CdS, these nano-rods are also tightly packed and oriented perpendicular to the glass/FTO substrates. The length and diameter of the nano-rods are ~60 nm (thickness of the ZnTe layer) and ~30 nm respectively. This nano-rod nature of ZnTe could reduce the recombination of electrons and holes and also minimise scattering at grain boundaries.



**Figure 5.9:** 3D-AFM image of ED-ZnTe grown on glass/FTO substrate at 1513 mV (courtesy: Inst. of Org. Catalysis & Electrochem., Kazakhstan).

### 5.5.7 Raman spectroscopy

The Raman spectra of ED-ZnTe were recorded using a RENISHAW InVia Raman Microscope. The Raman spectrum of ZnTe epilayer grown on GaAs substrate is shown in Figure 5.10 for comparison [9]. Figure 5.11 shows the Raman spectrum of ED-ZnTe layer grown on glass/FTO substrate at 1513 mV from lower concentration. Two peaks were observed at  $203\text{ cm}^{-1}$  and  $409\text{ cm}^{-1}$  which correspond to the first and second order longitudinal optical phonons (1LO) and (2LO) of ZnTe respectively. All these peaks are very close to those found by other researchers [10-13]. A similar observation of these two peaks has been reported by Szuszkiewicz et al. [12, 13]. They also reported that the group of lines observed between  $90\text{ cm}^{-1}$  and  $150\text{ cm}^{-1}$  (i.e. Te labelled) is due to Raman scattering at trigonal tellurium clusters. Furthermore, the LO phonon line intensity has a clear maximum for an excitation energy of 2.34 eV, close to the excitation energy of ZnTe.

A Raman spectrum shows that electrodeposited ZnTe films is Te-rich with a strong Te-peak observed. This indicates that the deposited film is Te-rich surface. Therefore, stoichiometric ZnTe must be produced which is necessary for good devices.

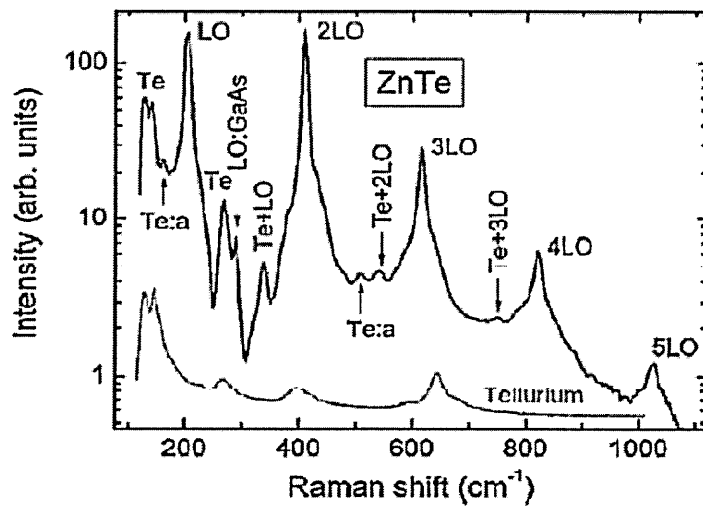


Figure 5.10: Raman spectra of ZnTe epilayer grown on GaAs substrate [9].

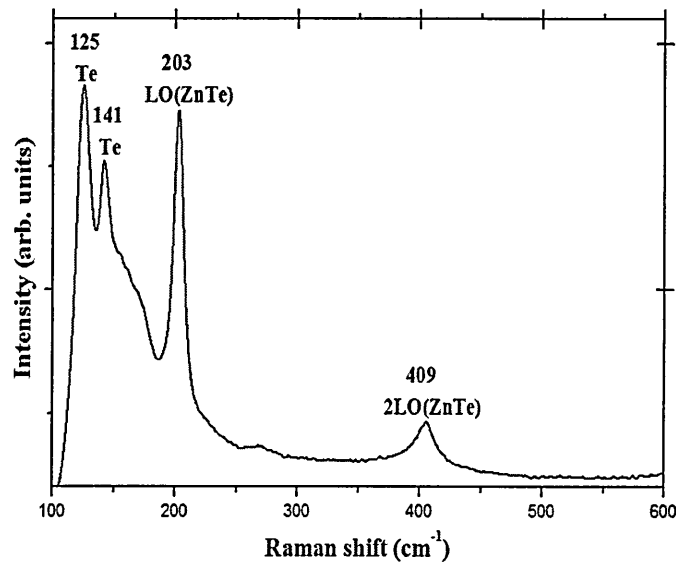
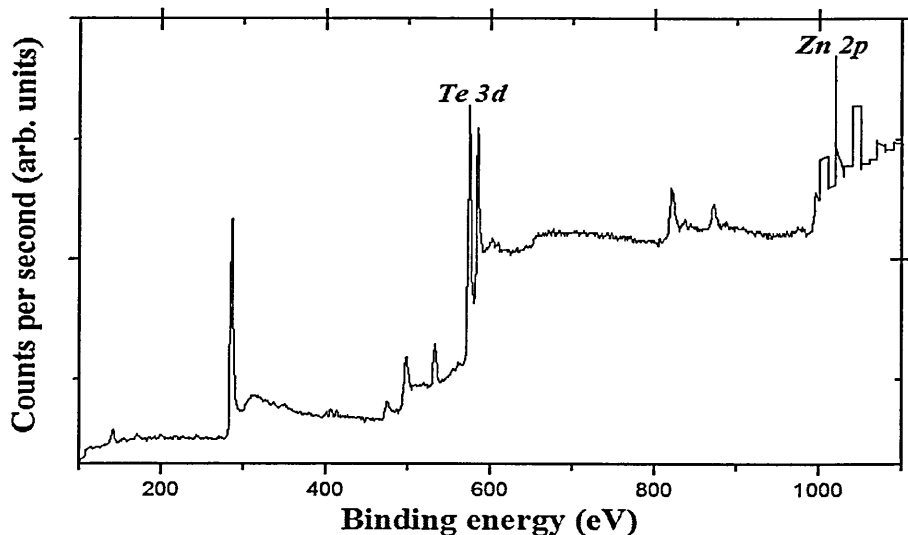


Figure 5.11: Raman spectrum of ED-ZnTe grown on glass/FTO substrate at 1513 mV (courtesy: Inst. of Mater. Research, Univ. of Leeds).

### 5.5.8 X-ray photoelectron spectroscopy

XPS studies were performed using an Escalab 250 spectrometer to obtain quantitative analysis of surface chemical states. A typical XPS survey spectrum of ED-ZnTe grown at 1513 mV is shown in Figure 5.12. Figures 5.13 and 5.14 shows the Te 3d and Zn 2p core-level XPS spectra indicating the presence of both Zn and Te in these layers. Two distinct Te 3d peaks (i.e.  $3d_{5/2}$  and  $3d_{3/2}$ ) are observed in Figure 5.13. As shown from the Figure, the binding energies associated with Te ( $3d_{5/2}$  and  $3d_{3/2}$ ) appeared at  $\sim 573$  and

~584 eV respectively. Similarly, Figure 5.14 shows the Zn 2p peak has a binding energy of ~1022 eV. The atomic ratio for Zn:Te given from the XPS spectra is 32.8:67.2. All these peaks and binding energies are very close to those found by other researchers [14-17]. The above atomic ratio indicates that the layers contain more Te in these electrodeposited materials. This explains why sharp peak of Te is observed in Raman spectra shown in Figure 5.11.



**Figure 5.12:** Typical XPS survey spectrum of ED-ZnTe pattern grown at 1513 mV (courtesy: Inst. of Mater. Research, Univ. of Leeds).

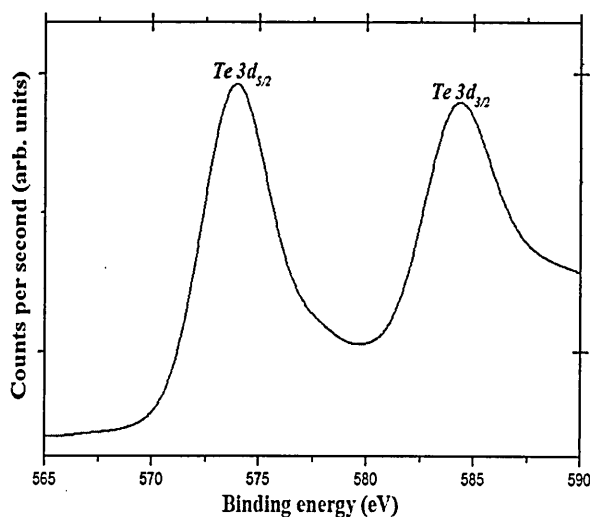


**Figure 5.13:** XPS spectrum of ED-ZnTe layers grown at 1513 mV indicating Te 3d core levels (courtesy: Inst. of Mater. Research, Univ. of Leeds).

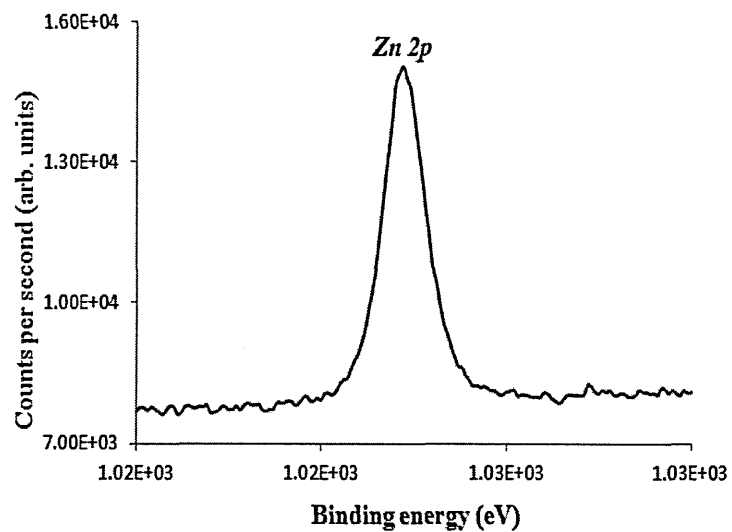


**Figure 5.14:** XPS spectrum of ED-ZnTe layers grown at 1513 mV indicating Zn 2p core levels (courtesy: Inst. of Mater. Research, Univ. of Leeds).

## 5.6 Summary

ZnTe has been deposited on glass/FTO substrates using low-cost aqueous electrodeposition method. The XRD results indicates that both as deposited and heat treated ED-ZnTe layers show that at lower Zn concentration in the bath, a strong peak is observed at  $2\theta = 24.05^\circ$  which corresponds to preferred orientation along (100) plane of hexagonal phase, but when the concentration increases the (100) becomes very weak.

PEC studies indicate p-type electrical conduction for electrodeposited ZnTe layers. Optical absorption measurement provides minimum bandgap of the as deposited ZnTe as  $\sim 2.28$  eV and  $2.65$  eV for  $0.02\text{M}$  and  $0.15\text{M}$  of  $\text{Zn}^{+2}$  concentration respectively. SEM studies indicates uniform distribution of grains size of  $\sim 15$  nm and  $\sim 10$  nm from lower and higher concentration of  $\text{Zn}^{+2}$  respectively.

3D-AFM measurements show that the ED-ZnTe layers consist of tightly packed and well defined nano-rods oriented perpendicular to the glass/FTO substrates. The 2D-AFM images show small clusters of ZnTe which indicates the uniform distribution of grain size. The SEM pictures of as deposited ZnTe layers indicates the uniform distribution of grains size of  $\sim 15$  nm and  $\sim 10$  nm from lower and higher concentrations of  $\text{Zn}^{+2}$  respectively.

Raman measurements have been shown to be a fast and convenient technique to use as a quality control method. Two peaks were observed at  $203\text{ cm}^{-1}$  and  $409\text{ cm}^{-1}$  which correspond to the first and second order longitudinal optical phonons (1LO) and (2LO) of ZnTe respectively. These act as finger prints to identify this phase. From the XPS spectrum, the binding energies associated with Te ( $3d_{5/2}$  and  $3d_{3/2}$ ) appeared at  $\sim 573$  and  $\sim 584$  eV respectively. The Zn 2p peak has the binding energy at  $\sim 1022$  eV.

XPS results indicate that the composition of ZnTe layers as 32.8:67.2, which means that the electrodeposited layers are rich in Te. This is again confirmed by the strong Te-peak appearing in Raman spectra. Both these experimental evidence indicate the preferential precipitation of Te during electrodeposition of ZnTe process.

In general, electrodeposited ZnTe films show a strong XRD peak from lower Zn concentration indicating better crystallinity when grown with lower Zn in the electrolyte. But other results (XPS, Raman and EDX) confirmed that the deposited films are rich in Te. Therefore, these three techniques used indicate that ZnTe is not stoichiometric but

---

contains excess Te. The future work must focus to reduce Te crystallisation in these layers and hence improve the composition ratio of Zn and Te. The presence of excess Te also explains p-type electrical conductivity of electrodeposited ZnTe materials. Furthermore, due to the peeling-off of ZnTe layers in acidic CdTe and CdS bath, the objective has not been achieved.

## References

1. T. Mahalingam, V. S. John, G. Ravi and P. J. Sebastian, *Crystal Research Technol.* 37(4), 329 (2002).
2. M. Neumann-Spallart and C. Konigstein, *Thin Solid Films* 265, 33 (1995).
3. I. M. Dharmadasa, *Curr. Appl. Phys.* doi: 10.1016/j.cap.2008.12.0121 (2009).
4. I. M. Dharmadasa, J. S. Roberts and G. Hill, *Sol. Energy Mater. Sol. Cells* 88, 413 (2005).
5. T. Mahalingam, V. S. John, S. Rajendran and P. J. Sebastian, *Semicond. Sci. Technol.* 17, 465 (2002).
6. S. Lalitha, R. Sathayamoorthy, S. Senthilarasu and A. Subbrayan, *Sol. Energy Mater. Sol. Cells* 90, 90 (2006).
7. M. Fahoume, O. Magfoul, M. Aggour, B. Hartiti, F. Chraïbi and A. Ennaoui, *Sol. Energy Mater. Sol. Cells* 90, 1437 (2006).
8. R. Chander and A. K. Raychaudhuri, *Solid State Communication* 145, 81 (2008).
9. V. Wiedemeier, G. Berth, A. Zrenner, E. M. Larramendi, U. Woggon, K. Lischka and D. Schikora, *Semicond. Sci. Technol.* 26, 105023 (2011).
10. K. Ersching, C. E. M. Campos, J. C. de Lima, T. A. Grandi, S. M. Souza, D. L. de Silva and P. S. Pizani, *J. of Appl. Phys.* 105, 123532 (2009).
11. E. Oh, A. K. Ramdas, N. Samarth, H. Luo and J. K. Furdyna, *Physical Review B* 47(12), 7288 (1993).
12. W. Szuskiewicz, J. F. Morhange, E. Dyanowaka, E. Janik, W. Zaleszczyk, A. Presz, G. Karczewski and T. Wojtowicz, *J. of Phys: Conf. Series* 92, 012040 (2007).
13. W. Szuskiewicz, J. F. Morhange, E. Janik, W. Zaleszczyk, G. Karczewski and T. Wojtowicz, *Phys. Status Solidi C* 6(9), 2047 (2009).
14. W. Wang, G. Xia, J. Zheng, L. Feng and R. Hao, *J. Mater. Sci: Mater. Electron* 18, 427 (2007).
15. K. R. Murali, M. Ziaudeen and N. Jayaprakash, *Solid-State Electronics* 50, 1692 (2006).
16. W. Wang, W. Bowen, S. Spanninga, S. Lin and J. Phillips, *J. of Electronic Materials* 38(1), 119 (2009).
17. B. Späth, J. Fritsche, F. Saüberlich, A. Klein and W. Jaegermann, *Thin Solid Films* 480-481, 204 (2005).

## Chapter 6: Growth and optimisation of CdTe deposition voltage

### 6.1 Motivation and objectives

The deposition voltage of CdTe thin film has been established by previous researchers in our group. It is within the range 1.500 - 1.600 V, and layers deposited from 1.560 to 1.585 V produce good devices. The aim of this chapter is to investigate the optimum deposition potential for CdTe film growth within this range

### 6.2 Introduction

Cadmium telluride (CdTe) is one of the most suitable materials for use in thin film photovoltaic structures and other electronic devices. It is a direct bandgap semiconductor with bandgap energy of 1.45 eV which is close to the optimum; theoretical calculation shows that semiconductors with bandgap energy of 1.00 – 2.00 eV are suitable for solar energy conversion [1, 2].

Only two microns of CdTe will absorb nearly 100% of incident solar radiation, whereas crystalline silicon needs to be at least 100  $\mu\text{m}$  thick to absorb the same amount of radiation [3, 4]. To date, CdTe-based solar cells have achieved efficiency of 17.3% [5] in small scale laboratory devices. CdTe thin film deposition has been discussed in details in section 3.4 of chapter 3.

### 6.3 Linear sweep voltammogram

Figure 6.1 shows a typical voltammogram related to the electrodeposition of CdTe layers. The voltage scan was run between 100 to 1700 mV cathodic voltages with a sweep rate of 5  $\text{mVs}^{-1}$ . As shown in Figure 6.1 (b), Te begins to be reduced when the current density starts to increase from cathodic voltages  $\sim 200$  mV to  $\sim 1400$  mV.

In this region, elemental Te is free and the layer deposited is a mixture of CdTe and Te. A small hump is observed around 1500 mV, and deposition of mainly CdTe layer is expected beyond 1550 mV cathodic voltage as can be seen from the Figure. A rapid increase in current at  $\sim 1600$  mV is due to the combination of deposition of elemental Cd and hydrogen evolution at the cathode. In the reverse direction, prominent peaks were

observed which are attributed to the removal of elemental Cd, Cd-from CdTe and then elemental Te at cathodic voltages 1000, 900 and 700 mV respectively.

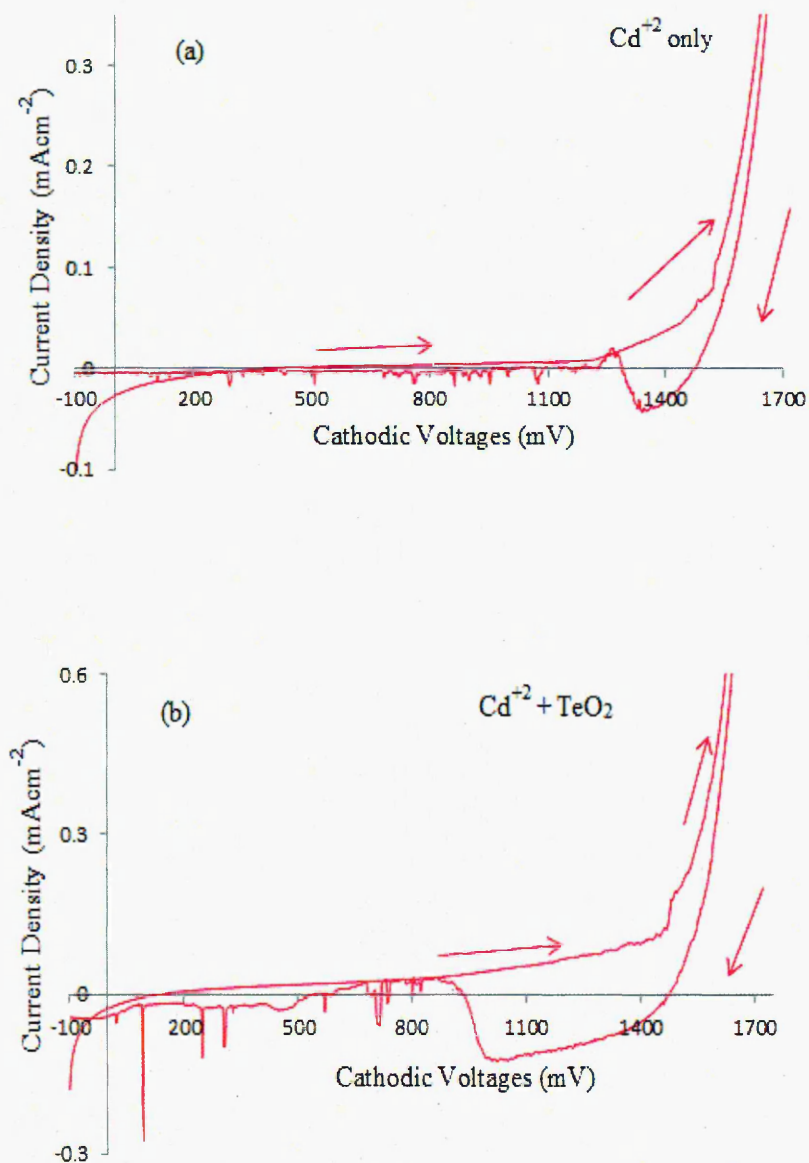


**Figure 6.1:** Typical voltammograms for electrolytic baths used for deposition of CdTe (a)  $\text{Cd}^{+2}$  only and (b)  $\text{Cd}^{+2} + \text{TeO}_2$ .

## 6.4 Characterisation of CdTe

### 6.4.1 Photoelectrochemical (PEC) cell

The Photoelectrochemical cell values of glass/FTO/CdTe layers grown at different cathodic voltages are shown in Table 6.1 and the PEC signal is shown in Figure 6.2.

**Table 6.1:** PEC cell results of glass/FTO/CdTe as a function of the growth voltage.

S/N	Growth voltage (V)	PEC signal (mV)
1	1.570	+3
2	1.571	+2
3	1.572	+2
4	1.573	+1
5	1.574	+1
6	1.575	+1
7	1.576	0
8	1.577	-1
9	1.578	-1
10	1.579	-2
11	1.580	-2

From the Table above, at lower cathodic voltages the polarity of the PEC signal was p-types and at higher cathodic voltages it was n- types, indicating Te-rich and Cd-rich respectively. At deposition voltage of 1.576 V the PEC signal shows intrinsic (i.e. stoichiometric). The PEC signal arises because of the formation of PV active depletion region as a result of moderate doping  $\sim(10^{14} - 10^{17}) \text{ cm}^{-3}$ . These results confirmed the work of other researchers who reported the possibility of getting either p- or n- type CdTe [6-8].

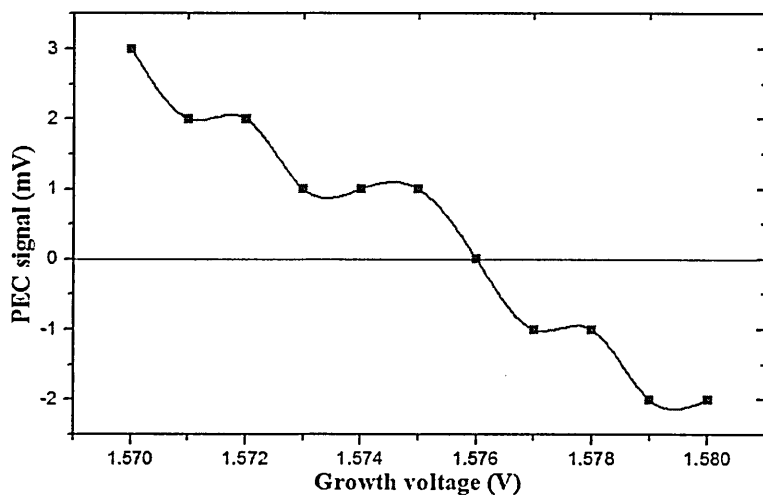


**Figure 6.2:** PEC signal as a function of growth voltage for glass/FTO/CdTe layers.

### 6.4.2 X-ray diffraction

Figure 6.3 shows the X-ray diffraction patterns for as deposited and heat treated CdTe layers (at 450°C for 15 minutes) deposited at different growth voltages. The main diffraction peak at  $2\theta = 23.642^\circ$  which corresponds to preferred orientation along (111) plane of cubic phase. This peak agrees with the JCPDS (01-075-2086) data of cubic CdTe. From these Figures, it is observed that at lower growth voltage (panel 1:  $V_g = 1.563$  V), Te is deposited more than Cd on the substrate surface, giving rise to Te-rich CdTe material. As the deposition potential increases, the Te peaks in the diffractograms diminish, at 1.574 V and above, only one peak ascribed to Te is seen.

At the higher of growth voltage (panel 8:  $V_g = 1.587$  V), more Cd atoms than Te atoms are deposited on the substrate surface and the resulting films produced are Cd-rich CdTe material. Weak Cd peaks were observed in this diffractogram. At the intrinsic composition 1.576 eV, the CdTe (111) peak is dominant and all other peaks diminished as shown in panel 5. As shown from the PEC result in section 6.4.1, this region is i-type in electrical conductivity which is similar to the results reported by Yang et al. [9].

After heat treatment in air, the intensity of the peaks was different. At lower and higher growth voltages, the intensity goes up as a result of the films become more crystalline. At the intrinsic potential and the potential which are very close to the stoichiometry, the intensity goes down due loss of the material through sublimation. The heat treatment enhances the recrystallisation of non-stoichiometric CdTe films reducing any stress within the films and due to sublimation of excess elements from the layers. The values of XRD intensity, FWHM and D at different growth voltages are presented in Table 6.2, estimated using equation 2.18 presented in section 2.2.1 in chapter 2.

Stoichiometric CdTe layers produce higher efficiency when the device fabricated due to the presence of atomic composition of Cd:Te ratio as 50:50. Away from the stoichiometric growth voltage, material layer will be either Te-rich or Cd-rich, and hence the efficiency suffers due to the presence of two phases.

**Table 6.2:** XRD intensity, FWHM and grain size of CdTe at different growth voltages for as deposited and heat treated layers.

Growth voltage (V)	XRD Intensity (arb. units)		FWHM		Grain size, D (nm)	
	AD	HT	AD	HT	AD	HT
1.563	706	1036	0.184	0.134	8.3	11.4
1.570	2044	3276	0.130	0.117	11.8	13.1
1.572	2502	3229	0.128	0.112	12.0	13.7
1.574	4324	3944	0.123	0.108	12.5	14.2
1.576	7169	4927	0.117	0.100	13.1	15.8
1.578	4500	4238	0.130	0.109	11.8	14.1
1.580	3060	3132	0.134	0.110	11.4	13.8
1.587	1200	2578	0.185	0.112	8.2	13.7

N/B: AD = as deposited and HT = heat treated.

From the Table, it is observed that crystallite size for heat treated sample increases and the FWHM decreases; this is due to the coalescence of small crystals and the formation of large grains. Furthermore, the FWHM was found to decrease as the growth voltage get to its stoichiometry, and start to increase as it goes away. The opposite is the case for crystallite size. Such effect is due to the decrease in the concentration of lattice imperfections as a result of a decrease in the internal micro strain within the films or an increase in the crystallite size. Figures 6.4, 6.5 and 6.6 shows the XRD intensity, FWHM and grain size at different growth voltages respectively.

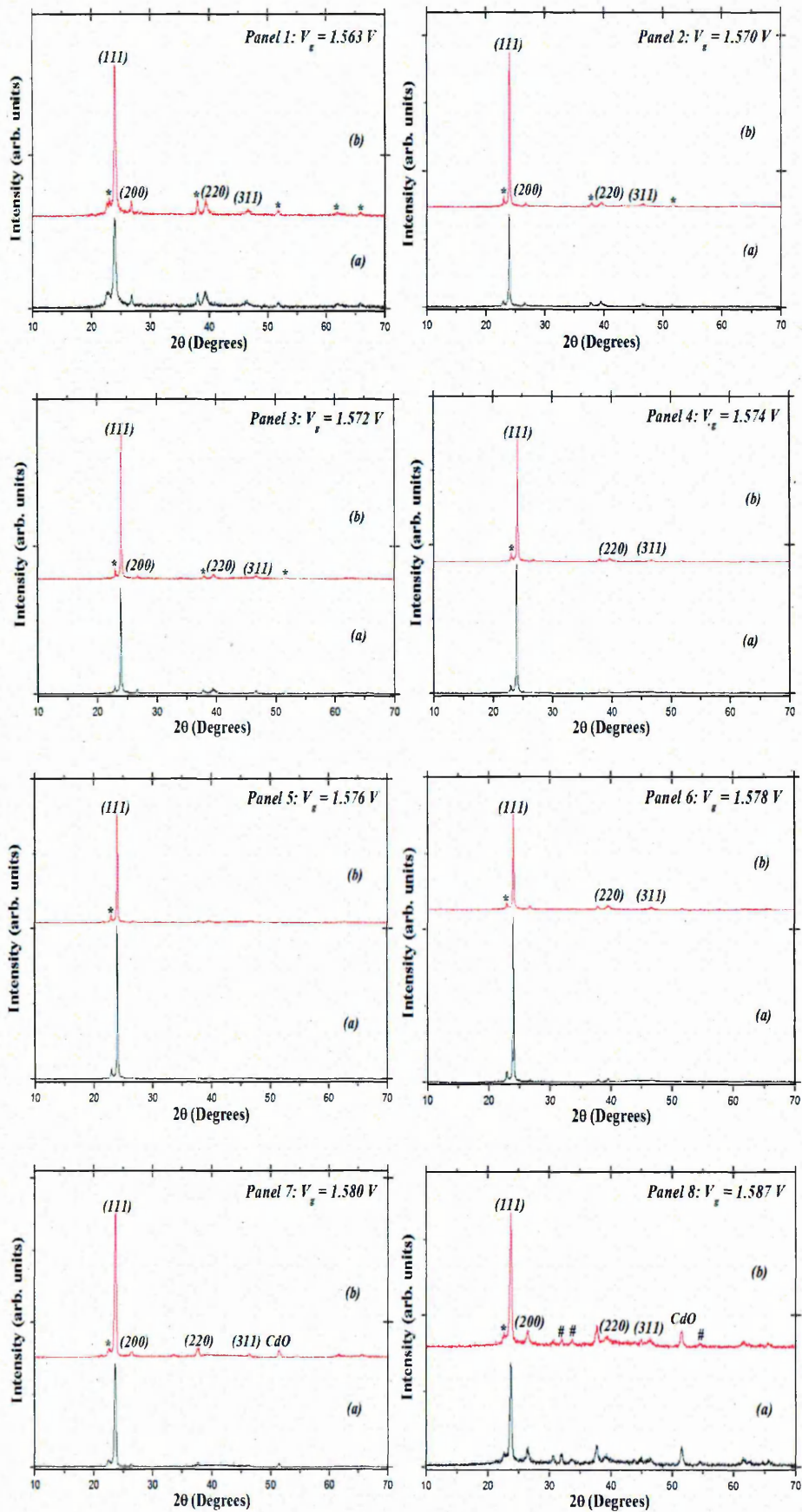


**Figure 6.3:** X-ray diffraction patterns for CdTe layers at different growth voltages (a) as deposited and (b) heat treated [\* and # indicates Te and Cd peaks respectively].

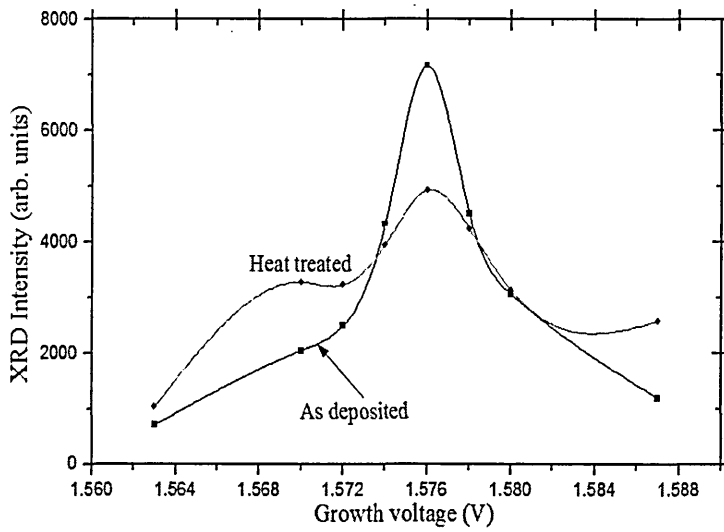


**Figure 6.4:** XRD Intensity of (111) peak observed for CdTe layers grown at different growth voltages.

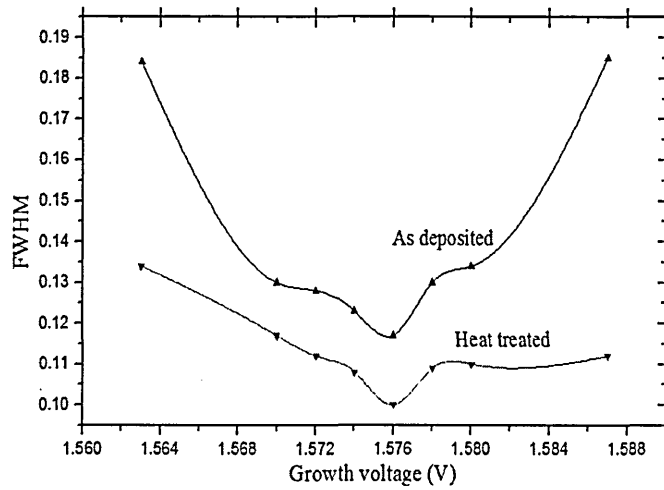


**Figure 6.5:** FWHM of (111) peak observed for CdTe layers grown at different growth voltages.

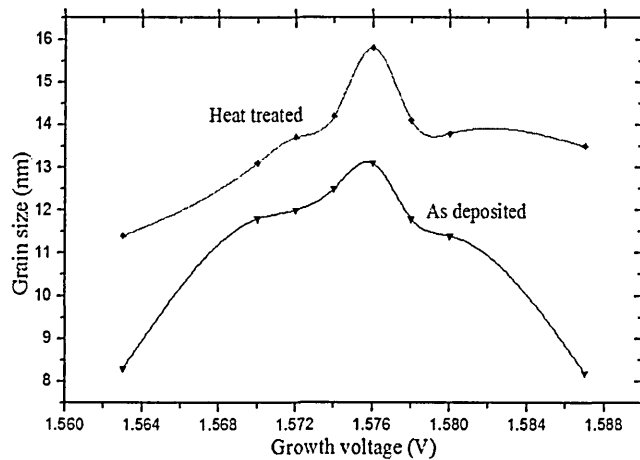


**Figure 6.6:** Grain sizes of (111) peak observed for CdTe layers grown at different growth voltages.

### 6.4.3 Optical absorption

Optical absorption measurements were carried out in order to evaluate the bandgap. Figure 6.7 shows the graphs of optical absorption for as deposited and heat treated CdTe samples. Using equation 2.21 on section 2.2.3 in chapter 2, the bandgap energy,  $E_g$  was determined by plotting the square of absorption ( $A^2$ ) against photon energy ( $h\nu$ ) for both as deposited and heat treated materials. The value of  $E_g$  for as deposited samples grown at or near stoichiometry is 1.55 eV. As films become increasingly non-stoichiometry  $E_g$  value increases. After heat treatment, the bandgap values decreased and the absorption edge of the curve sharpened. Bandgap energy for the stoichiometry films became 1.45 eV which is closer to the bulk CdTe value. The reason for the sharpening might be due to a change in the stoichiometry or reduction of intrinsic defect population of the treated samples. Table 6.3 gives the bandgap values for as deposited and heat treated CdTe layers at different growth voltages, and Figure 6.8 shows the bandgap energy at different growth voltages.

**Table 6.3:** Bandgap energy of CdTe layers at different growth voltages.

Growth voltage (V)	Bandgap (eV)	
	AD	HT
1.563	1.62	1.55
1.572	1.62	1.50
1.574	1.55	1.45
1.576	1.55	1.45
1.578	1.55	1.45
1.580	1.55	1.50
1.587	1.62	1.55

As shown from the Table, the bandgap energies increase as the growth voltage deviates from the stoichiometry value ( $V_g \sim 1.576$  V) for both as deposited and heat treated samples.

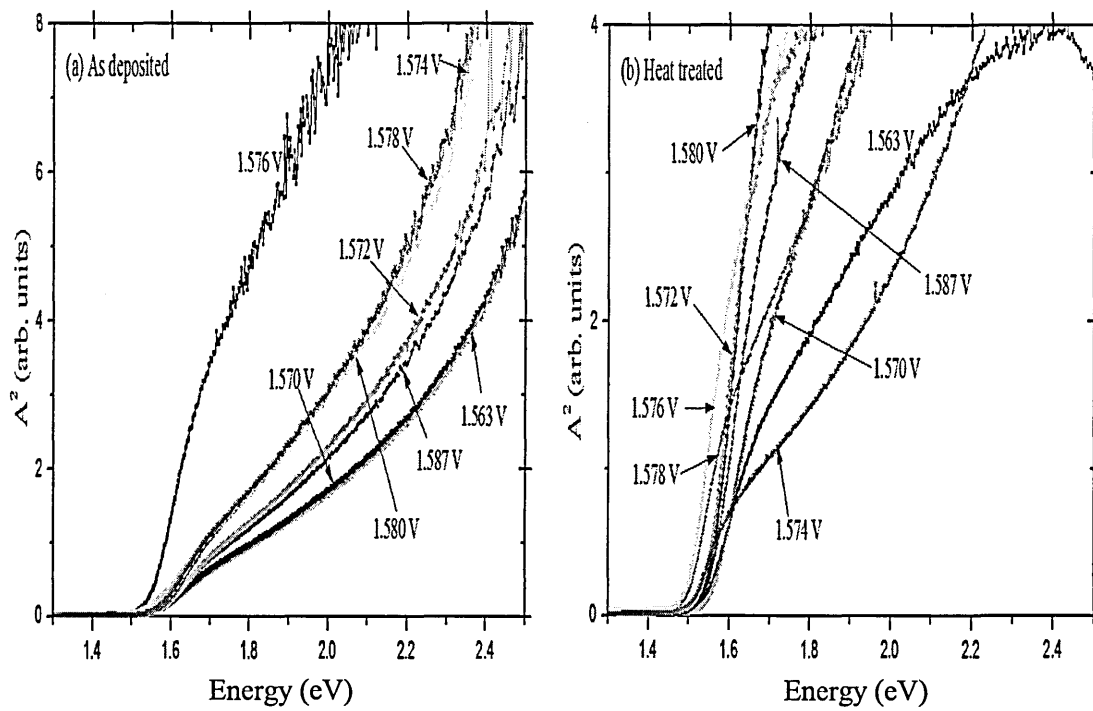


**Figure 6.7:** Optical absorption curves for (a) as deposited and (b) heat treated CdTe layers at different growth voltages.

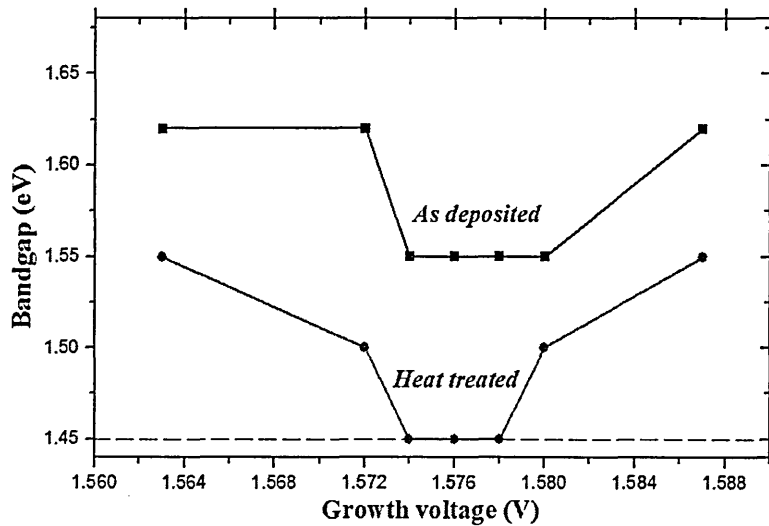


**Figure 6.8:** Bandgap energy for as deposited and heat treated CdTe layers at different growth voltages.

The optical transmission spectra for as deposited and heat treated CdTe layers are shown in Figure 6.9. Measurements were taken in the wavelength range 600 – 1000 nm on the deposited films. The transmission coefficient was found to be above 80% for all the as deposited films except the one grown at 1.576 V. After heat treatment at 450°C

for 15 minutes the transmission decreases and the absorption edge of all the CdTe films sharpened. Metin et al. [10] reported that, the sharper absorption edge indicates fewer defect and impurity energy levels in the film. From Figure 6.9 (b), it is observed that the band edge of the film deposited at 1.576 V gives the actual cut-off wavelength of CdTe  $\sim 852$  nm. Furthermore, growth voltages close to the stoichiometry produced sharper band edge close to the right bandgap. At higher and lower deposition potentials, a wide blue shift was observed for the band edge from the CdTe value.

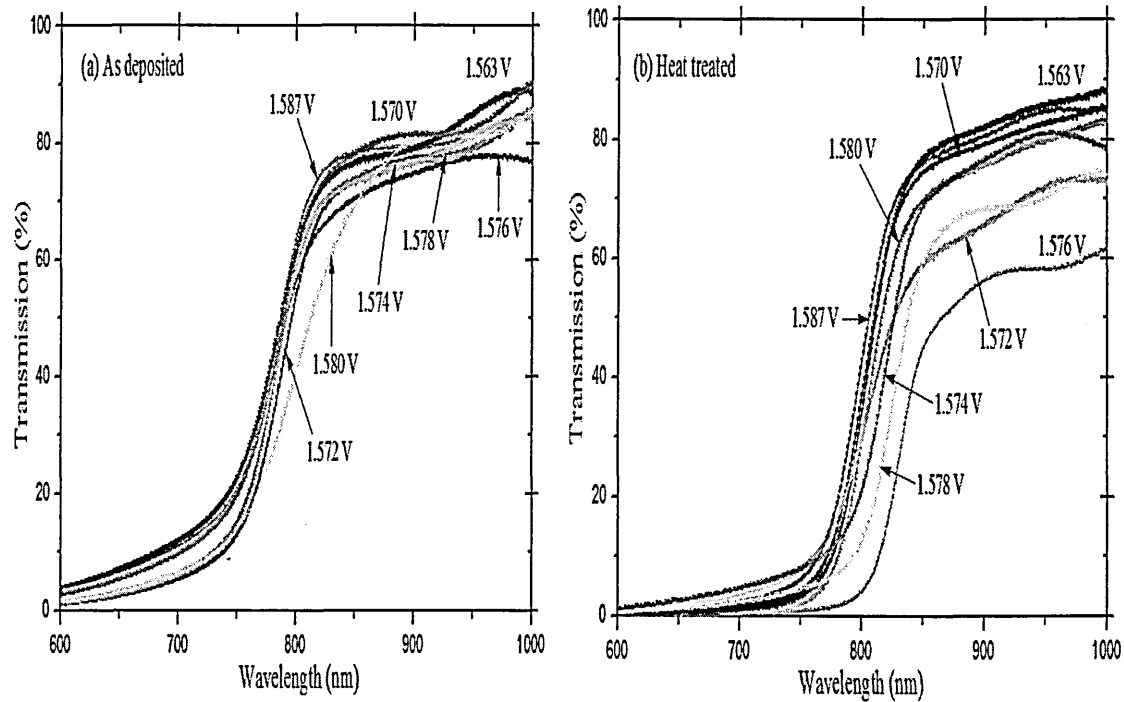


**Figure 6.9:** Transmission spectra for (a) as deposited and (b) heat treated CdTe layers at different growth voltages.

#### 6.4.4 Scanning Electron Microscopy

SEM studies were carried out to investigate the surface morphology, grain size and uniformity of CdTe layers. Three samples, grown at 1.563 V (Te-rich CdTe), 1.576 V (stoichiometric CdTe) and 1.587 V (Cd-rich CdTe), were selected for analysis. Figure 6.10 [a, b and c] and [d, e and f] shows the SEM images for the as deposited and heat treated CdTe thin films. As deposited layers show a lot of pin holes (gaps) between the grains. The proportion and size of pin holes depends on how far away from stoichiometry the film composition is. However, even at stoichiometry, pin holes are apparent. After heat treatment the grain size increased and no pin holes were apparent. The presence of these pin holes made the efficiency of solar cells poor by shorting the

back contact to the front TCO layer. These results confirmed that heat treatment enhances the recrystallisation and coalesce grains to fill the gaps and form a uniform thin layer of CdTe.

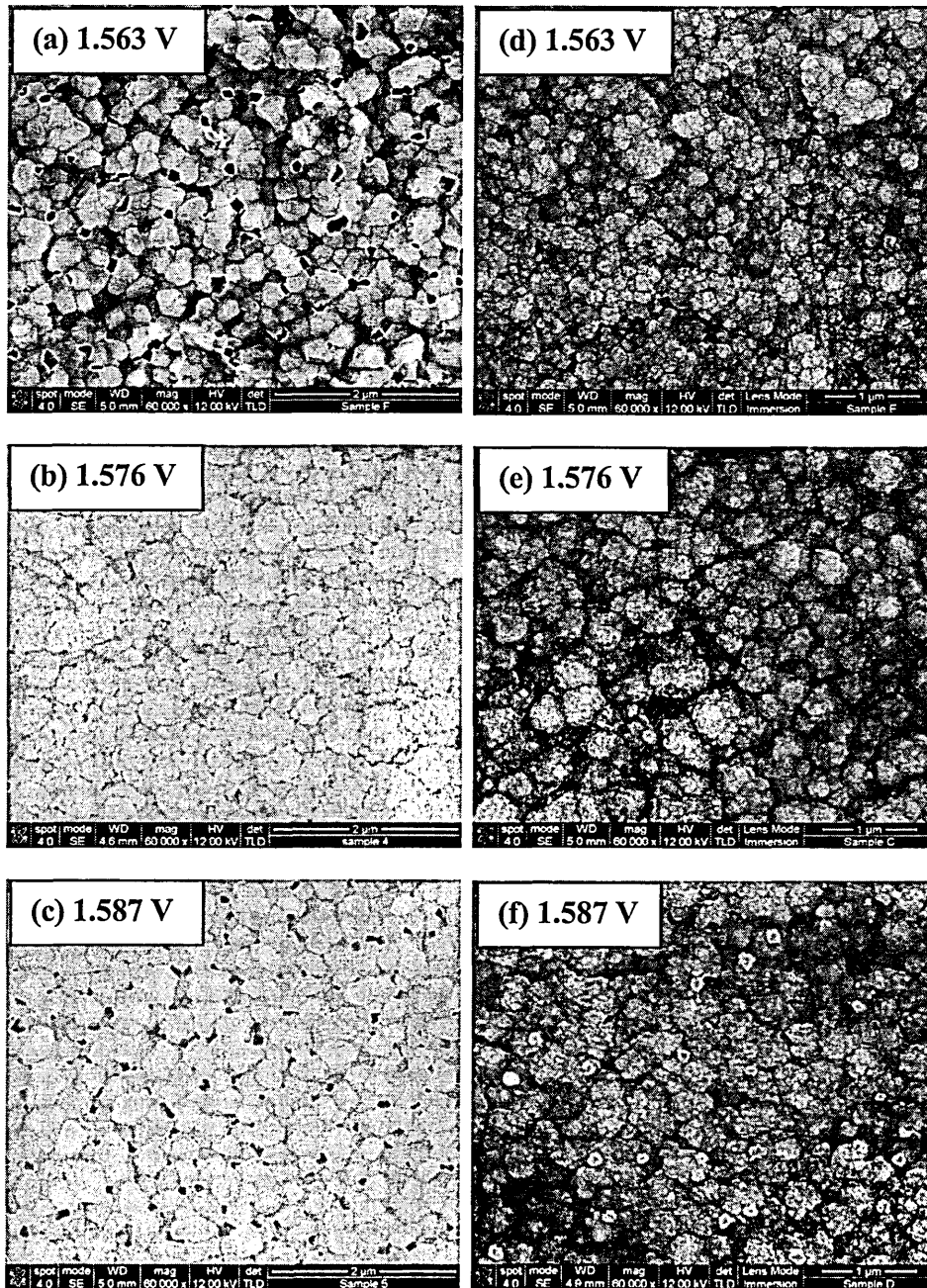


**Figure 6.10:** SEM images for [a, b and c] as deposited and [d, e and f] heat treated at 450°C for 15 minutes CdTe layers at different growth voltages.

### 6.4.5 Energy Dispersive X-ray

Energy dispersive x-ray (EDX) spectroscopy was carried out to investigate the qualitative elemental analysis of CdTe layers. Figure 6.11 and 6.12 show the EDX spectra of CdTe layers at three different growth voltages. In all the Figures the presence of both Cd and Te peaks were observed. Chlorine peak was found in all the heat treated samples. The percentage composition of Cd:Te calculated from the heat treated EDX spectra are 48.1:51.9, 52.3:47.7 and 50.4:49.6 at deposition potentials 1.563 V, 1.576 V and 1.587 V respectively.

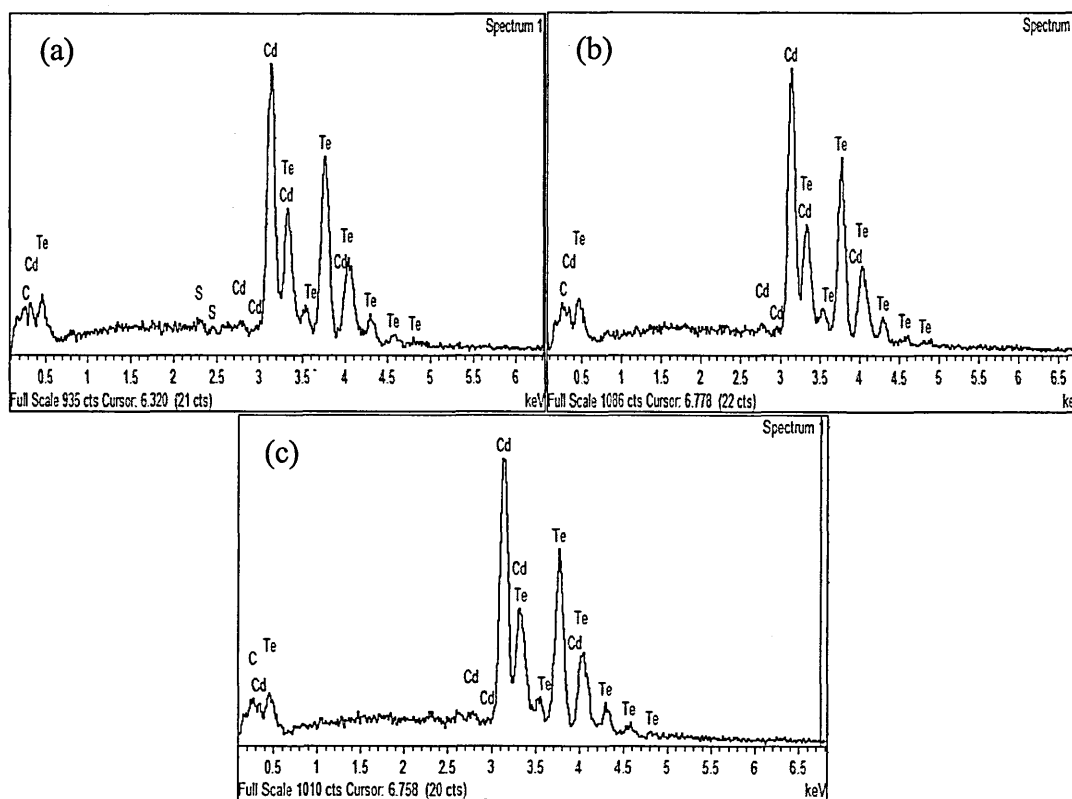


**Figure 6.11:** EDX spectra for as deposited CdTe layers at different growth voltages (a) 1.563 V, (b) 1.576 V and (c) 1.587 V.

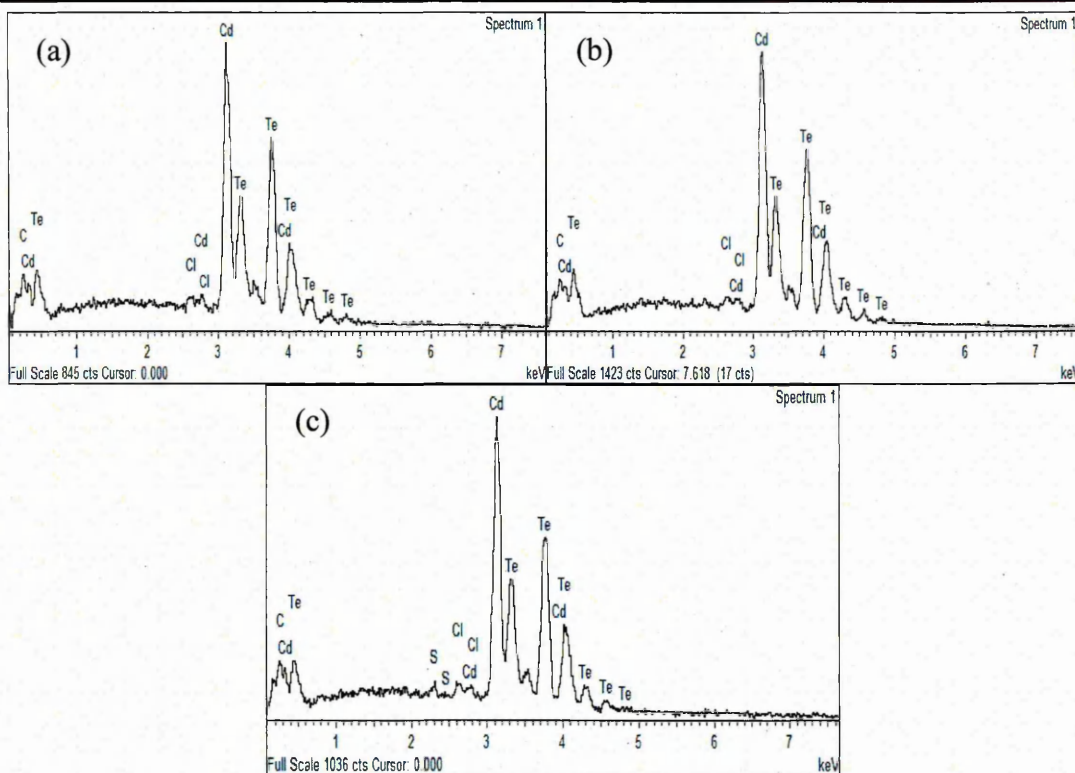


**Figure 6.12:** EDX spectra for heat treated CdTe layers at different growth voltages (a) 1.563 V, (b) 1.576 V and (c) 1.587 V.

#### 6.4.6 Atomic Force Microscopy

The 2D-AFM picture for heat treated CdTe layers grown at 1.576 V is shown in Figure 6.13. From the Figure it is observed the AFM image show a cluster of CdTe with large grains. The material clusters are in micro-scale range with an average size of  $\sim 1.2 \mu\text{m}$ . These grains seem to be well-connected to each other.

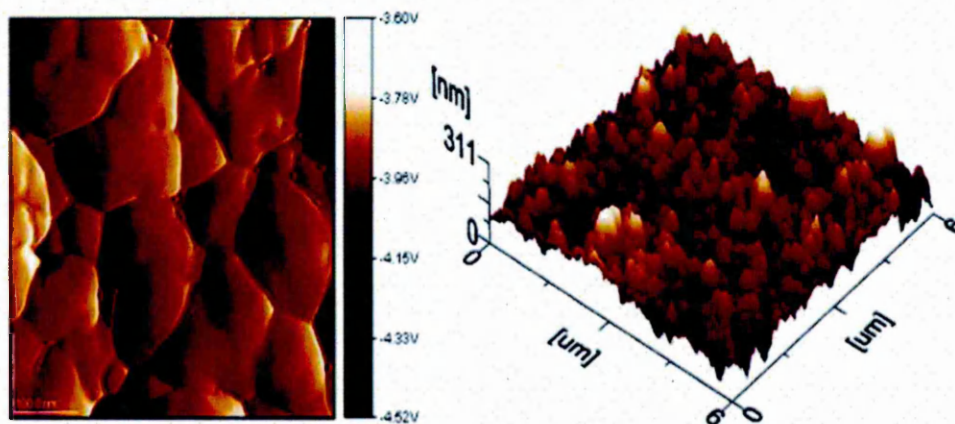


**Figure 6.13:** 2D-AFM images for heat treated CdTe layers grown at 1.576 V (courtesy: Inst. of Org. Catalysis & Electrochem., Kazakhstan).

Figure 6.14 shows the 3D-AFM image for heat treated CdTe layers grown at 1.576 V. As shown from the Figure, CdTe layers have highly-ordered and densely packed nano-rod arrays oriented perpendicular to the glass/FTO/CdS substrates. It is reported in chapter 4 CdS have nano-rod nature, this provides a good substrate for CdTe layers to grow well. The nano-rod nature of CdTe could reduce the recombination of photo-generated charge carriers and allows its passage with high mobility.

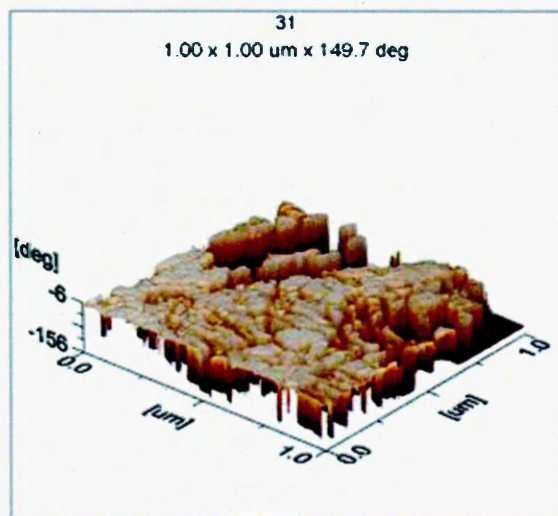


**Figure 6.14:** 3D-AFM image for heat treated CdTe layers grown at 1.576 V (courtesy: Inst. of Org. Catalysis & Electrochem., Kazakhstan).

#### 6.4.7 Raman Spectroscopy

The Raman technique gives information about the molecular structure of the material and hence is a useful technique for identifying phases. Figure 6.15 show the Raman spectra of a thick CdTe layer grown on InSb substrate, for comparison [11]. Figure 6.16 is the Raman spectrum for heat treated CdTe grown on glass/FTO/CdS at 1.576 V. As shown from the Figure, two peaks related to CdTe layers are identified at  $141\text{ cm}^{-1}$  and  $166\text{ cm}^{-1}$ , these correspond to the fundamental transverse (1TO) and longitudinal optical phonons (1LO) respectively. The other peak at  $123\text{ cm}^{-1}$  is known to be the A1 phonon of pure tellurium. All these peaks are similar to those reported by other researchers in the field [12-14].

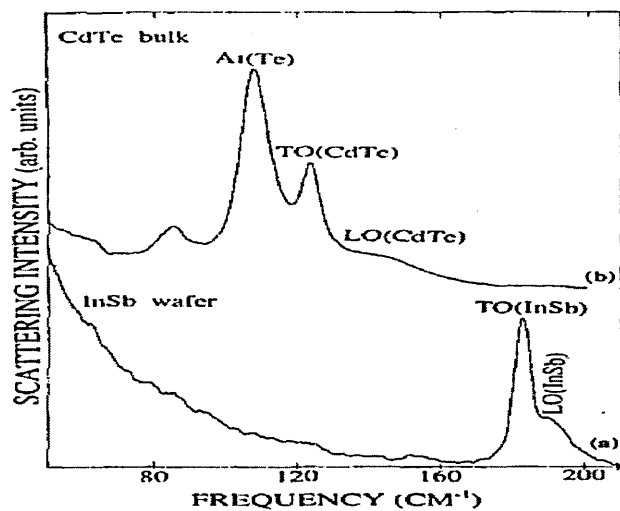


**Figure 6.15:** Raman spectrum of a thick CdTe layer grown on InSb substrate [11].

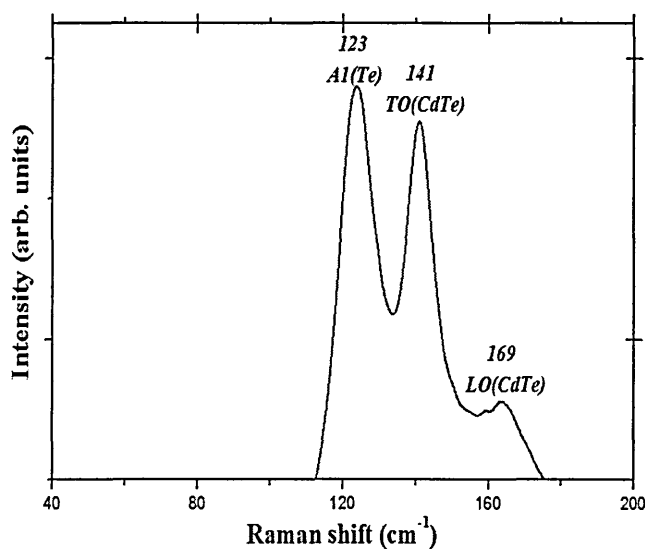


**Figure 6.16:** Raman spectrum for heat treated CdTe layer grown at 1.576 V (courtesy: Inst. of Mater. Research, Univ. of Leeds).

#### 6.4.8 X-ray photoelectron spectroscopy (XPS)

Both the qualitative and quantitative analysis of surface chemical states of the material are characterised by the XPS technique. The XPS spectrum of vacuum cleaved CdTe is shown in Figure 6.17. Figure 6.18 shows a typical survey spectrum for heat treated CdTe layers grown at 1.576 V. As discussed in chapter 4, C and O peaks are present in the XPS spectra obtained for electrodeposited CdTe, due to the surface contamination.

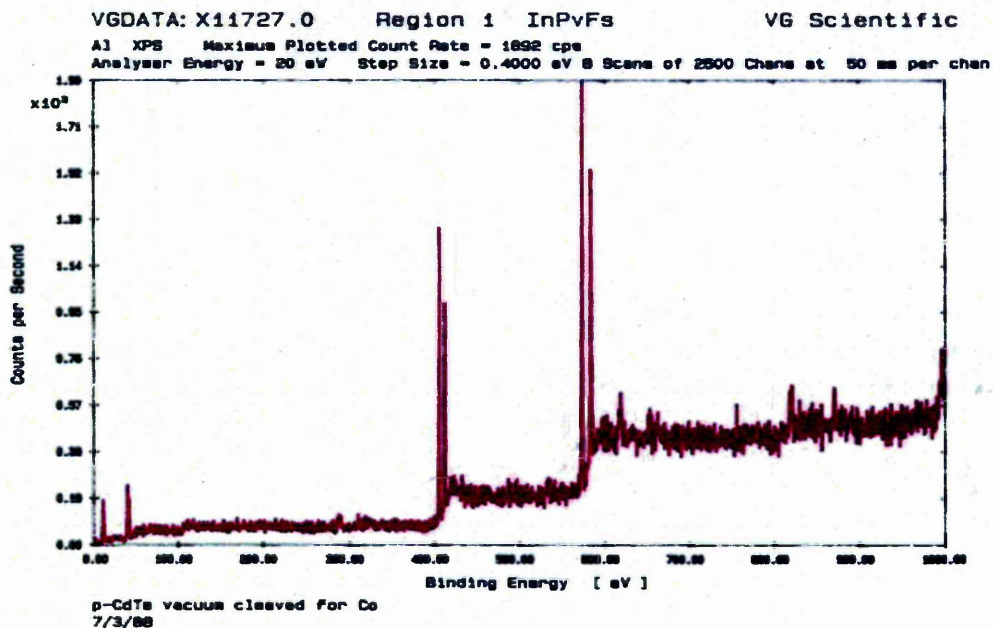


**Figure 6.17:** XPS spectrum of vacuum cleaved CdTe (courtesy: Prof. I. M. Dharmadasa).

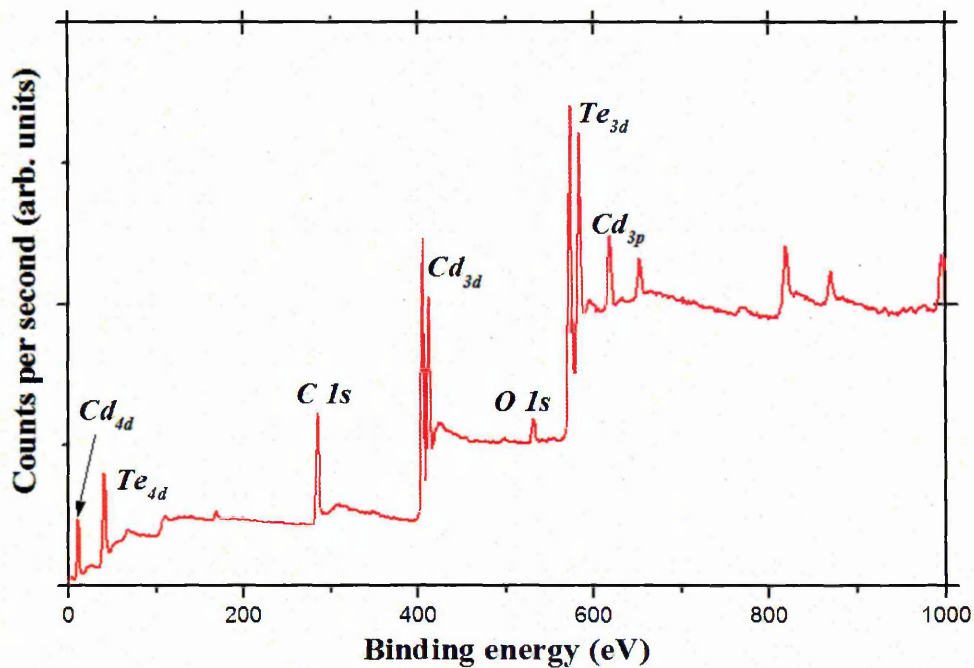


**Figure 6.18:** Typical XPS survey spectrum for heat treated CdTe layers grown at 1.576 V (courtesy: Inst. of Mater. Research, Univ. of Leeds).

From Figure 6.18, two distinct Te  $3d_{5/2}$  peaks (i.e.  $Te^{2-}$  and  $Te^{4+}$ ) were observed and presented clearly in Figure 6.19. The binding energies associated with  $Te^{2-}$  and  $Te^{4+}$  appeared at  $\sim 576$  and  $582.5$  eV respectively. The atomic ratio for Cd:Te obtained from the XPS spectra is 52.6:47.4. It was reported by [6, 15-17] that  $Te^{2-}$  and  $Te^{4+}$  states form are involved in the action of Te-Cd bonds and Te-O bonds respectively.

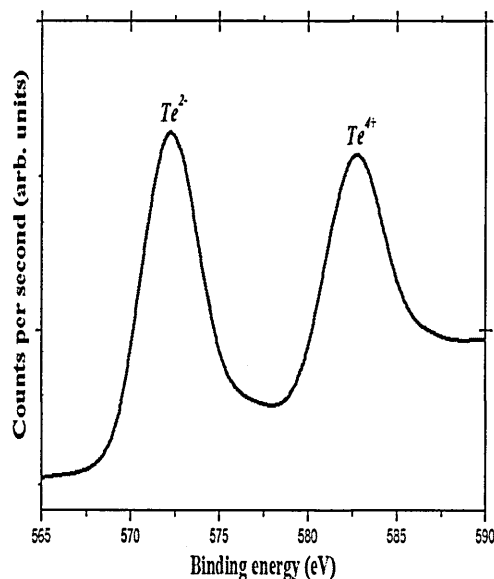


**Figure 6.19:** XPS spectrum for heat treated CdTe layers close-up survey for the Te 3d (courtesy: Inst. of Mater. Research, Univ. of Leeds).

## 6.5 Device characterisation

The CdTe layers grown on glass/FTO/CdS substrates were treated with  $CdCl_2$ /heat treated at  $450^\circ C$  for 15 minutes in air. Details of the processing procedures have been presented in sections 3.7 and 3.8 of chapter 3. Analysis of I-V characteristics has also described in section 2.3.1 of chapter 2

### 6.5.1 Current-voltage (I-V) characteristics

Figure 6.20 shows the linear I-V curves of glass/FTO/CdS/CdTe/Au contacts under AM 1.5 illuminations, for CdTe layers grown at different growth voltages. Table 6.4 shows the results of  $V_{oc}$ ,  $J_{sc}$ , FF and  $\eta$  of fully fabricated CdTe solar cells.

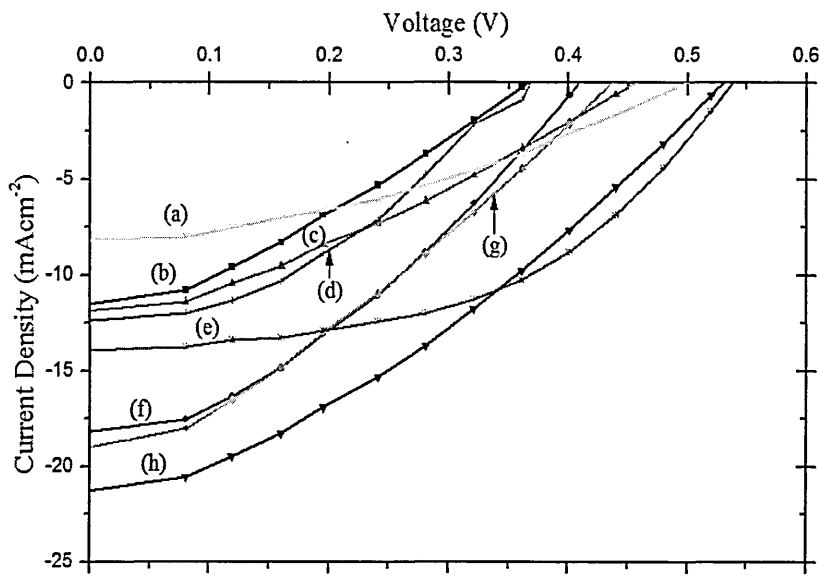


**Figure 6.20:** Linear I-V curve of glass/FTO/CdS/CdTe/Au contacts under AM 1.5 illumination condition for CdTe layers grown at; (a) 1.563 V, (b) 1.587 V, (c) 1.572 V, (d) 1.570 V, (e) 1.576 V, (f) 1.580 V, (g) 1.574 V and (h) 1.578 V.

**Table 6.4:** Cell parameters under illumination of CdTe thin film solar cells at different growth voltages.

Growth voltage (V)	Cell parameters			
	$V_{oc}$ (mV)	$J_{sc}$ (mAcm <sup>-2</sup> )	FF (%)	$\eta$ (%)
1.563	500	8	0.29	1.16
1.570	370	13	0.30	1.44
1.572	450	12	0.28	1.51
1.574	430	19	0.27	2.21
1.576	540	14	0.49	3.70
1.578	530	21	0.27	3.01
1.580	410	18	0.30	2.21
1.587	360	12	0.28	1.20

The maximum efficiency of 3.70% with  $V_{oc} \sim 540$  mV and FF  $\sim 0.49$  were achieved for stoichiometric devices with CdTe ( $V_g \sim 1.576$  V). The efficiency decreases as the material deviates from stoichiometry. This agrees with the PEC and XRD results discussed in section 6.4.1 and 6.4.2 respectively. At lower and higher growth voltages the CdTe compound formed is rich in Te and Cd respectively. The low FF of most of the devices at higher and lower growth voltages may be due to high resistance created

by small grains, large recombination process present or detrimental leakage paths present within the devices. Figure 6.21 shows the individual graphs of  $V_{oc}$ ,  $J_{sc}$ , FF and  $\eta$  of glass/FTO/CdS/CdTe/Au contacts.

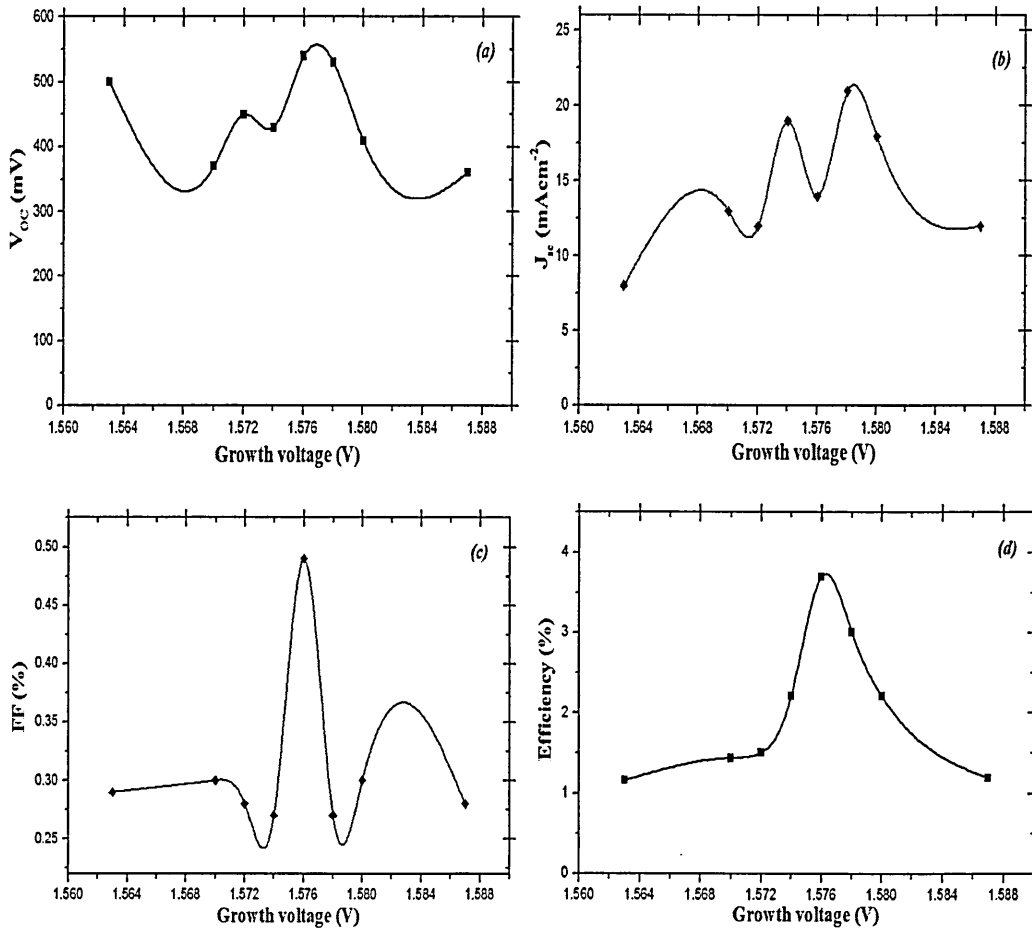


**Figure 6.21:** Cell parameters as function of growth voltages of CdTe layers (a)  $V_{oc}$  against Growth voltage, (b)  $J_{sc}$  against Growth voltage, (c) FF against Growth voltage and (d) Efficiency against Growth voltage.

## 6.6 Structure performance relationship

Table 6.5 shows the summary of the relationship between material properties and the device performance. The stoichiometric CdTe is grown at  $V_g = 1.576$  V, and hence the material contains larger crystallites, correct bandgap for CdTe (1.45 eV) and produce best efficiency values. At lower growth voltages material becomes Te-rich and at higher growth voltages material becomes Cd-rich and hence the crystallinity deteriorates due to

presence of two phases in the layer. Therefore the bandgaps increase due to quantum effects and the device efficiency reduces.

**Table 6.5:** Summary of the material structure and device performance relationship.

Growth voltage (V)	XRD parameters		Bandgap (eV)	Cell efficiency, $\eta$ (%)
	FWHM	Grain size, D (nm)		
1.563	0.134	11.4	1.55	1.16
1.576	0.100	15.8	1.45	3.70
1.587	0.112	13.7	1.55	1.20

## 6.7 Summary

CdTe has been deposited on glass/FTO/CdS substrates using a low-cost aqueous electrodeposition method using two-electrode system. PEC measurements confirmed that at lower and higher cathodic voltages from the stoichiometric voltage, the polarities of the PEC signal were p- and n- type indicating Te and Cd richness respectively. At a growth voltage of 1.576 V the PEC signal shows intrinsic implying the film has stoichiometric composition.

The XRD results for both as deposited and heat treated CdTe layers have cubic structure with the main diffraction peak at  $2\theta = 23.642^\circ$  which corresponds to preferred orientation along (111) plane of cubic phase. At voltages less than 1.576 V, the deposition rate of Te is greater than that of Cd, and hence the layers are rich in Te. When the growth voltage is higher than 1.576 V, the deposition rate of Cd is greater than that of Te, and therefore the layers are rich in Cd. When the CdTe composition is stoichiometric, only the (111) peak is dominant in the XRD diffractogram indicating a high degree of texture. Away from stoichiometry, crystallinity is poor due to presence of two phases.

The optical absorption measurement shows the value of bandgap,  $E_g$  for as deposited samples away from stoichiometry ranges from 1.62 eV to 1.55 eV. Similarly, after heat treatment, the bandgap values decreased and the absorption edge of the curve sharpened, giving a bandgap of 1.45 eV for the stoichiometric film. The optical transmission spectrum for as deposited samples was found to be above 80% except for the one grown at 1.576 V. After heat treatment the transmission decreases and the absorption edge of all the CdTe films sharpened.

SEM studies showed that as deposited layers had pin holes between the crystallites. These pin holes seem to be more common in the samples grown at lower deposition voltages. As the voltage increases, the pin holes diminish up to the stoichiometry voltage and then start appearing again. After heat treatment the grain size increase and the pin holes are reduced. The 3D-AFM image shows electrodeposited CdTe has highly-ordered and densely packed nano-rod arrays oriented perpendicular to the glass/FTO/CdS substrates. The nano-rod nature of CdTe could reduce the recombination of photo-generated charge carriers and allow their passage with high mobility. The 2D-AFM picture shows clusters of CdTe with large grains. The material clusters are in micro-scale range with an average size of  $\sim 1.2 \mu\text{m}$ .

Raman measurements show two peaks related to CdTe layers identified at  $141\text{ cm}^{-1}$  and  $166\text{ cm}^{-1}$  which correspond to the fundamental transverse and longitudinal optical phonons (1TO) and (1LO) respectively. The other peak at  $123\text{ cm}^{-1}$  is known to be the A1 phonon of pure tellurium. This result shows that the CdTe films are rich in Te by indicating a strong Te- peak. Raman spectroscopy has been shown to provide a good finger print for identifying CdTe layers. The XPS work reveals that electrodeposited CdTe has a similar spectrum to that of cleaved CdTe except for the additional presence of C and O peaks, as expected. The composition estimated for these layers by XPS is 53:47 (Cd:Te).

The linear I-V curve of glass/FTO/CdS/CdTe/Au contacts under AM 1.5 illumination at different growth voltages give the maximum efficiency of 3.70% with  $V_{oc} \sim 540\text{ mV}$  and FF  $\sim 0.49$  from the stoichiometric CdTe grown at 1.576 V. The efficiency decreases as it deviates from the stoichiometry. The low FF of most of the devices at higher and lower growth voltages may be due to high resistance created by small grains, large recombination process present or detrimental leakage paths present within the devices. From the results above, the optimum CdTe voltage has been determined as 1.576 V. Therefore, the objective has been achieved.

## References

1. A. Goetzberger, C. Hebling and H. W. Schock, *Mat. Sci. Eng.* 40, 1 (2003).
2. W. Jaegermann, A. Klein and T. Mayer, *Adv. Mater.* 21, 4196 (2009).
3. M. Hädrich, C. Kraft, C. Löffler, H. Metzner, U. Reislöhner and W. Witthuhn, *Thin Solid Films* 517, 2285 (2009).
4. E. Colombo, A. Bosio, S. Calusi, L. Giuntini, A. Lo Guidic, C. Manfredotti, M. Massi, P. Olivero, A. Romeo, N. Romeo and E. Vittone, *Nucl. Instrum. Math. B* 267, 2181 (2009).
5. (<http://www.firstsolar.com/>) retrieved July, 26<sup>th</sup> 2011.
6. I. M. Dharmadasa, J. M. Thornton and R. H. Williams, *Appl. Phys. Lett.* 54(2), 137 (1989).
7. S-Y Yang, J-C Chou and H-Y Ueng, *Thin Solid Films* 518, 4197 (2010).
8. S. Oktik, *Prog. Crystal Growth Charact.* 17, 171 (1989).
9. S-Y Yang, J-C Chou and H-Y Ueng, *Thin Solid Films* (2009), doi:10.1016/j.tsf.2009.12.077.
10. H. Metin and R. Esen, *Semicond. Sci. Technol.* 18, 647 (2003).
11. H-K Na and P-K Shon, *Solid State Communication* 85(7), 609 (1993).
12. J. Rouusset, E. Rzepka, D. Lincot, *J. Phys. Chem. B* 113, 4333 (2009).
13. Y. Jung, S. Chun, D. Kim and J. Kim, *J. Crystal Growth* 326, 69 (2011).
14. R. Ochoa-Landin, O. Vigil-Galan, Y. V. Vorobiev and R. Ramirez-Bon, *Sol. Energy Mat. Sol. Cells* 83, 134 (2009).
15. V. V. Ison, A. Ranga Rao and V. Dutta, *Solid State Sciences* 11, 2003 (2009).
16. K. Vamsi Krishna and V. Dutta, *Sol. Energy Mat. Sol. Cells* 80, 247 (2003).
17. J. Fritsche, D. Kraft, A. Thißen, T. Mayer, A. Klein and W. Jaegermann, *Thin Solid Films* 403 – 404, 252 (2002).

## Chapter 7: Effect of growth time on CdTe layer thickness

### 7.1 Motivation and objectives

It is known that thickness play an important role in the preparation of any material layer. For an efficient solar cell, adequate thickness is required to absorb all relevant photons, separate and collect photogenerated charge carriers by producing a healthy depletion region approximately equal to the thickness of the device. Thick layers unnecessarily use expensive semiconducting materials and introduce a high resistance to the device performance. A thinner layer allows the electrons tunnel through the junction, and leads to the increased recombination process. The aim of this chapter is to investigate the effect of CdTe layer thickness on devices performance.

### 7.2 Introduction

CdTe thin films are employed as an absorber layer with CdS as a window layer for CdS/CdTe hetero-structured solar cells. CdTe has a high absorption coefficient of  $10^4$  to  $10^5 \text{ cm}^{-1}$ . Film  $\sim 1\text{-}2 \mu\text{m}$  thick absorbs the entire incident light above the CdTe bandgap of 1.45 eV [1-3]. As discussed in chapter 6, it is possible to prepare films of different composition by controlling the growth voltage (i.e. n-, i- or p-type).

Dharmadasa et al. [4] reported that to produce high quality Schottky barriers at metal/n-CdTe interfaces, the CdTe surface must be rich in cadmium. Similarly, Gamboa et al. [5] reported that the stoichiometry of the CdTe film is improved by controlling the tellurium. In chapter 5 it was shown that n-type CdTe is Cd-rich. Therefore, all the work reported in this chapter is based on growth voltage regimes that produce n-i-p CdTe layers.

Six glass/FTO/ED-CdS substrates were used and the CdTe layers were grown for 3, 4, 5, 6, 7 and 8 hrs. This set of samples is called set 1. Another four samples (set 2) were grown for 3.5, 4.5, 5 and 5.5 hrs. Growth voltages of 1.578 V, 1.576 V and 1.574 V were chosen that correspond to the optimum growth voltages for n-type, i-type and p-type CdTe layers respectively (see chapter 6, especially section 6.4.1). The growth time was equally divided between the three voltages. Deposition of CdTe films have been discussed in section 3.4 of chapter 3.

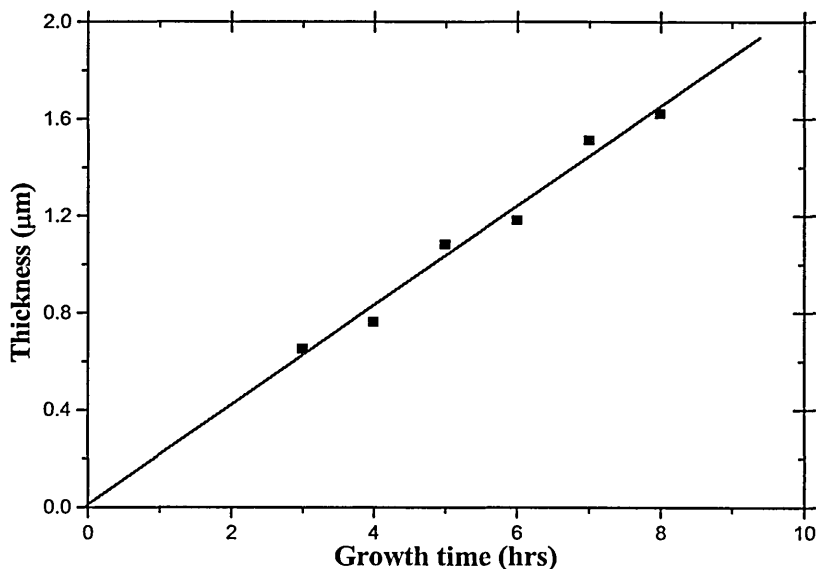
### 7.3 Thickness measurement

Table 7.1 shows the predicted thickness of CdTe layers grown for different times using Faraday's equation (discussed in section 2.1.6.2 of chapter 2). Similarly, Figure 7.1 shows the graph of CdTe thickness against growth periods.

**Table 7.1:** Predicted CdTe layer thickness against growth time.

Growth period (hrs)	Thickness $\pm 0.01$ ( $\mu\text{m}$ )
3	0.65
4	0.76
5	1.08
6	1.18
7	1.51
8	1.62

From Table 7.1, it is observed that as the growth period increases the thickness of the CdTe layer increases as expected. This is due to the deposition of more layers. As reported from literature [1-3], a CdTe thickness of  $\sim 1\text{-}2$   $\mu\text{m}$  is enough to absorb all incident light with energy above 1.45 eV.



**Figure 7.1:** (n-i-p) CdTe layer thickness as function of growth time.

## 7.4 Characterisation of CdTe thickness

### 7.4.1 X-ray diffraction

Figure 7.2 shows the X-ray diffraction patterns for as deposited and heat treated CdTe layers deposited at different growth times. The main diffraction peak at  $2\theta = 23.642^\circ$  corresponds to preferred orientation along (111) plane of cubic phase. These peaks were assigned according to the JCPDS (01-075-2086) data on cubic CdTe. From this Figure, it is observed that the main features of the diffraction patterns are the same but only the peak intensity is varied. As the growth periods increases, the diffracted intensity of (111) peak increased. A similar observation is reported by El-Kadry et al. [6]. Similarly, Basio et al. [7] reported that, for material characterisation the film thickness should be thick and for device fabrication thin layer is better.

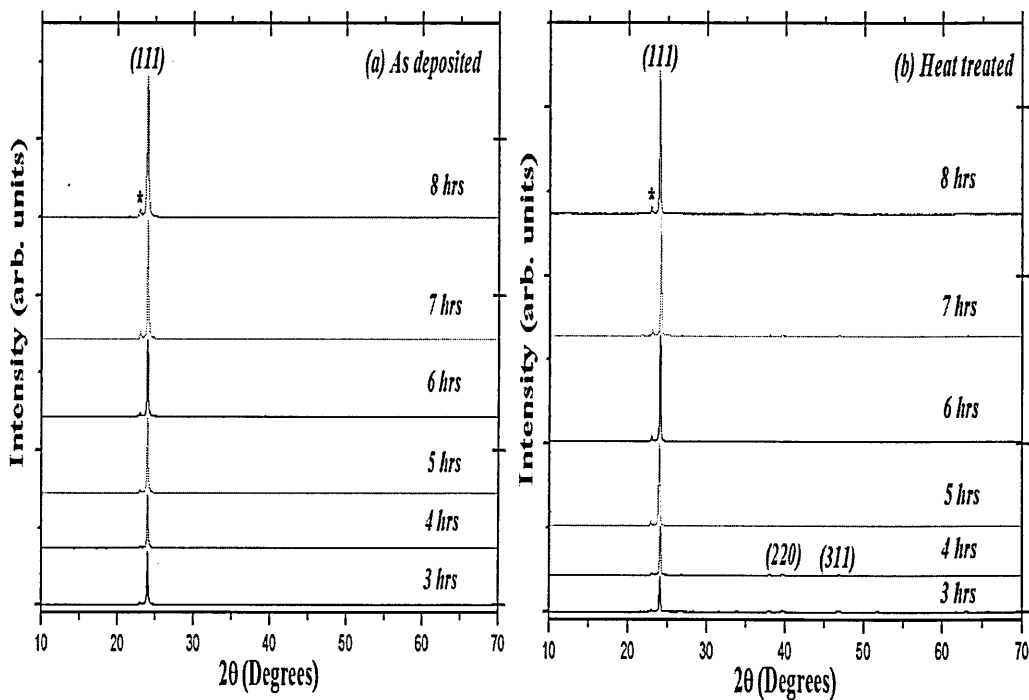


**Figure 7.2:** X-ray diffraction pattern of (n-i-p) CdTe layers at different growth time (a) as deposited and (b) heat treated (\* indicates Te peak).

After heat treatment in air at  $450^\circ\text{C}$  for 15 minutes, the intensity of most peaks decreases due to loss of material through sublimation. Two additional peaks (220) and (311) were observed at lower growth time periods which indicates polycrystalline nature of the film as shown in Figure 7.2 (b). The heat treatment enhances the recrystallisation of CdTe films reducing any stress within the films due to sublimation

of excess elements from the layer. The values of XRD intensity, FWHM and D at different growth time are presented in Table 7.2, estimated using equation 2.18 presented in section 2.2.1 of chapter 2.

**Table 7.2:** XRD intensity, FWHM and grain size of CdTe at different growth times for as deposited and heat treated layers.

Growth period (hrs)	XRD Intensity (arb. units)		FWHM		Grain size, D (nm)	
	AD	HT	AD	HT	AD	HT
3	7178	4188	0.234	0.201	6.3	7.4
4	6921	5770	0.267	0.217	5.5	6.8
5	9784	9853	0.251	0.217	5.9	6.8
6	9852	12478	0.234	0.217	6.3	6.8
7	15485	14308	0.234	0.184	6.3	8.1
8	18386	17068	0.318	0.184	4.7	8.1

N/B: AD = as deposited and HT = heat treated

From the Table, it is observed that the crystallite size for heat treated sample increases and the FWHM decreases; this is due to the coalescence of small crystals and the formation of larger grains. Furthermore, the FWHM was found to decrease as the growth time increased. Such an effect may be due to a decrease in the concentration of lattice imperfections as a result of a decrease in the internal micro strain within the films and/or an increase in the crystallite size. Figures 7.3, 7.4 and 7.5 show the XRD intensity, FWHM and grain size at different growth times respectively.

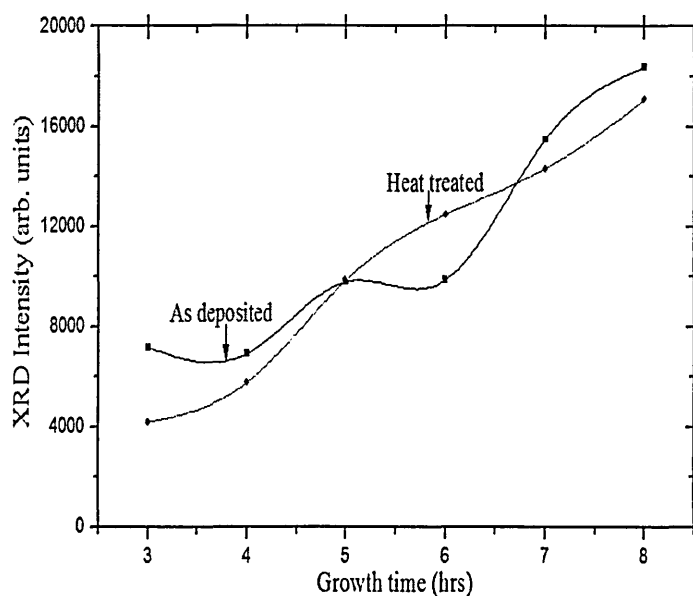


**Figure 7.3:** XRD intensity of (111) peak observed for (n-i-p) CdTe layers grown at different growth times.

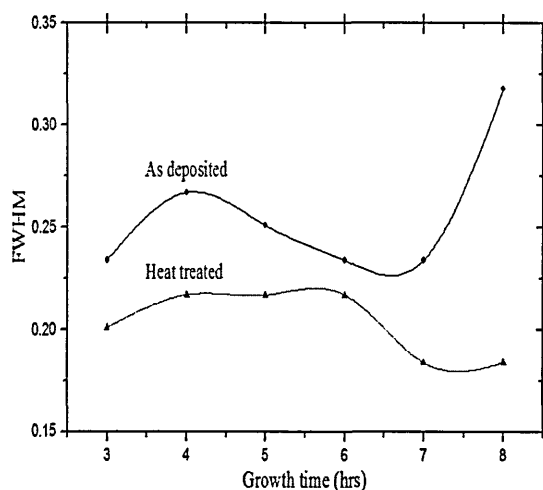


**Figure 7.4:** FWHM of (111) peak observed for (n-i-p) CdTe layers grown at different growth times.

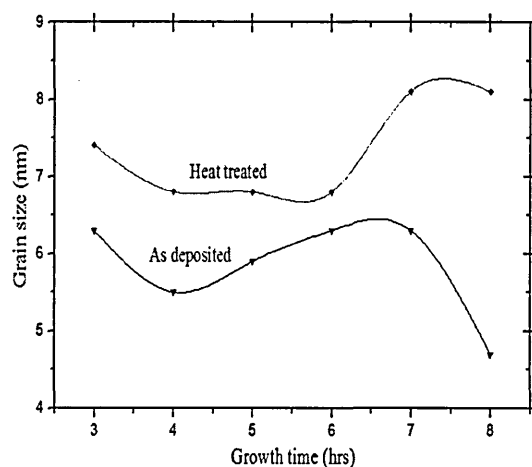


**Figure 7.5:** Grain sizes estimated from (111) peak observed for (n-i-p) CdTe layers grown at different growth times.

## 7.4.2 Optical absorption

Optical absorption measurements were carried out in order to determine the bandgap of the films. Figure 7.6 shows the graphs of optical absorption for as deposited and heat treated CdTe samples. Using equation 2.21 on section 2.2.3 in chapter 2, the bandgap energy values,  $E_g$  was determined by plotting the square of absorption ( $A^2$ ) against photon energy ( $h\nu$ ) for both as deposited and heat treated materials. The value of  $E_g$  for as deposited samples varies between 1.53 eV to 1.59 eV. Similarly, after heat treatment in air at 450°C for 15 minutes the bandgap values decreased and the absorption edge of the curve sharpened;  $E_g$  of 1.45 eV, which is closer to the CdTe bulk value, was obtained for all the samples but the absorption edge of individual samples varied. The reason for the sharpening might be due to a change in the stoichiometry or reduction of

intrinsic defect population of the treated samples. Table 7.3 gives the bandgap values for as deposited and heat treated CdTe layers at different growth times, and Figure 7.7 shows the bandgap energy at different growth times.

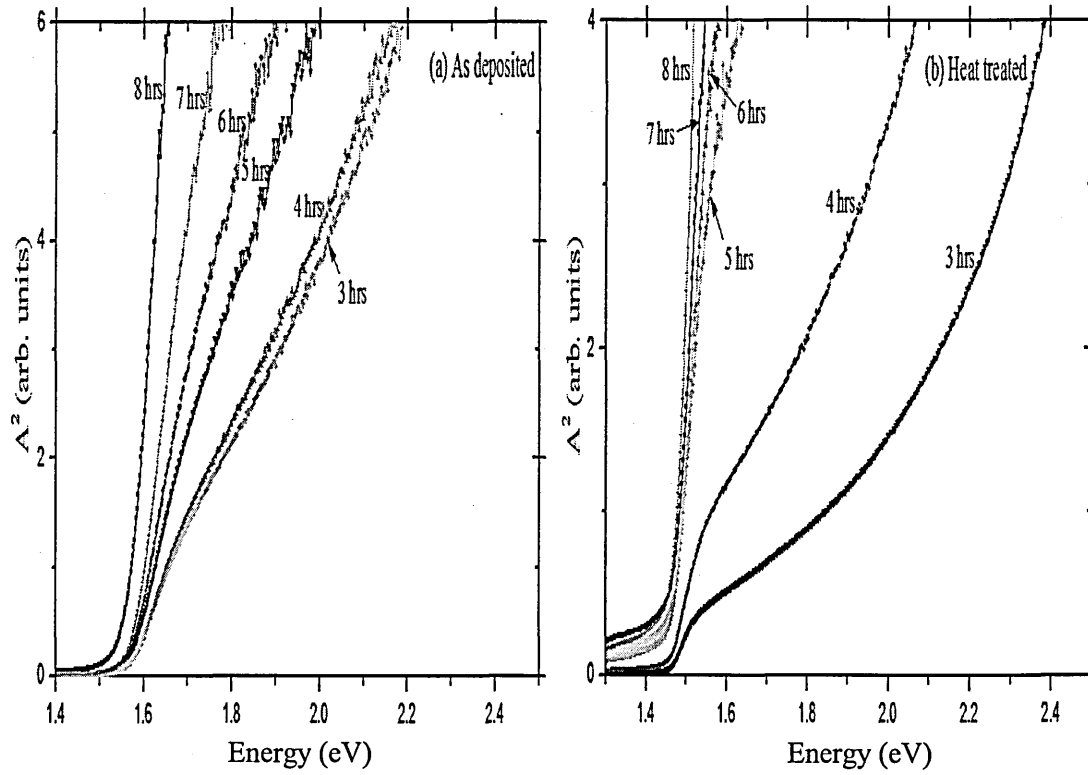


**Figure 7.6:** Optical absorption curves for (a) as deposited and (b) heat treated (n-i-p) CdTe layers at different growth times.

**Table 7.3:** Bandgap energy of (n-i-p) CdTe layers at different growth times.

Growth time (hrs)	Bandgap (eV)	
	AD	HT
3	1.55	1.45
4	1.55	1.45
5	1.57	1.45
6	1.59	1.45
7	1.56	1.45
8	1.53	1.45

As shown from the Table, the bandgap energies of as deposited samples fluctuate with the minimum 1.53 eV at growth time 8 hrs. After heat treatment the bandgap of all the samples gives 1.45 eV which is close to the bulk CdTe value. It is observed from Figure 7.6 (b) that the bandgap edge sharpened after heat treatment in the samples grown for 5 hrs or longer and became less sharp in the thinner films (growth time of 3 or 4 hrs).

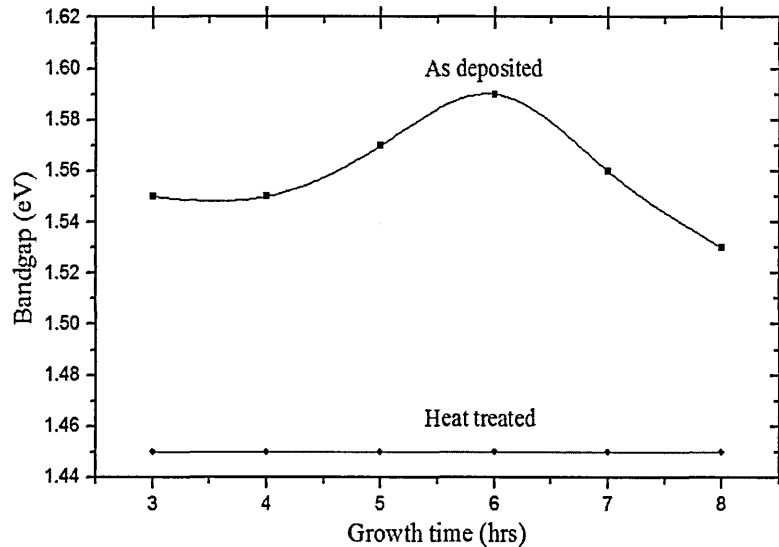


**Figure 7.7:** Bandgap energy for as deposited and heat treated CdTe layers at different growth times.

The optical transmission spectra for as deposited and heat treated CdTe layers are shown in Figure 7.8. Measurements were taken in the wavelength range 600 – 1000 nm on the deposited films. The transmission coefficient of as deposited samples grown below 7 hrs was found to be above 80%. After heat treatment the transmission decreases and the absorption edge of all the CdTe films sharpened. It has been reported that a sharper absorption edge indicates fewer defect and impurity energy levels in the film [8]. From Figure 7.8 (b), it is observed that the band edge of the film deposited for 5 and 6 hrs is ~852 nm (the cut-off wavelength of bulk CdTe) with a transmission coefficient around 50%. Films deposited for 3 and 4 hrs show a wide blue shift from the band edge of the CdTe value. As the thickness increases (growth time above 6 hrs) the band edge shifted to the red region.

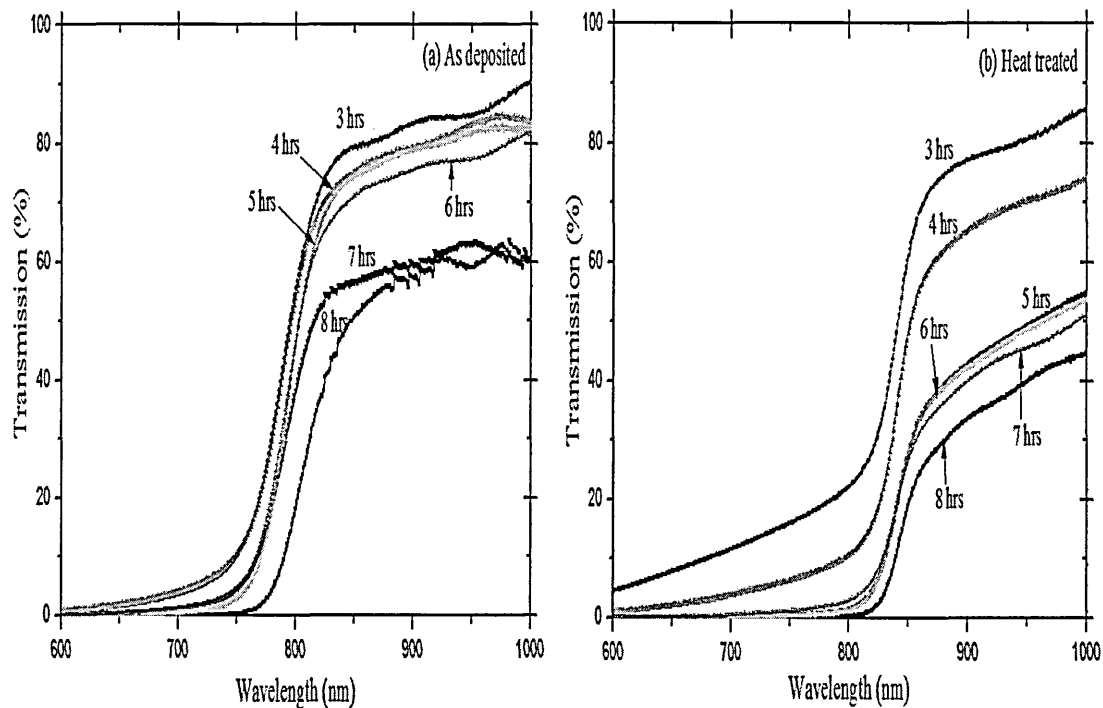


**Figure 7.8:** Transmission spectra for as deposited and heat treated (n-i-p) CdTe layers at different growth times (a) and (b) respectively.

### 7.4.3 Scanning Electron Microscopy

SEM studies were carried out to investigate the surface morphology, grain size and uniformity of CdTe layers. Three samples grown at 3, 5 and 8 hrs were selected for the measurement. Figure 7.9 [a, b and c] and [d, e and f] shows the SEM images for as deposited and heat treated CdTe thin films respectively. It is observed that all the as deposited samples show a lot of pin holes (gaps) between the grains. The sample grown for 3 and 8 hrs contain a higher proportion of pin holes than that grown for 5 hrs. For 5 hrs growth period, the number of gaps (holes) reduces indicating a suitable uniform thickness. After heat treatment the pin holes closed. These results confirmed that heat treatment enhances the recrystallisation and coalesce grains to fill the gaps and form a uniform thin layer of CdTe.

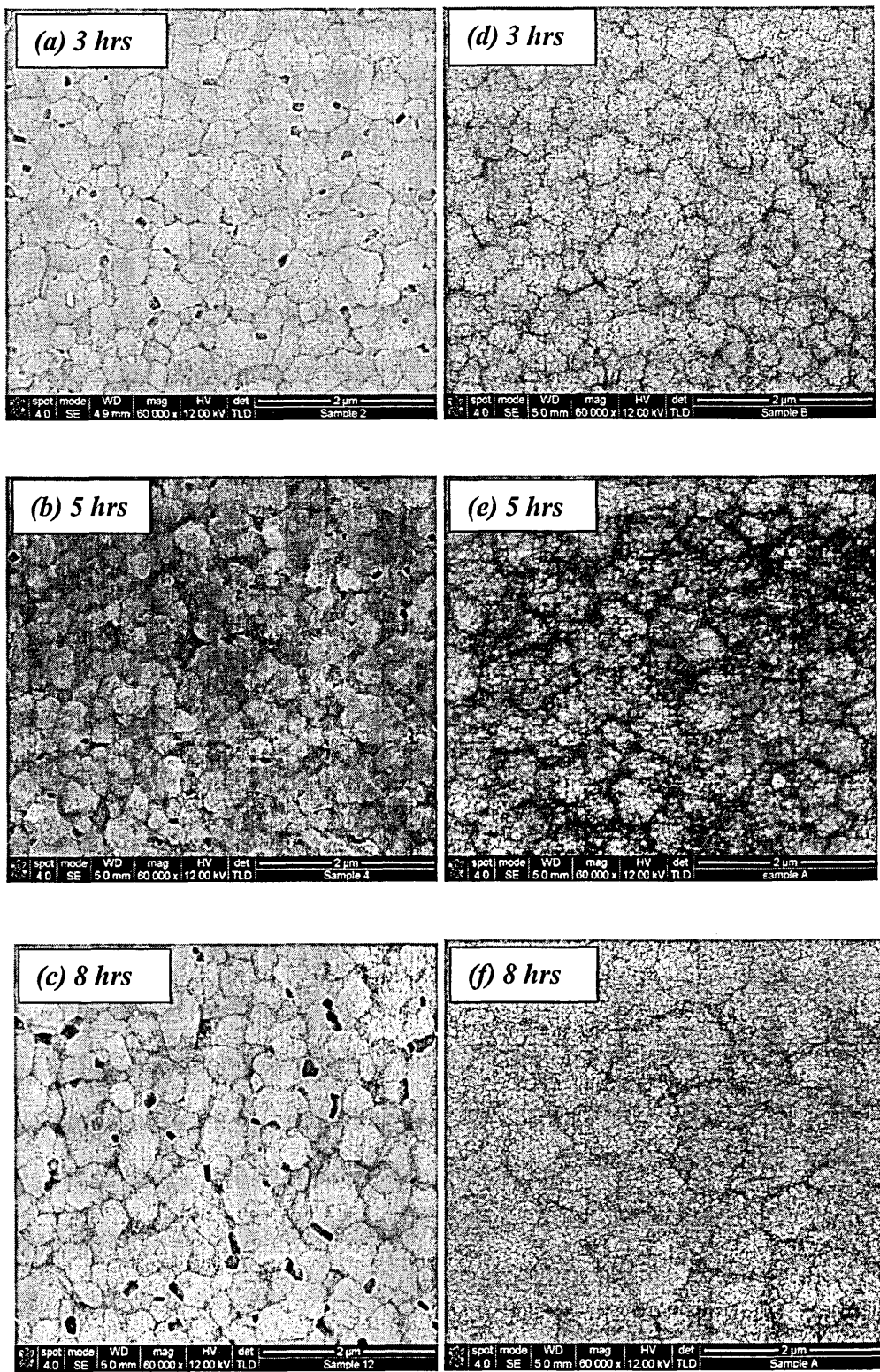


**Figure 7.9:** SEM images for [a, b, and c] as deposited and [d, e and f] heat treated (n-i-p) CdTe layers at different growth times.

### 7.4.4 Energy Dispersive X-ray

Energy dispersive x-ray (EDX) spectroscopy was used to determine the elemental analysis of the CdTe layers qualitatively. The EDX spectra of CdTe layers for three different growth times are shown in Figures 7.10, 7.11 and 7.12. In all these Figures the presence of both Cd and Te peaks were observed. After heat treatment, oxygen peak appears at lower growth time at 3 and 5 hrs. The percentage composition of Cd:Te estimated from the spectra is 49:51 for as deposited and 51:49 for heat treated CdTe layers.

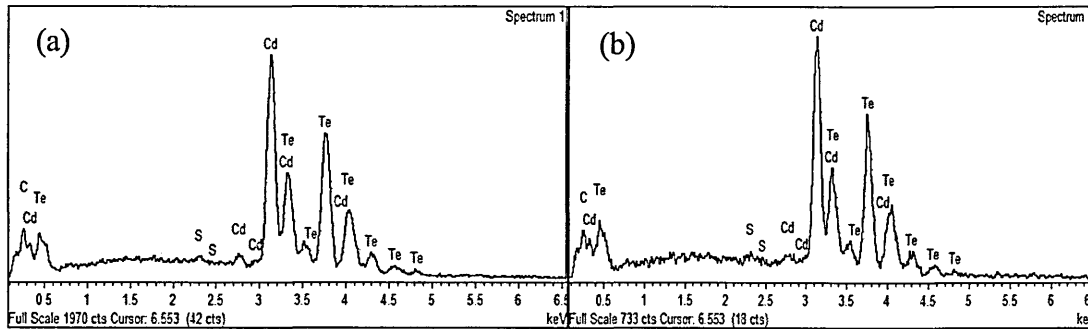


**Figure 7.10:** EDX spectra for (a) as deposited and (b) heat treated (n-i-p) CdTe layers grown for 3 hrs.

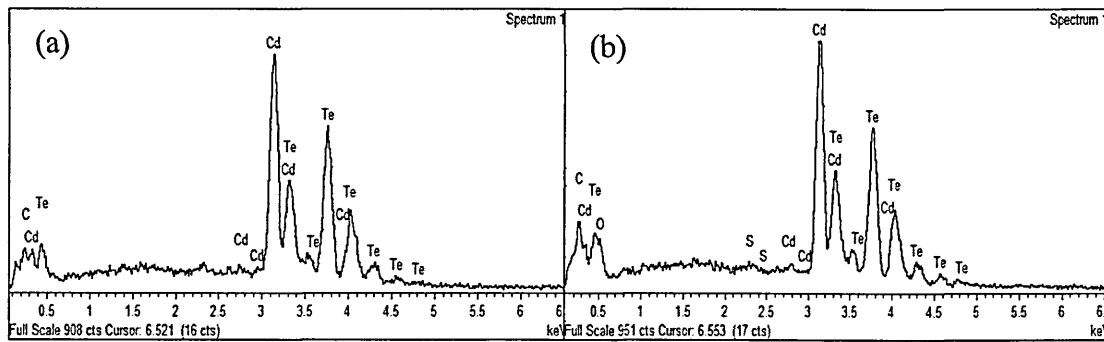


**Figure 7.11:** EDX spectra for (a) as deposited and (b) heat treated (n-i-p) CdTe layers grown for 5 hrs.

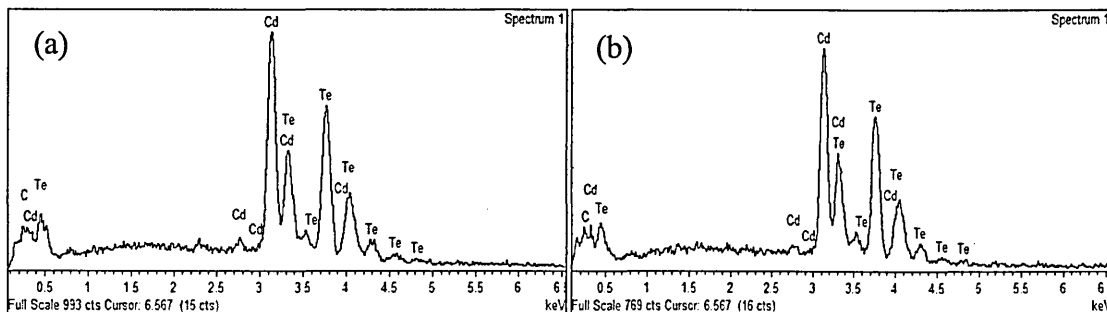


**Figure 7.12:** EDX spectrum for (a) as deposited and (b) heat treated (n-i-p) CdTe layers grown for 8hrs.

### 7.4.5 Raman Spectroscopy

The molecular structure and identification of phases of the material is given by Raman technique. Figure 7.13 shows the Raman spectra of a thick CdTe layer grown on InSb substrate, for comparison [9]. Figure 7.14 gives the Raman spectra for heat treated (n-i-p) CdTe layers grown at 3, 5 and 8 hrs growth time period.

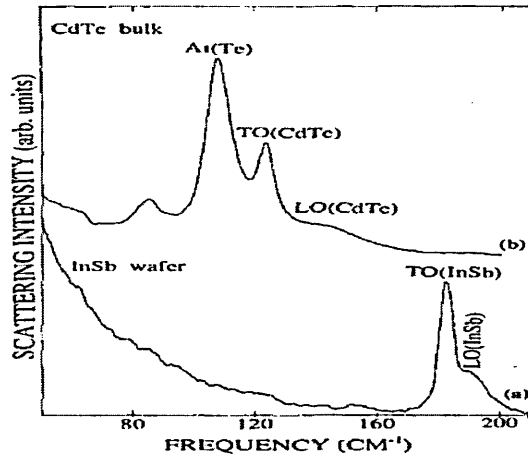


Figure 7.13: Raman spectra of a thick CdTe layer grown on InSb substrate [9].

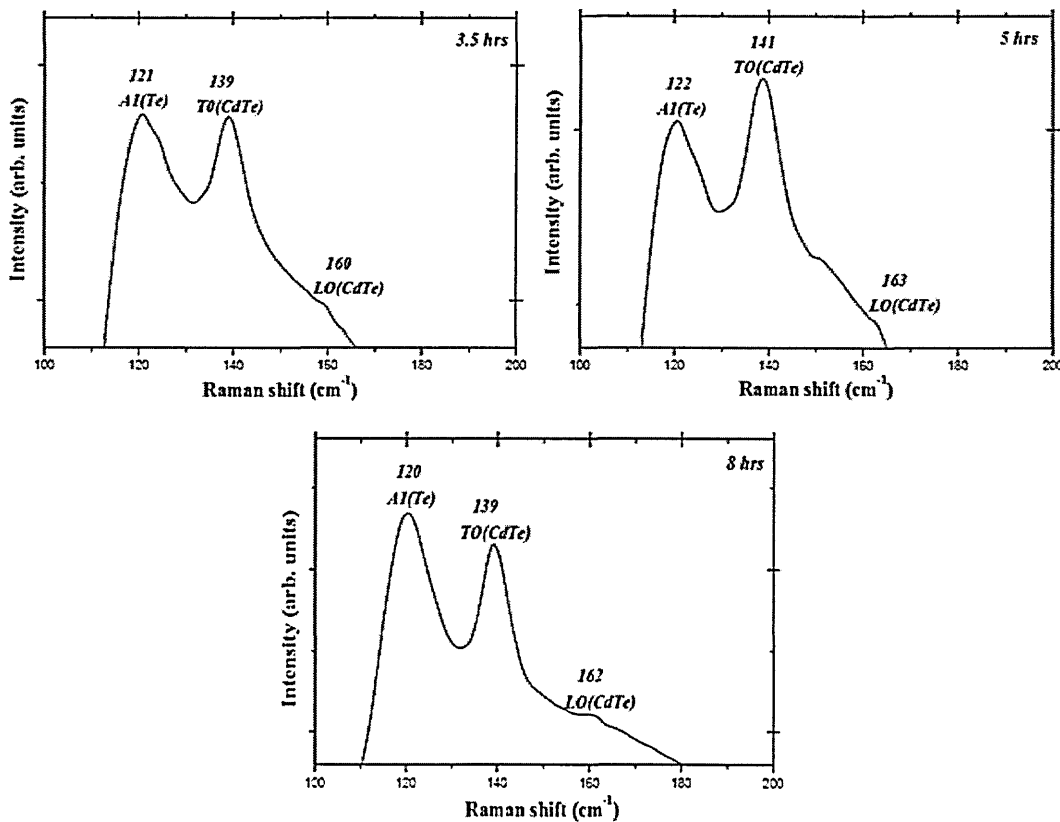


Figure 7.14: Raman spectra for heat treated (n-i-p) CdTe layers at different growth time (courtesy: Inst. of Mater. Research, Univ. of Leeds).

As shown from the Figure, two peaks related to CdTe layers are identified at 139 - 141  $\text{cm}^{-1}$  and 160 - 166  $\text{cm}^{-1}$  which correspond to fundamental transverse (1TO) and longitudinal optical phonons (1LO) respectively. Other peak at 120 - 121  $\text{cm}^{-1}$  is known to be the A1 phonon of the pure tellurium phase. It is observed that Te peak is dominant in the sample grown at 8 hrs which indicates CdTe layers start to become richer in Te. This may be due to the preferential dissolution of Cd in the acidic electro-bath solution. For sample grown at 3.5 hrs both Te and CdTe peaks intensity are almost the same, and the CdTe peak is dominant in the sample grown at 5 hrs. As reported in chapter 5, for the best devices the CdTe layer should be Cd-rich. Ison et al. [3] reported a similar observation on how these two peaks behaved. All these peaks are very close to those reported by other researchers in the field [3, 10-12]. For ideal CdTe material, without precipitation of elemental Te, the peak at 120-122  $\text{cm}^{-1}$  should not be detectable.

## 7.5 Device characterisation

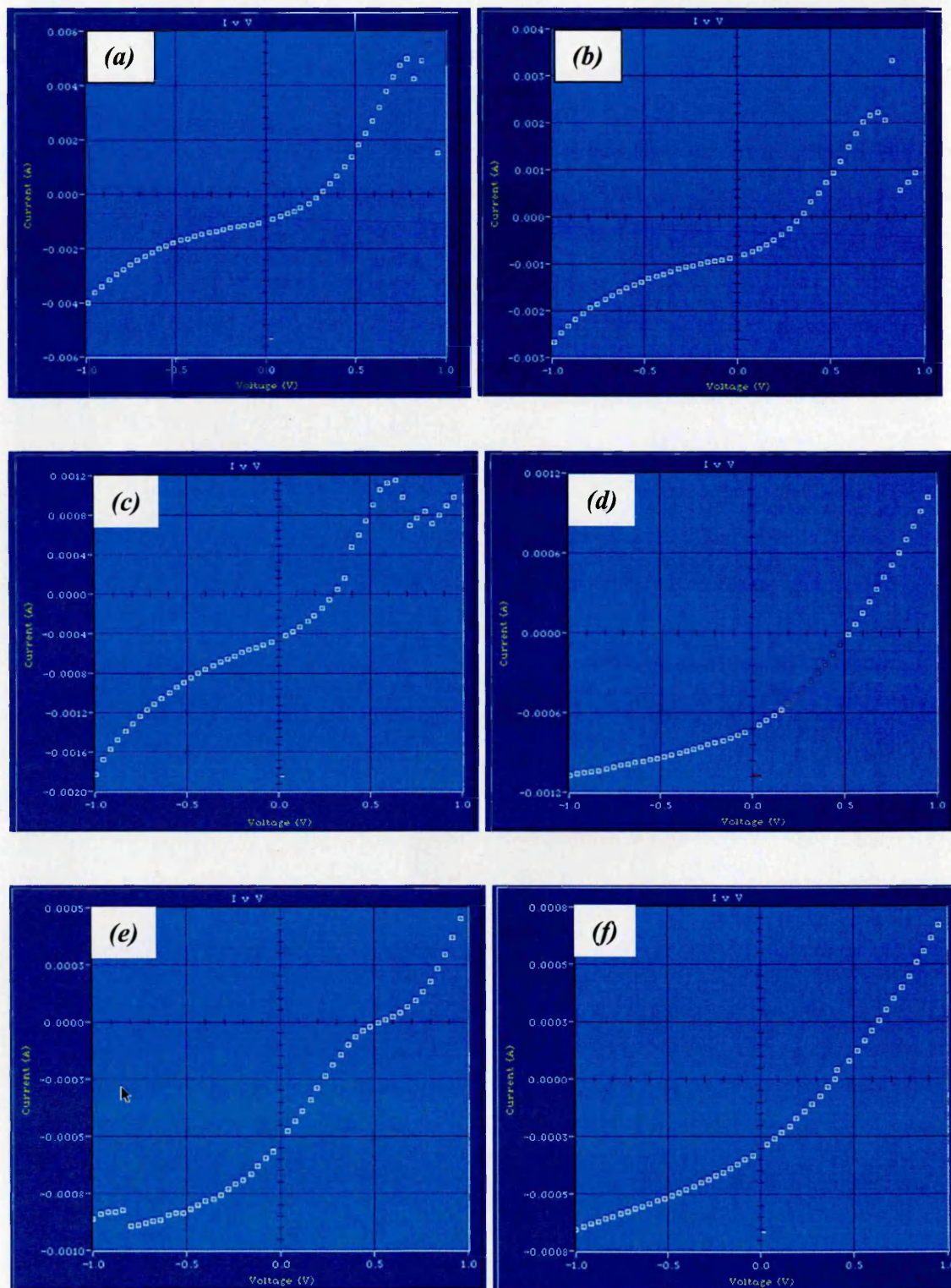
As discussed in chapter 6, the completed glass/FTO/CdS/CdTe/Au contacts were then assessed using I-V and C-V techniques. Furthermore, the C-V characteristics has also deal with in section 2.3.2 of chapter 2.

### 7.5.1 Current-voltage (I-V) characteristics

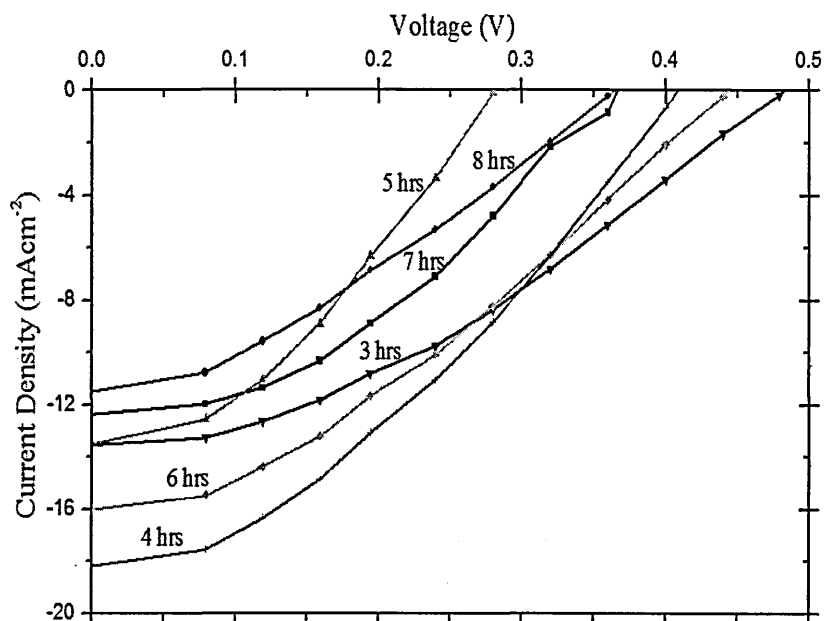
Figure 7.15 shows the print screen of linear I-V curves of glass/FTO/CdS/(n-i-p)CdTe/Au contacts under AM 1.5 illuminations, for devices with CdTe layers grown at different growth times. These are the initial measurements immediately after metallisation. Four weeks after the initial measurements, the devices were measured again. The devices had deteriorated drastically, by mainly the reduction of the current density as shown in Figure 7.16.

Table 7.4 shows the results of  $V_{oc}$ ,  $J_{sc}$ , FF and  $\eta$  of fully fabricated CdTe solar cells (set 1). The maximum efficiency of 3.55% with  $V_{oc} \sim 350$  mV and  $J_{sc} \sim 29$   $\text{mAcm}^{-2}$  were achieved for 4 hrs growth time after the first measurement. Four weeks later the measurements were repeated and the cell efficiency reduced down to 2.83%. Mendoza-Pérez et al [13] reported a similar observation and explained further, the efficiency and

the long-term stability of CdS/CdTe solar cells strongly depends on the materials used for back contact and the method of deposition.



**Figure 7.15:** Print screen of linear I-V curve of glass/FTO/CdS/CdTe/Au contacts under AM 1.5 illumination for (n-i-p) CdTe layers (set 1a) grown for; (a) 3 hrs, (b) 4 hrs, (c) 5 hrs, (d) 6 hrs, (e) 7 hrs and (f) 8 hrs.



**Figure 7.16:** Linear I-V curve of glass/FTO/CdS/(n-i-p)CdTe/Au contacts under AM 1.5 illumination for (n-i-p) CdTe layers (set 1b) grown at different growth times.

**Table 7.4:** Cell parameters (set 1) under illumination of (n-i-p) CdTe thin film solar cells at different growth times [(a) = initial cell parameters measurements and (b) = 4 weeks later].

Growth time (hrs)	Cell parameters (a)				Cell parameters (b)			
	$V_{oc}$ (mV)	$J_{sc}$ (mAcm <sup>-2</sup> )	FF (%)	$\eta$ (%)	$V_{oc}$ (mV)	$J_{sc}$ (mAcm <sup>-2</sup> )	FF (%)	$\eta$ (%)
3	300	32	0.32	3.07	400	13	0.36	2.25
4	350	29	0.35	3.55	410	18	0.39	2.83
5	320	16	0.30	1.54	280	13	0.35	1.27
6	520	22	0.30	3.40	440	16	0.38	2.68
7	530	19	0.27	2.72	370	12	0.39	1.73
8	400	11	0.27	1.89	360	11	0.33	1.30

From the Table, it is observed that a maximum current density of 32 mAcm<sup>-2</sup> was achieved at lower thickness of 3 hrs growth time and as the thickness increases the current density goes down to 11 mAcm<sup>-2</sup> for 8 hrs growth time. As shown in section 7.4.1, film grown at 8 hrs produced the highest intensity of the XRD but reverse is the case for device fabrication which agrees with the work reported by Bosio et al. [7]. Furthermore, Plotnikov et al [14] reported that efficiency greater than 12% can be

achieved for cells as thin as 1  $\mu\text{m}$ . Other researchers have reported that a thickness of CdTe between 0.67 and 1  $\mu\text{m}$  is enough to absorb  $\sim 80\%$  of solar radiation [15, 16].

As shown on Table 7.4, the best cell efficiency was achieved for between 4 – 6 hrs growth times for the CdTe layer with some possible error for 5 hrs growth time. To confirm this result, another set of samples were grown at 3.5, 4.5, 5 and 5.5 hrs. Figure 7.17 shows the linear I-V curves of this sets (i.e. set 2) and Table 7.5 shows the results of  $V_{oc}$ ,  $J_{sc}$ , FF and  $\eta$  of fully fabricated (n-i-p) CdTe solar cells for this set.

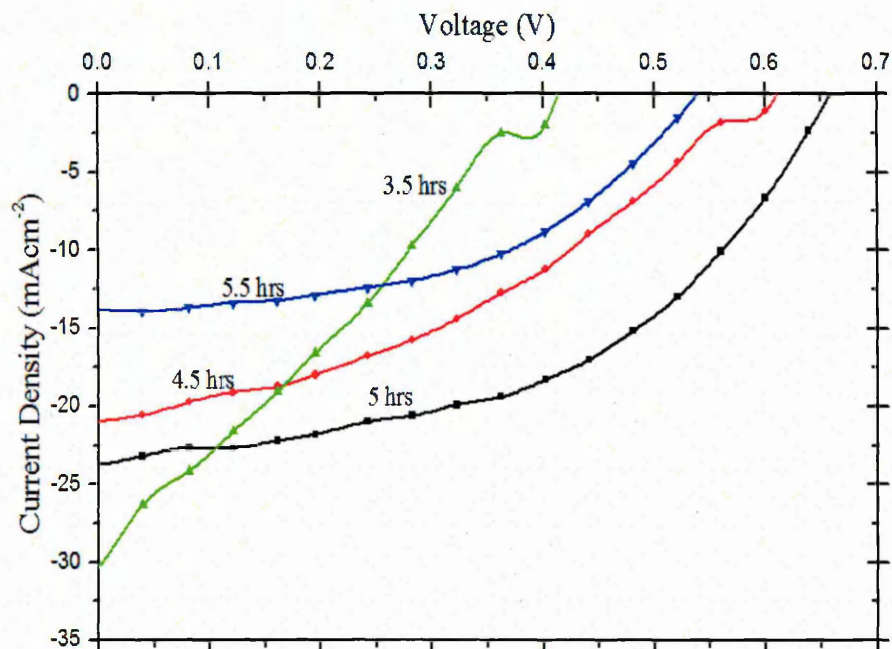


**Figure 7.17:** Linear I-V curve of glass/FTO/CdS/(n-i-p)CdTe/Au contacts under AM 1.5 illumination for (n-i-p) CdTe layers (set 2) grown at different growth times.

**Table 7.5:** Cell parameters (set 2) under illumination of (n-i-p) CdTe thin film solar cells at different growth time periods.

Growth periods (hrs)	Cell parameters			
	$V_{oc}$ (mV)	$J_{sc}$ ( $\text{mAcm}^{-2}$ )	FF (%)	$\eta$ (%)
3.5	410	30	0.27	3.32
4.5	610	21	0.36	4.61
5	660	24	0.48	7.60
5.5	540	14	0.45	3.40

It is observed from the Table above, a maximum efficiency of 7.60% with  $V_{oc} \sim 660$  mV,  $J_{sc} \sim 24$  mAcm<sup>-2</sup> and FF  $\sim 0.48$  was achieved for 5 hrs growth time. As the thickness of the CdTe layers increases or decreases, the efficiency of the cell goes down. At lower thickness the FF is poor which may be due to high resistance created by small grains, large recombination and generation process present or detrimental leakage paths present within the devices. It is known that current transport across the potential barrier at metal/semiconductor interface depends on thermionic emission, recombination and generation, field emission and thermionic field emission [17]. Peña et al have reported that series resistance effects limit the efficiency of solar cells [18]. Figure 7.18 (a) shows the log I against V of the best diode and its linear-linear equivalent under dark condition Figure 7.18 (b). The individual graphs of  $V_{oc}$ ,  $J_{sc}$ , FF and  $\eta$  of the two sets are shown in Figure 7.19.

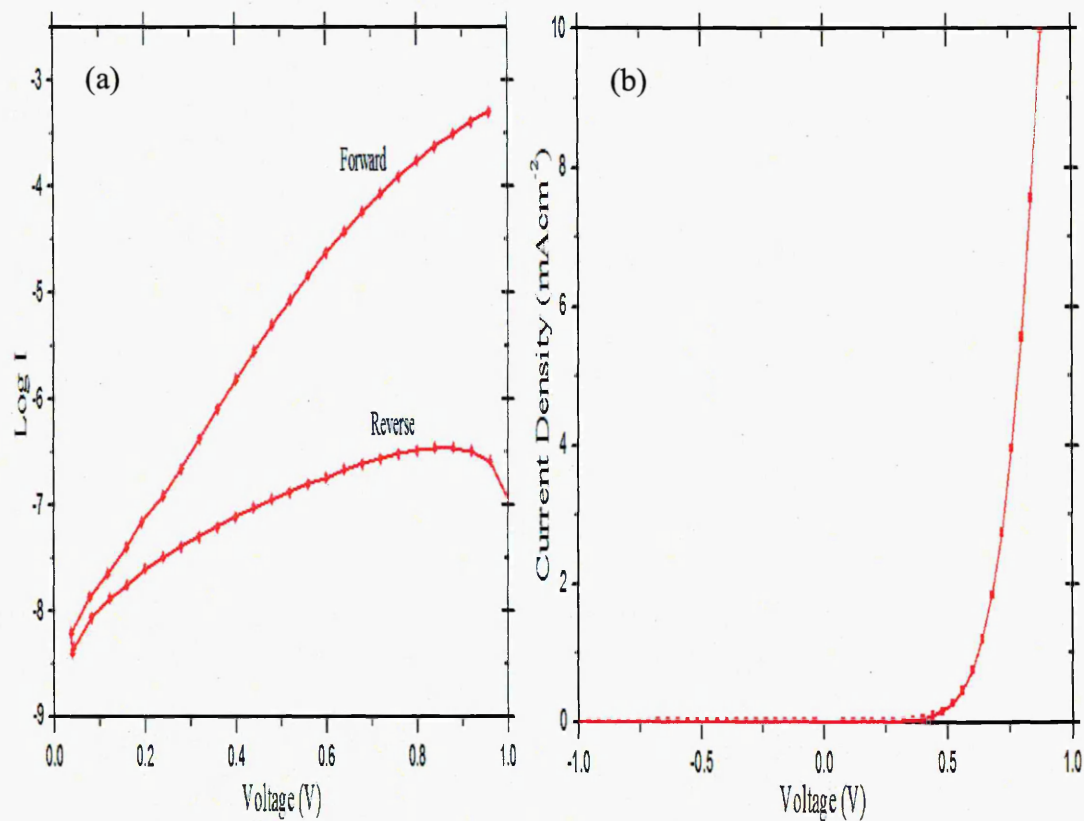


**Figure 7.18:** Log-linear (a) and linear-linear I-V curves (b) under dark condition for glass/FTO/CdS/(n-i-p)CdTe/Au contact with (n-i-p) CdTe grown for 5 hrs show rectification factor (RF)  $\sim 10^{3.5}$ , diode ideality factor ( $n$ )  $\sim 1.88$  and barrier height ( $\phi_B$ )  $\sim 1.20$  eV.

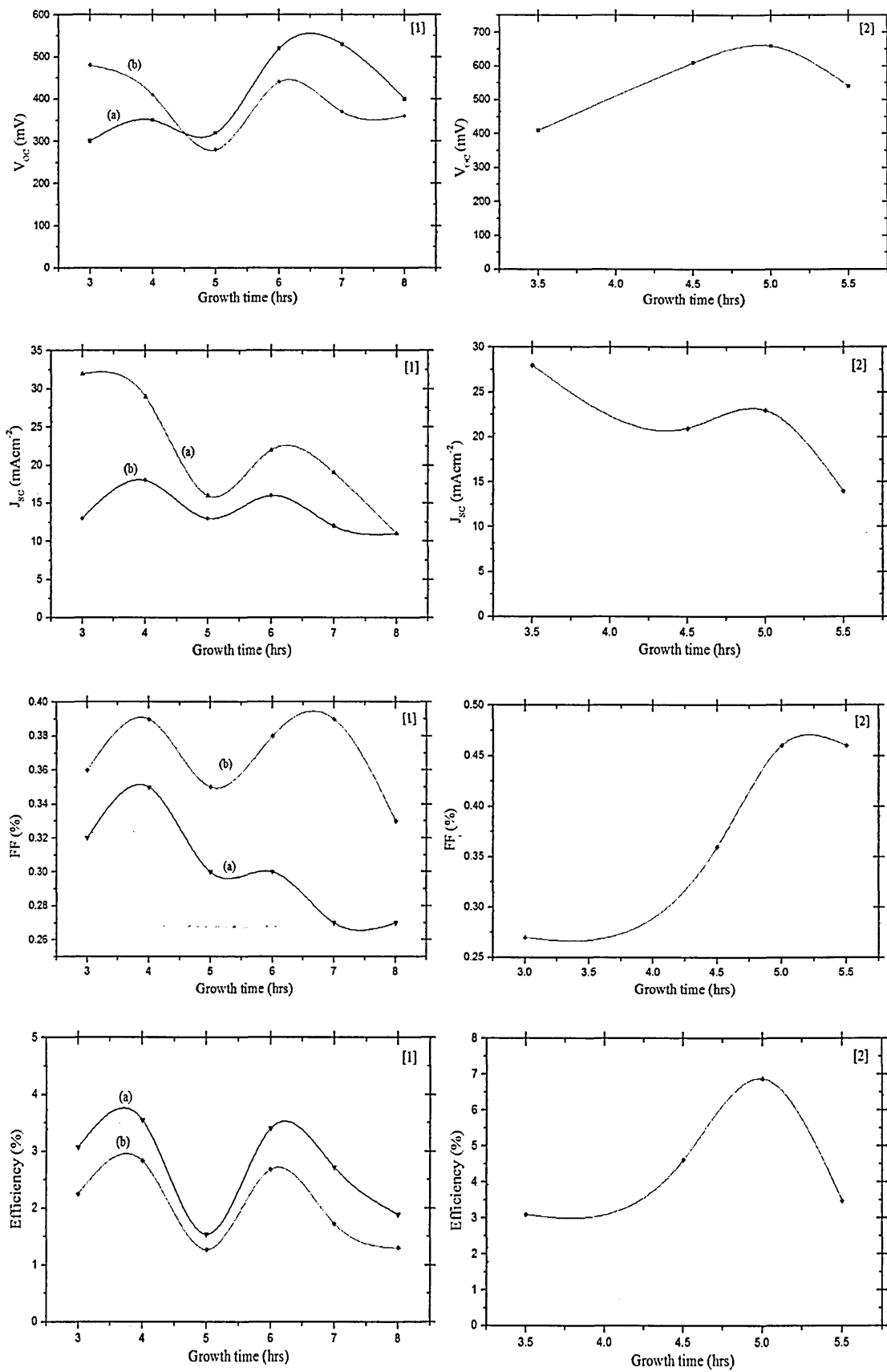


**Figure 7.19:** Cell parameters as a function of growth times of (n-i-p) CdTe layers, for set (1) and set (2). This indicates the performance drop for 5 hrs growth in set (1) due to some other factor.

### 7.5.2 Capacitance-voltage (C-V) measurement

The technique used to estimate doping concentration of the semiconductor and the diffusion voltage of the Schottky diode is the capacitance-voltage measurement. Due to the strong influence of defects in the diode, C-V measurements are unreliable for this purpose but it provides a good indication of the doping concentration of the semiconducting material. A Keithly 590 CV analyser operating up to 1 MHz modulation frequency was used for CV measurements on CdS/CdTe solar cells. Figure 7.20 show a typical capacitance value measured at 1 MHz frequency for 2 mm diameter Au contact on the best (highest efficiency) device [CdTe grown for 5 hrs (set 2)]. From the Figure, the built in potential ( $V_d$ ) was determined to be  $\sim 1.35$  eV. A doping concentration ( $N_D$ ) of  $\sim 2.0 \times 10^{17} \text{ cm}^{-3}$  was estimated from the gradient of the capacitance using equation 2.34 in section 2.3.2.

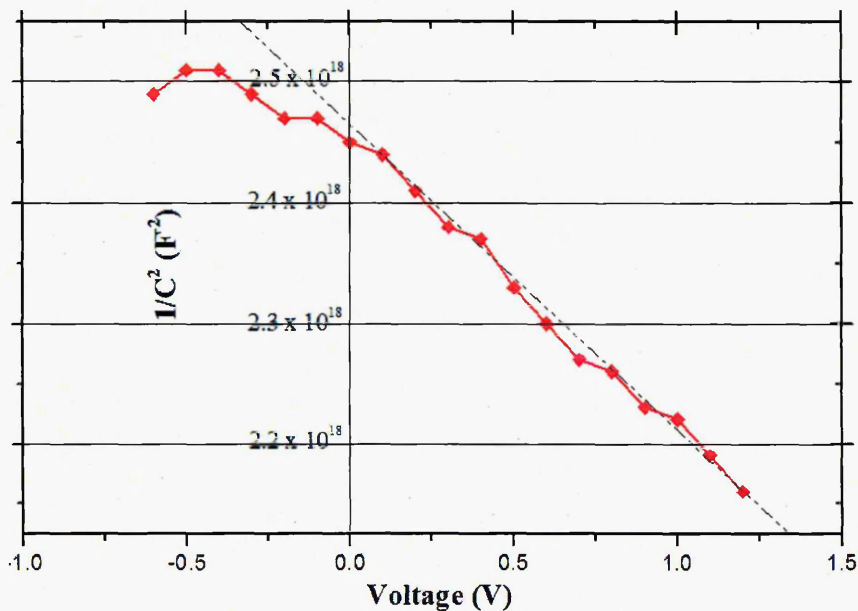


**Figure 7.20:** Schottky-Mott plots of (n-i-p) CdTe layer.

## 7.6 Growth process performance relationship.

Table 7.6 shows the summary of the relationship between growth process and the device performance.

**Table 7.6:** Summary of the growth process and device performance relationship.

Growth period (hrs)	XRD parameters		Bandgap (eV)	Cell efficiency $\eta$ (%)
	FWHM	Grain size, D (nm)		
3	0.201	7.4	1.45	2.25
5	0.217	6.8	1.45	7.60
8	0.184	8.1	1.45	1.80

From the Table, the CdTe grown for 5 hrs produce the highest efficiency of 7.60%. As the thickness of the CdTe layers increases or decreases, the efficiency of the cell goes down. These decreases in the efficiency may be due to high resistance created by small grains, large recombination and generation process present or detrimental leakage paths present within the devices.

## 7.7 Summary

CdTe (n-i-p) films have been deposited on glass/FTO/CdS substrates using an aqueous electrodeposition method. The XRD results for both as deposited and heat treated CdTe layers show the cubic CdTe phase with the main diffraction peak at  $2\theta = 23.6^\circ$  which corresponds to preferred orientation along (111) plane of cubic phase. The main features of the diffraction patterns are the same but the peak intensity varies for both as deposited and heat treated. As the growth periods increases, the intensity of the (111) peak also increases. Two additional peaks (220) and (311) were observed at lower growth time periods which indicates a reduced texture in the thinner films.

Optical absorption measurements show that the bandgap,  $E_g$ , for as deposited samples lies in the range 1.53 to 1.59 eV. After heat treatment the bandgap values decreased, and the absorption edge of the curve sharpened, with  $E_g \sim 1.45$  eV in all the samples which is closer to the CdTe bulk value. The transmission coefficient of as deposited samples grown for less than 7 hrs was found to be above 80%. After heat treatment the transmission decreases and the absorption edge of all the CdTe films sharpened and yield the band edge of the film deposited at 5 and 6 hrs gives the actual cut-off wavelength of CdTe  $\sim 852$  nm. Furthermore, film deposited below 5 hrs shows a wide blue shift and red shift is observed for film deposited above 6 hrs from the band edge of the CdTe value.

SEM studies shows as deposited layers have pin holes between the grains. These are seen most clearly in the samples grown for 3 and 8 hrs. At 5 hrs growth time, the gaps reduce which indicate reasonable thickness. After heat treatment the grain size increased and reduced the pin holes. Raman measurements show two peaks related to CdTe layers identified at  $139\text{-}141\text{ cm}^{-1}$  and  $160\text{-}66\text{ cm}^{-1}$  which correspond to the fundamental transverse and longitudinal optical phonons (1TO) and (1LO) respectively. Another peak at  $120\text{-}121\text{ cm}^{-1}$  is known to be the A1 phonon of the pure tellurium phase. The Te peak is dominant in the sample grown at 8 hrs and start to decrease as the growth time reduced.

The linear I-V curves of glass/FTO/CdS/(n-i-p)CdTe/Au devices at different growth times (set 1) give a maximum efficiency of 3.55% with  $V_{oc} \sim 350$  mV and  $J_{sc} \sim 29$  mAcm<sup>-2</sup> for the structure with a CdTe layer grown 4 hrs after the first measurement and drops to 2.83% 4 weeks later. The results from set 2 samples give a maximum

efficiency of 7.60% with  $V_{oc} \sim 660$  mV,  $J_{sc} \sim 24$  mAcm<sup>-2</sup> and FF  $\sim 0.48$  for 5 hrs growth of CdTe. As the thickness of the CdTe layer increases or decreases from the optimum, the efficiency of the cell goes down. At lower thickness the FF is poor, which may be due to high resistance created by small grains, large recombination process present or detrimental leakage paths present within the devices. From Log I vs. V results, RF  $\sim 10^{3.5}$ , n value  $\sim 1.88$  and  $\phi_B \sim 1.20$  eV were achieved. The capacitance-voltage measurement gives the  $V_d \sim 1.35$  eV and doping concentration ( $N_D$ ) of  $\sim 2.0 \times 10^{17}$  cm<sup>-3</sup>. The results show that adequate thickness of CdTe films is required, hence the objectives is achieved.

## References

1. M. Hädrich, C. Kraft, C. Löffler, H. Metzner, U. Reislöhner and W. Witthuhn, *Thin Solid Films* 517, 2285 (2009).
2. E. Colombo, A. Bosio, S. Calusi, L. Giuntini, A. Lo Guidic, C. Manfredotti, M. Massi, P. Olivero, A. Romeo, N. Romeo and E. Vittone, *Nuclear. Instrum. Method. B* 267, 2181 (2009).
3. V. V. Ison, A. R. Rao and V. Dutta, *Solid State Sciences* 11, 2003 (2009).
4. I. M. Dharmadasa, J. M. Thornton and R. H. Williams, *Appl. Phys. Lett.* 54(2), 137 (1989).
5. S. A. Gamboa, P. J. Sebastian, X. Mathew, H. Nguyen-Cong and P. Chartier, *Sol. Energy Mater. Sol. Cells* 59, 115 (1999).
6. N. El-Kadry, A. Ashour and S. A. Mahmoud, *Thin Solid Films* 269, 112 (1995).
7. A. Bosio, N. Romeo, S. Mazzamuto and V. Canevari, *Prog. in Cryst. Growth and Charact. of Mater.* 52, 247 (2006).
8. H. Metin and R. Esen, *Semicond. Sci. Technol.* 18, 647 (2003).
9. H-K Na and P-K Shon, *Solid State Communication* 85(7), 609 (1993).
10. Y. Jung, S. Chun, D. Kim and J. Kim, *J. Crystal Growth* 326, 69 (2011).
11. J. Rouusset, E. Rzepka, D. Lincot, *J. Phys. Chem. B* 113, 4333 (2009).
12. R. Ochoa-Landin, O. Vigil-Galan, Y. V. Vorobiev and R. Ramirez-Bon, *Sol. Energy Mat. Sol. Cells* 83, 134 (2009).
13. R. Mendoza-Pérez, J. Sastre-Hernández, G. Conteraras-Puente and O. Vigil-Galán, *Sol. Energy Mater. Sol. Cells* 93, 79 (2009).
14. V. Plotnikov, X. Liu, N. Paudel, D. Kwon, K.A. Wieland and A. D. Compaam, *Thin Solid Films* (2011), doi:10.1016/j.tsf.2010.12.179.
15. V. Fthenakis, *Renewable Sustainable Energy Rev.* 13, 2746 (2009).
16. K. Zweibel, *Science* 328, 699 (2010).

17. E. H. Rhoderick and R. H. Williams, *Metal-Semiconductor Contacts* 2<sup>nd</sup> edition, Oxford University Press, New York, (1988).
18. J. L. Peña, O. Arēs, V. Rejón, A. Rios-Flores, J. M. Camacho, N. Romeo and A. Basio, *Thin Solid Films* (2011), doi:10.1016/j.tsf.2011.04.193.

## Chapter 8: Effect of CdCl<sub>2</sub>/heat treatment on CdS/CdTe solar cells

### 8.1 Motivation and objectives

The grains of as deposited samples are disconnected and have a high defect density which limits the efficiency of device performance of the solar cells. It is believed that CdCl<sub>2</sub>/heat treatment removes and eliminates these defects and increases the grains to become very large. This treatment is an essential step for increasing the efficiency of CdS/CdTe solar cell. The aim of this work is to further investigate this crucial step.

### 8.2 Introduction

CdCl<sub>2</sub>/heat treatment is necessary on CdS and CdTe layers before their use in active PV solar cells. This treatment provides interfacial intermixing and device activation. Samples are heated rapidly and cooled down slowly allowing optimum grain growth during recrystallisation, and therefore improve the overall efficiency of the solar cells.

Many researchers in the field [1-4] have reported that, during this treatment chlorine helps the n-type doping, reduce the series resistance and improve the FF. Another benefit mentioned is the cementing effect of chlorine to form larger grains. Some of the methods used for this treatment includes: vapour [5], evaporated [6] and solution [7] CdCl<sub>2</sub> treatments. Kampmann et al. [8] reported that solution CdCl<sub>2</sub> treatment is the most common and simple process which involves soaking CdS and CdTe in methanol containing dissolved CdCl<sub>2</sub> powder, drying and then heat treatment.

Six glass/FTO/ED-CdS substrates were used to grow the CdTe layers, three as deposited and the remaining CdCl<sub>2</sub>/heat treated. The growth times for the ED-CdS were 40, 60 and 80 minutes, and each one of this sample is used to grow the CdTe film for 5 hrs. The growth voltages were changed in order for the deposition of CdTe layers to form (n-i-p), as discussed in chapter 7. Deposition of CdTe films have been discussed in section 3.4 of chapter 3.

## 8.3 Characterisation of CdTe

### 8.3.1 X-ray diffraction

Figure 8.1 shows the X-ray diffraction patterns for as deposited and heat treated CdTe layers deposited on ED-CdS with and without CdCl<sub>2</sub>/heat treatment. The main diffraction peak at  $2\theta = 23.642^\circ$  corresponds to preferred orientation along (111) plane of cubic phase. This peak was assigned according to the JCPDS (01-075-2086) data on cubic CdTe. Figure 8.1 [panel 1, 3 and 5] shows the as deposited ED-CdS for 40, 60 and 80 minutes used to grow CdTe film, while [panel 2, 4 and 6] are the CdCl<sub>2</sub>/heat treated ED-CdS for the same purpose. From the Figure, apart from the main peak (111), other peaks identified from the diffractogram are (220) and (311). These peaks are present in all the CdTe films deposited on CdS without CdCl<sub>2</sub>/heat treatment.

After CdCl<sub>2</sub>/heat treatment in air at 400°C for 20 minutes (in case of ED-CdS) and 450°C for 15 minutes (in case of CdTe), the intensity of all the peaks decreases due to loss of material through sublimation. The decrease in FWHM indicates an increase in grain size and/or an improvement in crystallinity. As shown from the Figure, panel 2 gives the best CdTe film which indicates crystalline material with diminishing of other peaks. Apart from this treatment thickness play an important role in this process. Basio et al. [9] reported that CdCl<sub>2</sub> acts as a catalyst in the film growth which increases the mobilities of Cd atoms and TeO<sub>2</sub> molecules. The heat treatment enhances the recrystallisation of CdTe films reducing any stress within the films and due to sublimation of excess elements from the layer.

The values of XRD intensity, FWHM and grain size of CdTe layers deposited on CdS with and without CdCl<sub>2</sub>/heat treatment are presented in Table 8.1, estimated using equation 2.18 presented in section 2.2.1 of chapter 2.

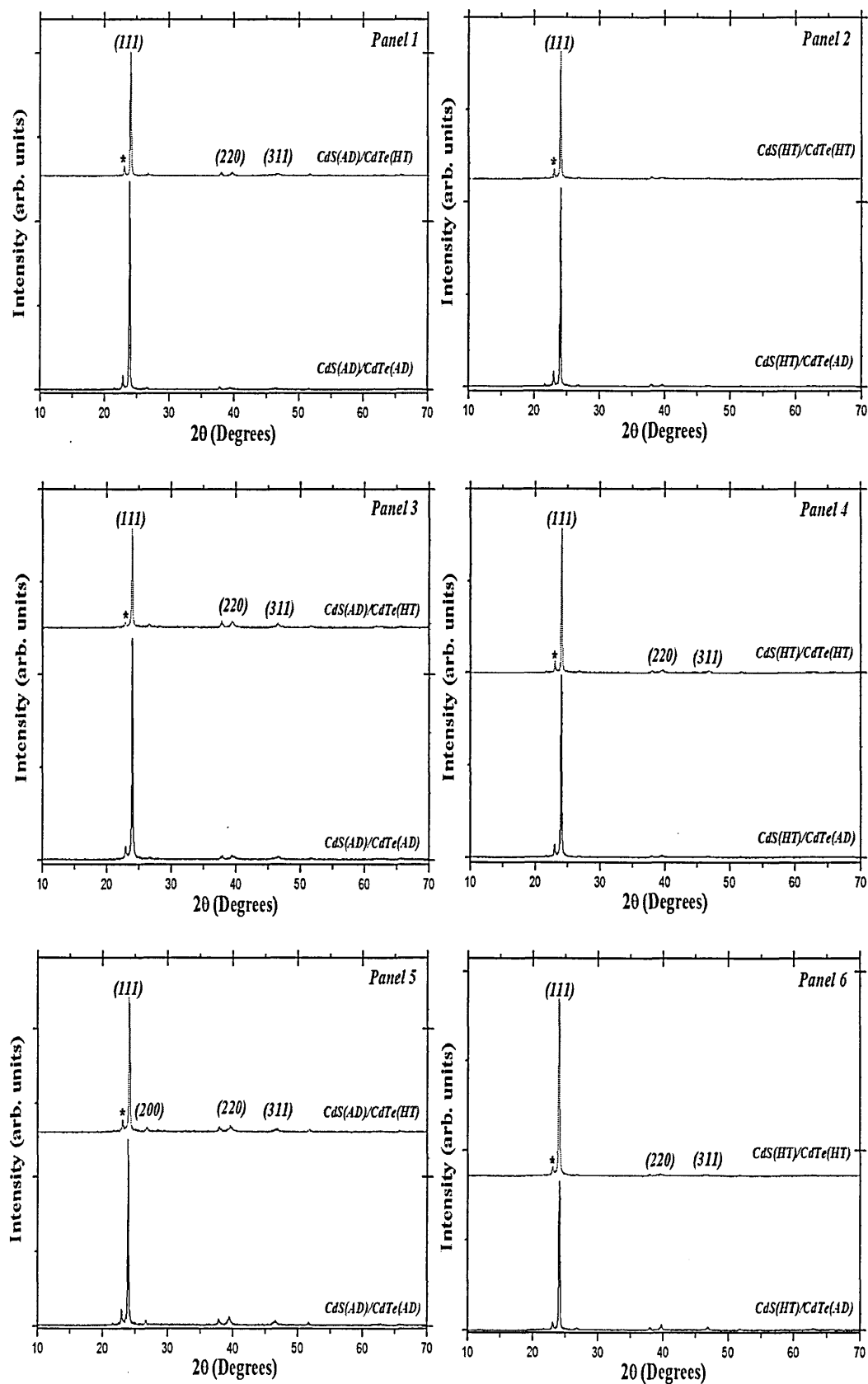


**Figure 8.1:** X-ray diffraction patterns for as deposited and  $\text{CdCl}_2$ /heat treated (n-i-p) CdTe layers grown on ED-CdS as deposited [panel 1 = 40 min, panel 3 = 60 min and panel 5 = 80 min] and  $\text{CdCl}_2$ /heat treated [panel 2 = 40 min, panel 4 = 60 min and panel 6 = 80 min] (\* indicates Te peak).

**Table 8.1:** XRD intensity, FWHM and grain size of CdTe layers grown on ED-CdS with and without CdCl<sub>2</sub>/heat treatment. [AD = as deposited and HT = heat treated]

Growth period of ED-CdS (minutes)	XRD Intensity (arb. units)			
	AD/AD	AD/HT	HT/AD	HT/HT
40	6198	3648	8617	5319
60	4753	1943	6930	5180
80	3143	2133	6921	5770
	FWHM			
40	0.150	0.134	0.117	0.107
60	0.177	0.137	0.117	0.100
80	0.251	0.217	0.163	0.152
	Grain size (nm)			
40	11.4	11.9	13.1	14.4
60	10.2	10.8	12.3	13.1
80	8.4	9.1	10.2	11.5

From the Table, it is observed that the crystallite size for heat treated sample increases and the FWHM decreases; this is due to the coalescence of small crystals and the growth of larger grains. Furthermore, the FWHM was found to decrease after CdCl<sub>2</sub>/heat treatment. Such an effect is due to the decrease in the concentration of lattice imperfections as a result of a decrease in the internal micro strain within the films or an increase in the crystallite size. Figures 8.2, 8.3 and 8.4 show the XRD intensity, FWHM and grain size at various CdCl<sub>2</sub>/heat treatment conditions. These results indicate that the largest grains size of CdTe is obtained when CdTe layers are grown on heat treated CdS, and CdTe layer is heat treated.

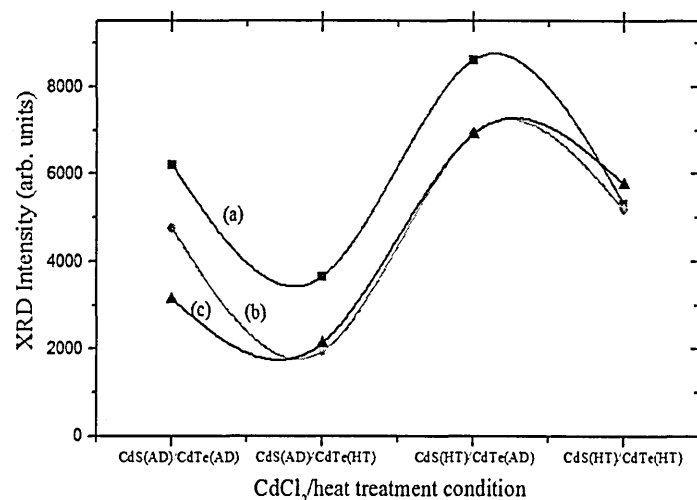


**Figure 8.2:** XRD intensity of (111) peak observed for (n-i-p) CdTe layers at different conditions grown on ED-CdS (a) 40 minutes, (b) 60 minutes and (c) 80 minutes.

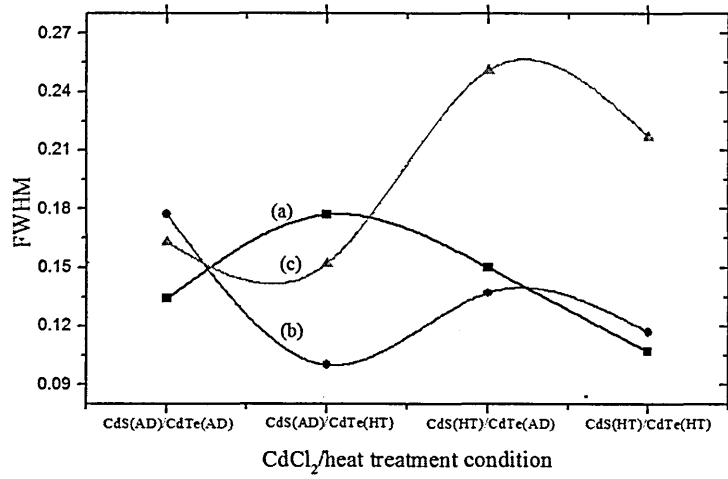


**Figure 8.3:** FWHM of (111) peak observed for (n-i-p) CdTe layers at different conditions grown on ED-CdS (a) 40 minutes, (b) 60 minutes and (c) 80 minutes.

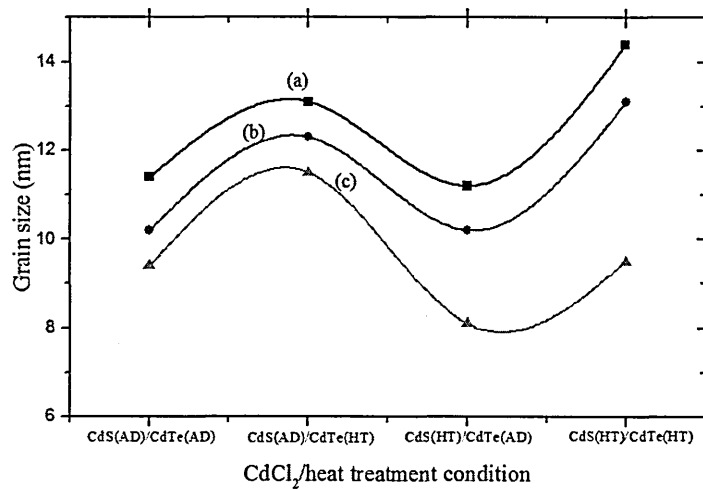


**Figure 8.4:** Grain size of (111) peak observed for (n-i-p) CdTe layers at different conditions grown on ED-CdS (a) 40 minutes, (b) 60 minutes and (c) 80 minutes.

### 8.3.2 Optical absorption

Optical absorption measurements were carried out in order to evaluate the bandgap of materials. Figure 8.5 shows the graphs of optical absorption for as deposited and CdCl<sub>2</sub>/heat treated CdTe layers grown on ED-CdS with and without CdCl<sub>2</sub>/heat treatment. Using equation 2.21 on section 2.2.3, chapter 2, the bandgap energy,  $E_g$  was determined by plotting the square of absorption ( $A^2$ ) against photon energy ( $h\nu$ ). As shown from the Figure, the treated CdS/CdTe films had a sharp absorption edge of the curve and  $E_g$  is 1.45 eV, which is close to the bulk value for CdTe. The reason for the sharpening might be due to a change in the stoichiometry or reduction of intrinsic defect population of the treated samples. Rami et al. [3] reported that the shift in the bandgap

after this treatment is due to the formation of  $\text{CdS}_x\text{Te}_{(1-x)}$ . The bandgap energy of the untreated  $\text{CdS}/\text{CdTe}$  films deteriorates and its absorption edge shifted to the blue region. This must be due to the quantum effects arising from small grains present in the layers. Table 8.2 gives the bandgap values of  $\text{CdTe}$  layers grown on ED- $\text{CdS}$  with and without  $\text{CdCl}_2/\text{heat}$  treatment and Figure 8.6 shows the bandgap energy at different  $\text{CdCl}_2/\text{heat}$  treatment conditions.

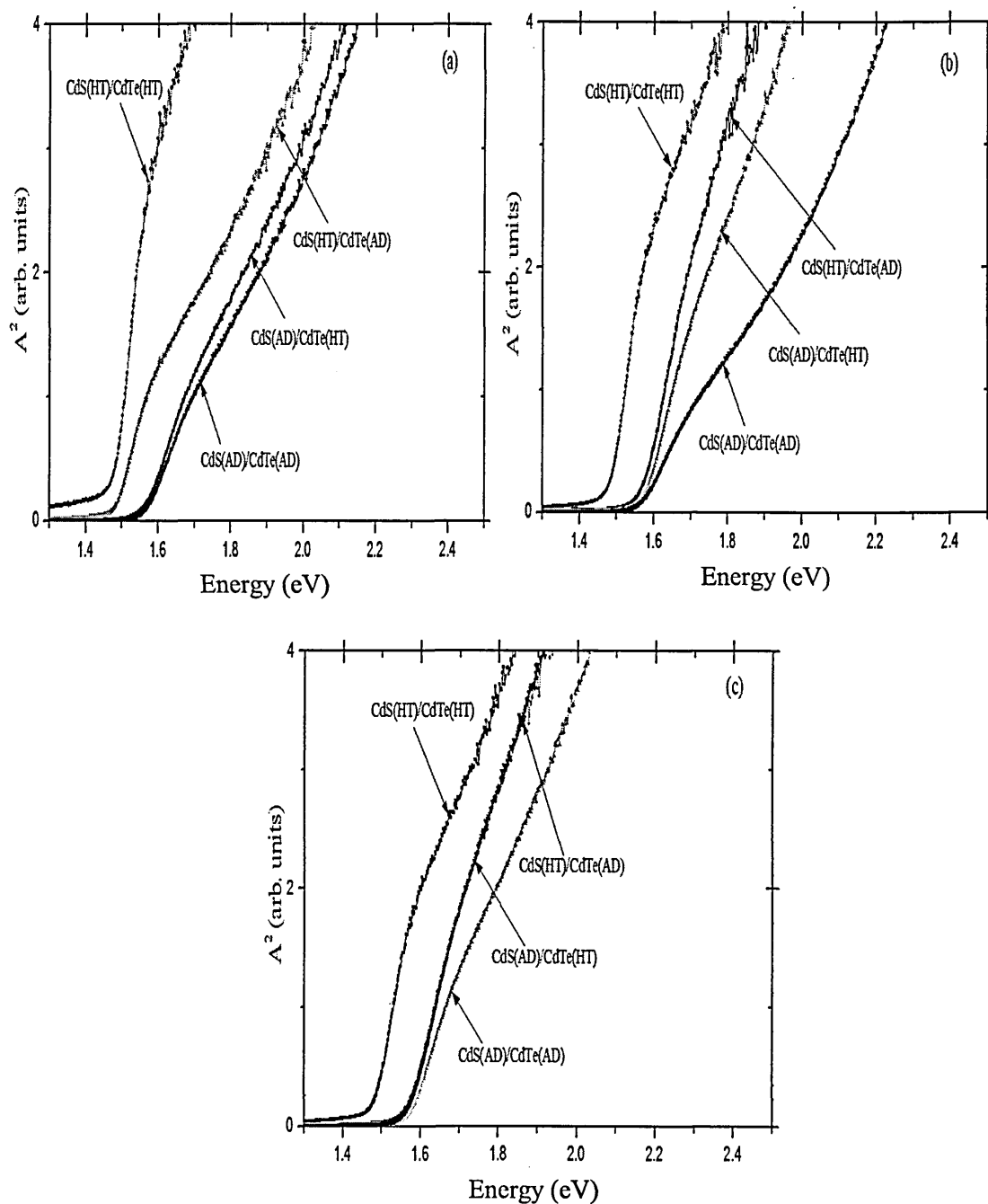


**Figure 8.5:** Optical absorption curves for (n-i-p) CdTe layer grown on ED-CdS without and with  $\text{CdCl}_2/\text{heat}$  treatment. ED-CdS layers used were grown for (a) 40 minutes, (b) 60 minutes and (c) 80 minutes.

**Table 8.2:** Bandgap energy of CdTe layers grown on ED-CdS with and without CdCl<sub>2</sub>/heat treatment [AD = as deposited and HT = heat treated].

Growth period of ED-CdS (minutes)	Bandgap (eV)			
	AD/AD	AD/HT	HT/AD	HT/HT
40	1.57	1.55	1.48	1.45
60	1.58	1.56	1.55	1.46
80	1.58	1.57	1.56	1.47

As shown from Table 8.2, the bandgap energies of the untreated CdS/CdTe films are higher and decrease gradually as the condition improved. The bandgap energy for the treated films gives ~1.45 – 1.47 eV. The reason for this may be due to a change in the stoichiometry, reduction of intrinsic defect population and improved crystallinity removing quantum effects after the CdCl<sub>2</sub>/heat treatment condition. The slight increase of the bandgap from 1.43 eV is ascribed to the intermixing of CdS and CdTe at the interface to form CdS<sub>x</sub>Te<sub>(1-x)</sub>.

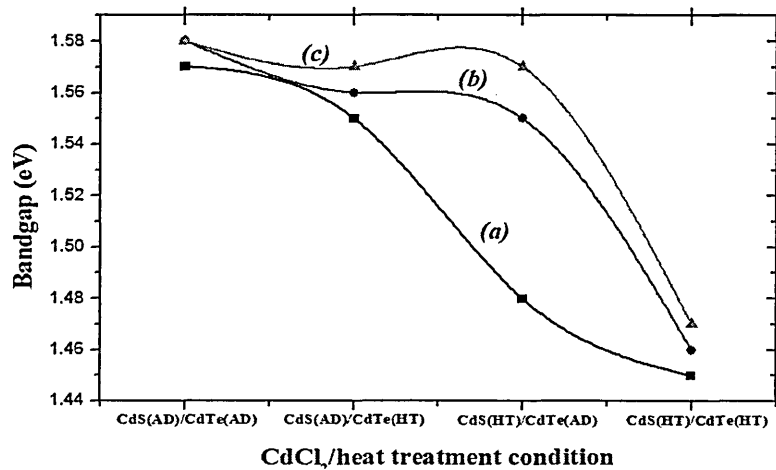


**Figure 8.6:** Bandgap energy for (n-i-p) CdTe layer grown on ED-CdS without and with CdCl<sub>2</sub>/heat treatment. ED-CdS layers used were grown for (a) 40 minutes, (b) 60 minutes and (c) 80 minutes.

The optical transmission spectra for as deposited and CdCl<sub>2</sub>/heat treated CdTe layers grown on ED-CdS with and without CdCl<sub>2</sub>/heat treatment are shown in Figure 8.7. Measurements were taken in the wavelength range 600 – 1000 nm on the deposited films. The transmission coefficient of all the untreated CdS/CdTe films was found to be above 80% with the absorption edge shifted to the blue region. As the condition

improved, the transmission coefficient and the absorption edge decrease. Furthermore, it is observed from the Figure, the band edge of the treated films gives the cut-off wavelength of CdTe  $\sim 852$  nm and the absorption edge shifted to the red region. These results confirm the effective absorption of IR-radiation by the CdS(HT)/CdTe(HT) layers, making the layers most suitable as absorber layer in solar cells. The red-shift also confirms the reduction of  $E_g$  value reaching the bulk- $E_g$  value of CdTe due to improved crystallinity by heat treatment.

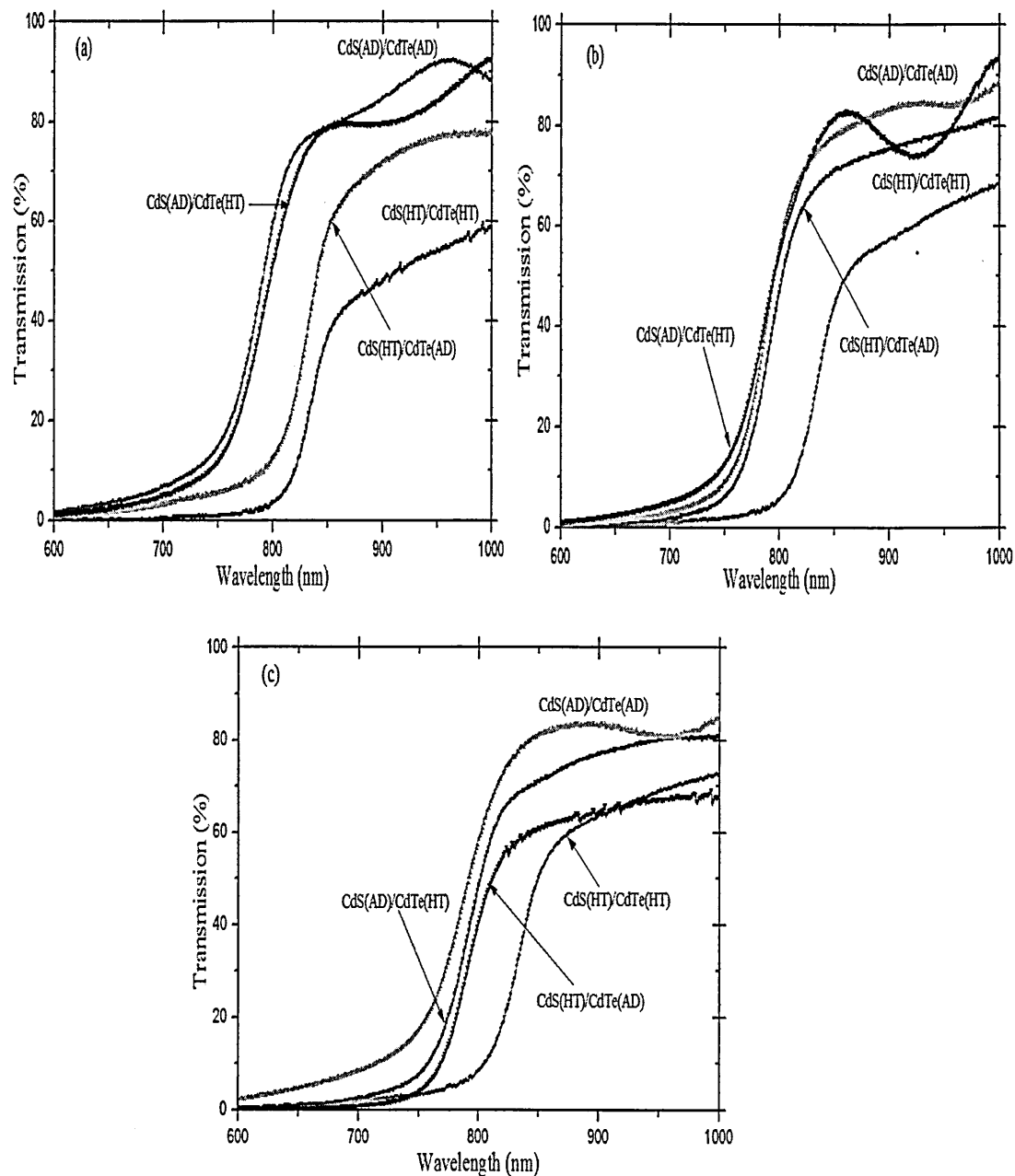


**Figure 8.7:** Transmission plots for (n-i-p) CdTe layer grown on ED-CdS without and with CdCl<sub>2</sub>/heat treatment. ED-CdS layers used were grown for (a) 40 minutes, (b) 60 minutes and (c) 80 minutes.

### 8.3.3 Scanning Electron Microscopy

SEM studies were carried out to investigate the surface morphology, grain size and uniformity of CdTe layers grown on ED-CdS with and without CdCl<sub>2</sub>/heat treatment. Figure 8.8 shows the SEM images of CdTe layers at different CdCl<sub>2</sub>/heat treatment conditions. As shown from the Figure, untreated samples show a lot of pin holes (gaps) between the grains, as results it shorts the devices and therefore the efficiency suffers. The pin hole (gap) diminishes as the treatment condition improved. These results confirmed that heat treatment enhances the recrystallisation and coalesce grains to fill the gaps and forms a uniform thin layer of CdTe.

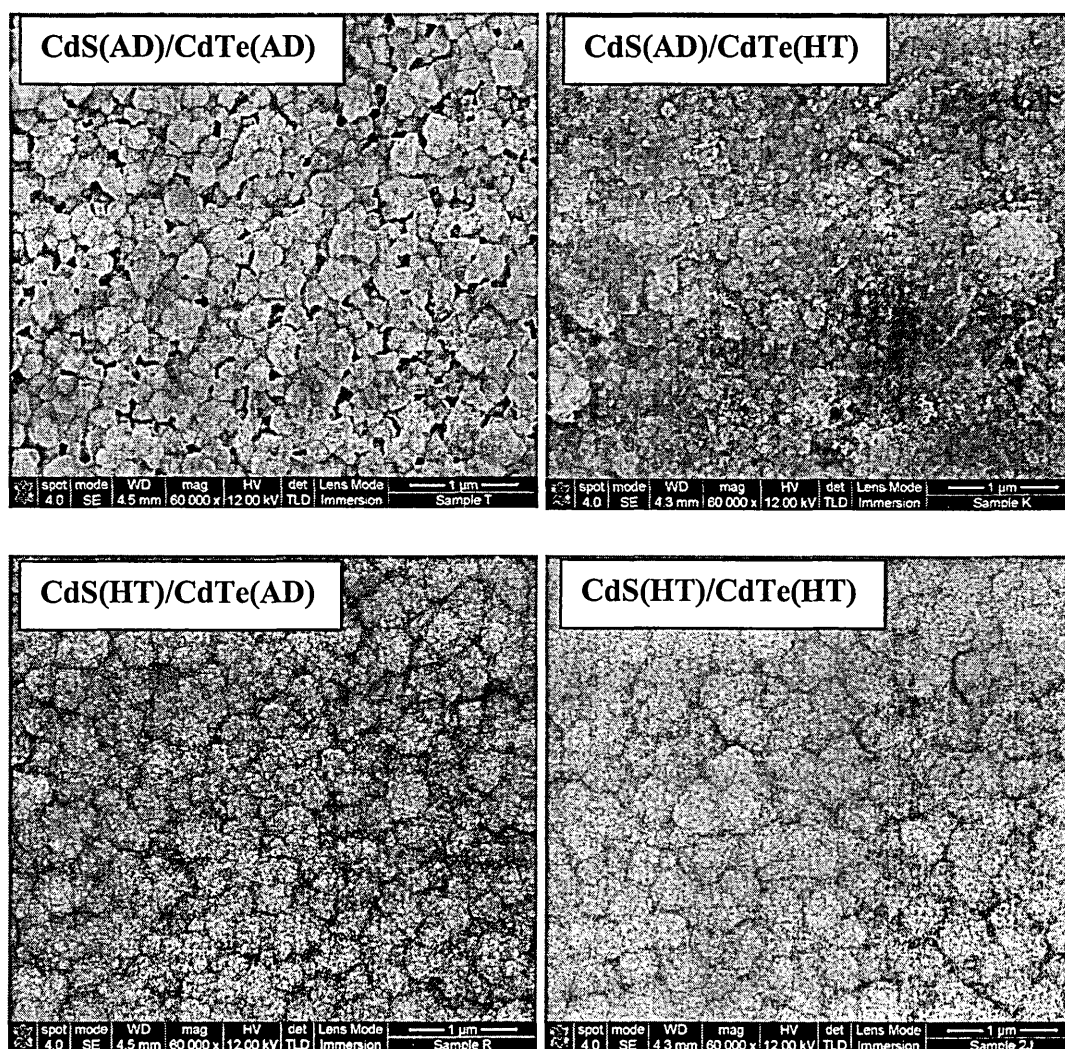


**Figure 8.8:** SEM images of (n-i-p) CdTe layers at different CdCl<sub>2</sub>/heat treatment conditions.

### 8.3.4 Energy Dispersive X-ray

Energy dispersive x-ray (EDX) technique was carried out to investigate the qualitative elemental analysis of CdTe layers. The EDX spectra of (n-i-p) CdTe layers grown on ED-CdS at different CdCl<sub>2</sub>/heat treatment conditions are shown in Figures 7.9. In all these spectra, the presence of both Cd and Te was observed. The appearance of chlorine peak was seen on the treated CdS/CdTe films. The atomic composition of Cd:Te estimated from the spectra is 57.4:42.6 for untreated sample and 58.3:41.7 for treated CdS/CdTe films. This analysis confirms the reduction of Te in layers after CdCl<sub>2</sub> treatment.

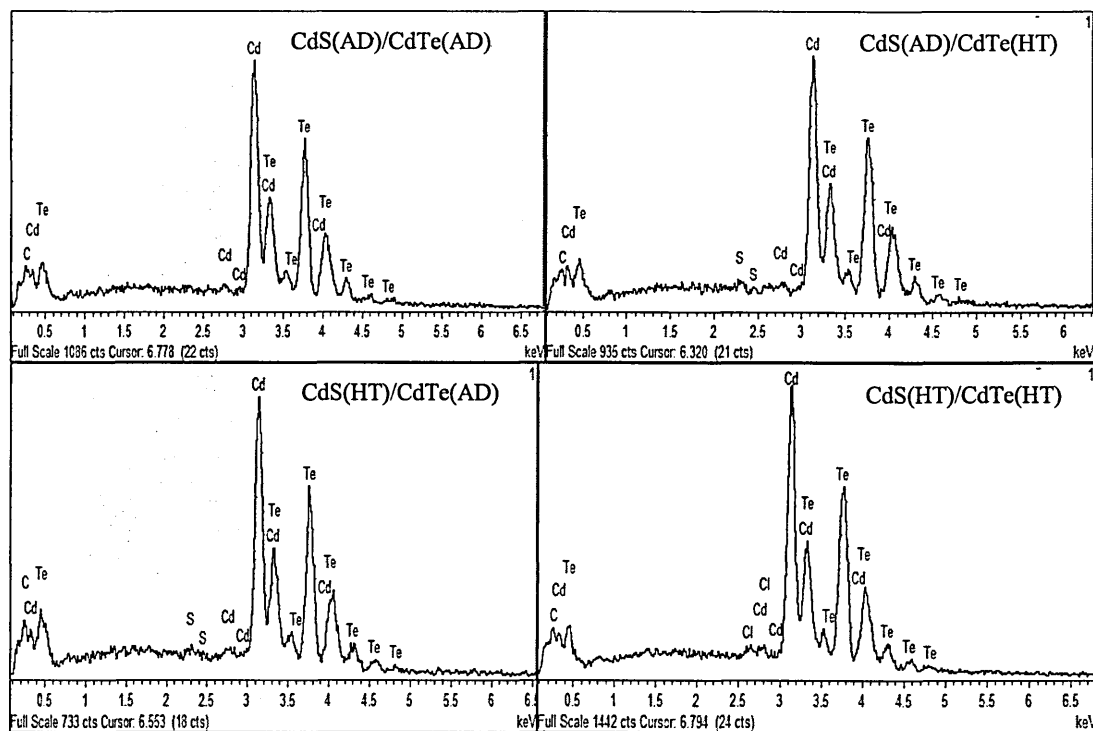


**Figure 8.9:** EDX spectra of (n-i-p) CdTe layers at different CdCl<sub>2</sub>/heat treatment conditions.

### 8.3.5 Raman Spectroscopy

The molecular structure and identification of phases of the material was explored using Raman technique. Figure 8.10 shows the Raman spectra of a thick CdTe layer grown on InSb substrate, for comparison [10]. Also shown in Figure 8.11 are the Raman spectra of CdTe layers grown on ED-CdS without (a) and with (b) CdCl<sub>2</sub>/heat treatment.

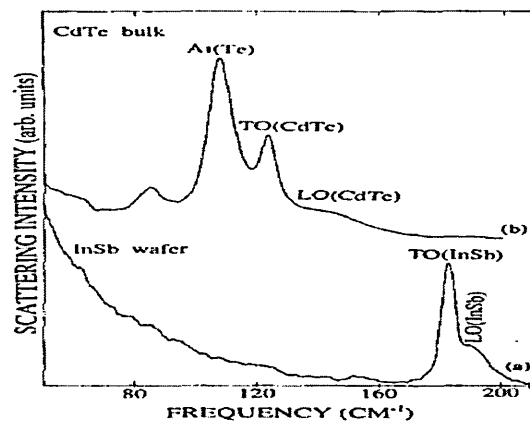


**Figure 8.10:** Raman spectra of a thick CdTe layer grown on InSb substrate [10].

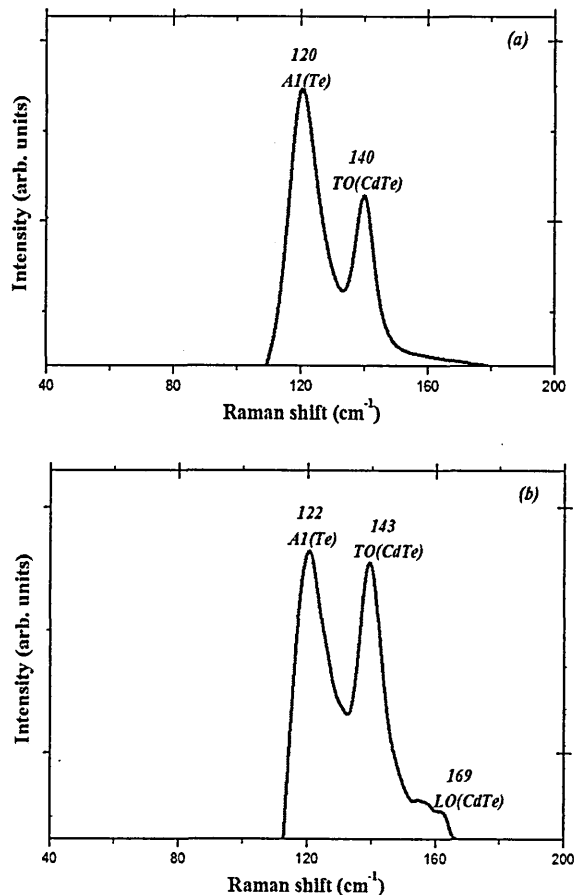


**Figure 8.11:** Raman spectra of (n-i-p) CdTe layers grown on ED-CdS (a) CdS(AD)/CdTe(AD) and (b) CdS(HT)/CdTe(HT) (courtesy: Inst. of Mater. Research, Univ. of Leeds).

As shown in Figure 8.11 (a), only one peak related to CdTe layers identified at  $140\text{ cm}^{-1}$  which correspond to fundamental transverse optical phonons (1TO), while the other peak disappeared. The A1 phonon of the pure tellurium phase appears at  $120\text{ cm}^{-1}$  indicating presence of precipitated Te in the layers. The formation of tellurium in the

film is detrimental to the CdTe layer which could lead to short-circuiting in the device performance. The presence of Te in the CdTe layer reduces the crystallinity. This also makes the CdTe layer p-type instead of n-type, required for high efficiency solar cells. The two peaks related to CdTe layers identified at  $143\text{ cm}^{-1}$  and  $169\text{ cm}^{-1}$  are present indicating the improvement of CdTe quality in the films as shown in Figure 8.11 (b). These peaks correspond to (1TO) and (1LO) respectively. The pure tellurium peak also observed at  $122\text{ cm}^{-1}$  corresponding to A1 phonon. All these peaks are very close to those reported by other researchers in the field [11-13]. After  $\text{CdCl}_2$  treatment, the intensity of A1(Te) has reduced indicating the reduction of precipitated Te in the layers during  $\text{CdCl}_2$  treatment, improving the quality of CdTe layer. This treatment also helps in doping the CdTe layer, n-type using the well-known dopant (Cl) of CdTe.

## 8.4 Device characterisation

As discussed in chapter 6, the completed glass/FTO/CdS/CdTe/Au contacts were then assessed using I-V technique.

### 8.4.1 Current-voltage (I-V) characteristics

Figures 8.12, 8.13 and 8.14 show the linear I-V curves of glass/FTO/CdS/CdTe/Au contacts under AM 1.5 illuminations, for devices with CdTe layers grown on ED-CdS at different  $\text{CdCl}_2$ /heat treatment conditions. Table 8.3 shows the results of  $V_{oc}$ ,  $J_{sc}$ , FF and  $\eta$  of fully fabricated CdTe solar cells. The maximum efficiency of 3.71% with  $V_{oc} \sim 530$  mV and FF  $\sim 0.50\%$  were achieved for devices with CdTe layers grown on ED-CdS deposited for 40 minutes with  $\text{CdCl}_2$ /heat treatment.

**Table 8.3:** Cell parameters under illumination of (n-i-p) CdTe thin film solar cells at different  $\text{CdCl}_2$ /heat treatment conditions.

Growth period of ED-CdS (minutes)	$V_{oc}$ (mV)			
	AD/AD	AD/HT	HT/AD	HT/HT
40	450	440	450	530
60	530	440	460	440
80	380	370	440	410
	$J_{sc}$ ( $\text{mAcm}^{-2}$ )			
40	7	7	10.5	14
60	6	7	12	18
80	5	12.5	16	18

	FF (%)			
40	0.27	0.37	0.36	0.50
60	0.26	0.37	0.33	0.38
80	0.26	0.44	0.35	0.37
	Efficiency (%)			
40	0.85	1.14	1.70	3.71
60	0.82	1.14	1.82	3.01
80	0.50	2.04	2.46	2.73

N/B: AD = as deposited and HT = CdCl<sub>2</sub>/heat treated

From the Table above, it is observed that the efficiency increases as the CdCl<sub>2</sub>/heat treatment condition improved. It is reported by Romeo et al. [14] and Mazzamuto et al. [6] that, a weak junction is formed if the CdTe grows on the surface of untreated CdS surface. This is because the CdS crystallites are very small and expose a large surface to CdTe attack, thus allowing a slow transition CdS → CdTe. On the other hand, if the CdTe grows on the surface of a CdS layer previously treated with CdCl<sub>2</sub>, then the good morphology and compactness of the polycrystalline film does not allow marked mixing thereby favouring the formation of an abrupt junction. Figure 8.15 show the individual graphs of V<sub>oc</sub>, J<sub>sc</sub>, FF and η of glass/FTO/CdS/CdTe/Au/contacts.

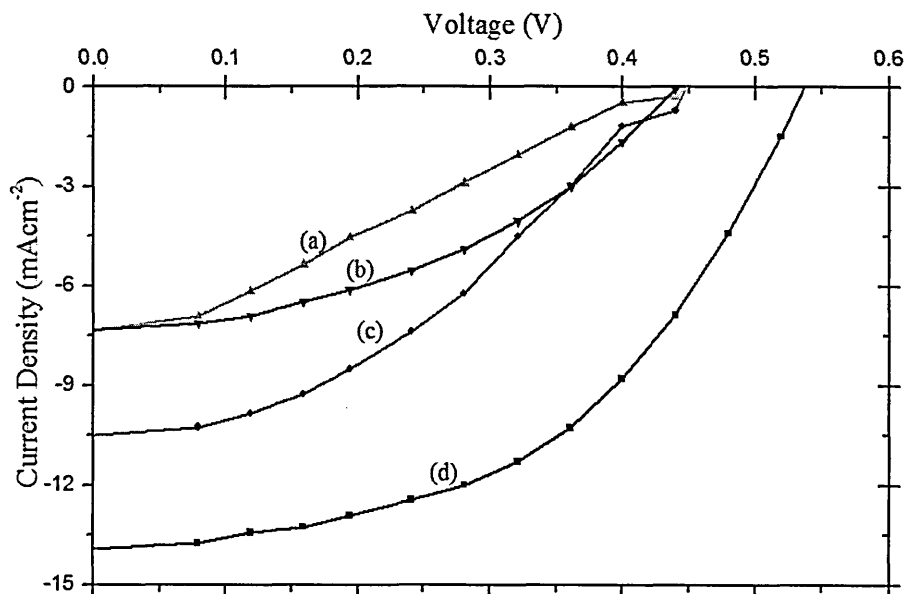


**Figure 8.12:** Linear I-V curve of glass/FTO/CdS/CdTe/Au contacts under AM 1.5 illumination condition for (n-i-p) CdTe layers grown on ED-CdS deposited at 40 minutes; (a) CdS(AD)/CdTe(AD), (b) CdS(AD)/CdTe(HT), (c) CdS(HT)/CdTe(AD) and (d) CdS(HT)/CdTe(HT).

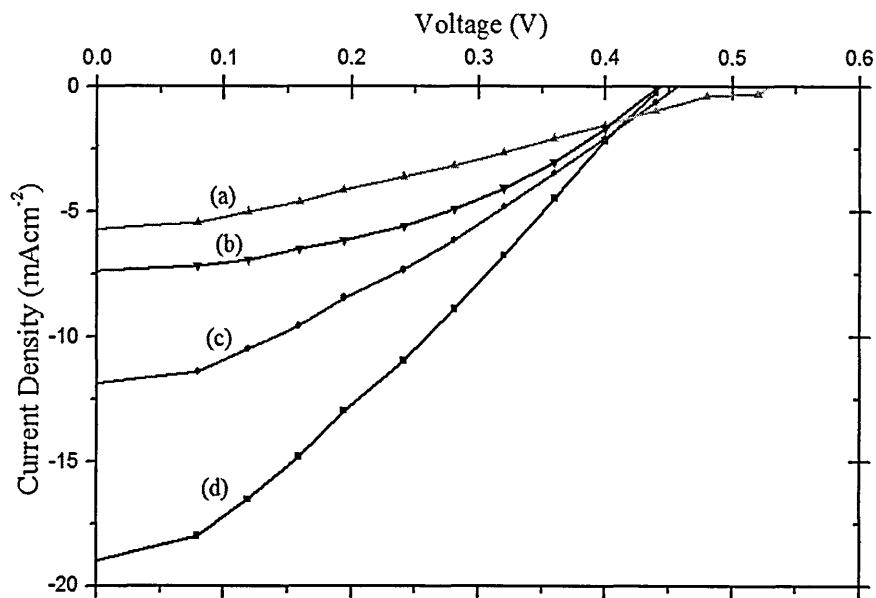


**Figure 8.13:** Linear I-V curve of glass/FTO/CdS/CdTe/Au contacts under AM 1.5 illumination condition for (n-i-p) CdTe layers grown on ED-CdS deposited at 60 minutes; (a) CdS(AD)/CdTe(AD), (b) CdS(AD)/CdTe(HT), (c) CdS(HT)/CdTe(AD) and (d) CdS(HT)/CdTe(HT).

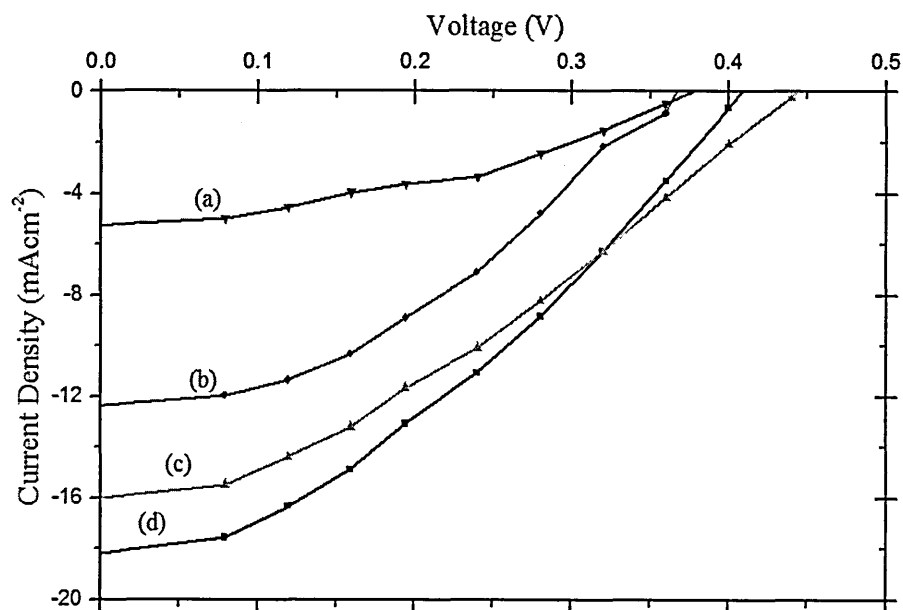


**Figure 8.14:** Linear I-V curve of glass/FTO/CdS/CdTe/Au contacts under AM 1.5 illumination condition for (n-i-p) CdTe layers grown on ED-CdS deposited at 80 minutes; (a) CdS(AD)/CdTe(AD), (b) CdS(AD)/CdTe(HT), (c) CdS(HT)/CdTe(AD) and (d) CdS(HT)/CdTe(HT).

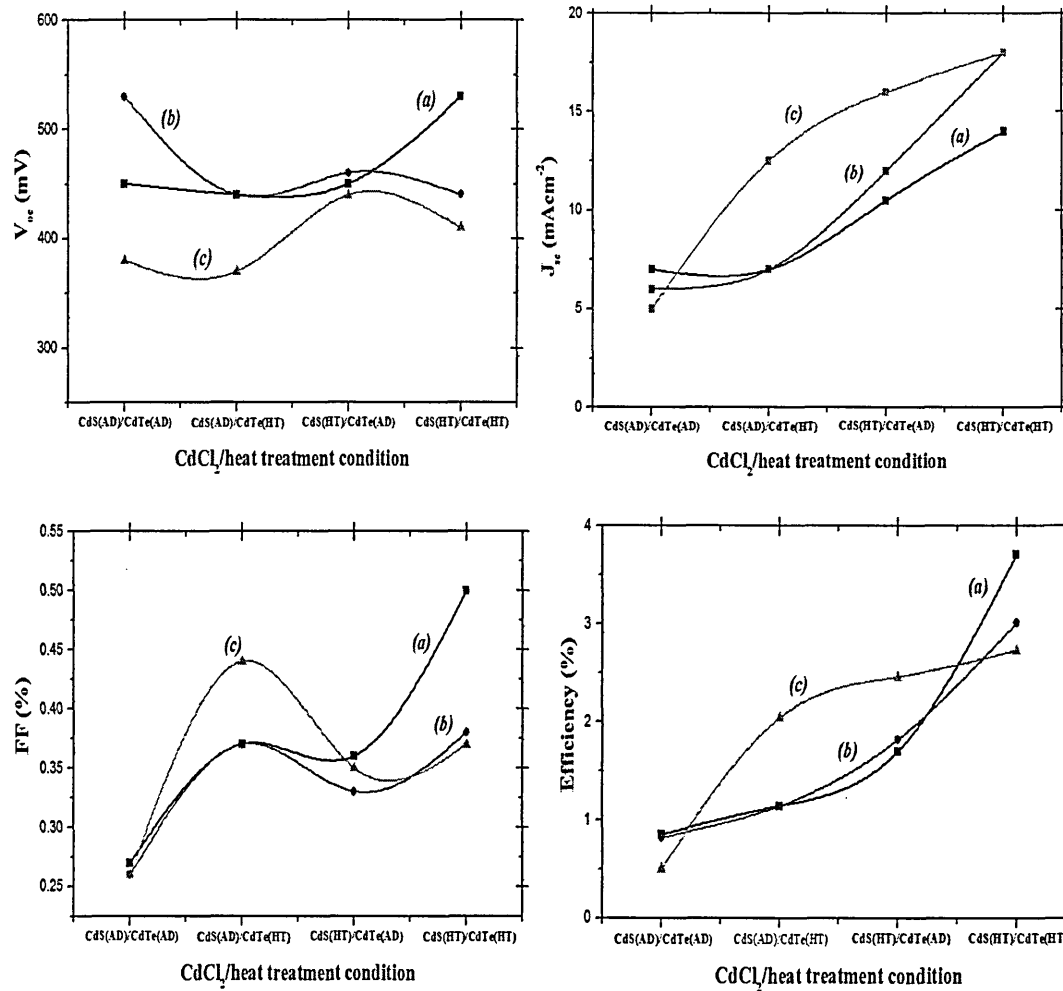


**Figure 8.14:** Cell parameters of (n-i-p) CdTe layers grown on ED-CdS at (a) 40 minutes, (b) 60 minutes and (c) 80 minutes under different CdCl<sub>2</sub>/heat treatment conditions.

### 8.5 Process performance relationship.

Table 8.6 shows the summary of the relationship between the device processing and performance. This process focuses on the effect of treated and untreated CdS and CdTe layers. It is clear that, the crystallite size for heat treated sample increases and the FWHM decreases, while the bandgap energies of the untreated CdS/CdTe films are higher. Furthermore, the maximum efficiency of 3.71% was achieved for devices with CdTe layers grown on ED-CdS deposited for 40 minutes with CdCl<sub>2</sub>/heat treatment.

**Table 8.5:** The summary of relationship between process and device performance.

Growth period of CdS (min)	XRD parameters				Bandgap (eV)		Cell efficiency, $\eta$ (%)	
	FWHM		Grain size, D (nm)					
	AD	HT	AD	HT	AD	HT	AD	HT
40	0.150	0.100	11.4	14.1	1.57	1.45	0.85	3.71
60	0.177	0.107	10.2	13.1	1.58	1.46	0.82	3.01
80	0.251	0.152	8.4	11.5	1.58	1.47	0.50	2.73

**N/B:** AD = untreated films (both CdS and CdTe are as deposited) and HT = treated films (both CdS and CdTe are heat treated).

## 8.6 Summary

CdTe has been deposited on glass/FTO/CdS substrates using low-cost aqueous electrodeposition method using a two-electrode system. The XRD results for both as deposited and heat treated CdTe layers have cubic structure with the main diffraction peak at  $2\theta = 23.642^\circ$  which corresponds to preferred orientation along (111) plane of cubic phase. Apart from the main peak (111), other peaks identified from the diffractogram are (220) and (311). These peaks are present in all the CdTe films deposited on untreated ED-CdS and as the condition improves the two peaks almost diminish for treated films grown on ED-CdS for 40 minutes. This indicates the presence of only (111) peak for highly textured films which have larger grains.

The optical absorption measurement shows that the treated CdS/CdTe films have a sharp absorption edge and a bandgap of 1.45 eV which is closer to the CdTe bulk value. The bandgap energy of the untreated CdS/CdTe films is larger and its absorption edge deviated from its sharp nature. The transmission coefficient of all the untreated CdS/CdTe films was found to be above 80% with the absorption edge shifted to the blue region. As the condition improve, the transmission coefficient reduces and the absorption edge increases giving the actual cut-off wavelength of CdTe  $\sim 852$  nm for treated films. Therefore, treated films are the most suitable absorbers for fabrication of solar cells, based on CdS/CdTe system.

SEM studies show that untreated samples show higher density of pin holes or gaps between the grains. The pin holes density diminishes as the treatment condition improved and the presence of these voids seem to be one of the main reasons for poor and inconsistent device performance. EDX spectra indicate the presence of both Cd and Te in these layers. The approximate atomic composition of Cd:Te estimated from the spectra is 57.4:42.6 for untreated sample and 58.3:41.7 for treated CdS/CdTe films. The  $\text{CdCl}_2$  treatment reduces the amount of precipitated Te in these layers, hence improving the device performance. The layers used in this work are rich in Cd, deviating from stoichiometric situation. This may be one reason for low efficiencies ( $\sim 3\text{-}4\%$ ) of devices fabricated using these layers.

Raman measurements indicate the presence of elemental Te in these thin films most probably due to precipitation. A strong Te- peak is observed in the untreated sample, the formation of Te in the film is detrimental to the CdTe layer which could lead to short-

circuiting in the device performance. The presence of Te in the CdTe layer reduces the crystallinity. This is confirmed by the presence of strong A1 phonons for pure Te at 120-122  $\text{cm}^{-1}$ . The presence of Te in CdTe (Te-rich CdTe) is detrimental for device performance since Te-rich CdTe layers have defects at 0.65 eV and 0.72 eV as reported by Dharmadasa [15]. These defects are right in the middle of the bandgap and hence maximise recombination process, drastically reducing the device performance. This also makes the CdTe layer p-type instead of n-type, required for high efficiency solar cells. After  $\text{CdCl}_2$ /heat treatment, the Te peak intensity reduces, and CdTe peaks improve appearing the second peak at 169  $\text{cm}^{-1}$ . This is strong evidence for removal of precipitated Te from CdTe layer during  $\text{CdCl}_2$ -heat treatment process. If there is any surface Te-layer,  $\text{CdCl}_2$ -treatment helps in converting some of the free Te into CdTe compound. This treatment also helps in doping the CdTe layer, n-type using the well-known dopant (Cl) of CdTe.

The linear I-V curves of glass/FTO/CdS/CdTe/Au contact under AM 1.5 illumination at different  $\text{CdCl}_2$ /heat treatment condition indicate that a maximum efficiency of 3.71% with  $V_{oc} \sim 530$  mV and FF  $\sim 0.50\%$  was achieved by CdTe layers grown on treated ED-CdS deposited for 40 minutes. The efficiency decreases drastically as a result of poor or weak interface formed if the CdTe grows on the surface of untreated CdS surface. This is because the CdS crystallites being very small expose to a large surface area to CdTe attack, thus allowing a slow transition  $\text{CdS} \rightarrow \text{CdTe}$ . Literature shows that the presence of  $\text{Cl}^-$  has a cementing effect in order to make larger grains. The pin holes are dominant in the untreated sample as a result it shorts the devices and therefore the efficiency suffers as shown from the I-V measurements. Although the number of measured devices are low (12-devices) for statistics, the emergence of groups of  $V_{oc}$  are apparent as first reported by Dharmadasa et al in 2002 [1]. The objectives of this chapter has been achieved, therefore, both layers (CdS and CdTe) must undergo  $\text{CdCl}_2$ /heat treatment.

## References

1. I. M. Dharmadasa, A. P. Samantilleke, N. B. Chaure and J. Young, *Semiconductor Science Technology* 17, 1238 (2002).
2. P. D. Paulson and V. Dutta, *Thin Solid Films* 370, 299 (2000).
3. M. Rami, E. Benamar, M. Fahoume, F. Chraibi and A. Ennaoui, *Material Journal Condense Matter* 3(1), 66 (2000).
4. I. M. Dharmadasa, S. M. McGregor, I. Wadsworth and C. M. Care, *Optical Materials* 6, 75 (1996).
5. A. Rios-Flores, J. L. Peña, V. Castro- Peña, O. Ares, R. Castro-Rodríguez and A. Bosio, *Solar Energy* 84, 1020 (2010).
6. S. Mazzamuto, L. Vaillant, A. Bosio, N. Romeo, N. Armani and G. Salviati, *Thin Solid Films* 516, 7079 (2008).
7. T. Potlog, L. Ghimpu, P. Gashin, A. Pudov, T. Nagle and J. Sites, *Sol. Energy Mater. Sol. Cells* 80, 327 (2003).
8. A. Kampmann and D. Lincot, *J. Electroanal. Chem.*, 418, 73 (1996).
9. A. R. Flores, R. Castro-Rodríguez , J. L. Peña, N. Romeo and A. Bosio, *Appl. Surface Science* 255, 7012 (2009).
10. H-K Na and P-K Shon, *Solid State Communication* 85(7), 609 (1993).
11. J. Rouusset, E. Rzepka, D. Lincot, *J. Phys. Chem. B* 113, 4333 (2009).
12. Y. Jung, S. Chun, D. Kim and J. Kim, *J. Crystal Growth* 326, 69 (2011).
13. R. Ochoa-Landin, O. Vigil-Galan, Y. V. Vorobiev and R. Ramirez-Bon, *Sol. Energy Mat. Sol. Cells* 83, 134 (2009).
14. N. Romeo, A. Basio, R. Tedeschi, A. Romeo and V. Canevari, *Sol. Energy Mater. Sol. Cells* 58, 209 (1999).
15. I. M. Dharmadasa, *Prog. Cryst. Growth & Charact.* 36(4), 249 (1998).

## **Chapter 9: Effect of CdS thickness on CdS/CdTe solar cell performance**

### **9.1 Motivation and objectives**

The aim of this chapter is to investigate the effect of CdS layer thickness on CdS/CdTe solar cell performance. If a CdS film is very thin, pin holes generation is possible due to the growth of CdS crystal/grains as islands. Again, when the CdS is very thick, CdTe growth is difficult may be due to the resistive layer created. It is known in the literature, that CdTe solar cell performance strongly depends on the CdS layer thickness.

### **9.2 Introduction**

CdS, being a window layer, is exposed to the incident radiation and absorbs light of short wavelength while the rest is transmitted through to the CdTe material. A CdS layer provides a better nucleation surface for CdTe layer to grow uniformly and contributes to the internal electric field necessary for separation of photogenerated charge carriers to prevent recombination within the PV cell.

Han et al [1] have reported that the performance of CdTe solar cells strongly depends on the CdS layer thickness. They have also explained that at lower thickness an appropriate  $J_{sc}$  can be achieved but the  $V_{oc}$  and FF suffer due to pin holes and leakage along the grain boundaries. Similarly, Rose et al [2] have reported that, when the thickness is higher, the  $J_{sc}$  value suffers due to absorption within the CdS layer. Therefore, the thickness of CdS should be optimised. The work presented in this chapter is to investigate the effect of CdS layer thickness on CdS/CdTe solar cells performance.

Five glass/FTO/ED-CdS substrates with different CdS layer thickness were used to grow the CdTe layers. The growth times for the ED-CdS were 20, 30, 40, 50 and 60 minutes, and each one of these samples is used to grow the CdTe film for 5 hrs. The growth voltages were changed in order for the deposition of CdTe layers to form (n-i-p), as discussed in chapter 7. Deposition of CdTe films have been discussed in section 3.4 of chapter 3.

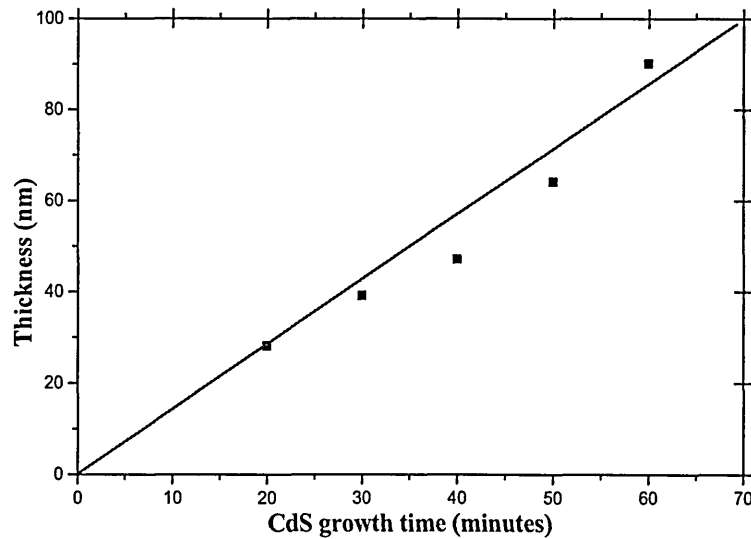
### 9.3 Thickness measurement

Table 9.1 shows the predicted thickness of CdS layer grown for different growth times using Faraday's equation (discussed in section 2.1.6.2 of chapter 2). Figure 9.1 shows the graph of CdS layer thickness against growth time.

**Table 9.1:** Predicted CdS thickness against growth time.

Growth time (seconds)	Thickness $\pm 5$ (nm)
20	28
30	39
40	47
50	64
60	90

As shown on the Table, as the growth time increases the thickness of the CdS layer is predicted to increase. Chu et al [3] have reported that a CdS layer ~90 nm thick can absorb about 63% of the incident radiation that has photon energy greater than the bandgap.



**Figure 9.1:** CdS thickness as a function of growth time.

## 9.4 Characterisation of CdTe

### 9.4.1 X-ray diffraction

Figure 9.2 shows the X-ray diffraction patterns for as deposited and heat treated CdTe layers deposited on ED-CdS for different times. The main diffraction peak at  $2\theta = 23.642^\circ$  corresponds to preferred orientation along (111) plane of cubic phase. This peak was assigned according to the JCPDS (01-075-2086) data on cubic CdTe. From the Figure, apart from the main peak (111), other peaks identified from the diffractogram are (220) and (311). These peaks are present in all the CdTe films deposited on CdS except for 40 minutes. This indicates that at lower and higher thickness of CdS the CdTe films grow with lower crystallinity.

After heat treatment in air at  $450^\circ\text{C}$  for 15 minutes, the intensity of all the peaks except for the thinnest decreases, possibly due to loss of material through sublimation. The decrease in FWHM indicates an increase in grain size and/or an improvement in crystallinity. The heat treatment enhances the recrystallisation of CdTe films reducing any stress within the films and due to sublimation of excess elements from the layer. The values of XRD intensity, FWHM and D of (n-i-p) CdTe layers deposited on CdS at different growth time are presented in Table 9.2 using equation 2.18 given in section 2.2.1 of chapter 2.

**Table 9.2:** XRD intensity, FWHM and grain size of CdTe grown on CdS at different growth time [AD = as deposited and HT = heat treated].

Growth time (minutes)	XRD Intensity (arb. units)		FWHM		Grain size, D (nm)	
	AD	HT	AD	HT	AD	HT
20	5264	5661	0.167	0.150	9.2	11.0
30	6441	5992	0.150	0.134	10.2	12.2
40	8000	7000	0.117	0.100	13.1	15.3
50	7683	6159	0.148	0.130	10.7	11.9
60	9786	5876	0.150	0.134	10.2	11.4

From the Table, it is observed that the grain size for heat treated sample increases and the FWHM decreases; this is due to the coalescence of small crystals and the formation of large grains. Furthermore, at higher and lower thickness of CdS (i.e. greater or less than 40 minutes) the grain size decreases and FWHM increases. This shows that

thickness plays an important role in giving a better nucleation surface for CdTe growth. Figures 9.3, 9.4 and 9.5 shows the XRD intensity, FWHM and grain size of CdTe layer grown on CdS at different growth period.

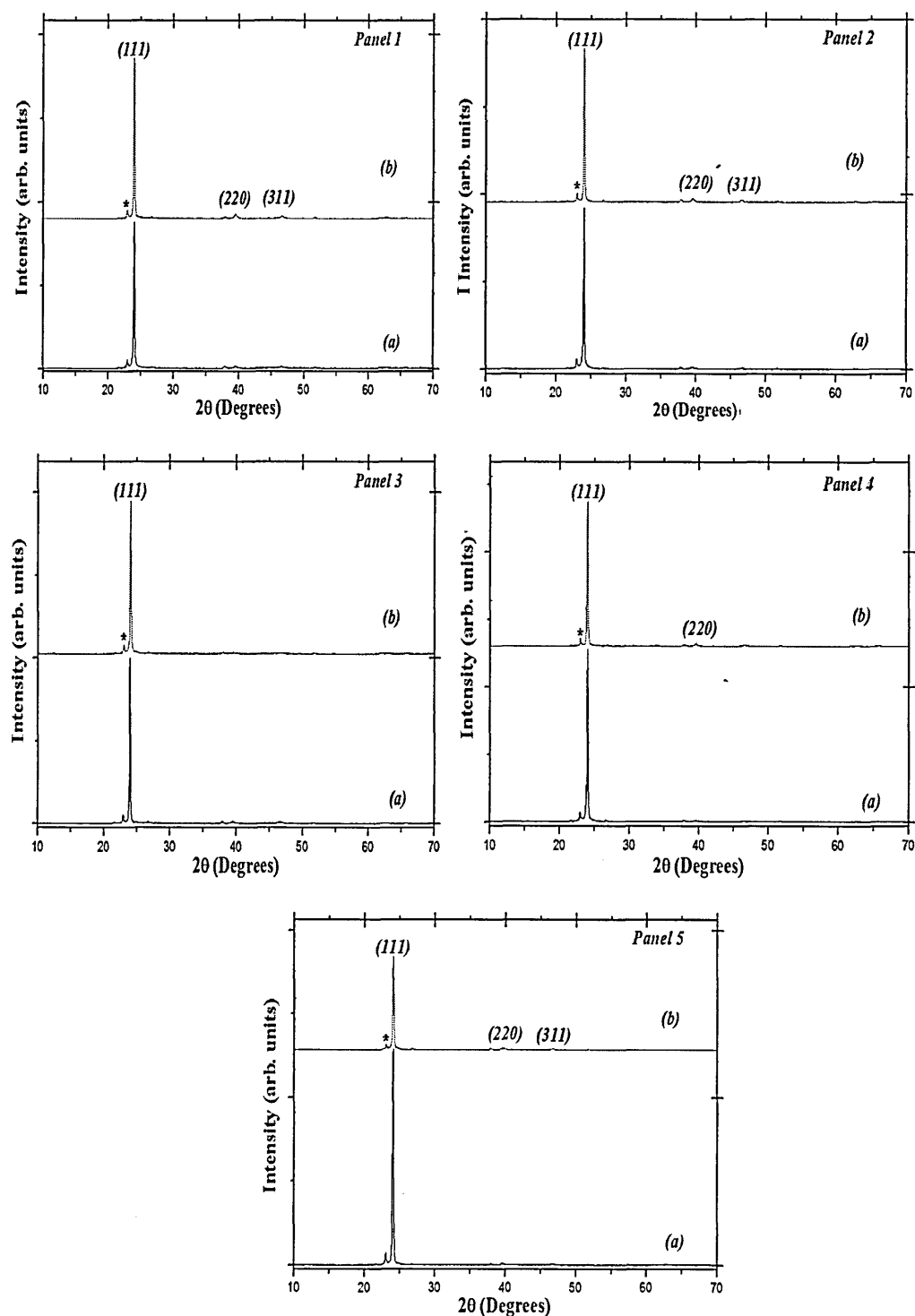


**Figure 9.2:** X-ray diffraction pattern of CdTe layer grown on different CdS grown for [panel 1 = 20 min, panel 2 = 30 min, panel 3 = 40 min, panel 4 = 50 min and panel 5 = 60 min] (a) as deposited and (b) heat treated (\* indicates Te peak).

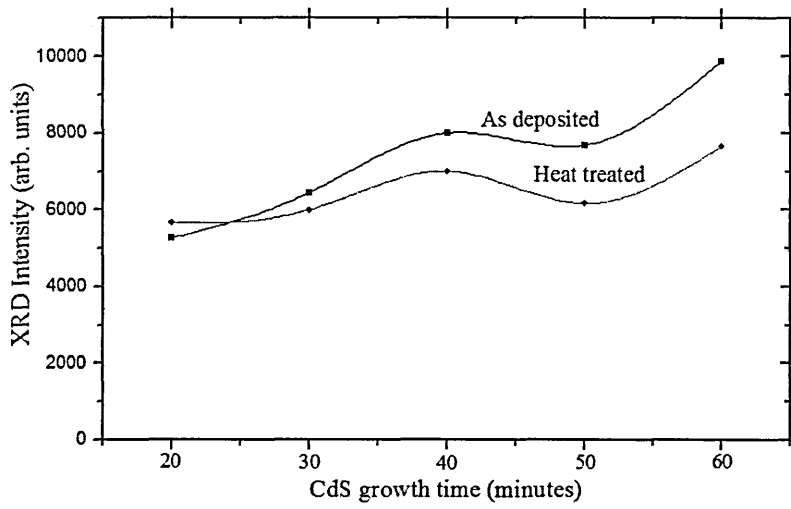


**Figure 9.3:** XRD intensity of (111) peak observed for (n-i-p) CdTe layers grown on different CdS thickness.

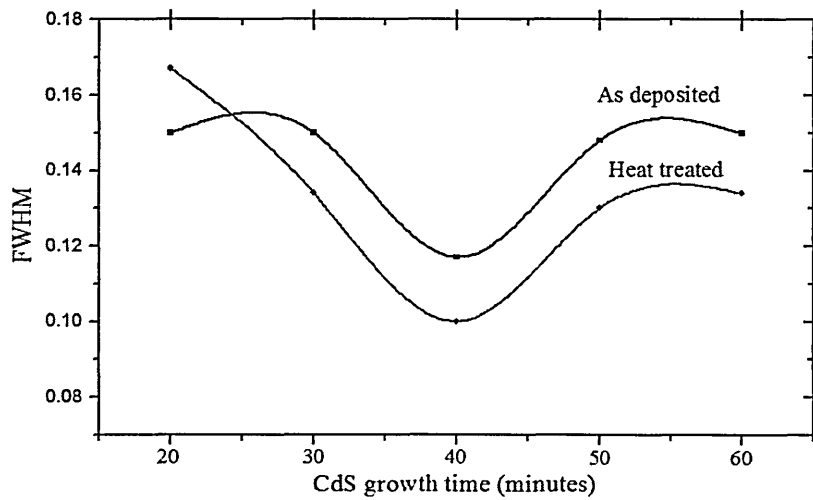


**Figure 9.4:** FWHM of (111) peak observed for (n-i-p) CdTe layers grown on different CdS thickness.

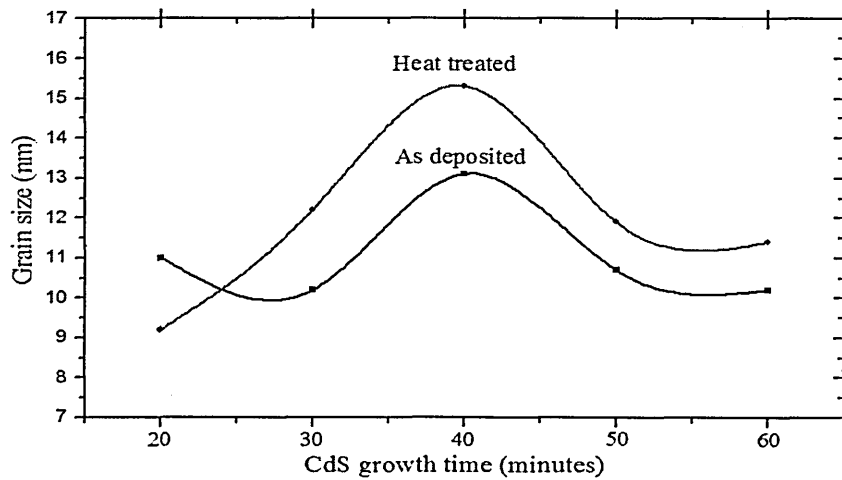


**Figure 9.5:** Grain sizes estimated from (111) peak observed for (n-i-p) CdTe layers grown on different CdS thickness.

## 9.4.2 Optical absorption

Optical absorption measurements were carried out in order to evaluate the bandgap of materials. Figure 9.6 shows the graphs of optical absorption for as deposited and heat treated CdTe layers grown on ED-CdS at different growth time. Using equation 2.21 on section 2.2.3 in chapter 2, the bandgap energy,  $E_g$  was determined by plotting the square of absorption ( $A^2$ ) against photon energy ( $h\nu$ ). As shown from the Figure, the value of  $E_g$  for as deposited CdTe is between 1.56 - 1.55 eV. After heat treatment in air at 450°C for 15 minutes there was a sharp absorption edge of the curve and a bandgap of 1.45 eV which is close to the bulk value for CdTe. The reason for the absorption edge sharpening might be due to a change in the stoichiometry or reduction of intrinsic defect population of the treated samples. Table 9.3 gives the bandgap values of CdTe layers grown on different thicknesses of CdS and Figure 9.7 shows the graphical presentation of the same results.

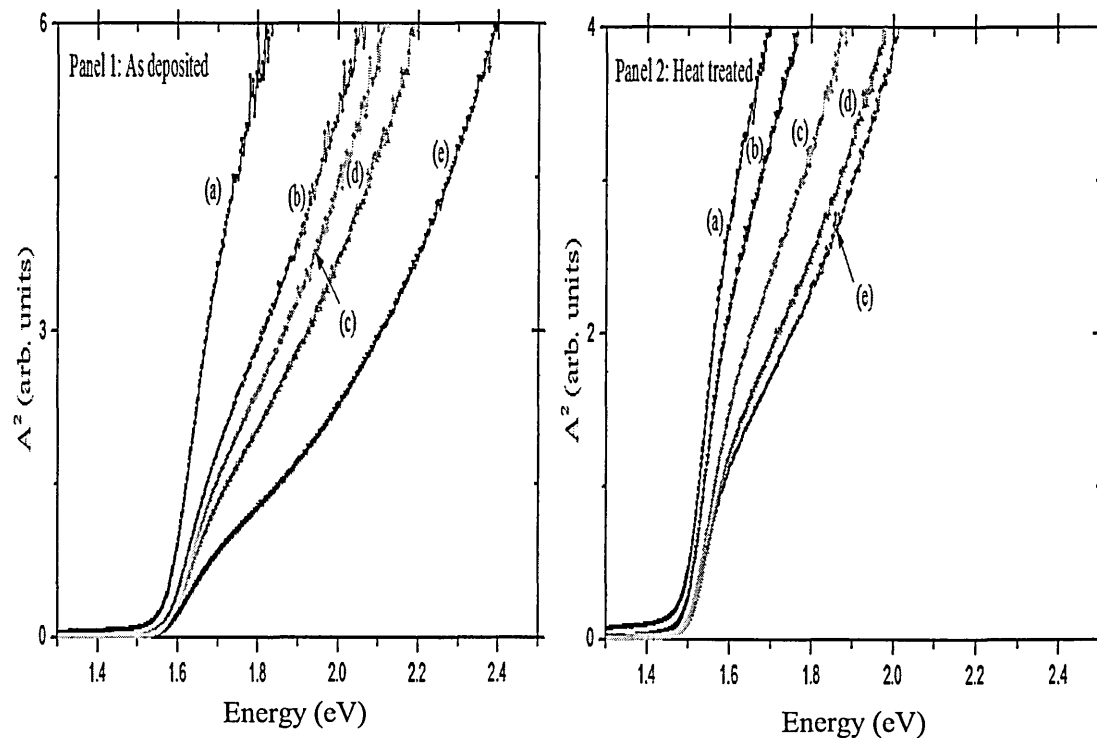


**Figure 9.6:** Optical absorption curves for (n-i-p) CdTe layers grown for 5 hrs on CdS grown for [a = 40 min, b = 30 min, c = 50 min, d = 60 min and e = 20 min] (panel 1) as deposited and (panel 2) heat treated.

**Table 9.3:** Bandgap energy of (n-i-p) CdTe layers grown on ED-CdS at different growth time [AD = as deposited and HT = heat treated].

Growth time (minutes)	Bandgap (eV)	
	AD	HT
20	1.56	1.45
30	1.55	1.45
40	1.55	1.45
50	1.56	1.45
60	1.56	1.45

As shown from Table 9.3, the bandgap energies for as deposited CdTe films are higher than bulk, whereas the bandgap energy of all the films after heat treatment is 1.45 eV which is close to the bulk CdTe value. The reason for this may be a change in the stoichiometry, a reduction in the intrinsic defect population and improved crystallinity, or a larger grain size removing quantum effects.

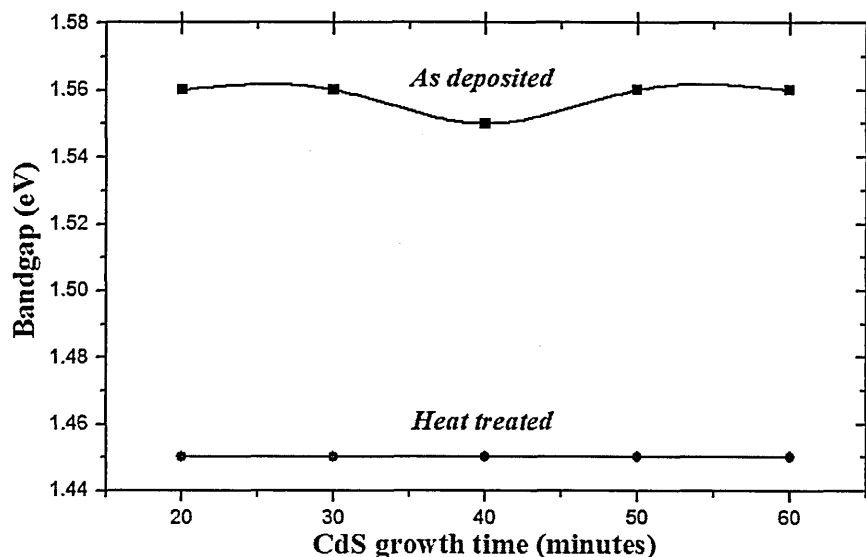


**Figure 9.7:** Bandgap energy for (n-i-p) CdTe layer grown on ED-CdS at different growth time.

The optical transmission spectra for as deposited and heat treated (n-i-p) CdTe layers grown on ED-CdS at different thickness are shown in Figure 9.8. Measurements were taken in the wavelength range 600 – 1000 nm on the deposited films. The transmission coefficient for as deposited CdTe layers grown on CdS deposited for 40 minutes was

found to be less than 70% while others have more than 80% with the absorption edge shifted to the blue region. After heat treatment the transmission coefficient decreases and the absorption edge of all the CdTe films sharpened with a slight shift to the red. Metin and Esen [4] reported that a sharper absorption edge indicates fewer defect and impurity energy levels in the film. It has also been reported that when the CdS is very thin, there is higher transmission of photons [5]. Furthermore, it is observed from Figure 9.8 panel 2 that the band edge of the films grown on CdS deposited for 40 minutes gives the cut-off wavelength of CdTe  $\sim 852$  nm with a transmission coefficient  $\sim 43\%$  and the absorption edge shifted to the red. This shows that light absorption is very good in CdTe and hence generation of e-h pairs is higher, improving the efficiency of the devices. At higher and lower CdS thickness, light absorption is weak which made the efficiency poor.

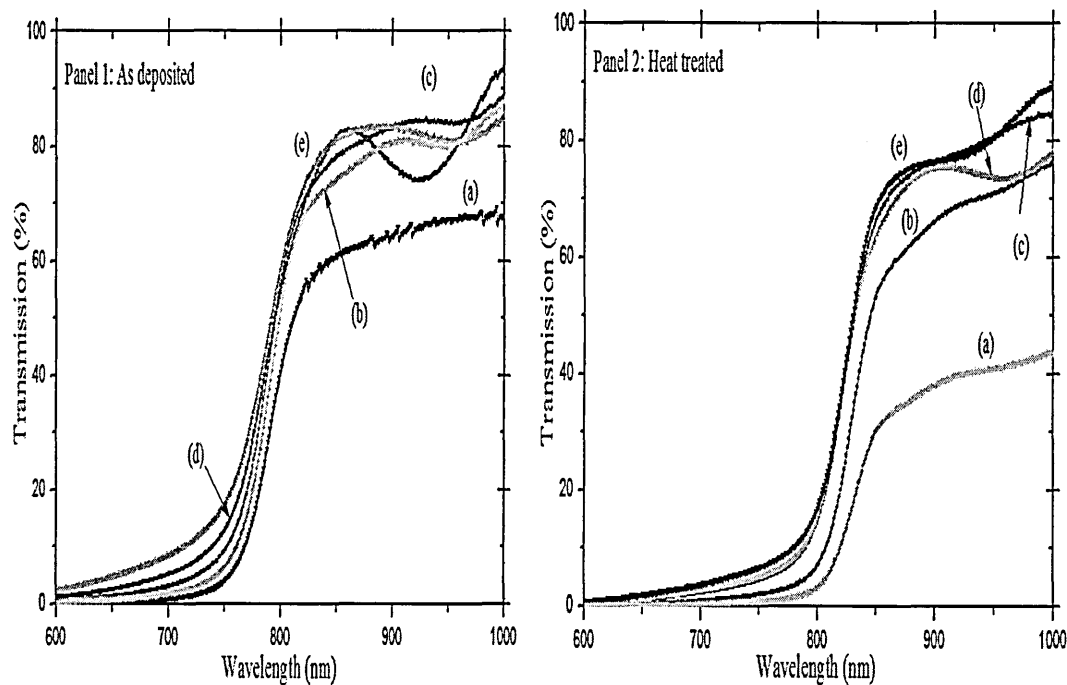


**Figure 9.8:** Optical absorption curves for (n-i-p) CdTe layers grown on CdS deposited for [a = 40 min, b = 30 min, c = 50 min, d = 60 min and e = 20 min] (panel 1) as deposited and (panel 2) heat treated.

#### 9.4.3 Scanning Electron Microscopy

SEM studies were carried out to investigate the surface morphology, grain size and uniformity of CdTe layers grown on ED-CdS at different thickness. Figure 9.9 [a, b and c] and [d, e and f] shows the SEM images of CdTe layers grown for 5 hrs on CdS grown

for 20, 40 and 60 minutes, as deposited and heat treated respectively. As seen in the Figure, the as deposited samples show a lot of pin holes (gaps) between the grains. The gaps seem to be dominant in CdTe grown on the thinnest CdS layer. If a CdS film is very thin, pin holes generation is possible due to the growth of CdS as islands, and therefore the device performance is poor due to shorting the back metal contact to the front TCO layer. CdTe grows better on CdS layers with moderate thickness. The pin holes reduce after the heat treatment, with larger grains observed on the CdTe films deposited on CdS layers grown for 40 minutes. These results confirmed that heat treatment enhances the recrystallisation and coalesce grains to fill the gaps between grains.

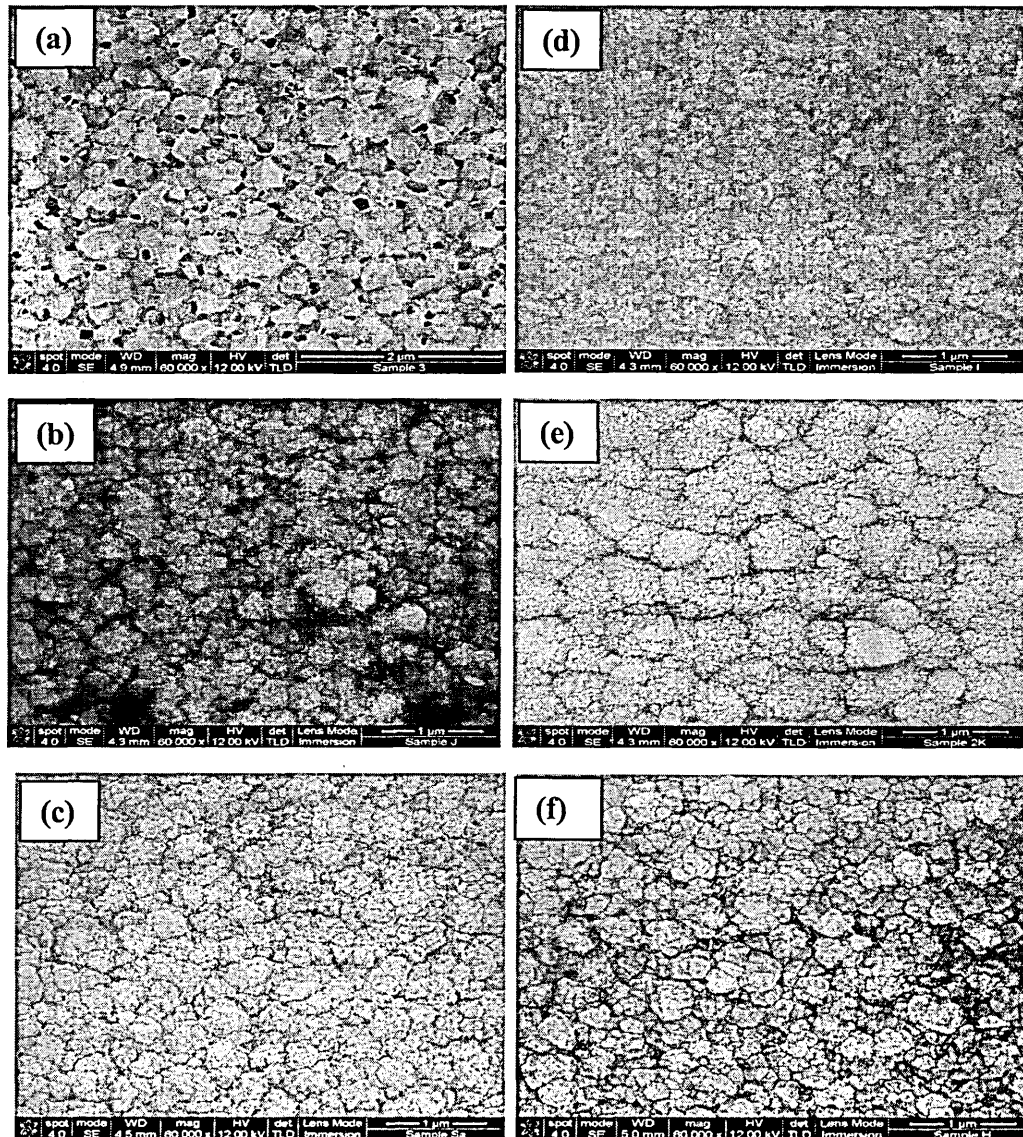


**Figure 9.9:** SEM images for (n-i-p) CdTe layers grown on CdS deposited for [a = 20 min, b = 40 and c = 60 min] as deposited and [d = 20 min, e = 40 min and f = 60 min] heat treated.

These undesirable gaps are also found in CdTe layers grown on ED-CdS layers grown for 60 minutes. The CdTe growth is columnar and therefore some layers grow on the FTO and others on the CdS producing two parallel diodes with very different qualities. Similarly, when the CdS is very thick, CdTe growth is difficult may be due to the resistive layer created.

### 9.4.4 Energy Dispersive X-ray

Energy dispersive x-ray (EDX) technique was carried out to investigate the qualitative elemental analysis of the CdTe layers. The EDX spectra of (n-i-p) heat treated CdTe layers grown on ED-CdS at different thickness are shown in Figures 9.10. In all these spectra, the presence of both Cd and Te peaks were observed. The appearance of sulphur peaks in (a) is may be due to the thickness of the CdS layer used which is ~28 nm estimated from Table 9.1 in section 9.3. Chlorine peak is also observed in (b) as a result of moderate thickness of CdS ~47 nm. The atomic composition of Cd:Te estimated from the spectra are 45.7:54.3, 53.2:46.8 and 51.6:48.4 for CdTe layers grown on CdS deposited for 20, 40 and 60 minutes respectively.

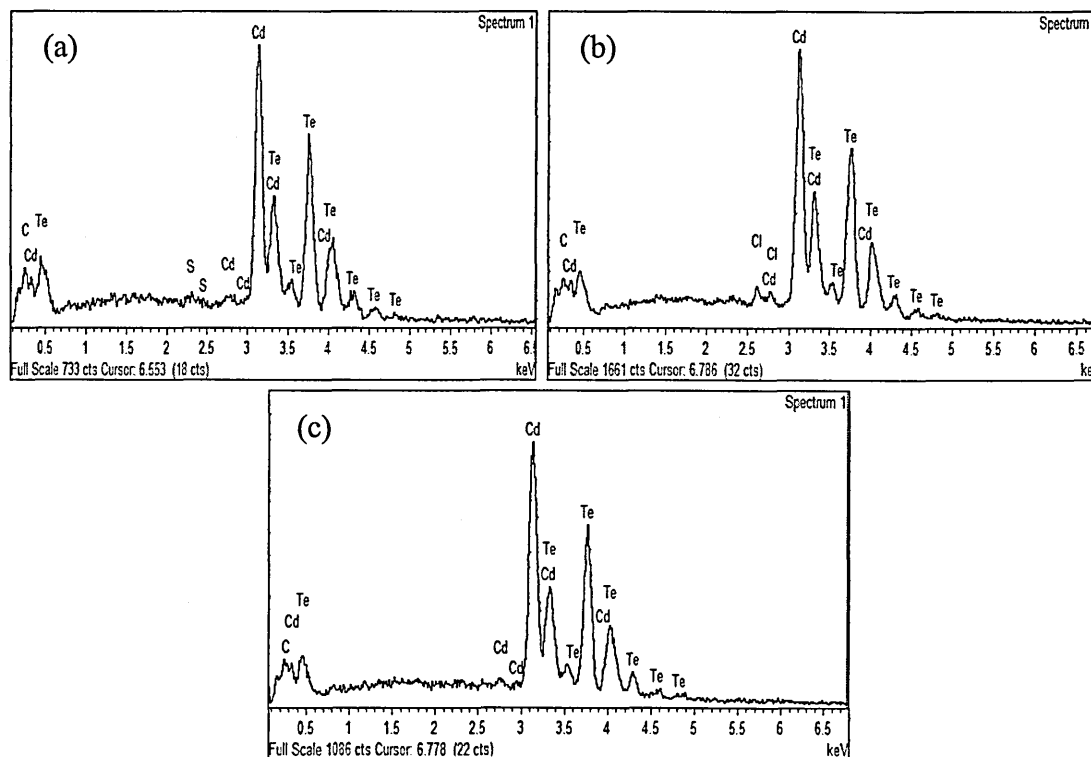


**Figure 9.10:** EDX spectra for heat treated (n-i-p) CdTe layers grown on CdS deposited for (a) 20 min, (b) 40 min and (c) 60 minutes.

### 9.4.5 Raman Spectroscopy

The molecular structure and identification of phases in films was explored using Raman spectroscopy. The Raman spectrum of a thick CdTe layer grown on InSb substrate is shown in Figure 9.11 for comparison [6]. Figure 9.12 shows the Raman spectra for heat treated (n-i-p) CdTe layers grown on CdS at different thickness.

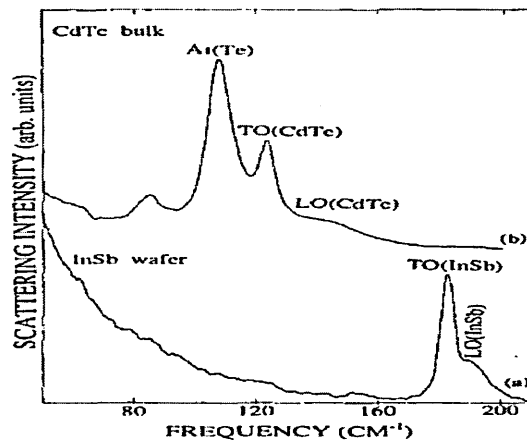


Figure 9.11: Raman spectrum of a thick CdTe layer grown on InSb substrate [6].

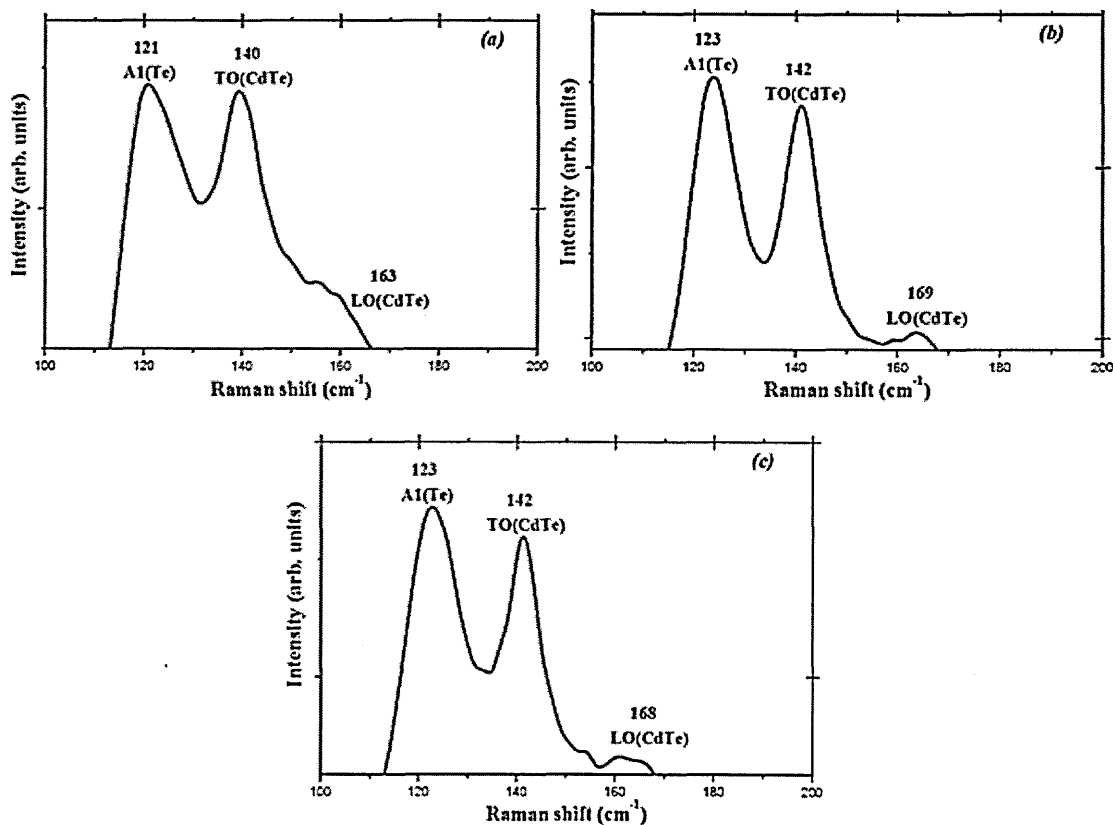


Figure 9.12: Raman spectra for heat treated (n-i-p) CdTe layers grown on CdS for (a) 20 minutes, (b) 40 minutes and (c) 60 minutes (courtesy: Inst. of Mater. Research, Univ. of Leeds).

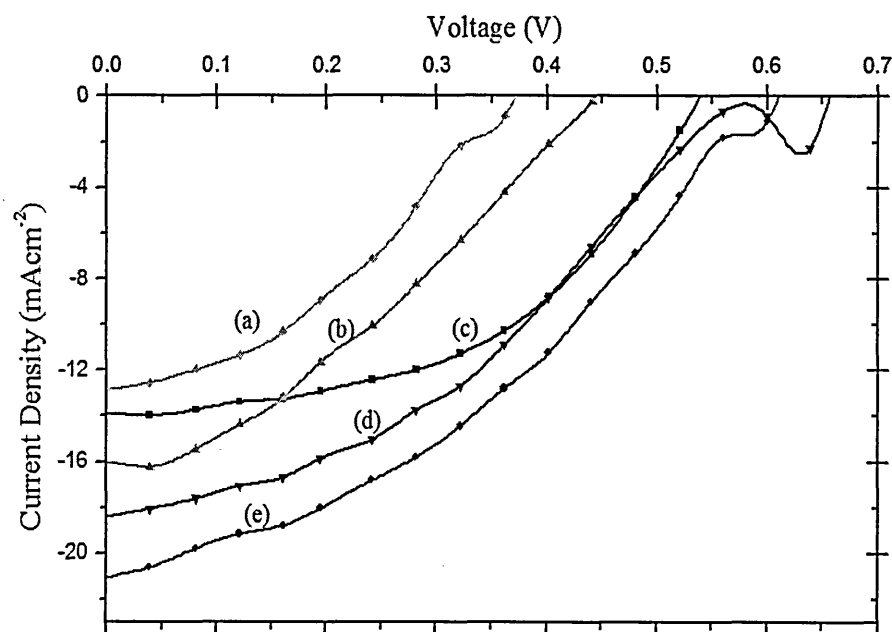
As shown in Figure 8.12, the A1 phonon  $121 - 123 \text{ cm}^{-1}$  of the pure tellurium phase is present in all the films. Also observed are two peaks related to CdTe which correspond to fundamental transverse (1TO)  $140 - 142 \text{ cm}^{-1}$  and longitudinal optical phonons (1LO)  $163 - 169 \text{ cm}^{-1}$ . The LO(CdTe) peak is very weak in the film grown on CdS deposited for 20 minutes. All these peaks are very close to those reported by other researchers in the field [7-9]. For ideal CdTe material, where there is no precipitation of elemental Te, the peak at  $121-123 \text{ cm}^{-1}$  should not be present.

## 9.5 Device characterisation

As discussed in chapter 6, the completed glass/FTO/CdS/(n-i-p)CdTe/Au contacts were then assessed using I-V technique.

### 9.5.1 Current-voltage (I-V) characteristics

Figure 9.13 show the linear I-V curves of glass/FTO/CdS/(n-i-p)CdTe/Au contacts under AM 1.5 illumination for devices with CdTe layers grown on ED-CdS of different thickness.



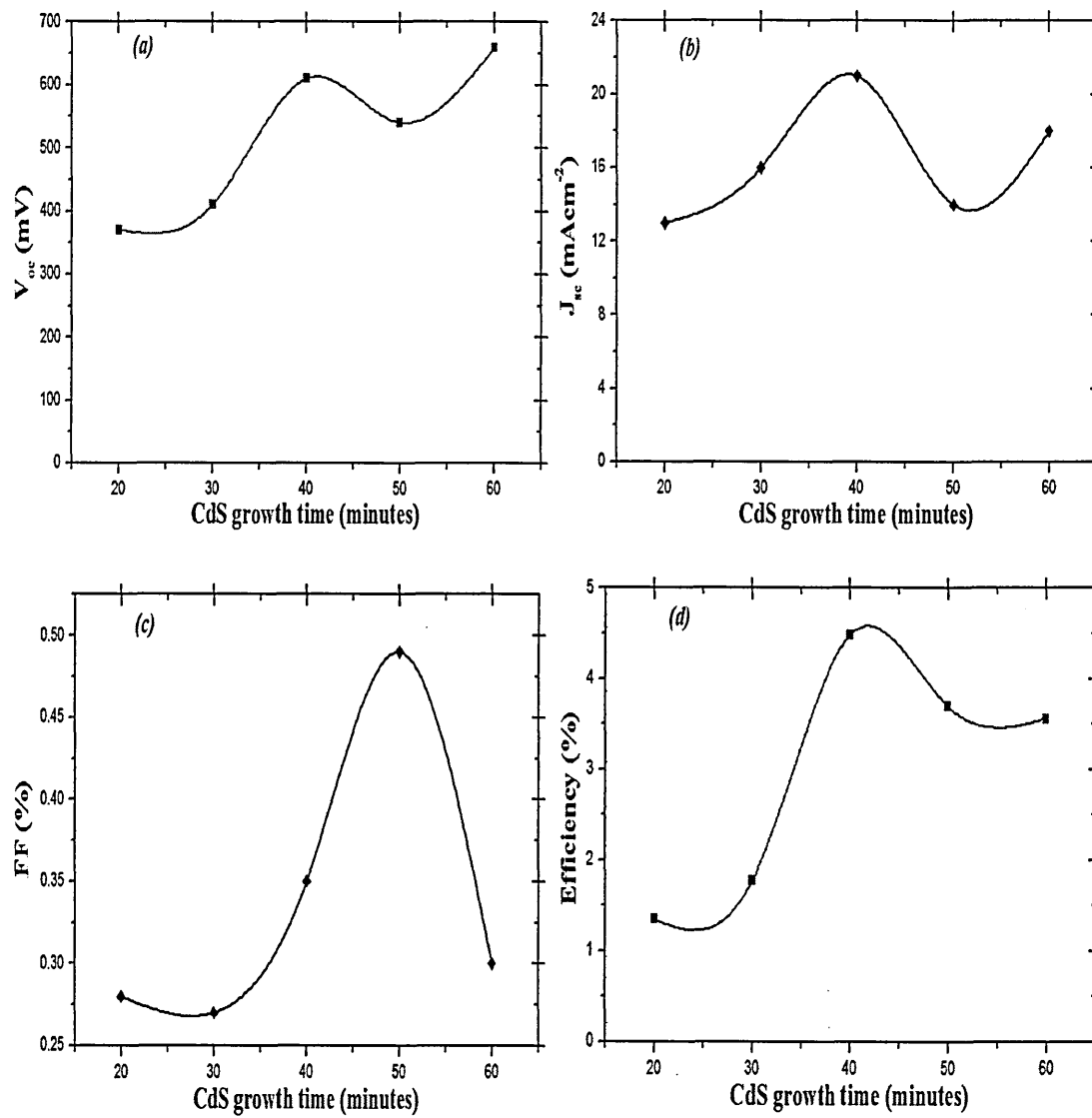
**Figure 9.13:** Linear I-V curve of glass/FTO/CdS/(n-i-p)CdTe/Au contact under AM 1.5 illumination condition for CdTe layers grown on ED-CdS deposited for (a) 20 minutes, (b) 30 minutes, (c) 50 minutes, (d) 60 minutes and (e) 40 minutes.

Table 9.4 gives the values of  $V_{oc}$ ,  $J_{sc}$ , FF and  $\eta$  of the fully fabricated CdTe solar cells. A maximum efficiency of 4.48% with  $V_{oc} \sim 610$  mV and  $J_{sc} \sim 21$  mAcm<sup>-2</sup> was achieved for devices with CdTe layers grown on ED-CdS deposited for 40 minutes.

**Table 9.4:** Cell parameters under illumination of CdTe thin film solar cells grown on CdS at different thicknesses.

Growth time (minutes)	Cell parameters			
	$V_{oc}$ (mV)	$J_{sc}$ (mAcm <sup>-2</sup> )	FF (%)	$\eta$ (%)
20	370	13	0.28	1.35
30	410	16	0.27	1.77
40	610	21	0.35	4.48
50	540	14	0.49	3.70
60	660	18	0.30	3.56

From the Table above, it is observed that the efficiency of the CdTe films grown on CdS of lower and higher thicknesses decreases. It has been reported by Han et al. [1] that the poor performance is due to more shunt paths in the thinner CdS layer or inter-diffusion at the interface between CdTe & CdS. Similar observations are reported by Hadrich et al [10] and Krishnakumar et al [11]. It is desirable to reduce the CdS thickness in order to reduce losses in quantum efficiency and  $J_{sc}$  [10, 11]. Figure 9.14 shows the individual graphs of  $V_{oc}$ ,  $J_{sc}$ , FF and  $\eta$  of glass/FTO/CdS/(n-i-p)CdTe/Au/contacts.



**Figure 9.14:** Cell parameters of (n-i-p) CdTe layers grown on ED-CdS for different thickness.

### 9.6 Process performance relationship.

Table 9.6 shows the summary of the relationship between the process and device performance. It is clear from the results that CdTe deposited on CdS grown for 40 minutes (~47 nm) produce devices with better performance.

**Table 9.5:** The summary of process performance relation according to growth periods of CdS.

Growth time of CdS (min)	XRD parameters		Bandgap (eV)	Cell efficiency, $\eta$ (%)
	FWHM	Grain size, D (nm)		
20	0.167	9.2	1.45	1.35
40	0.100	15.3	1.45	4.48
60	0.134	11.4	1.45	3.56

## 9.7 Summary

CdTe has been deposited on glass/FTO/CdS substrates using a low-cost aqueous electrodeposition method using two-electrode system. The XRD results for both as deposited and heat treated CdTe layers have cubic structure with the main diffraction peak at  $2\theta = 23.642^\circ$  which corresponds to preferred orientation along (111) plane of cubic phase. Apart from the main peak (111), other peaks identified from the diffractogram are (220) and (311). These peaks are present in all the CdTe films grown on CdS except for 40 minutes. This indicates that at lower and higher thickness the CdTe films grow with lower preferred orientation.

The optical absorption measurements show the bandgap,  $E_g$  for as deposited samples is between 1.56 - 1.55 eV. After heat treatment in air at  $450^\circ\text{C}$  for 15 minutes the bandgap values of all the films decreased and produced a sharp absorption edge with a bandgap of 1.45 eV which is closer to the  $E_g$  of the CdTe bulk material. The transmission of as deposited CdTe layers grown on CdS deposited for 40 minutes was found to be less than 70% while all the others have more than 80%. After heat treatment the transmission decreases and the absorption edge of all the CdTe films sharpened with a slight shift to the red region. It is known from the literature [1], that CdTe solar cell performance strongly depends on the CdS layer thickness. The transmission coefficient shows ~43% for the CdTe deposited on CdS grown for 40 minutes. This shows that light absorption is very good in CdTe and hence generation of e-h pairs is higher, improving the efficiency of the devices. At higher and lower CdS thickness, light absorption is weak which made the efficiency poor.

As shown from the SEM results, as deposited samples show a lot of pin holes (gaps) between the grains. The pin holes density is higher in the films grown on the thinnest CdS layer. The pin holes diminish after the heat treatment with larger grains observed on the CdTe films deposited on CdS for 40 minutes. These undesirable gaps are also found in CdTe layers grown on ED-CdS layers grown for 60 minutes. CdTe grows better on CdS layers with moderate thickness. If a CdS film is very thin, pin holes generation is possible due to the growth of CdS as islands. The CdTe growth is columnar and therefore some layers grow on the FTO and others on the CdS producing two parallel diodes with very different qualities. Similarly, when the CdS is very thick, CdTe growth is difficult may be due to the resistive layer created.

The EDX spectra of (n-i-p) heat treated CdTe layers grown on ED-CdS of different thicknesses indicate the presence of both Cd and Te in the films. The approximate atomic composition of Cd:Te estimated from the spectra are 45.7:54.3, 53.2:46.8 and 51.6:48.4 for CdTe layers grown on CdS deposited for 20, 40 and 60 minutes respectively. Raman spectra show that A1 phonon of elemental tellurium is present in all the films. Also observed are two peaks related to CdTe layers which correspond to the fundamental transverse (1TO) and longitudinal optical phonons (1LO) respectively.

The linear I-V curves of glass/FTO/CdS/(n-i-p)CdTe/Au devices grown with different CdS thicknesses have a maximum efficiency of 4.48% with  $V_{oc}$  ~610 mV and  $J_{sc}$  ~21  $\text{mAcm}^{-2}$ , which was achieved for devices with CdTe layers grown on ED-CdS deposited for 40 minutes. The efficiency of the films grown on thicker or thinner CdS decreases as a results of poor performance which may be due to shunt paths or inter-diffusion at the interface between CdTe & CdS. As shown from the results above, CdTe solar cell performance strongly depends on the CdS layer thickness. Therefore the objectives have been achieved.

## References

1. J. Han, C. Spanheimer, G. Haindl, G. Fu, V. Krishnakumar, J. Schaffner, C. Fan, K. Zhao, A. Klein and W. Jaegermann, *Sol. Energy Mater. Sol. Cells* 95, 816 (2011).
2. D. H. Rose, F. S. Hasoon, R. G. Dhere, D. S. Albin, R. M. Ribeln, X. S. Li, Y. Mahathongdy, J. A. Gessert and P. Sheldon, *Prog. Photovolt: Research Appl.* 7, 331 (1999).
3. T. L. Chu and S. S. Chu, *Solid State Electronics* 38(3), 533 (1995).
4. H. Metin and R. Esen, *Semicond. Sci. Technol.* 18, 647 (2003).
5. K. Durose, P. R. Edwards and D. P. Halliday, *J. of Crystal Growth* 197(3), 733 (1999).
6. H-K Na and P-K Shon, *Solid State Communication* 85(7), 609 (1993).
7. Y. Jung, S. Chun, D. Kim and J. Kim, *J. Crystal Growth* 326, 69 (2011).
8. J. Roussel, E. Rzepka, D. Lincot, *J. Phys. Chem. B* 113, 4333 (2009).
9. R. Ochoa-Landin, O. Vigil-Galan, Y. V. Vorobiev and R. Ramirez-Bon, *Sol. Energy Mat. Sol. Cells* 83, 134 (2009).
10. M. Hadrich, C. Kraft, H. Metzner, U. Reislohner, C. Loffler and W. Witthuhn, *Phys. Status Solidi C* 6(5), 1257 (2009).
11. V. Krishnakumar, J. Han, A. Klein and W. Jaegermann, *Thin Solid Films* (2010), doi:10.1016/j.tsf.2010.12.118.

## Chapter 10: Effect of different Transparent Conducting Oxides (TCOs) on the CdTe layer

### 10.1 Motivation and objectives

Buffer layers such as i-ZnO and ZnO:Al play an important role in developing stable and high efficiency solar cells. There is suggestion that these layers act as a barrier layer which prevents Na diffusion into the CdTe solar cells during heat treatment at higher temperatures especially when the material layer is grown on a soda-lime glass. The aim of this chapter is to investigate the effect of different Transparent Conducting Oxides (TCOs).

### 10.2 Introduction

Transparent Conducting Oxides (TCOs) are suitable for a great variety of applications due to their high transparency and near-metallic electrical conductivity. TCOs are key components in most optoelectronic devices. In solar cells, TCOs are used as the current collector; they are applied as an n-type transparent electrical contact with a free carrier concentration between  $10^{18} \text{ cm}^{-3}$  and  $10^{20} \text{ cm}^{-3}$  [1, 2]. The bandgap energy,  $E_g$  of these oxide layers is in the range of 3.50 to 4.30 eV and their optical transmission is in the range of 80 - 85% in the visible-near IR range depending on the deposition process [2-4]. In this work, five different TCOs have been examined for material characterisation and device analysis. They includes FTO (TEC-7 & TEC-15), ZnO:Al, i-ZnO and ITO. Detailed properties of various TCOs used in this work have been discussed in Section 1.7 of chapter 1.

Five glass/TCO substrates, each with a different TCO were used to grow the CdS and CdTe layers. The growth voltages were changed in order for the deposition of CdTe layers to form (n-i-p), as discussed in chapter 7. Deposition of CdTe films have been discussed in section 3.4 of chapter 3.

### 10.3 Characterisation of CdTe grown with different TCOs

#### 10.3.1 X-ray diffraction

Figure 10.1 shows the X-ray diffraction patterns for as deposited and heat treated (n-i-p) CdTe layers deposited on ED-CdS grown on different TCO substrates. The main diffraction peak at  $2\theta = 23.642^\circ$  corresponds to preferred orientation along (111) plane of the cubic phase. This peak was assigned according to the J JCPDS (01-075-2086) data on cubic CdTe. Other peaks identified from the diffractogram are (220) and (311). These peaks are present in all the CdTe films but their intensity was depended on the TCO layer.

After heat treatment in air at  $450^\circ\text{C}$  for 15 minutes the intensity of all the peaks decreases due to loss of material through sublimation. The decrease in FWHM indicates an increase in grain size and/or an improvement in crystallinity. The heat treatment enhances the grain growth of CdTe films, reducing residual stress within the films and may also cause sublimation of excess elements from the layer. The values of XRD intensity, FWHM and D of (n-i-p) CdTe layers deposited on CdS grown on different TCOs are presented in Table 10.1 using equation 2.18 given in section 2.2.1 of chapter 2.

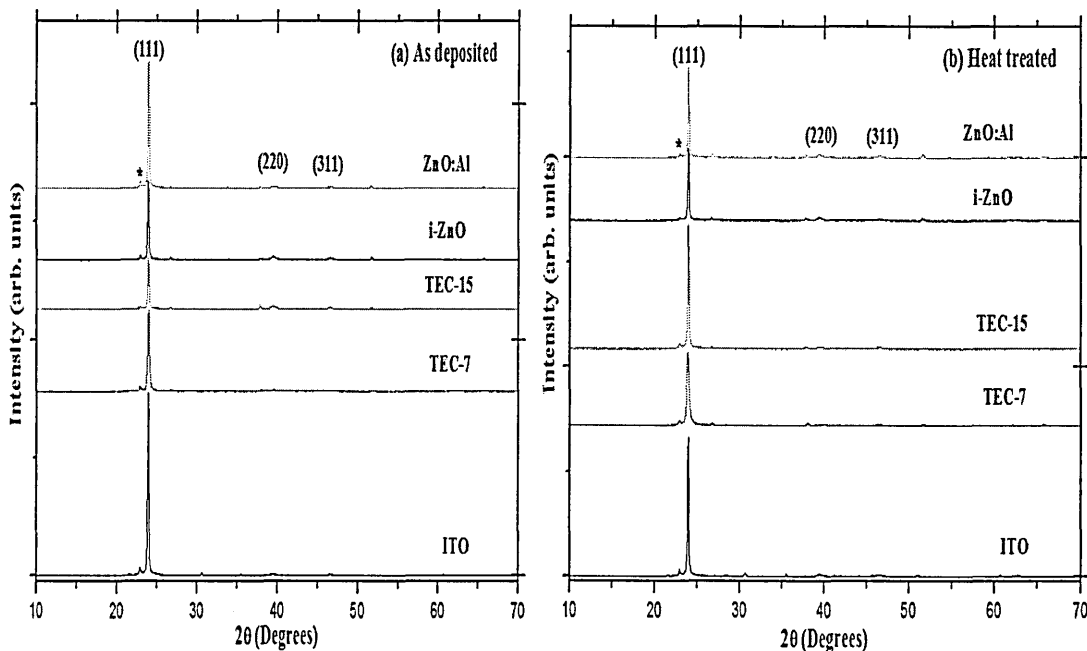


**Figure 10.1:** X-ray diffraction patterns of (n-i-p) CdTe layers grown on ED-CdS deposited on different TCOs (a) as deposited and (b) heat treated (\* indicates Te peak).

**Table 10.1:** XRD intensity, FWHM and grain size of (n-i-p) CdTe layers grown on ED-CdS deposited on substrate with different TCOs [AD = as deposited and HT = heat treated].

TCOs	XRD Intensity (arb. units)		FWHM		Grain size (nm)	
	AD	HT	AD	HT	AD	HT
ITO	7635	5600	0.140	0.120	10	13
TEC-7	3331	2772	0.175	0.140	8	15
TEC-15	2700	4753	0.184	0.152	6	10
i-ZnO	3200	2768	0.100	0.090	15	17
ZnO:Al	5293	3266	0.120	0.095	13	15

From the Table, it is observed that the crystallite size for heat treated sample increases and the FWHM decreases; this is due to the coalescence of small crystals and the formation of large grains. Furthermore, the FWHM was found to decrease after heat treatment. Such effect is due to the decrease in the concentration of lattice imperfections as a result of a decrease in the internal micro strain within the films or an increase in the crystallite size. It is observed that the smallest FWHM is found in the film grown on glass/FTO/i-ZnO substrate, which suggests that this may be a good substrate for CdS/CdTe thin film growth. Mazzamuto et al [5] and Dhere et al [6] reported that CdS/CdTe films grown on glass/FTO/ZnO:Al have better performance than those grown on FTO without a buffer, because of reduced surface roughness at the TCO/CdS interface. The buffer layer also hinders Na diffusion from the glass through the FTO into the active layers. Figures 10.2, 10.3 and 10.4 show the XRD intensity, FWHM and grain size of CdTe layers grown on CdS deposited on different TCOs.

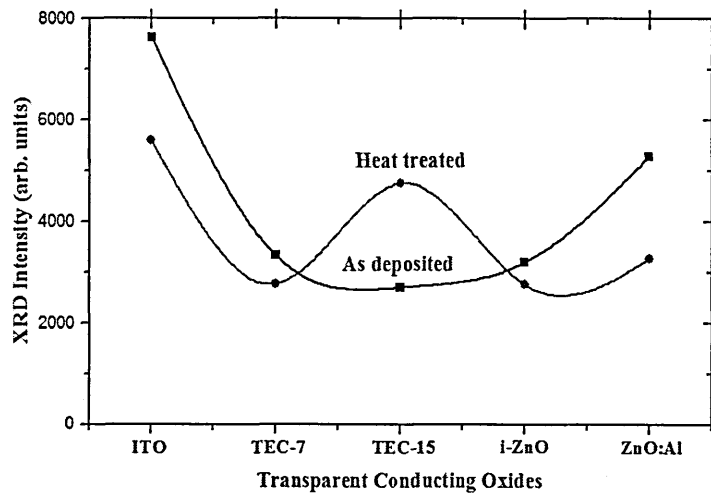


**Figure 10.2:** XRD intensity of (111) peak observed for (n-i-p) CdTe layers grown on CdS deposited on different TCOs.

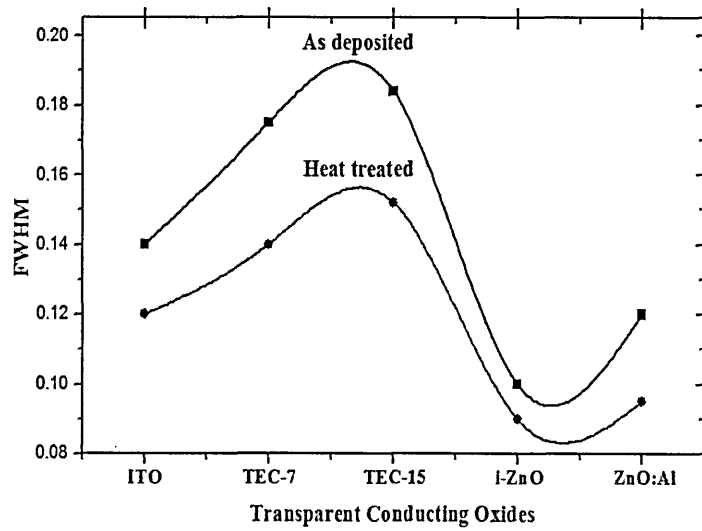


**Figure 10.3:** FWHM of (111) peak observed for (n-i-p) CdTe layers grown on CdS deposited on different TCOs.

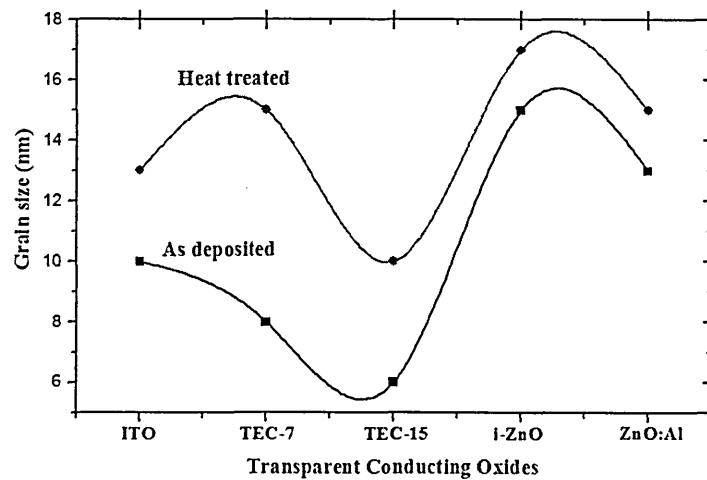


**Figure 10.4:** Grain sizes estimated from (111) peak observed for (n-i-p) CdTe layers grown on CdS deposited on different TCOs.

### 10.3.2 Optical absorption

Optical absorption measurements were carried out in order to evaluate the bandgap of the CdTe layer. Figure 10.5 shows the graphs of optical absorption for as deposited and heat treated (n-i-p) CdTe layers grown on ED-CdS deposited on different TCOs. Using equation 2.21 on section 2.2.3 in chapter 2, the bandgap energy values,  $E_g$  was determined by plotting the square of absorption ( $A^2$ ) against photon energy ( $h\nu$ ). As shown from the Figure, the value of  $E_g$  for as deposited samples varies between 1.53 eV and 1.55 eV. After heat treatment in air at 450°C for 15 minutes the bandgap values of all the samples decreased, and the absorption edge of the curve sharpened;  $E_g$  reduces to 1.45 eV which is closer to the  $E_g$  of CdTe bulk material. The reason for the sharpening might be due to a change in the stoichiometry or reduction of intrinsic defect population after heat treatment. Rami et al. [7] reported that the shift in the bandgap after heat treatment is due to the formation of  $CdS_xTe_{(1-x)}$ . Table 10.2 gives the bandgap values of (n-i-p) CdTe layers grown on ED-CdS deposited on different TCOs and Figure 9.6 shows the graphical presentation of the same results.

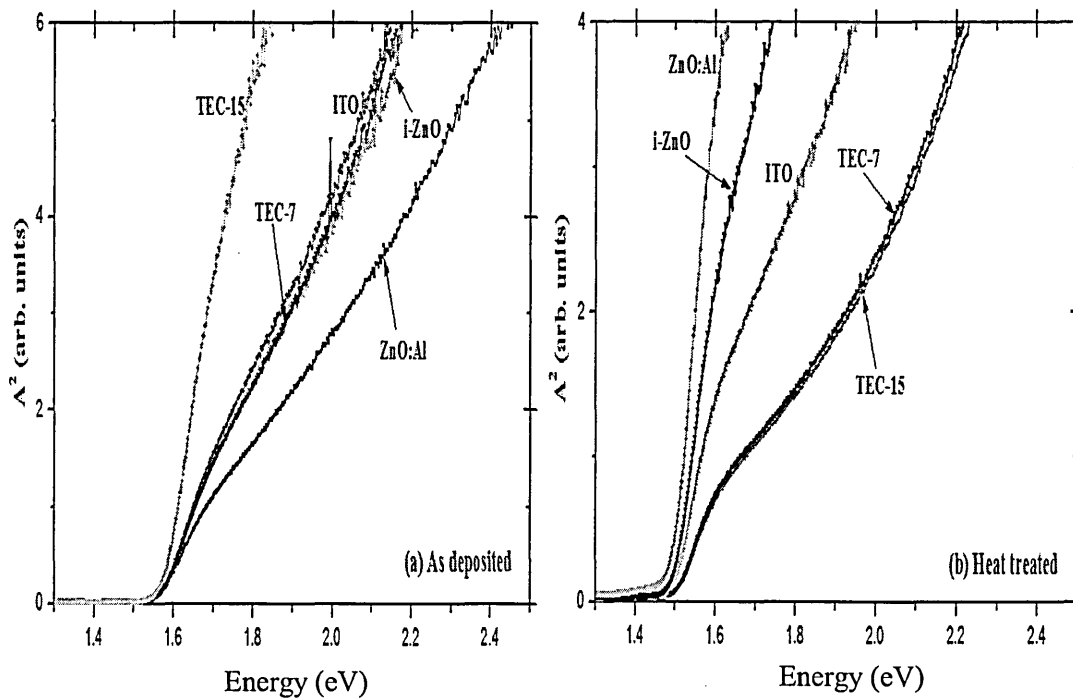


**Figure 10.5:** Optical absorption curves for (a) as deposited and (b) heat treated (n-i-p) CdTe layers grown on CdS deposited on different TCOs.

**Table 10.2:** Bandgap energy of (n-i-p) CdTe layers grown on CdS deposited on different TCOs [AD = as deposited and HT = heat treated].

TCOs	Bandgap (eV)	
	AD	HT
ITO	1.53	1.45
TEC-7	1.53	1.45
TEC-15	1.55	1.45
i-ZnO	1.53	1.45
ZnO:Al	1.53	1.45

As shown from Table 10.2, the bandgap energies of the as deposited CdTe samples is around 1.55 eV. This must be due to the quantum effects arising from small grains present in the layers. After heat treatment the bandgap the CdTe in all the samples are 1.45 eV which is close to the bulk CdTe value. The reason for this may be some or all of the following: a change in the stoichiometry, reduction of the intrinsic defect population and improved crystallinity.

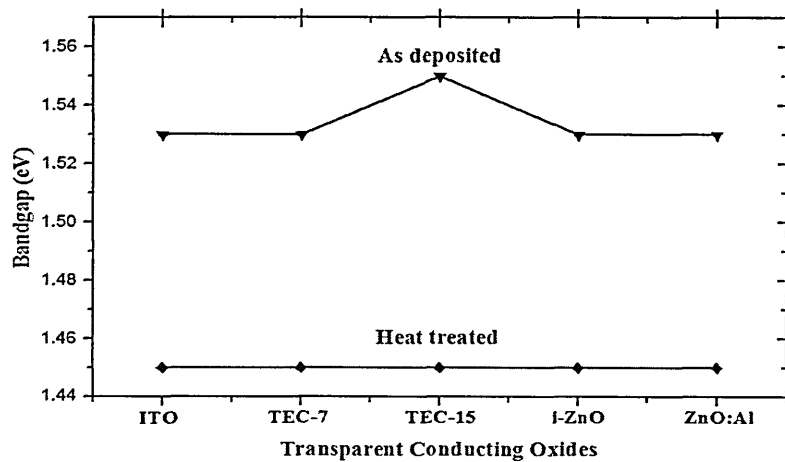


**Figure 10.6:** Bandgap energy of (n-i-p) CdTe layer grown on ED-CdS deposited on different TCOs.

The optical transmission spectra for as deposited and heat treated (n-i-p) CdTe layers grown on ED-CdS deposited on different TCOs are shown in Figure 10.7. Measurements were taken in the wavelength range 600 – 1000 nm on the deposited films. The transmission of all the as deposited films was found to be above 80% except for films grown on ZnO:Al and ITO where the absorption edge shifted to the blue region. After heat treatment the transmission decreases and the absorption edge

decreases. Furthermore, it is observed from Figure (b), the band edge of ZnO:Al gives the actual cut-off wavelength of CdTe  $\sim 852$  nm and the absorption edge shifted to the red region. Metin and Esen [8] reported that a sharper absorption edge indicates fewer defects and impurity energy levels in the bandgap of the material.

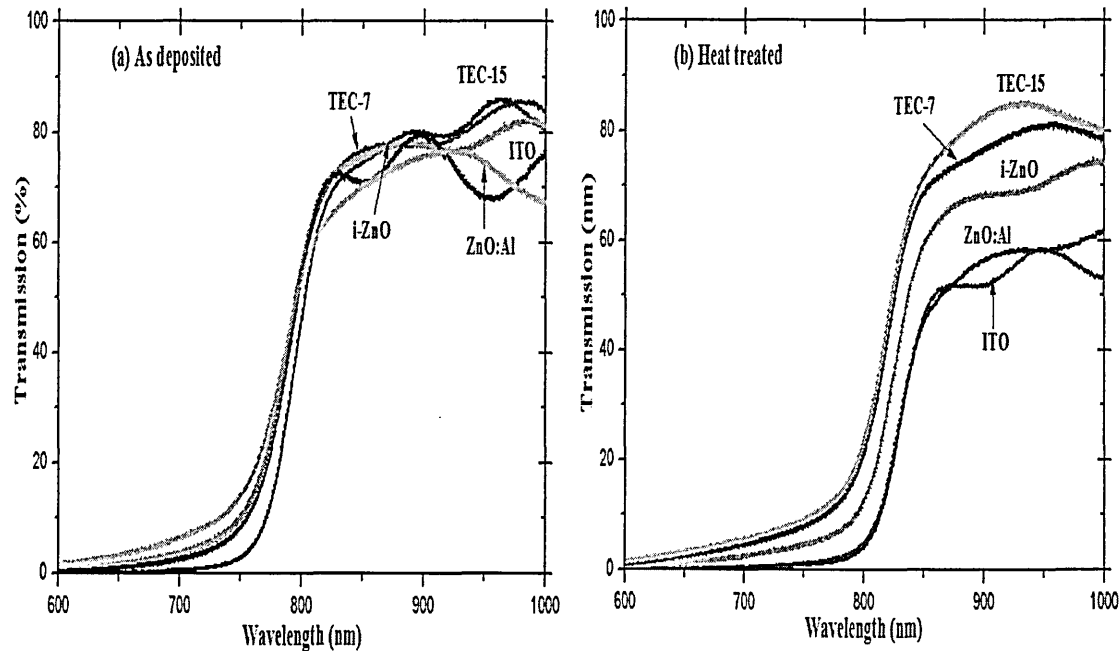


**Figure 10.7:** Transmission spectra for (a) as deposited and (b) heat treated (n-i-p) CdTe layers grown on CdS deposited on different TCOs.

### 10.3.3 Scanning Electron Microscopy

SEM studies were carried out to investigate the surface morphology, grain size and uniformity of the CdTe layers. Figure 10.8 shows the SEM images of (n-i-p) CdTe layers grown on CdS deposited on different TCOs. As shown from the Figure, as deposited samples show a lot of pin holes (gaps) between the grains especially on FTOs/CdS/CdTe substrates. One of the functions of the buffer layers is to reduce gaps and pin holes in the CdTe layer minimising leakage paths. It is known that Na diffuse into the CdTe solar cells during heat treatment and therefore limits the efficiency. Since Na is a p-type dopant, self-compensation takes place within the n-type CdTe. The use of buffer layer prevents this diffusion and hence helps to reduce this detrimental Na-

addition process. Buffer layer may also help the CdS growth uniformly or epitaxial instead of islands growth as seen from SEM images.

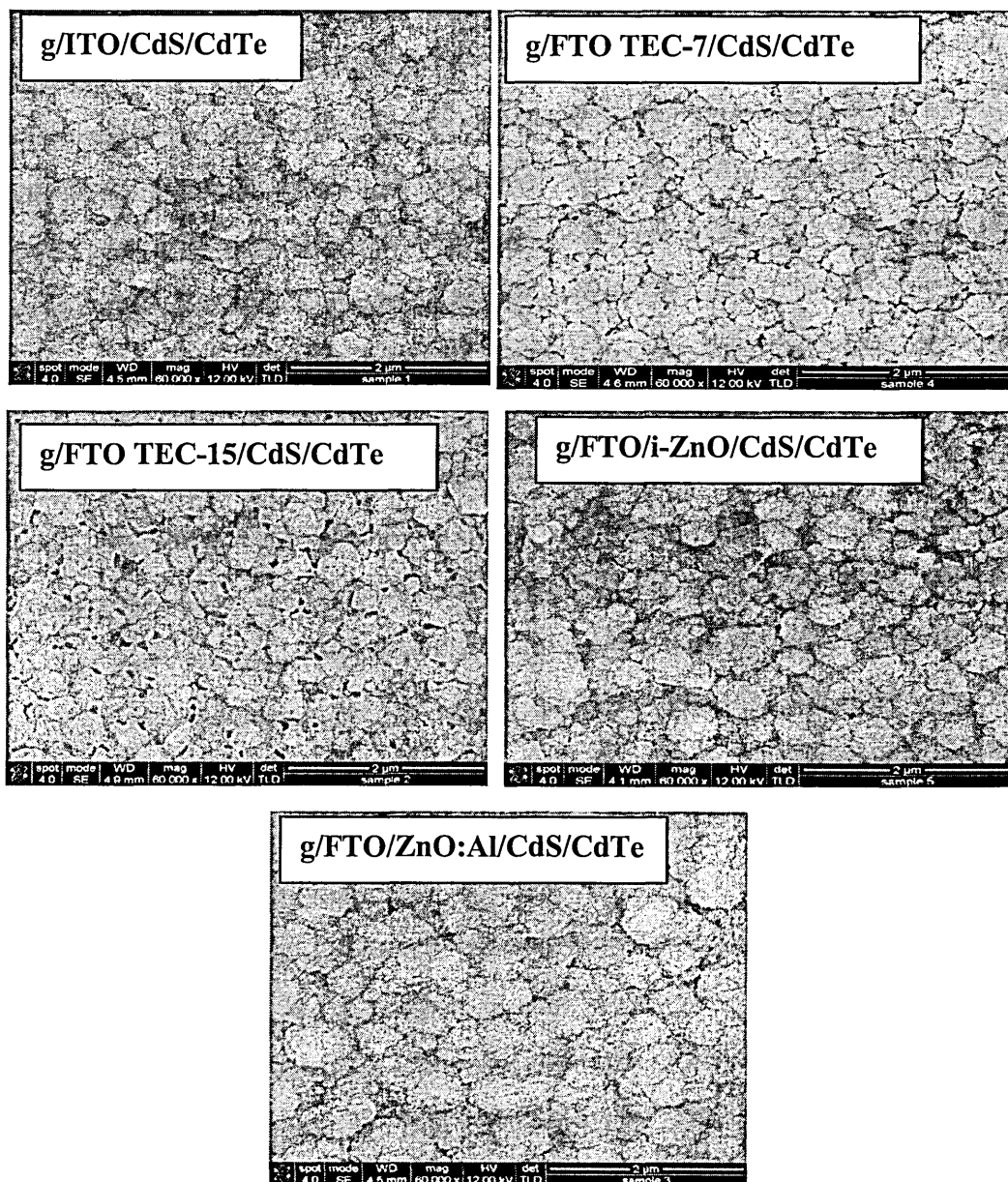


**Figure 10.8:** SEM images of as deposited (n-i-p) CdTe layers grown on CdS deposited on different TCOs.

Figure 10.9 shows the heat treated SEM images of (n-i-p) CdTe layers. After heat treatment the grain size increased and almost covered all the gaps. These result confirmed that heat treatment enhances the recrystallisation and coalescence of the grains to fill the gaps between the grains and forms a uniform thin layer of CdTe.

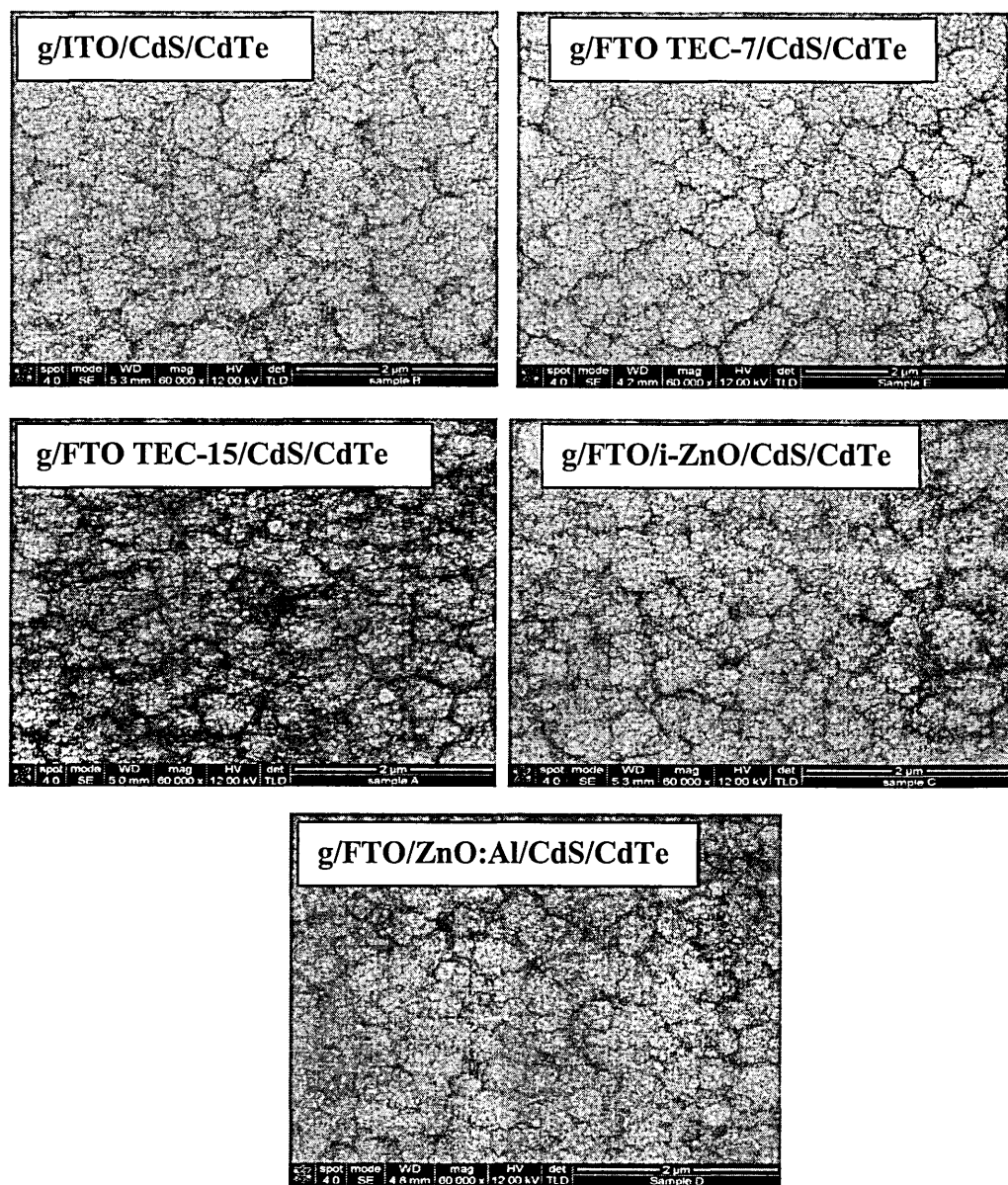


**Figure 10.9:** SEM images for heat treated (n-i-p) CdTe layers grown on CdS deposited on different TCOs.

### 10.3.4 Energy Dispersive X-ray

Energy dispersive x-ray (EDX) technique was carried out to investigate the qualitative elemental analysis of CdTe layers. The EDX spectra of heat treated (n-i-p) CdTe layers grown on ED-CdS deposited on different TCOs are shown in Figure 10.10. In all these spectra, the presence of both Cd and Te peaks were observed. The atomic composition of Cd:Te estimated from the spectra are 52.7:47.3, 51.2:48.8, 47.9:52.1, 50.8:49.2 and 54.1:45.9 for CdTe layers grown on CdS deposited on ITO, TEC-7, TEC-15, i-ZnO and ZnO:Al respectively.

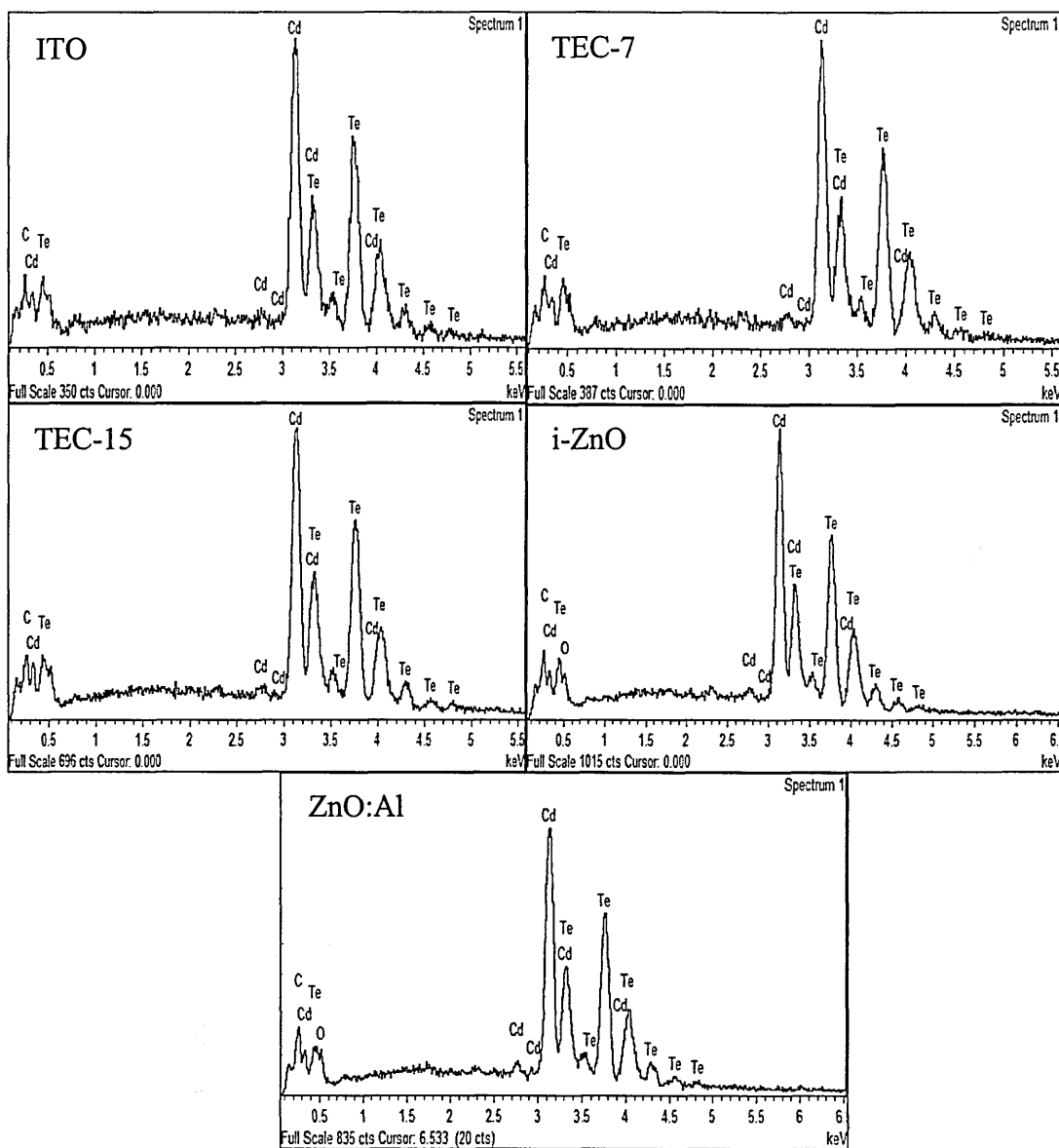


**Figure 10.10:** EDX spectra for heat treated (n-i-p) CdTe layers grown on CdS deposited on different TCOs.

### 10.3.5 Raman Spectroscopy

The molecular structure and identification of phases of the material is explored using Raman technique. Figure 10.11 shows the Raman spectra of a thick CdTe layer grown on InSb substrate, for comparison [9]. Also shown in Figure 10.12 are the Raman spectra of CdTe layers grown on ED-CdS deposited on various TCOs.

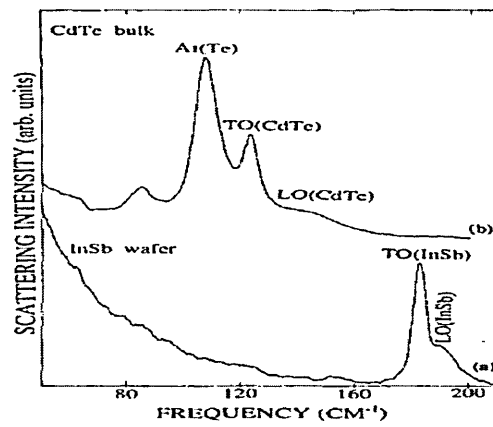


Figure 10.11: Raman spectra of a thick CdTe layer grown on InSb substrate [9].

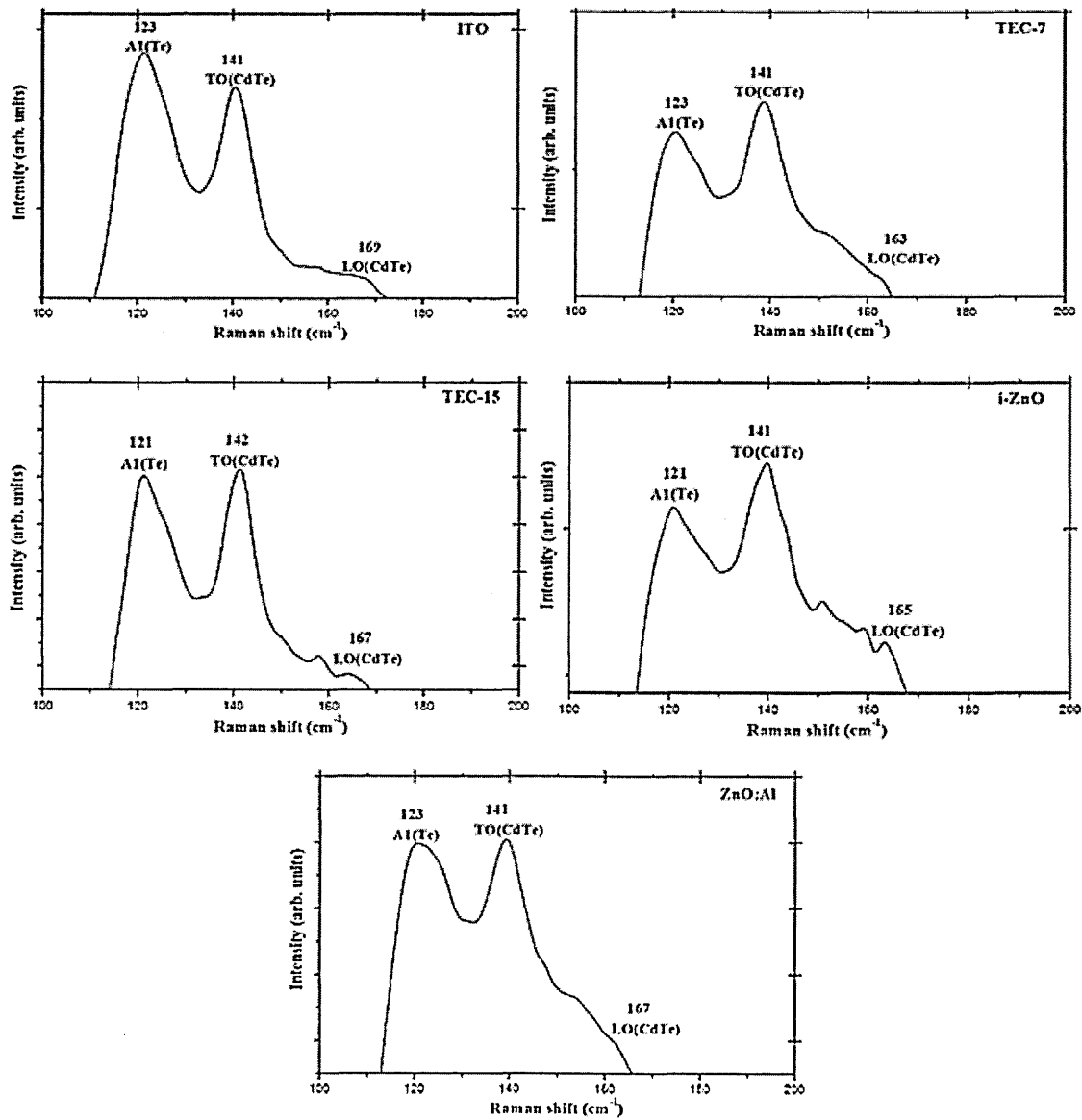


Figure 10.12: Raman spectra of (n-i-p) CdTe layers grown on ED-CdS deposited on various TCOs (courtesy: Inst. of Mater. Research, Univ. of Leeds).

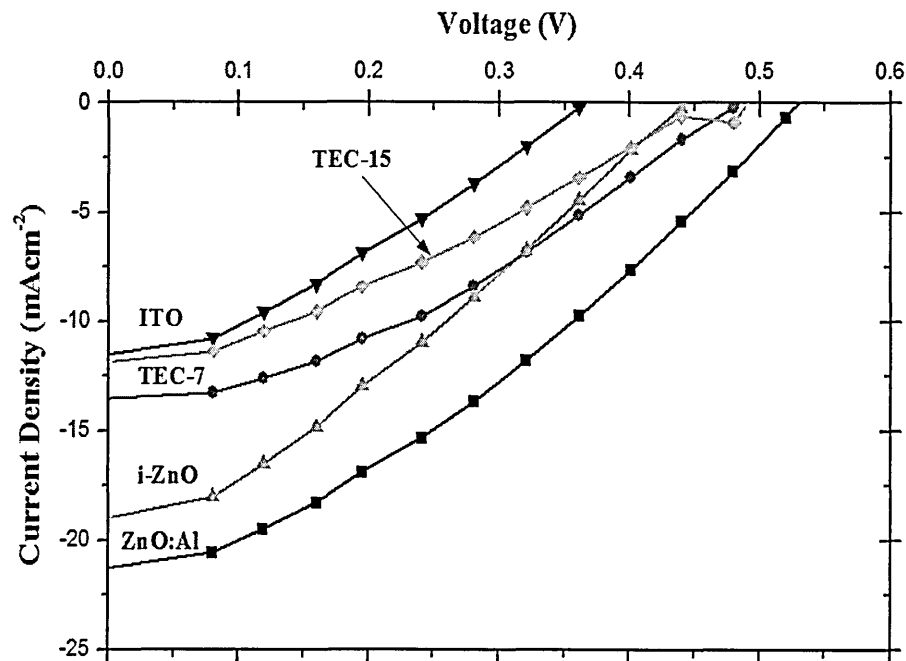
As shown in Figure 10.11, two peaks related to CdTe layers are identified at 141 - 142  $\text{cm}^{-1}$  and 165 - 169  $\text{cm}^{-1}$  and correspond to the fundamental transverse (1TO) and longitudinal optical phonons (1LO) respectively. Another peak at 121 - 123  $\text{cm}^{-1}$  is known to be the A1 phonon of the elemental tellurium. It is observed from the spectra that the features related to CdTe layer are most prominent in the film on the i-ZnO substrate which indicates the advantages of using a buffer layer in making solar cells. Furthermore, the TO(CdTe) is also dominant in this spectrum and the A1(Te) intensity has reduced, improving the quality of CdTe layer. All these peaks are very close to those reported by other researchers in the field [10-12].

#### 10.4 Device characterisation

As discussed in chapter 6, the completed glass/TCO/CdS/(n-i-p)CdTe/Au contacts were then assessed using I-V technique.

##### 10.4.1 Current-voltage (I-V) characteristics

Figure 10.13 show the linear I-V curves of glass/TCO/CdS/(n-i-p)CdTe/Au contacts under AM 1.5 illumination, for devices with CdTe layers grown on ED-CdS deposited on different TCOs.



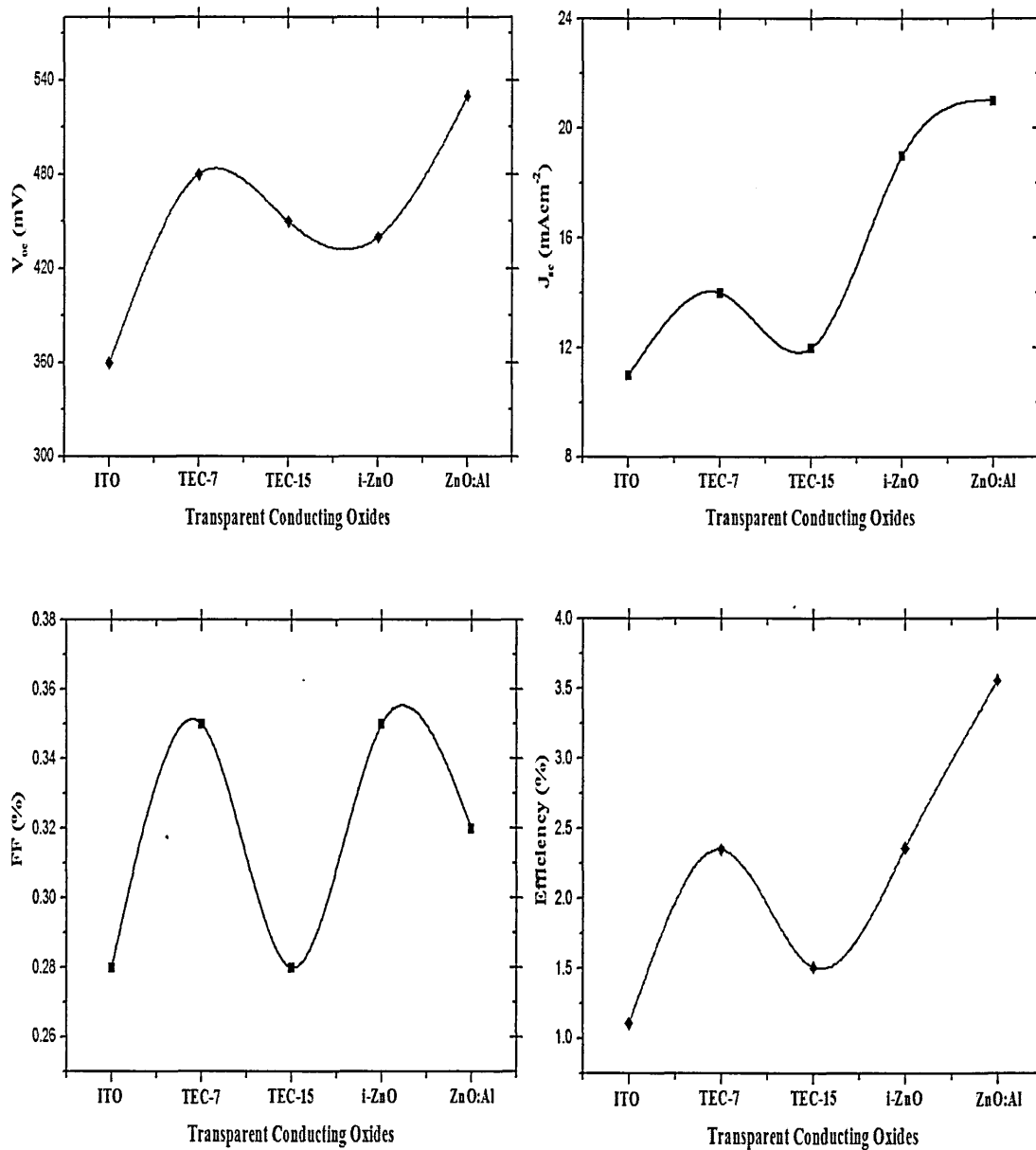
**Figure 10.13:** Linear I-V curve of glass/TCO/(n-i-p)CdS/CdTe/Au contacts under AM 1.5 illumination condition for (n-i-p) CdTe layers grown on ED-CdS deposited on different TCOs.

Table 10.3 shows the results of  $V_{oc}$ ,  $J_{sc}$ , FF and  $\eta$  of fully fabricated CdTe solar cells. A maximum efficiency of 3.56% with  $V_{oc} \sim 530$  mV and  $J_{sc} \sim 21$  mAcm<sup>-2</sup> were achieved for devices with CdTe layers grown on ED-CdS deposited on ZnO:Al substrate.

**Table 10.3:** Cell parameters under illumination of (n-i-p) CdTe thin film solar cells grown on CdS deposited on different TCOs.

TCOs	Cell parameters			
	$V_{oc}$ (mV)	$J_{sc}$ (mAcm <sup>-2</sup> )	FF (%)	$\eta$ (%)
ITO	360	11	0.28	1.11
TEC-7	480	14	0.35	2.35
TEC-15	450	12	0.28	1.51
i-ZnO	440	19	0.35	2.35
ZnO:Al	530	21	0.32	3.56

From the Table above, it is observed that the highest current density of 21 and 19 mAcm<sup>-2</sup> were achieved for ZnO:Al and i-ZnO which indicate that a buffer layer improves the performance of the solar cells. Mazzamuto et al [5] reported that to prevent Na diffusion into CdTe film during heat treatment through FTO, a buffer layer (e.g. ZnO:Al) must be used. It also separates the CdS from FTO in order to limit the effect of eventual pinholes that could be present in CdS. Figure 10.14 show the individual graphs of  $V_{oc}$ ,  $J_{sc}$ , FF and  $\eta$  of glass/TCO/CdS/(n-i-p)CdTe/Au/contacts. It was reported in the literature [1] to obtain a high efficiency the sheet resistance of the TCO must be less than 10  $\Omega/\square$ . The highest efficiency obtained is from ZnO:Al which have 3.8  $\Omega/\square$ .



**Figure 10.14:** Cell parameters of (n-i-p) CdTe layers grown on ED-CdS deposited on different TCOs.

### 10.5 Relationship between performance and TCOs.

Table 10.4 shows the summary of the relationship between the device performance and the TCO used. According to these results, the largest grains are grown on ZnO substrates, and the highest efficiency is produced with ZnO:Al. The high performance must be due to the formation of large grains combined with low sheet resistance of ZnO:Al.

**Table 7.5:** Summary of relationship between the cell performance and the TCO used.

TCOs	XRD parameters		Bandgap (eV)	Cell efficiency, $\eta$ (%)
	FWHM	Grain size, D (nm)		
ITO	0.120	13.0	1.45	1.11
TEC-7	0.140	15.0	1.45	2.35
TEC-15	0.152	10.0	1.45	1.51
i-ZnO	0.090	17.0	1.45	2.35
ZnO:Al	0.095	15.0	1.45	3.56

## 10.6 Summary

CdTe have been deposited on glass/TCOs/CdS substrates using low-cost aqueous electrodeposition method using two-electrode system. The XRD results for both as deposited and heat treated CdTe layers show a cubic structure with the main diffraction peak at  $2\theta = 23.642^\circ$  which corresponds to preferred orientation along (111) plane of cubic phase. Apart from the main peak (111), other peaks identified from the diffractogram are (220) and (311). These peaks are present in all the CdTe films but their intensity was different. When the CdTe layer is stoichiometric, these two peaks diminish indicating an increase in preferred orientation.

The optical absorption measurement shows the value of bandgap,  $E_g$  for as deposited samples vary in the range 1.53 eV - 1.55 eV. After heat treatment in air at  $450^\circ\text{C}$  for 15 minutes the bandgap values of all the samples decreased and absorption edge of the curve sharpened and gives 1.45 eV which is closer to  $E_g$  of the CdTe bulk material. The transmission of all the as deposited films was found to be above 80% except for ZnO:Al and ITO with the absorption edge shifted to the blue region. After heat treatment the transmission decreases, and the cut-off wavelength is close to that reported for CdTe  $\sim 852$  nm for the film grown on ZnO:Al; the absorption edge shifted to the red region.

SEM studies of as deposited samples show a lot of pin holes (gaps) between the grains especially on FTO/CdTe substrates. The presence of these empty spaces seems to be one of the main reasons for poor performance and inconsistent device performance. After heat treatment the grain size increased and almost covered all the gaps. It is clear that buffer layers such as i-ZnO and ZnO:Al help in drastically reducing the density of pin holes (gaps) in CdTe layer. Buffer layer may also help the CdS growth uniformly or epitaxial instead of islands growth as seen from SEM measurement.

EDX spectra of heat treated (n-i-p) CdTe layers indicate the presence of both Cd and Te in these layers. The approximate atomic composition of Cd:Te estimated from the spectra is 52.7:47.3, 51.2:48.8, 47.9:52.1, 50.8:49.2 and 54.1:45.9 for CdTe layers grown on CdS deposited on ITO, TEC-7, TEC-15, i-ZnO and ZnO:Al respectively. From the results the CdTe layers deposited on ZnO:Al substrate are rich in Cd, most probably due to slight change in Te-addition during CdTe layer deposition. Raman measurements indicate the prominent feature in the i-ZnO substrate is related to CdTe which confirm the EDX data showing that this film is close to stoichiometry. The

presence of a Te signal indicates the precipitation or presence of crystalline Te layer on CdTe surface in most films.

The linear I-V curves of glass/TCO/CdS/(n-i-p)CdTe/Au devices grown on CdS deposited with different TCOs gives a maximum efficiency of 3.56% with  $V_{oc}$  ~530 mV and  $J_{sc}$  ~21 mAcm<sup>-2</sup>; these parameters were achieved for devices with CdTe layers grown on ED-CdS deposited on ZnO:Al substrate. Furthermore, i-ZnO substrate produces the second best current density of 19 mAcm<sup>-2</sup>. It is known that Na diffuse into the CdTe solar cells during heat treatment and therefore limits the efficiency. Since Na is a p-type dopant, self-compensation takes place within the n-type CdTe. The use of buffer layer prevents this diffusion and hence helps to reduce this detrimental Na-addition process. The results from I-V measurement confirmed this situation. These results suggest that use of an appropriate buffer layer improves the quality of the solar cells. The work presented in this chapter indicates that the main effect of buffer layers like i-ZnO and ZnO:Al is to reduce pin holes or gaps in CdTe by changing the wetting properties at relevant interfaces, therefore the objectives have been achieved.

## References

1. A. Bosio, N. Romeo, S. Mazzamuto and V. Canevari, *Prog. in Cryst. Growth and Charact. of Mater.* 52, 247 (2006).
2. B. Szyszka, P. Loebmann, A. Georg, C. May and C. Elsaesser, *Thin Solid Films* 518, 3109 (2010).
3. D. Bonnet, In proc: 14<sup>th</sup> EUPSEC, Barcelona, Spain, 2688 (1997).
4. J. Britt and C. Ferekides, *Appl. Phys. Lett.* 62, 2851 (1993).
5. S. Mazzamuto, L. Vaillant, A. Bosio, N. Romeo, N. Armani and G. Salviati, *Thin Solid Films* 516, 7079 (2008).
6. R. G. Dhere, M. Bonnet-Eymard, E. Charlet, E. Peter, J. N. Duenow, J. V. Li, D. Kuciauskas and T. A. Gessert, *Thin Solid Films* (2010), doi:10.1016/j.tsf.2010.11.095.
7. M. Rami, E. Benamar, M. Fahoume, F. Chraibi and A. Ennaoui, *Mater. J. Condense Matter* 3(1), 66 (2000).
8. H. Metin and R. Esen, *Semicond. Sci. Technol.* 18, 647 (2003).
9. H-K Na and P-K Shon, *Solid State Communication* 85(7), 609 (1993).
10. J. Rouusset, E. Rzepka, D. Lincot, *J. Phys. Chem. B* 113, 4333 (2009).
11. Y. Jung, S. Chun, D. Kim and J. Kim, *J. Cryst. Growth* 326, 69 (2011).
12. R. Ocho-Landin, O. Vigil-Galan, Y. V. Vorobiev and R. Ramirez-Bon, *Sol. Energy Mater. Sol. Cells* 83, 134 (2009).

## Chapter 11: Future Work

CdS thin films have been deposited on glass/FTO substrates using a low-cost two electrode aqueous electrodeposition method. The XRD results indicate that both as deposited and heat treated ED-CdS layers are polycrystalline and have hexagonal structure with preferential orientation along the (101) direction. Photoelectrochemical (PEC) measurements show that the deposited layers are all n-type in electrical conduction. Optical absorption measurements give a bandgap of  $\sim 2.42$  eV for heat treated samples. 3D-AFM measurements shows that the layers consist of tightly packed and well defined nano-rods. Both 3D-AFM and SEM results reveal that these are holes or gaps in the CdS layer indicating island-type growth of CdS layers. This type of growth could leave detrimental effects on fully fabricated devices. XRF and XPS measurements show that the atomic ratio of Cd:S are close to stoichiometry. Raman spectroscopy identifies two peaks which are related to CdS.

The stability of CdS bath and its lifetime should be improved. In this work, the methods used to maintain a stable bath is reducing the pH and temperature. There is a need to control the sulphur precipitation in the CdS bath because films grown in this condition produce non-uniform layer and generate pin holes. Starting layer of CdS is crucial for developing high efficiency solar cells minimising leakage. The use of buffer layers such as i-ZnO and ZnO:Al in making solar cells is also recommended as it improves the efficiency of the device.

Thin film of ZnTe has been deposited on glass/FTO substrates by low-cost two electrode aqueous electrodeposition method using two different  $\text{Zn}^{2+}$  concentrations. A strong peak of ZnTe is observed at lower  $\text{Zn}^{2+}$  concentration from the XRD measurement showing better crystallinity of the film. The electrical conductivity of the deposited layer shows p-type from both lower and higher  $\text{Zn}^{2+}$  concentration using PEC measurement. 3D-AFM shows the presence of nano-rods like material layers. XPS results indicate that the compositions of ZnTe layer as 32.8:67.2 showing the electrodeposited layers are rich in Te. Raman measurement confirmed this by observing a strong Te- peak in the spectrum.

The deposition of ZnTe is successful but our aim is to use it in graded bandgap multi-layer solar cells. It is reported from literature that multi-layer solar cells produce higher

efficiency due to the higher internal electric field ( $E_i$ ) created within the device. ZnTe film grown in this work is Te-rich as shown from Raman, XPS and EDX measurements. Work should be continued to improve the layer and produce the stoichiometric ZnTe which is necessary for good devices. It is also necessary to investigate why ZnTe layer always peel-off when inserting into CdS and CdTe baths.

CdTe has been deposited on glass/FTO/ED-CdS substrates using a low-cost two electrode aqueous electrodeposition method. PEC measurements confirmed that electrodeposited layers produced n-, i- and p-type CdTe simply by changing the deposition voltage. The XRD results for both as deposited and heat treated materials confirm cubic structure with (111) preferred orientation. Close to the stoichiometric growth region only (111) peak is dominant indicating better crystallinity due to the presence of a single phase, CdTe. Away from stoichiometric region, crystallinity is poor due to presence of two phases either Te or Cd in addition to CdTe phase.

SEM studies show that the deposited layers had pin holes between crystallites. Their proportion depends on how far away from the stoichiometric position. 3D-AFM images show CdTe has highly-ordered and densely packed as columns perpendicular to the substrate. Two peaks related to CdTe and one Te peak was identified from Raman spectroscopy indicating presence of excess Te in electrodeposited layers. XPS work reveals that electrodeposited CdTe has a similar spectrum to that of clean cleaved CdTe except for the additional presence of C and O peaks which may be due to surface contamination.

It is established that thickness of CdTe has an impact on the solar cell performance. For comparison, six samples grown at different thickness were characterised by various techniques. I-V measurements for completed glass/FTO/ED-CdS/CdTe/Au devices give the maximum efficiency of 7.60% with  $V_{oc} \sim 660$  mV,  $J_{sc} \sim 24$  mAcm<sup>-2</sup> and FF  $\sim 0.48$  were achieved for 5 hrs growth of CdTe. The efficiency goes down as the thickness increase or decrease. From log I vs. V results, rectification factor (RF)  $\sim 10^{3.7}$ , n value  $\sim 1.88$  and  $\phi_B \sim 1.20$  eV were achieved. The capacitance-voltage measurement gives  $V_d \sim 1.35$  eV and doping concentration ( $N_D$ ) of  $\sim 2.0 \times 10^{17}$  cm<sup>-3</sup>.

One of the main challenges facing most of the growth techniques is the reproducibility. The electrolytic bath composition should be continuously monitored. There is a need to

use double-distilled water instead of de-ionised water in preparing our electrolytic baths. This will enable the researchers to minimise impurities in electrolytic baths.

The use of graphite carbon rod as a cathode and an anode need serious consideration. During the growth process, the graphite carbon particles sometimes fall into the bath which alters the uniformity and adhesion of the deposited layer. This could also be a continuous impurity source to the electrolyte. It is therefore necessary to replace this graphite carbon electrode with high purity cadmium electrode.

Te- addition method is another task to be improved. It is very difficult to know exactly the amount of  $\text{TeO}_2$  inside our bath. It has been found that the growth of stoichiometric CdTe is possible by careful control of the Te- addition. It is recommended to use a pump which may be able to control the Te- addition to the bath. The work presented in this thesis shows the presence of excess Te in both ZnTe and CdTe layers. Efforts should be made to minimise these excess Te in order to improve device efficiencies.

Thickness is a very important parameter to know when growing semiconductor materials. The methods usually employed to obtain the thickness of our material layers is Faraday's estimation and DEK-TAK method. In the future work, other methods such as SEM cross section, gravimetry and ellipsometry should be used for comparison. Furthermore, we need to know the sheet resistance of the TCOs which is also necessary. Methods used to measure this parameter include transmission-line model (TLM) measurement, four-point probe, microwave probes etc.